Modelling rock fractures using SPH with an embedded fracture process zone

Yingnan Wang

BEng (First Hons)

A thesis submitted for the degree of Doctor of Philosophy at Monash University in 2019

Department of Civil Engineering

Copyright Notice

Abstract

Fractures in rock or rock-like materials play a vital role in many geophysical processes and engineering applications involving rocks, such as excavations, earthquakes, rock blasts and energy extraction of gas and petroleum. Numerous experimental studies have been conducted to characterise mechanical and fracture properties of these materials, as well as to investigate their failure mechanisms. In parallel with this, numerous constitutive models have also been developed, taking into consideration insights from the experimental studies, to describe the material responses under various loading conditions. However, most existing constitutive models developed at laboratory scale do not possess intrinsic length scale, thus often failing to correctly describe failure mechanisms of rock materials when being used for large-scale engineering applications. Consequently, the use of existing models for large-scale applications must be undertaken with care, as it can lead to inaccurate predictions, over-engineered designs or, in the worst scenario, catastrophic disasters such as mine tunnel collapses or leakage of poisonous gases.

In order to enhance the capability of existing computational tools for modelling rock fractures, the aim of this research is to develop an advanced computational framework that includes intrinsic spatial and temporal scales. In this computational framework, a new continuum-based constitutive model with embedded discontinuity is developed and then incorporated into the mesh-free smoothed particle hydrodynamics (SPH) method, capable of handling problems involving complex fracture networks. In particular, a length scale parameter is introduced into the constitutive equations to take into account the relative size of the fracture process zone and its surrounding rock masses, thereby naturally capturing the spatial scale effects of rock fractures. A mixed-mode cohesive fracture law for capturing the plastic and damage evolutions of material under various loading conditions is formulated and coupled with the continuum constitutive framework with the embedded discontinuity that possesses the length scale effect. The combination of the two constitutive models results in a novel continuum constitutive model capable of predicting mixed-mode rock fractures across scales.

Apart from the spatial scale effect, the strong dependence of fracture processes and mechanical properties of rocks on loading rates is also considered in this study, using two different approaches. In the first approach, the strain rate effect on tensile strength is incorporated into the mixed-mode cohesive fracture model, which is represented by a dynamic increase factor

with respect to the strain rate. In this approach, the boundary condition is treated in the same way as quasi-static cases in which a constant velocity is applied to the boundary particles. In the second approach, the strain rate effect is introduced by applying an elliptical-shaped force history to the boundary particles. The rate effect of rocks, in this case, can be automatically captured thanks to the dynamic nature of SPH method.

The proposed framework is shown to be capable of dealing with complex crack patterns and large deformations because the fracture patterns are represented by a set of damaged SPH particles, each of which possesses its own fracture process zone in arbitrary orientation depending upon the stress condition. This new framework can also predict the underlying failure mechanisms of different rock types under a wide range of loading conditions. Importantly, the proposed framework is also able to take into account intrinsic regularisation effects and size-dependent behaviour, thanks to the introduction of a length scale parameter into the constitutive structure. Furthermore, the proposed numerical approach is shown to successfully capture the strain rate effect on mechanical properties and fracturing processes of rocks for comparison with experimental results. To this end, this research provides an accurate and realistic numerical approach capable of modelling mixed-mode complex rock fractures across spatial and time rate scales.

Declaration

This thesis contains no material which has been accepted for the award of any other degree or diploma at any university or equivalent institution and that, to the best of my knowledge and belief, this thesis contains no material previously published or written by another person, except where due reference is made in the text of the thesis.

Signature:

Print Name: Yingnan Wang

Date: 4th of December, 2019

List of Publications

✓ *Journal paper*

1. Wang, Y., Bui, H. H., Nguyen, G. D., & Ranjith, P. G. (2019). A new SPH-based continuum framework with an embedded fracture process zone for modelling rock fracture. International Journal of Solids and Structures, 159, 40-57.

2. Tran, H. T., Wang, Y., Nguyen, G. D., Kodikara, J., Sanchez, M., & Bui, H. H. (2019). Modelling 3D desiccation cracking in clayey soils using a size-dependent SPH computational approach. Computers and Geotechnics, 116, 103209.

3. Wang, Y., Tran, T. H., Bui, H. H., Nguyen, G. D., & Ranjith, P. G. (2019). Simulation of mixed-mode fracture using SPH particles with an embedded fracture process zone. International Journal for Numerical and Analytical Methods in Geomechanics. *(Accepted, in-press)*

4. Wang, Y., Bui, H. H., Nguyen, G. D., & Ranjith, P. G. (2019). Modelling 3D dynamic rock fractures using SPH method with an embedded mixed cohesive fracture law. International Journal of Rock Mechanics and Mining Sciences *(In preparation)*

✓ *Conference paper*

1. Wang, Y., Bui, H. H., Nguyen, G. D., & Ranjith, P. G. (2017). A Mesh-Free Continuum Based Computational Approach to Modelling Rock Fracture. In 6th Biot Conference on Poromechanics (pp. 2041-2048). American Society of Civil Engineers.

2. Wang, Y., Bui, H. H., Nguyen, G. D., & Gamage, R. P. (2017). Numerical simulation of size effect on rock fracture using SPH and a size-dependent constitutive model. In 9th Australasian Congress on Applied Mechanics (ACAM9) (p. 741). Engineers Australia.

Thesis Including Published Works Declaration

I hereby declare that this thesis contains no material which has been accepted for the award of any other degree or diploma at any university or equivalent institution and that, to the best of my knowledge and belief, this thesis contains no material previously published or written by another person, except where due reference is made in the text of the thesis.

This thesis includes one original paper published in peer reviewed journal, one published conference paper and one submitted publication. The core theme of the thesis is to development an advance computational framework for simulating rock fractures. The ideas, development and writing up of all the papers in the thesis were the principal responsibility of myself, the student, working within the Department of Civil Engineering at Monash under the supervision of Dr. Ha Hong Bui. The inclusion of co-authors reflects the fact that the work came from active collaboration between researchers and acknowledges input into team-based research.

In the case of Chapter 5 and 6, my contribution to the work involved the following:

Thesis Chapter	Publication Title	Status	Nature and % of student contribution	Co-author name(s) Nature and % of Co-author's contribution*	Co-author(s), Monash student Y/N*
5	A new SPH-based continuum framework with an embedded fracture process zone for modelling rock fracture	Published	70%, Idea, model, analysis, write up	1) Ha H. Bui, idea, interpretation, reviewing, 20% 2) Giang D. Nguyen, idea, reviewing, 5% 3) Ranjith, P.G., idea, reviewing, 5%	No No No
5	Numerical simulation of size effect on rock fracture using SPH and a size-dependent constitutive model	Published	70%, Idea, model, analysis, write up	1) Ha H. Bui, idea, interpretation, reviewing, 20% 2) Giang D. Nguyen, idea, reviewing, 5% 3) Ranjith, P.G., idea, reviewing, 5%	No No No
6	Simulation of mixed-mode fracture using	Accepted, in-press	60%, Idea, model,	1) Tran, H.T., idea, interpretation, 10%	Yes

	SPH particles with an embedded fracture process zone		analysis, write up	2) Ha H. Bui, idea, interpretation, reviewing, 20% 3) Giang D. Nguyen, idea, reviewing, 5% 4) Ranjith, P.G., idea, reviewing, 5%	No No No

I have renumbered sections of submitted or published papers in order to generate a consistent presentation within the thesis.

Student signature: **Date: 4th of December, 2019**

The undersigned hereby certify that the above declaration correctly reflects the nature and extent of the student's and co-authors' contributions to this work. In instances where I am not the responsible author I have consulted with the responsible author to agree on the respective contributions of the authors.

Main Supervisor signature: **Date:4th of December, 2019**

Acknowledgement

The journey of my Ph.D was just like climbing a high mountain step by step, and I couldn't reach the peak without the help from a great many people including my supervisors, my colleagues and my family. Therefore, I would like to give my deep and sincere gratitude to these people for their support, help and encouragement throughout this journey.

First of all, I would like to thank my main supervisor Dr. Ha Hong Bui for giving me the opportunity to study at Monash University and providing invaluable guidance and support in the last five years. His vision, sincerity and attitude to work inspire me to overcome all the ups and downs during this journey. I would like to acknowledge the valuable support from my co-supervisors, A. Professor Giang Nguyen at the University of Adelaide and Professor Ranjith Pathegama Gamage at Monash University. They provided insightful comments to improve my research papers. I especially thank A. Professor Giang Nguyen for the help and support during the development of constitutive models. His expertise in specialised knowledge and rigorous attitude to research motivated me a lot.

I would also like to thank all the Monash Computational Geomechnical Lab (MCG Lab) members. It was a great pleasure working with them and I appreciate their ideas and helps to my research. Special thank goes to Dr. Hieu Tran for his help and patience during the research collaboration with me. I am also grateful to Ms Jane Moody and Ms Joan Rosenthal for their proofreading of my thesis.

My deepest appreciation belongs to my parents (Bin Wang & Ruifang Ge) who tried their best to provide me the best education resources and offer me limitless love and support. I also acknowledge their support and sacrifices from my parents in law (Binzheng Zhao & Qiaoling Gao) during the journey of my PhD. Finally, I want to give my thanks to my husband, Shaohan Zhao. He is not just my partner, but a teammate, sidekick and best friend. Thanks for his accompany, encouragement and support at work and in our lives. Special thanks go to my son Henry and the little one who is now healthily growing in my belly. Thank them for filling my heart with love and happiness and motivating me to be a better person. Being a mother of two beautifully angels has been, without a doubt, my greatest source of achievement, pride and inspiration.

Yingnan Wang

Dec 2019

Table of Contents

List of Figures

List of Tables

Chapter 1

Introduction

1.1. Problem Statement

Rock fractures plays an important role in both civil and mining engineering applications. Understanding rock fracture processes under a wide range of loadings will contribute to the reduction of both the cost of engineering projects and the risks that exist at construction sites. Common engineering activities which involve rock fracture problems are as follows: first, tunnel construction requires the control of rock behaviour, especially when excavating techniques are used; second, the mining industry specifies certain rock sizes for mineral samples, thus, setting the loading rates at which the crusher is operated to output such mineral is critical, requiring excellent understanding of rock behaviour under dynamic loads; third, pit/foundation excavation in rock materials using blasting techniques must be backed up with good knowledge of rock behaviour in order to create the desired geometry of the excavation area. These applications all indicate the importance of a comprehensive understanding of the behaviour of rock fractures.

In the past few decades, both experimental and numerical analyses have been conducted to simulate rock fractures. In experimental studies, rock mechanical and fracture properties have been intensively investigated by conducting uniaxial or triaxial compression tests (Frew et al. 2010), tensile tests (Asprone et al. 2009) and shear tests (Lipkin et al. 1979). The findings show that the mechanical properties of rock, such as compression strength, tensile strength, shear strength and dynamic fracture toughness, are strongly affected by the loading/strain rates. Moreover, experimental results show that the behaviour of rock fractures is also dependent on rock size under both quasi-static and dynamic loadings (Li et al. 1993). Many attempts have been made to derive empirical equations to express the relationship between the loading/strain

rate and the strengths based on these laboratory results. However, the mechanism of fracture behaviour of rock is still unclear.

On the other hand, numerical approaches have been developed to tackle this problem. Studies in this area have been conducted based on both classical continuum theory and discontinuous theory. In classical continuum theory, however, it is well known that the computational solutions present ill-posed boundary problems as well as mesh dependency problems when the constitutive relation comes into a softening region. Several attempts have been made to address these issues in different ways through introducing a smeared crack band (Bažant and Oh 1983), a high order strain gradient (Askes et al. 2002), rate-dependent theories (Saksala 2010) and extended finite element method (Belytschko and Black 1999). Although these remedial approaches can predict the fracture behaviour to a limited extent, most ignore the size and loading rate effects observed in the laboratory. Moreover, the underlying constitutive relationships adopted in these approaches rely heavily on the stress-strain curve calibrated from experiments, thus failing to provide an accurate solution under loading rates beyond the calibration ranges. These problems in classical continuum theory make it difficult to reliably predict rock fracture. Discontinuum-based methods show more flexibility when dealing with rock fractures. Examples are discrete element methods (Cundall and Strack 1979), discontinuous deformation analysis (Mortazavi and Katsabanis 2001), manifold methods (Shi 1992) and the hybrid FEM/DEM method (Coggan, Pine et al. 2003). Unlike continuum-based methods, they present the computation domain as an assembly of separate blocks or particles, and thus providing good capacity to deal with large deformation and complete detachment problems. However, the computational costs incurred are prohibitively high for even a laboratory-size simulation, due to the discrete nature of the modelling, not to mention a real-life engineering scale.

The outline provided highlights the current knowledge gap in modelling rock fractures. To address this problem, a robust computational framework that possesses both intrinsic length and time scales capable of describing size- and rate-dependent behaviour under complex loadings is needed.

1.2. Aims and Scope of the Study

This study aims to develop a robust computational model to simulate rock fractures under a wide range of loading conditions and also to predict the loading effect and the size effect on rock fracture behaviour. Emphasis is placed on developing an advanced continuum constitutive

model with embedded discontinuity. The novel constitutive model will be incorporated into a robust computational approach based on smoothed particle hydrodynamics (SPH) for simulating the behaviour of rock fractures with high computation efficiency.

The necessary objectives to achieve the stated aim of this project are as follows:

1. To develop a robust SPH framework for simulation of rock fractures;

   Although traditional SPH has been widely used in many geoengineering applications, it still suffers some inherent numerical instabilities such as tensile instability and particle inconsistency, especially when SPH particles experience tensile loading. As rock fracture problems are closely related to tensile loading or tensile-shear loading, some enhancements must be implemented to improve the numerical stability of the SPH framework in simulating rock fracture problems.

2. To develop a continuum constitutive model with embedded time and length effects to simulate rock fractures under various loading conditions;

   A continuum-based constitutive framework with embedded discontinuity will be proposed by combining a double-scale continuum framework with an intrinsic length scale and a mixed-mode rate-dependent cohesive fracture law. For this purpose, a size-dependent constitutive model based on the double-scale model is proposed to capture the size effect on the material under pure mode I loading. Then the constitutive model is further developed for predicting both tensile and shear failure at the constitutive level by incorporating a mixed-mode cohesive fracture law. The final part of the development of the constitutive model is the introduction of a rate-sensitive component into the cohesive fracture law in order to capture the rate-dependent behaviour of rock fractures.

3. To accurately predict the rock fracturing processes across spatial and temporal scales by using the novel constitutive model and the new SPH numerical framework.

   In the final research aim, the novel constitutive model is incorporated into the new SPH framework for developing a new continuum numerical framework in simulating dynamic rock fractures. The proposed framework is capable of predicting rock fracturing processes under a wide range of loading conditions. Due to the inclusion of length- and rate-sensitive parameters in the constitutive model and the dynamic nature of the SPH method, the proposed numerical framework is capable of predicting the effects of size and loading rates on rock fractures.

The contribution of this study will be the establishment of an accurate and realistic approach for predicting rock fractures under a wide range of complex loadings.

1.3. Outline of the Thesis

This thesis is organised into eight chapters which can be grouped into four parts, shown in Figure 1.0–1. The first group includes the introduction of this thesis in Chapter 1 and a literature review of rock fractures in Chapter 2. The second group is the numerical methodology consisting of the SPH framework (Chapter 3) and constitutive models for rock fractures (Chapter 4). The third group is the key part of this thesis, which presents the numerical results and discussion of this research on rock fractures. This section consists of three chapters (Chapters 5-7). The last section is the conclusions and recommendations for future research. A description of each chapter in this thesis follows.

Chapter 1 is the introduction of this thesis. The background of rock fractures has been provided, followed by the research aims in this study.

Chapter 2 comprehensively presents a review of extant literature on rock fractures. Analytical, experimental and numerical studies of rock fractures are reviewed. The effects of loading rate and specimen size on the behaviour of rock fractures are emphasised. In particular, an overview of existing numerical methods for simulating rock fractures is provided. The limitations of each approach in capturing complex fracturing processes across spatial and temporal scales are discussed. This underlies the motivation in this study to develop a continuum-based rate-dependent computational approach that possesses an intrinsic length scale for modelling rock fractures under both quasi-static and dynamic loading conditions.

Chapter 3 presents the mesh-free smoothed particle hydrodynamics (SPH) framework which is adopted in this study as the numerical platform for the implementation of constitutive models. The basic formulations of SPH are listed, followed by the introduction of some enhancements for minimising the inherent instabilities in traditional SPH, thereby improving the stability of numerical solutions. Some SPH simulation examples on elastic solids are presented at the end of this section.

Chapter 4 is about constitutive modelling of rock fractures. In this chapter, existing constitutive frameworks for modelling of fractures are reviewed, from simple frameworks such as the damage model to complex frameworks such as the strong discontinuity approach. Key formulations, together with the strengths and limitations of the existing models, are listed.

Based on the review of those models, a constitutive concept to correctly represent localised failure of rocks is established.

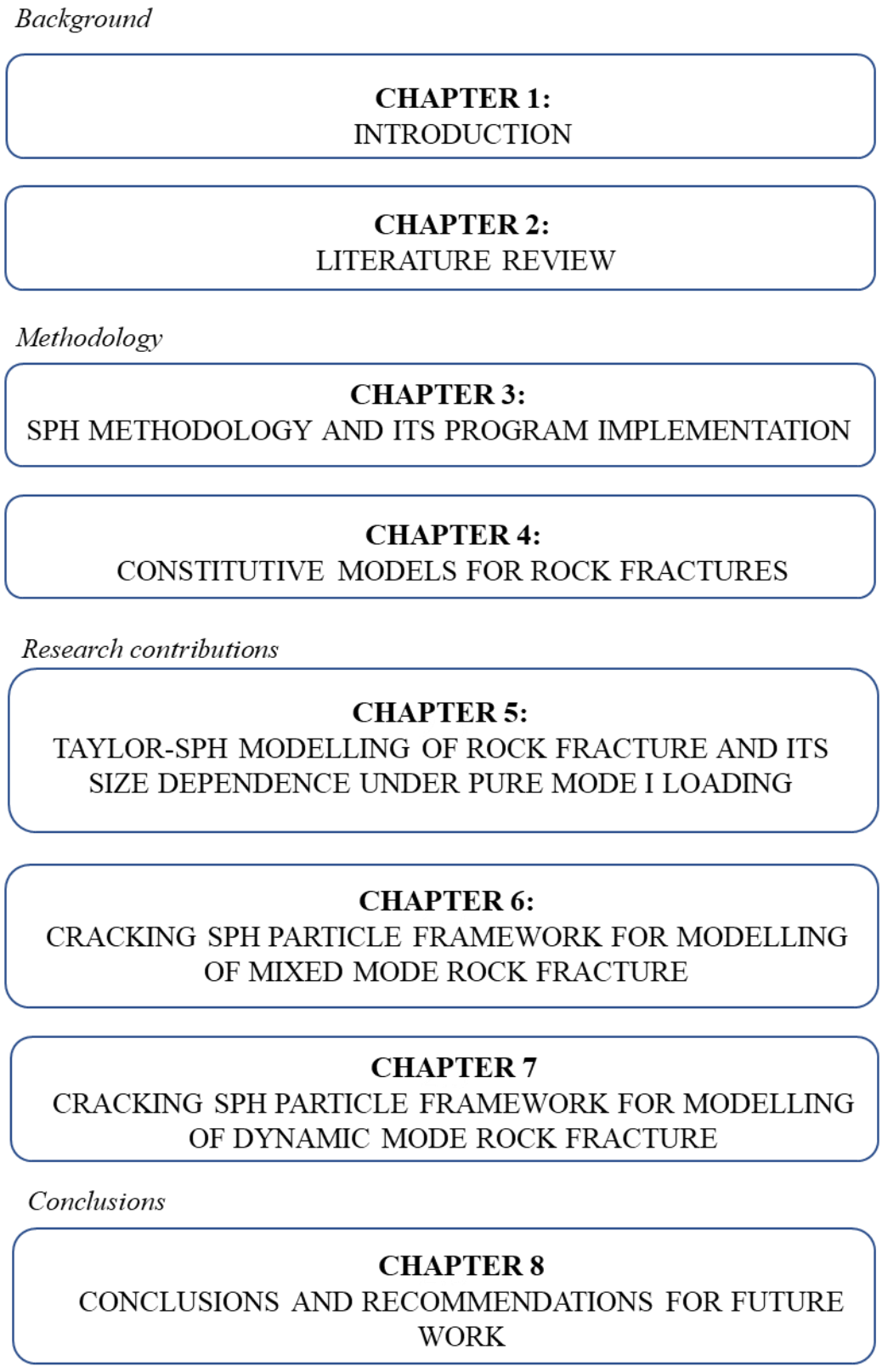

Figure 1.0–1. Thesis outline

In Chapter 5, the behaviour of rock fracture and its size effect under pure mode I loading is simulated using the proposed computational framework by combining the Taylor SPH framework with a new continuum constitutive model containing an embedded fracture process zone. As Taylor SPH is an improved SPH method which does not suffer from any tensile instability, and meanwhile the proposed constitutive model takes into account the localisation of failure within the fracture process zone of rocks, the new framework can easily handle large deformation occurring in rock fractures. The size effect on rock fractures is also examined in this section and compared with experiments. Although only tensile failure is captured, due to the incorporation of a simple pure mode I cohesive fracture law, this section provides a fundamental basis bridging the constitutive and structural aspects, via a length scale directly obtained from the particle size, for further development in SPH towards better modelling of fracture and fragmentation.

Chapter 6 focuses on the mixed-mode failure of rock materials under quasi-static loading. A computational framework based on the traditional SPH is developed, providing an alternative method for simulating rock fractures apart from the one proposed in Chapter 5. To solve the numerical instabilities in traditional SPH, some techniques such as artificial viscosity, tensile instability and corrective SPH are used. Unlike the work presented in Chapter 5 which focuses on pure mode I fracture, the fracture process zone in this study is described by a mixed-mode cohesive fracture law for capturing the plastic and damage evolutions of material under various loading conditions. The constitutive behaviour under mixed-mode conditions is examined, followed by simulation of mixed-mode rock applications.

In Chapter 7, two numerical approaches to simulate rock fractures under dynamic loadings are proposed, dividing this chapter into two sections. In the first approach, the computational framework proposed in Chapter 6 is further developed by incorporating the strain rate effect for rock or similar quasi-brittle material on tensile strength into the mixed-mode cohesive fracture model. In the second approach, an elliptical force history with time is imposed on the boundary particles in SPH for simulating dynamic loading. Thanks to the dynamic nature of SPH, the computational approach presented in Chapter 6 together with the implementation of dynamic loading can handle dynamic rock fractures naturally without any special treatment. Both approaches are validated by comparing the numerical results with the experimental results.

Chapter 8 presents the conclusions and recommendations for future research, summarising the main findings of the research and providing suggestions for future work on this topic.

Chapter 2

Literature Review

2.1. Introduction

Understanding of rock fracture behaviour under complex loading conditions is important in civil engineering applications and energy exploration activities such as tunnel construction, oil and gas extraction and underground water transport. Numerous research efforts have been made in investigating rock fracture problems under a wide range of loadings in the last few decades, which can be divided into analytical, experimental and simulation studies.

Analytical studies of rock fractures are introduced first, which can be traced back to the invention of linear elastic fracture mechanics in the previous century. Since then, many criteria, including the maximum stress criterion, the minimum strain energy density criterion and the maximum energy release rate criterion, have become well established and applied for predicting mixed-mode fracture initiation and propagation. The linear elastic fracture mechanics and mixed-mode theoretical criteria, together with basic modes of fracturing are briefly explained in Section 2.2. Experimental studies of rock fractures are also reviewed in this chapter. The popular experimental tests used for quasi-static and dynamic rock strengths and fracture properties are introduced in detail, which include uniaxial or triaxial compression tests, tensile tests, shear tests, and rock fracture tests under quasi-static and dynamic loadings. The influences of loading rates and specimen size on the fracture behaviour and mechanical properties of rocks are highlighted. After the review of experimental studies in Section 2.3, the popular constitutive models and numerical methods for simulating rock fractures are discussed in Section 2.4. In particular, a detailed review of numerical methods for rock fractures is provided, with reference to their advantages and limitations, which can be divided into four categories: continuum mesh-based methods, continuum mesh-free methods, discontinuum-based methods and coupled methods. After all the reviews of analytical, experimental and

numerical studies on rock fractures, the existing knowledge gap for modelling rock fractures is detailed.

2.2. Theory of fracture mechanics

2.2.1. Modes of fracture

In fracture mechanics, fracture of a solid body which consists of a crack can be divided into three basic types, Mode I, Mode II and Mode III fractures (Irwin 1958). The division is based on how the two crack faces move with respect to each other when subjected to external loads. Supposing that a crack of a solid body is located in a local Cartesian coordinate system, the crack front which is perpendicular to the x-axis as depicted in Figure 2.0–1, the relative movements due to different modes of fracture or failure can be described as follows:

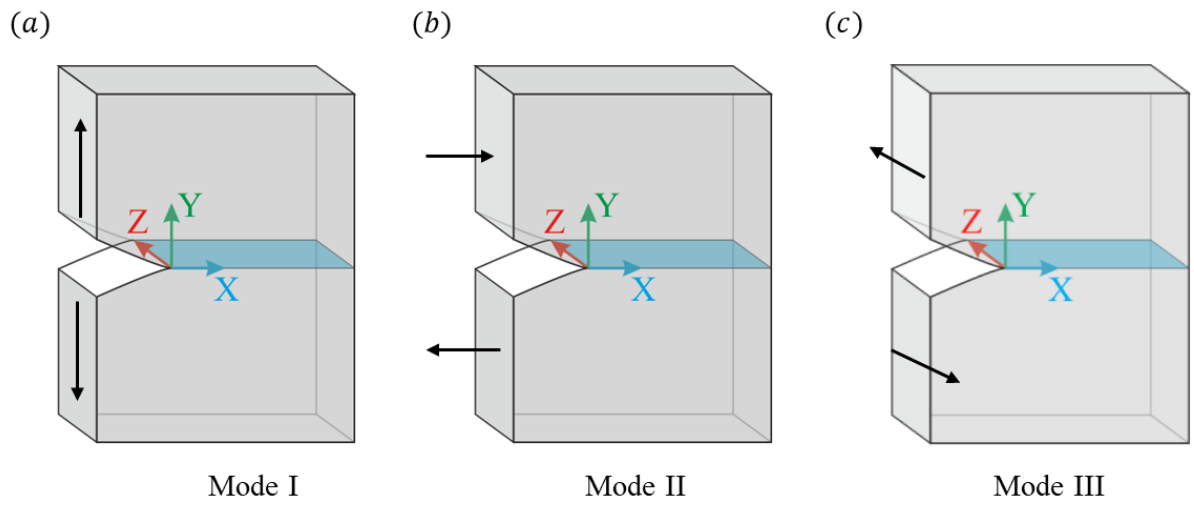

Figure 2.0–1. Stress loading modes: (a) Mode I (tension); (b) Mode II (in-plane shear); (c) Mode III (out-of-plane shear)

- In Mode I, the crack tip is subjected to a displacement of u_y, resulting in fracture propagating within its plane direction. This fracture mode normally occurs when a tensile loading is applied along the y-axis;
- In Mode II, the two crack surfaces slide next to each other along the x-axis, which means that in-plane shear displacement is visible. This fracture mode normally occurs when a shear stress parallel to the fracture plane but perpendicular to the crack tip is applied;

- In Mode III, the two crack surfaces experience shear displacement in the z-axis direction. This fracture mode normally occurs when a shear stress parallel to the fracture plane and parallel to the crack tip is applied.

Any fracture mode in a cracked body can be described by one of the above three basic modes or any combination of them. It is noted here that in real applications, rock fractures normally occur under very complex loading conditions. And the failure of rocks is also highly affected by other factors such as the size, temperature and confining pressures. Thus, a specific mode of failure is not necessarily induced by the same mode of loading.

2.2.2. Stress field ahead of the crack front

These three basic modes of failure or deformation can be expressed by the displacements and the associated stresses near the tip of a crack using Westergaard's function. The details of derivations and formulations can be found in Westergaard (1939). Supposing that a crack exists in a two-dimensional linearly elastic solid, the simple form of displacements and stresses defining those three modes can be represented as:

$$u_i = \frac{K_k}{8\mu\pi}\sqrt{2\pi x} f_i(\theta) \tag{2.1a}$$

$$\sigma_{ij} = \frac{K_k}{\sqrt{2\pi x}} f_{ij}(\theta) \tag{2.1b}$$

where u_i and σ_{ij} are the displacement and the stress tensor of an analysed representative volume element (RVE) in the local Cartesian coordinate system, K_k is the stress intensity factor of different modes k; θ and x are respectively the angle and distance between the analysed RVE and the crack plane; f is a geometric stress factor depending on θ.

In Mode I failure, the explicit formulations of displacements and associated stress field near the crack tip are expressed as:

$$\begin{cases} u_x = \frac{K_I}{8\mu\pi}\sqrt{2\pi x}\left[(2\kappa - 1)\cos\frac{1}{2}\theta - \cos\frac{3}{2}\theta\right] \\ u_y = \frac{K_I}{8\mu\pi}\sqrt{2\pi x}\left[(2\kappa + 1)\sin\frac{1}{2}\theta - \sin\frac{3}{2}\theta\right] \end{cases} \tag{2.2a}$$

$$\begin{cases} \sigma_{xx} = \frac{K_I}{\sqrt{2\pi x}}\cos\frac{1}{2}\theta\,(1 - \sin\frac{1}{2}\theta\cos\frac{3}{2}\theta) \\ \sigma_{yy} = \frac{K_I}{\sqrt{2\pi x}}\cos\frac{1}{2}\theta\,(1 + \sin\frac{1}{2}\theta\cos\frac{3}{2}\theta) \\ \sigma_{xy} = \frac{K_I}{\sqrt{2\pi x}}\sin\frac{1}{2}\theta\cos\frac{3}{2}\theta\cos\frac{1}{2}\theta \end{cases} \tag{2.2b}$$

where K_I is the applied stress intensity factor under Mode I condition, which depends on the applied load and the crack geometry. When $\theta = 0$, the Mode I stress intensity factor of a cracked solid with a crack length of a is related to the final applied loading σ_0, written as:

$$K_I = \sigma_0 \sqrt{\pi a} \tag{2.3}$$

It can be seen from Equation (2.2b) that the stresses have an inverse square root singularity at the crack tip ($x = 0$), which makes the classical strength of materials failure criteria inapplicable (Sun et al. 2012). Based on this observation, Irwin (1959) proposed a fracture criterion in which crack propagation occurs when the stress intensity factor reaches a critical value. In Mode I failure, this stress-field-based approach can be described as:

$$K_I = K_{IC} \tag{2.4}$$

where K_{IC} is the fracture toughness of the material, which characterises the resistance of a material to initiation and the propagation of a crack. The value of fracture toughness can be measured using a standard specimen in experiments.

Irwin's theory focuses on the stress field near the crack tip within a solid exhibiting linear elastic behaviour. Therefore, the validity of this theory is based on the assumption that the fracture process zone is sufficiently small so that it is well contained inside the singular stress field expressed in Equation (2.2b).

2.2.3. Energy release rate

Another important material parameter related to solid fractures is the energy release rate G. This parameter characterises the rate at which energy is lost due to the fracture occurring, which is defined as follows:

$$G = -\frac{d\Pi}{da} \tag{2.5}$$

where $d\Pi$ is the change in the potential energy, which is a function of the crack length da, expressed as:

$$-d\Pi = 2da\gamma \quad \text{or} \quad -\frac{d\Pi}{da} = 2\gamma \tag{2.6}$$

where γ is the surface energy per unit area, which can be calculated from solid-state physics. In 1921, Griffith proposed another fracture criterion based on the energy balance during crack extension, which states that the fracture will begin to propagate when the energy release rate reaches the critical energy release rate:

$$G = G_c = 2\gamma \tag{2.7}$$

where G_c is the critical energy release rate, which can be calculated experimentally.

The failure load, σ_f is defined by Griffith's theory as follows:

$$\sigma_f = \sqrt{\frac{2E'\gamma}{\pi a}} \tag{2.8}$$

where $E' = E$ for plane stress and $E' = E/(1-\nu^2)$ for the plane strain condition in which E is the Young's modulus, ν the Poisson's ratio.

The failure load can be linked with the energy release rate by combining Equations (2.7) and (2.8) as:

$$G_c = \frac{\pi a {\sigma_f}^2}{E'} \tag{2.9}$$

Unlike the Irwin approach, which focuses on the local stress field near the crack tip, the Griffith surface energy criterion considers the global energy balance during the crack. However, both these criteria are developed based on the linear elasticity and are equivalent in elastic media, expressed as:

$$K_I = K_{IC} \leftrightarrow G = G_c \tag{2.10}$$

The fracture toughness and critical energy release rate can be therefore linked together by making $\sigma_f = \sigma_0$ and then combining Equations (2.3) and (2.9), finally leading to:

$$G_c = \frac{K_{IC}^2}{E'} \tag{2.11}$$

Equation (2.11) has been widely used to link critical energy release with fracture toughness. In fracture mechanics, two novel concepts (stress intensity factor and energy release rate) were introduced, which distinguish fracture mechanics from the classical failure criteria (Sun et al. 2012). Those two quantities also lay the foundation of linear elastic fracture mechanics in which the solid with a crack is considered as linear elastic and the nonlinear effects are ignored. Since the invention of the linear elastic fracture concept, many theories have been proposed to predict crack propagation in the mixed-mode condition by linking the principles of fracture mechanics to practical fracture problems. For example, the maximum tangential stress criterion was originally developed by Erdogan and Sih (1963), stating that a crack would propagate in a direction perpendicular to the maximum value of the tensile stress. This criterion was further extended and applied to the prediction of failure of different materials such as ceramics (Aliha

and Ayatollahi 2012), interfaces between zirconia (Mirsayar and Park 2016), and veneer and shaft (Li et al. 2013). After the development of the maximum tangential stress criterion, some energy concepts including minimum strain-energy density (Sih 1973) and maximum energy release rate criterion (Hussain et al. 1974) were also proposed. In the minimum strain energy density criterion, also called the S criterion, a crack will propagate when the minimum strain-energy density around the crack tip reaches a critical value. Work relevant to this criterion includes that of Theocaris and Andrianopoulos (1982), Sih and Madenci (1983), Ayatollahi and Sedighiani (2012), Ayatollahi et al. (2015), to list a few. For maximum energy release rate, the G-criterion is based on the Griffith energy release rate concept. In this criterion, the energy release rate is determined as a function of the direction of propagation and the crack propagates following the direction where the maximum energy release rate occurs. Originally developed by Hussain et al. (1974), the G-criterion has been used extensively for the prediction of fracture initiation and propagation under combined loading in two- and three-dimensional problems (Wu 1978, Claydon 1992).

2.3. Experimental tests of rock fractures

Apart from theoretical studies, a large number of experimental studies have been conducted to study rock fracture behaviour in the past few decades, which can be divided into two groups based on the applied loadings on rock specimens. In this section, a review of experimental tests of rock fractures under quasi-static loading conditions is presented first, followed by a review of experimental tests of rock fractures under dynamic loading conditions.

2.2.4. Experimental tests of rock fractures under quasi-static loading conditions

According to the classification by Sharpe (2008), the rock tests under the strain rate ranging from 10^{-5} to 10^{-1} s^{-1} belong to quasi-static tests. As suggested by the International Society for Rock Mechanics (ISRM) and the American Society for Testing and Materials (ASTM), core-shaped samples are recommended for determining mechanical properties of rock materials under quasi-static conditions due to simple preparation (Zhang and Zhao 2013). Quasi-static experiments can be classified into two major groups: rock strength tests and fracture tests under low loading rates. Experiments for testing rock strength normally include uniaxial or triaxial compression tests, tensile tests and shear tests, while fracture toughness as the most prevalent fracture parameter has been investigated by conducting different tests with various specimen geometries. In this section, a review of rock strength and fracture tests under quasi-static conditions is presented.

- *Compression tests*

The popular compression tests under quasi-static conditions are uniaxial compression tests and triaxial compression tests. Uniaxial compression tests depicted in Figure 2.0–2a are the most common tests for characterising the uniaxial compressive strength of rock materials, while triaxial compression tests shown in Figure 2.0–2b are often performed for the development and calibration of the constitutive model and yield criteria for numerical simulations. The rock specimen in quasi-static compression tests is recommended to be a circular cylinder having a length-to-diameter ratio of 2.5-3.0 and a diameter to the size of the largest grain of at least 10:1 (Kovari et al. 1983). A review of empirical methods for determining uniaxial compressive strengths was provided by Cargill and Shakoor (1990). Apart from the standard uniaxial compression tests, other empirical methods such as the point load (Reichmuth 1962, Reichmuth 1967, Bieniawski 1974, Bieniawski 1975, Norbury 1986, Rusnak and Mark 2000), the Schmidt hammer (Hucka 1965, Sheorey 1984, Haramy and DeMarco 1985, Katz et al. 2000, Aydin and Basu 2005), the Los Angeles Abrasion (Shakoor and Brown 1996, Kahraman and Fener 2007, Kahraman and Toraman 2008, Ugur et al. 2010, Ozcelik 2011) and slake durability (Franklin and Chandra 1972, Dhakal et al. 2002, Singh et al. 2005) tests were also introduced in his work.

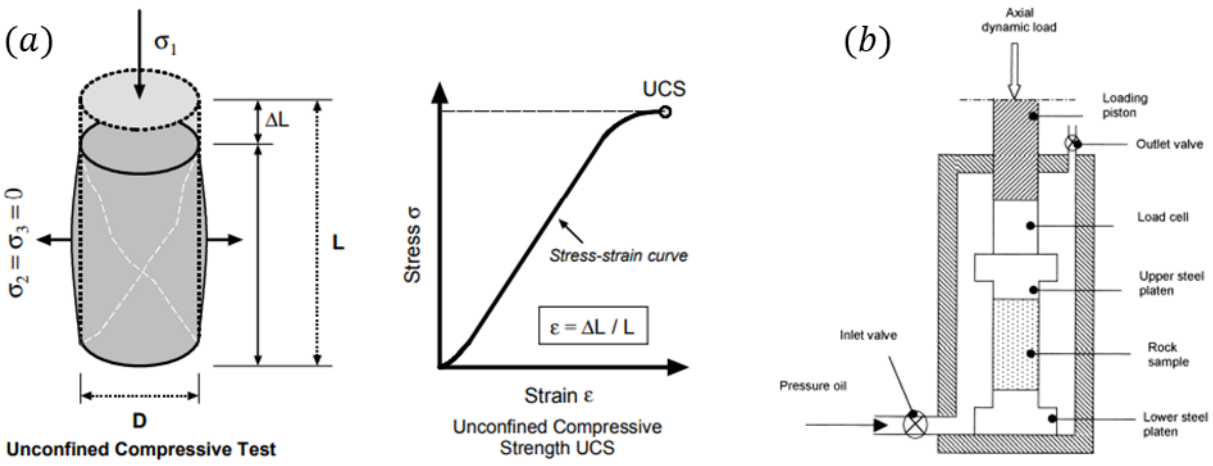

Figure 2.0–2. Quasi-static compression tests of rocks: (a) The rock specimen in uniaxial compression test and its stress-strain relationship; (b) The rock specimen in triaxial confining pressure cell system (Li et al. 1999)

On the other hand, experimental data from triaxial compression tests have been processed to obtain the differential stress-axial strain curves under various ranges of confining pressure. The

quasi-static differential stress-strain curves of Indiana limestone under different confining pressures provided by Frew et al. (2010) are plotted in Figure 2.0–3, showing that dynamic differential peak stress increases with an increase in confining pressure under quasi-static loading. A brittle-to-ductile transition showing that shear behaviour transits from the typical brittle behaviour to the fully ductile behaviour occurs when the confining pressure is around 50MPa. In the triaxial compression tests, the strength value of rocks and the corresponding confining pressures can be plotted for the different specimens. A strength envelope can be determined by fitting a mean curve to these plotted points.

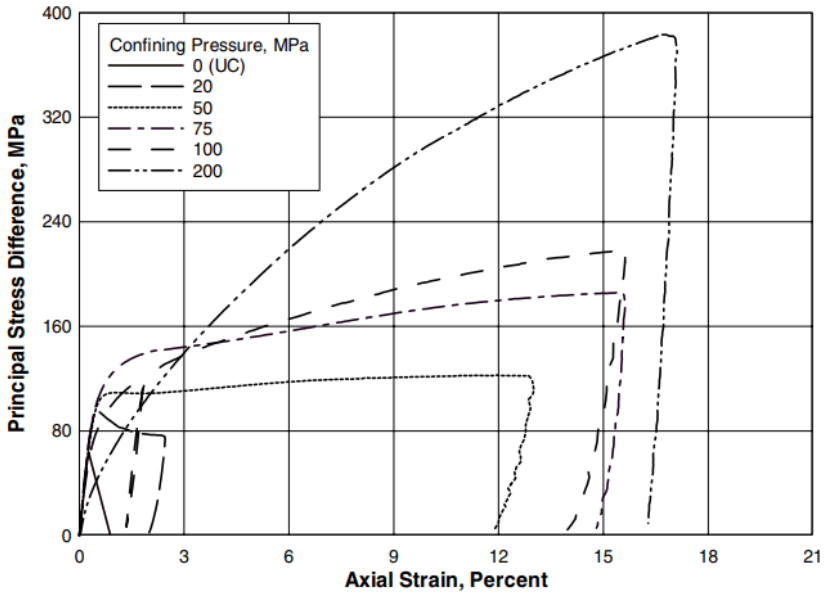

Figure 2.0–3. Differential stress-strain curves in triaxial compression test using Indiana limestone specimen (Frew et al. 2010)

- *Tensile tests*

As tensile strength is an important aspect of the resistance to failure of rocks, numerous tensile tests of rocks for determining the quasi-static tensile strength of rocks have been conducted, which can be divided into direct tensile tests and indirect tensile tests. Direct tensile test in which a specimen of the dog bone shape is used as illustrated in Figure 2.0–4a is regarded as the most valid method for determining the true tensile strength of rocks (Hoek 1964). However, this shape of rock specimen required in direct tensile tests is not easy to prepare, and thus indirect tensile tests such as Brazilian disc tests, sleeve-fracturing test and modified tensile tests illustrated in Figure 2.0–4b-d respectively are preferred by many researchers.

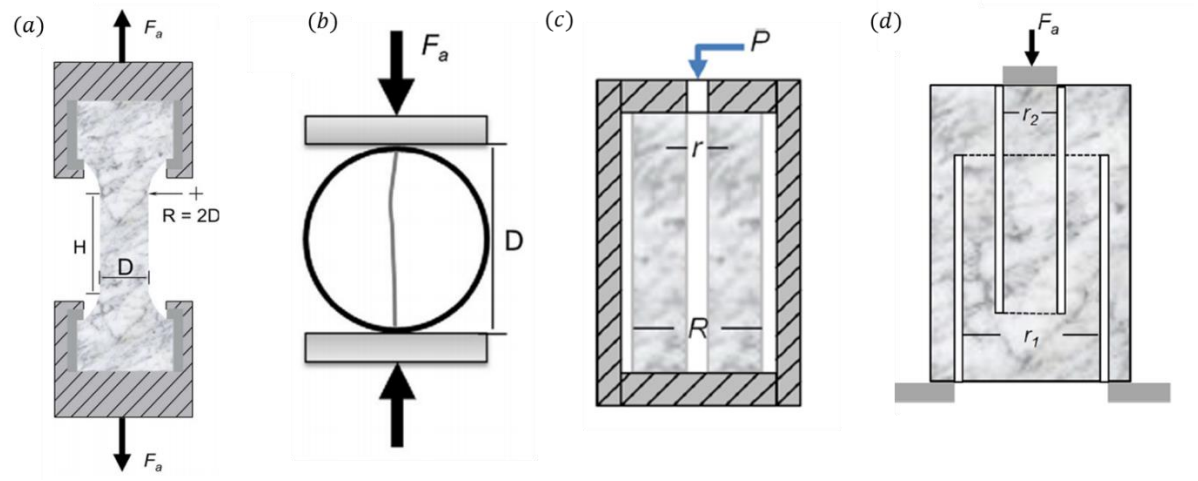

Figure 2.0–4. Tensile tests under quasi-static loading condition: (a) Direct tensile test; (b) Brazilian disc test; (c) Sleeve-fracturing test and (d) Modified tension test.(Perras and Diederichs 2014).

After the introduced by Carneiro (1943) and Akazawa (1943), the Brazilian disc test has been one of the most popular indirect tests to obtain the tensile strength of brittle materials including rocks due to its simplicity in specimen preparation and setup (Andreev 1991, Andreev 1991, Chen et al. 1998, Alehossein and Boland 2004, Wang et al. 2004, Jianhong et al. 2009, Yin et al. 2015). And a comprehensive review of the development of the Brazilian disc specimen has been given by Li and Wong (2013). In this test, a thin circular disc is diametrically compressed to failure, and the indirect tensile strength is typically calculated based on the assumption that failure occurs at the point of maximum tensile strength. The expression of the indirect tensile strength using Brazilian disc tests is written as:

$$\sigma_t = \frac{2F_a}{\pi D t} \tag{2.12}$$

where F_a is the applied force to the Brazilain disc speciemn, D and t are the diameter and thickness of the Brazilian disc specimen.

Sleeve-fracturing and modified tensile tests are two alternative indirect tensile testing methods. The sleeve-fracturing test is a variation of a dilatometer test which can be sued in situ to determine the deformability of a rock mass (Perras and Diederichs 2014). The studies on rock material properties using sleeve-fracturing methods can be found in Brenne et al. (2013), Charsley (2000), Charsley et al. (2003), Ljunggren and Stephansson (1986) and Stephansson (1983), to mention a few. Another test for quasi-static tensile strength is the modified tension test (Franklin and Dusseault 1989, Luong 1990). During the test, a tensile zone develops within an over cored specimen. As this test requires no special device for specimen gripping and

compressive loads and no particular preparation for the specimen, the modified tension can be easily conducted. The expressions of tensile strength in both sleeve fracturing and modified tensile test are presented as follows.

Sleeve-fracturing test: $$\sigma_t = P\frac{R^2+r^2}{R^2-r^2} \quad (2.13a)$$

Modified tensile test: $$\sigma_t = \frac{F_a}{\pi {r_1}^2 - \pi {r_2}^2} \quad (2.13b)$$

where P is water pressure, r and R are the inner and outer radius of sleeving fracture apparatus respectively, F_a is applied force, r_1 and r_2 are the inner and outer radius of modified tensile apparatus.

- *Shear tests*

Torsion tests have been widely used to study large shear strains of rock materials (Paterson and Olgaard 2000). To investigate the high strain in pure shear is important as this phenomenon can be often observed in many geotechnical applications on many scales. Although the cylindrical specimen, illustrated in Figure 2.0–5a, was initially used in torsion test, the hollow cylindrical specimen shown in Figure 2.0–5b, is more popular in the literature as a great deal of data can be acquired by only testing a single specimen (Hight et al. 1983, Talesnick and Frydman 1990, Talesnick and Ringel 1999).

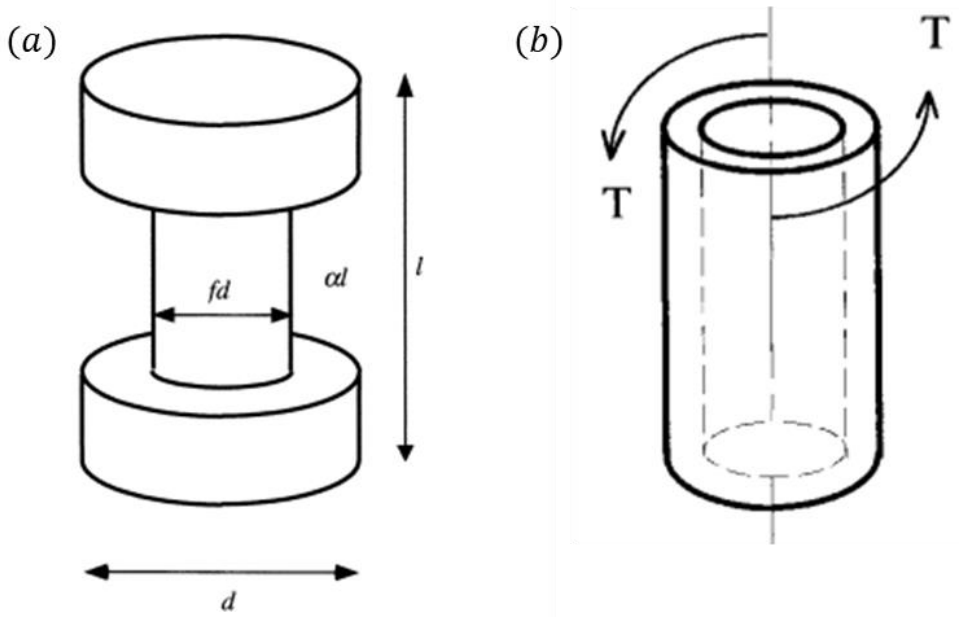

Figure 2.0–5. Torsion tests of rocks: (a) cylindrical specimen (Paterson and Olgaard 2000); (b) hollow cylindrical specimen (Talesnick and Ringel 1999).

The equipment of the hollow cylinder method comprises of a loading frame and a simple pressure chamber. Three types of stress conditions such as uniaxial compression, radial compression and radial tension can be applied for determining the required material properties (Talesnick and Bloch-Friedman 1999). The hollow cylinders in torsion tests have been successfully employed to determine the deformation moduli (Obert 1964). The elastic parameters such as Young's modulus and Poisson's ratio can also be easily obtained by conducting a single torsion test using the hollow cylinder (Talesnick et al. 1995). In addition, the effect of the intermediate principal stress on rock failure was also investigated using the hollow cylinder specimens by Hoskins (1969) and Handin et al. (1967). Later, torsion tests on hollow cylinders were extended to investigate material behaviour under tensile stresses (Talesnick and Brafman 1998, Talesnick and Bloch-Friedman 1999).

- *Rock fracture tests*

Apart from quasi-static rock strength tests, quasi-static fracture tests have been extensively conducted to investigate the mechanism of rock fractures and to determine the static fracture toughness under low loading rates. Although the chevron bend (CB) and the short-rod (SR) specimens were recommended by ISRM, these specimens only allow tensile cracks to be developed due to the specimen geometry, therefore they are not appropriate for determining the fracture toughness of rocks under mixed mode or pure mode II cases (Lim et al. 1994, Fowell et al. 1995). Some of the well-known test configurations for determining mode I and mode II fracture toughness under mixed-mode fracturing tests are the cracked chevron-notched Brazilian disc (CCNBD) under diametral compression (Yarema and Krestin 1967, Atkinson et al. 1982, Shetty et al. 1987, Krishnan et al. 1998, Khan and Al-Shayea 2000, Chang et al. 2002, Al-Shayea 2005, Ayatollahi and Aliha 2008, Ayatollahi and Sistaninia 2011), chevron-notch SCB specimens subjected to three- point loading (Lim et al. 1993, Lim et al. 1994, Lim et al. 1994, Ayatollahi et al. 2006, Ayatollahi and Aliha 2007, Aliha and Ayatollahi 2011), the angled internal cracked plate under biaxial far field loading (Williams and Ewing 1972, Yukio et al. 1983), asymmetric four-point bend loading (Ingraffea 1981, Kenner et al. 1982, Jian-An and Sijing 1985, He et al. 1990, Suresh et al. 1990, Margevicius et al. 1999, Wang et al. 2016), the compact shear-tension specimen (Richard and Benitz 1983, Banks-Sills and Bortman 1986, Zipf Jr and Bieniawski 1986, Buchholz et al. 1987, Zipf and Bieniawski 1988, Mahajan and Ravi-Chandar 1989). The schematic of fracture tests using CCNBD, Notched SCB and notch four-point bend specimens and the corresponding fracture patterns under pure mode I and

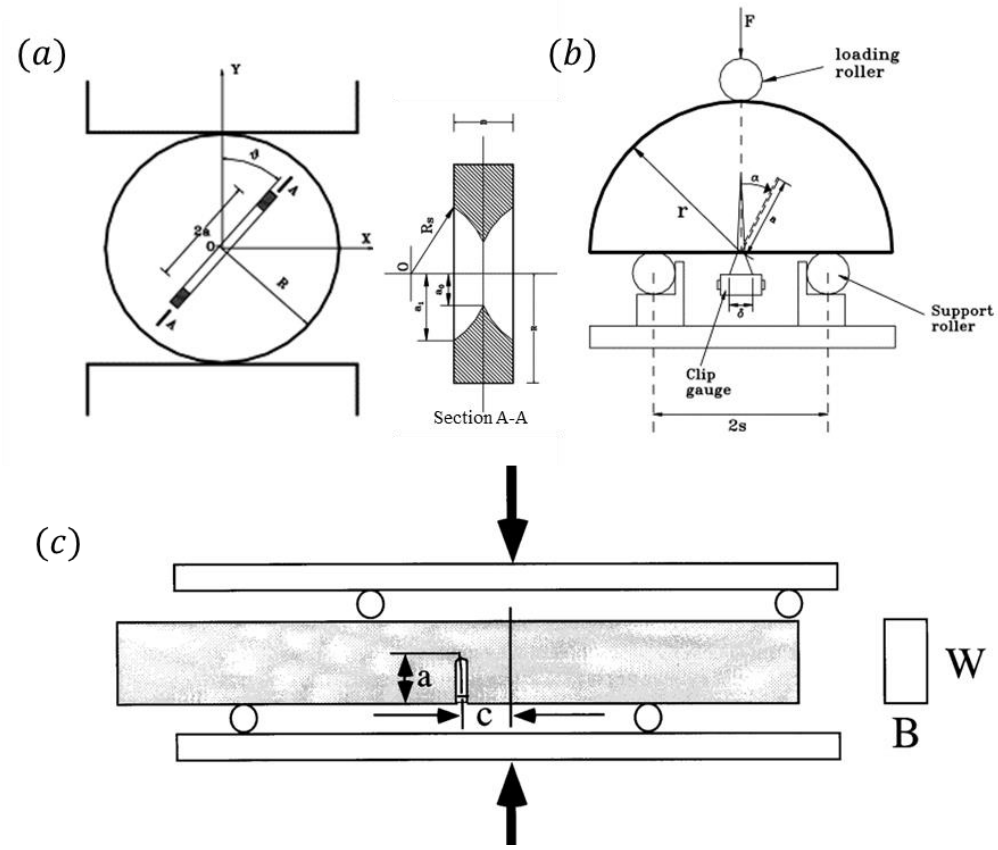

Figure 2.0–6. Schematic of fracture toughness testing methods: (a) CCNBD specimen under compression (Chang et al. 2002); (b) Notched semi-circular bending specimen (Chang et al. 2002); (c) Notch four-point bending specimen (Margevicius et al. 1999).

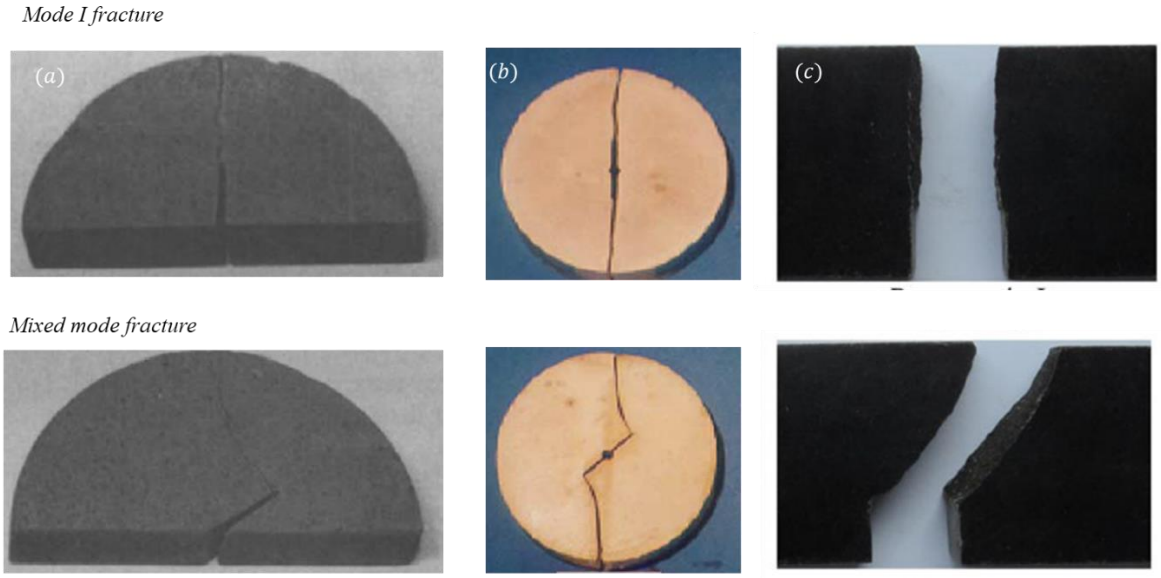

Figure 2.0–7. Mode I and mixed mode fracture patterns of rocks in (a) Notched semi-circular bending specimen (Lim et al. 1994); (b) CCNBD specimen(Al-Shayea 2005); (c). Notch four-point bending specimen (Wang et al. 2016).

mixed mode are presented in Figure 2.0–6 and Figure 2.0–7 respectively. It can be seen from Figure 2.0–7 that the fracture patterns are distinct when different loading conditions are applied. Fracture occurs within a rock mas due to tensile loading under pure mode loading, while rock experiences both tensile and shear deformation under mixed mode loading. The failure of rocks under loading is a consequence of the coalescence of many microcracks. As loading stress increases and rock failure is approached, the microcrack population changes spatially from random to locally intense zones of cracking, resulting in the existence of a high gradient of deformation within the macroscopic failure zone (Kranz 1983).

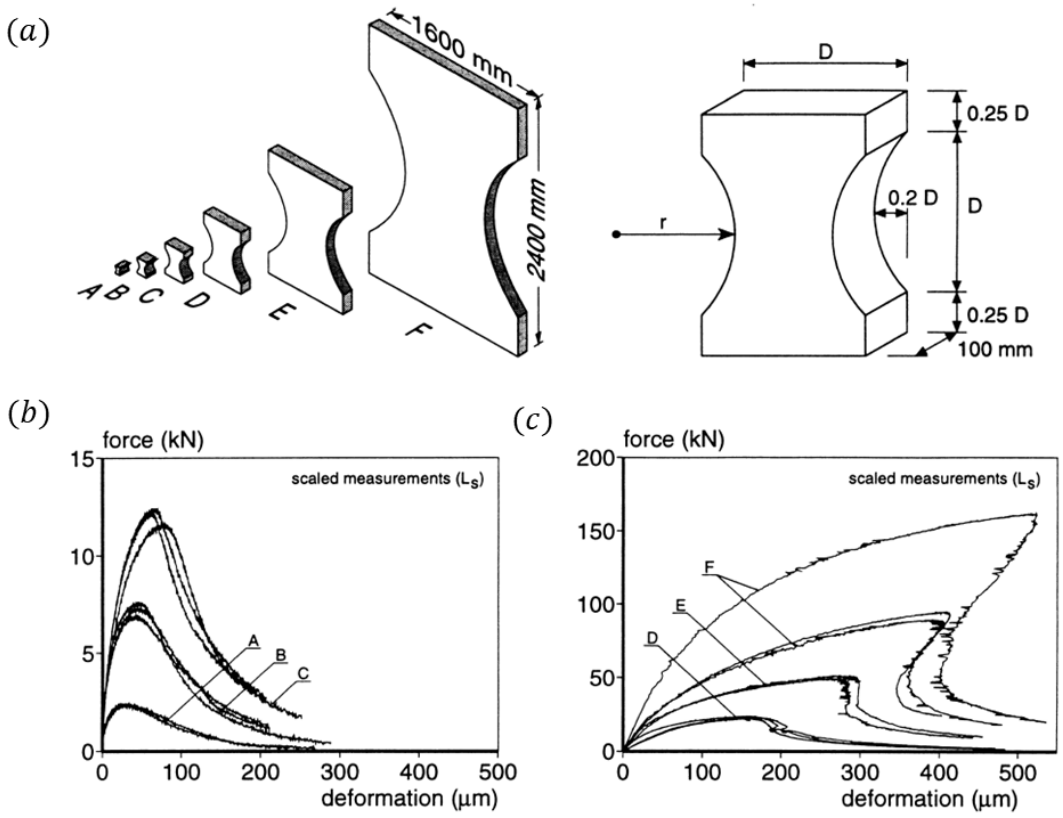

Figure 2.0–8. Direct tensile tests on sandstone by Van Vliet and Van Mier (2000): (a) Specimen dimensions; (b) Force-deformation curve of specimen A-C; (c) Force-deformation curve of specimen D-F.

Apart from the applied loading, the fracture behaviour of rocks or rock-like materials is also strongly dependent on the specimen size. The two kinds of size effects, are statistical and energetic (or deterministic), can affect the response of rocks or rock-like materials (Van Vliet and Van Mier 2000, Elkadi and Van Mier 2006). In 1921, Griffith compared the nominal strengths of glass fibres with two different diameters (0.0042in. and 0.00013in). Their

experimental results showed that the glass fibre with the larger diameter had lower nominal strength. The author explained that the result was due the presence of more discontinuities or flaws in glass fibres with larger diameters. Later, the Weibull statistical theory was developed to explain that statistical size effect (Weibull et al. 1949, Weibull 1951). Weibull pointed out that the size effect on the nominal strength arose from the fact that larger solids had higher probability of encountering a material element of small strength. However, when dealing with quasi-brittle materials which exhibit non-negligible material length, classical Weibull theory is no longer applicable as it ignores the absence of characteristic length of the material and the stress redistribution due to localised deformation.

In this case, another type of size effect, namely the deterministic size effect was discovered, which was distinguished from the statistical size effect. The deterministic size effect is caused by stress redistribution in the structure due to large deformation in the localization zone. Both statistical and deterministic size effects were examined by Van Vliet and Van Mier (2000), who conducted a series of direct tensile tests on bone-shaped sandstone specimens of different sizes, as shown in Figure 2.0–8a. The force-deformation curves for specimens are plotted in Figure 2.0–8b-c. It can be seen that the peak force increases with the increase in specimen size. The authors also pointed out, on the basis of experimental observation, that the statistical size effect due to the randomness of strength could be overruled by the deterministic effect due to the high gradient of deformation when a macro-crack initiated from a RVE whose size was not negligible compared to the structure size.

2.2.5. Experimental tests of rock fractures under dynamic loading conditions

After introducing the rock experiments under quasi-static loading conditions, the experiments of rocks for determining mechanical and fracture properties under dynamic loading conditions are presented in this section with the emphasis of rate dependency. Among many different studies, the split Hopkinson Pressure Bar (SHPB), invented by Kolsky (1949), is the most popular and is a commonly accepted loading technique used to obtain high strain rates ($10^1 \sim 10^4/s$). The SHPB system is comprised of a striker bar, an incident bar, a transmission bar, and a rock sample sandwiched between the incident bar and the transmitted bar (Figure 2.0–9). A compressive pulse is generated by the striker bar's impacting on the incident bar. Part of the pulse is transmitted into the transmitted bar through the sample, while the remaining is reflected by sample and received by the incident bar. A strain gauge is used to measure incident (ε_i), reflected (ε_r) and transmitted (ε_t) pulses acting on the cross-section of the

specimen. The dynamic forces (P_1, P_2) at the bar-sample interface are defined based on the elastic one-dimensional stress wave propagation theory as:

$$P_1 = A_B E_B(\varepsilon_i + \varepsilon_r), \quad P_2 = A_B E_B \varepsilon_t \tag{2.12}$$

where A_B and E_B are respectively the cross-sectional area and Young's modulus of the steel bar.

The strain rate of the test specimen ($\dot{\varepsilon}$) can be calculated from elementary wave theory as:

$$\dot{\varepsilon} = \frac{C_B}{L_s}(-\varepsilon_i + \varepsilon_r + \varepsilon_t) \tag{2.13}$$

where L_s is the length of the test specimen, and C_B is the longitudinal wave speed of the striker.

The strain rate of the specimen can also be computed using the velocities $(\dot{u}_1, \dot{u}_2)$ at the bar-sample interface as

$$\dot{\varepsilon} = \frac{(\dot{u}_1 - \dot{u}_2)}{L_s} \tag{2.14}$$

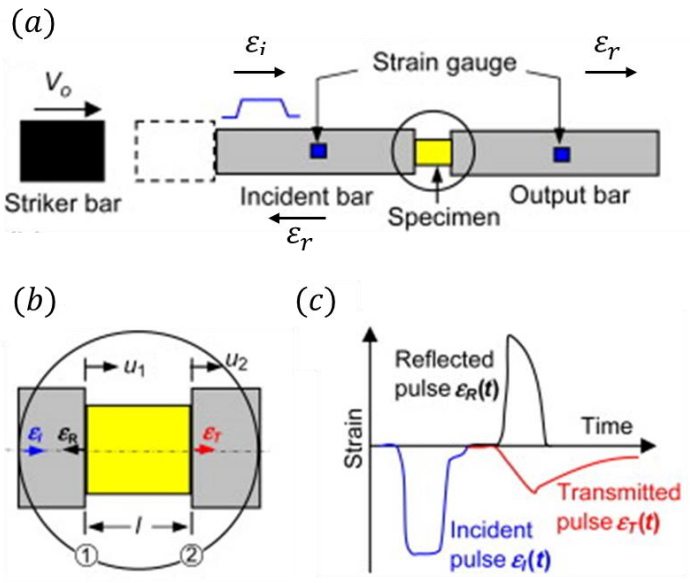

Figure 2.0–9. The split Hopkinson pressure bar (SHPB):(a) Schematic of SHPB; (b) enlarged view of specimen; (c) strain wave across interfaces (Wong and Mai 2015).

The stress-strain curve of a test specimen under high strain rates is another important experiment output as many material parameters such as Young's modulus, Poisson's ratio, strain to failure and strengths can be obtained from the stress-strain curves. Therefore, many approaches have been developed to determine the stress-strain relationship in the SHPB system,

such as the one-, two- or three-wave analysis (Gray III and Blumenthal 2000), direct estimate (Mohr et al. 2010), foot-shifting (Mohr et al. 2010) and hybrid analysis (Shan et al. 2000, Gilat et al. 2009). Similar to the rock experiments under low loading rates, core-shaped samples are also frequently used for determining material properties of rocks under high loading rates. In the following section, the emphasis is focused on the effect of the strain/loading rate on the mechanical and fracture properties of rocks through the review of strength tests and fracture tests. The dynamic strength tests can be grouped into uniaxial compression tests, triaxial compression tests, tension tests and shear tests, similar to quasi-static strength tests.

- *Uniaxial compression tests*

Numerous uniaxial compression tests on circular cylinders have been conducted with different specimen sizes and different length-to-diameter ratios of the specimens (Hauser 1966, Zhao and Gary 1996, Zhang and Zhao 2013). Gray III and Blumenthal (2000) suggested that choosing a length-to-diameter ratio between 0.5 and 1.0 and minimising the mismatch between the specimen and the bars could help to reduce the end friction effect between the specimen and loading device and inertia effect due to Poisson's ratio. To investigate the stress-strain relationship under uniaxial compression tests, Perkins et al. (1970) performed a series of compression tests on porphyritic tonalite using traditional SHPB techniques. The plotted stress-strain curves under different loading rates are shown in Figure 2.0–10a, which shows that an increase in strain rate causes an increase in the tangent stiffness. The same conclusion was drawn by Eibl (1988), who developed a semi-empirical relationship between dynamic elastic modulus and dynamic strain rate, expressed as:

$$E_d = E(\dot{\varepsilon}/\dot{\varepsilon}_s)^{0.026} \tag{2.15}$$

in which $\dot{\varepsilon}_s = 3 \times 10^{-5}/s$ is the strain rate under static loading.

The sensitivity of compressive strength to compressive strain rates can also be observed in Figure 2.0–10a. As the strain rate increases, so does the compressive strength. Many studies have investigated the effect of loading rate on compressive strength of different materials such as granite (Masuda et al. 1987, Zhao et al. 1999), limestone (Lankford 1981), tuff (Lankford 1981), sandstone (Singh et al. 1989) and marble (Liu 1980), to name a few. Zhang and Zhao (2014) collected data of normalised uniaxial compression strength (ratio of dynamic uniaxial compression strength to quasi-static strength) from various experiments over last five decades, as shown in Figure 2.0–10b. When the applied strain rate is smaller than 10/s, the normalised dynamic compressive strength increases linearly with the increase in strain rate. However,

rocks exhibit a stronger rate effect when the strain rate is greater than 10/s. An exponential compressive strength-strain rate relationship is observed.

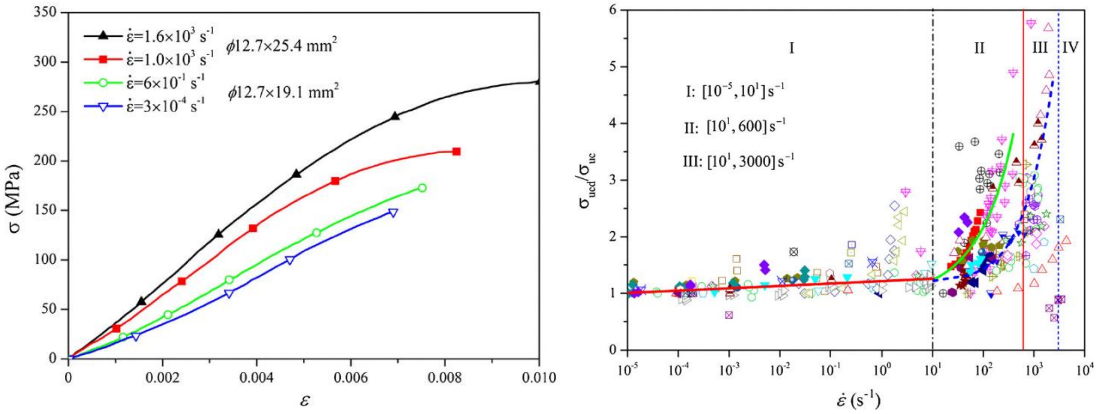

Figure 2.0–10. Uniaxial compression test: (a) Stress-strain relationship (Perkins et al. 1970);(b) normalized uniaxial compression strength and strain rate relationship (Zhang and Zhao 2014).

- *Triaxial compression tests*

Triaxial loading in the triaxial compression tests can be applied to a specimen through either a pressure or displacement boundary conditions. In pressure-applied tests, the specimen is normally placed inside a pressure chamber (Gary and Bailly 1998) or a triaxial SHPB apparatus (Cadoni and Albertini 2011) and then isotopically loaded by hydrostatic pressure up to 10-50MPa depending on the confining fluids (Gary and Bailly 1998). In displacement-applied tests, the specimen is placed in a shrink-fit metal sleeve (Chen and Ravichandran 1997, Rome et al. 2002, Forquin et al. 2008) or a passive thick vessel (Gong and Malvern 1990) for imposing lateral confinement. Numerous triaxial compression tests have been conducted for investigating the mechanical properties of different rock or rock-like materials such as granite (Logan and Handin 1970), limestone (Frew et al. 2001), sandstone (Jin et al. 2012), marble (Yu 1992) and concrete (Gran et al. 1989).

In the review of the rock behaviour under quasi-static triaxial compression test, it was found that the strength of rock material is pressure dependent under low loading rates. The pressure-sensitivity of rock materials under high loading rates was also studied by Gran et al. (1989), who calculated differential stress-strain curves using a wave analysis method as shown in Figure 2.0–11. In this test, different loading rates ($\dot{\varepsilon} = 10^{-5}$/s for quasi-static loading and 300/s for dynamic loading) and confining pressures ranging from 0.1 to 85MPa were applied to examine the effect of loading rate and confining pressure on the mechanical behaviour of

rocks. It can be seen that rocks are also sensitive to loading rates, apart from confining pressures. The differential peak stress in the triaxial compression test increases as the loading rates increases. It also can be seen from Figure 2.0–11 that the transition pressure at which the specimen experiences a transition from brittle failure to ductile failure under static loading is about 50 to 80 MPa, while the brittle-ductile transition occurs under dynamic loading when the confining pressure is around 10 to 35 MPa. That implies a more ductile response of rocks occurs under dynamic loading compared with static loading. However, this conclusion differs from the experimental observation using Indiana limestone specimen by Frew et al. (2010) and Berea Sandstone specimen by Blanton (1981), in which a higher transition confining pressures at high rates were observed, indicating that rocks were more brittle at higher strain rates.

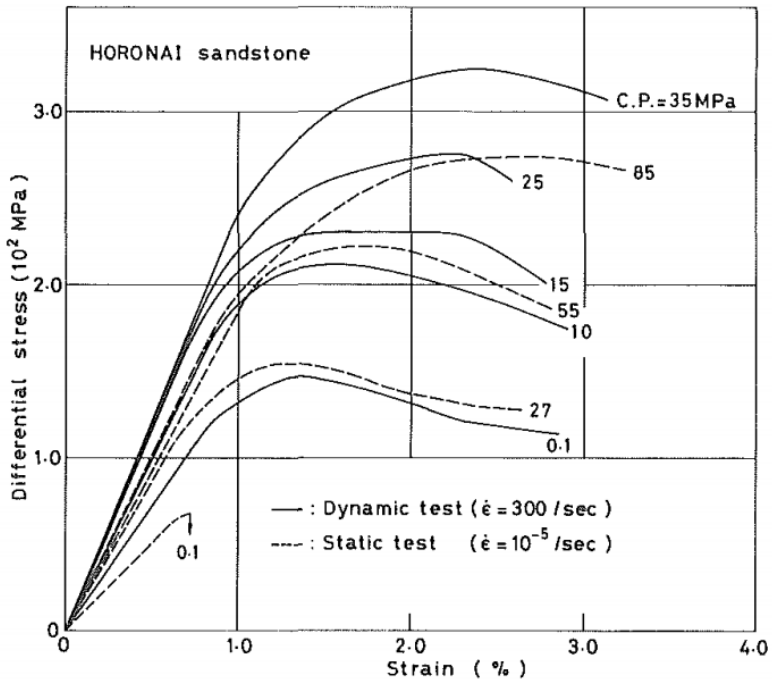

Figure 2.0–11. Differential stress-strain curves in triaxial compression test using Horonai sandstone specimen (Gran et al. 1989).

In order to further analyse the effect of loading rates on different rock materials, Zhang and Zhao (2013) summarised the normalised dynamic differential peak stresses under different loading rates in the triaxial compression tests on different types of rocks such as Indiana limestone (Frew et al. 2010), Horonai sandstone (Kawakita and Kinoshita 1981), basalt (Lindholm 1974) and sandstone (Christensen et al. 1972), as shown in Figure 2.0–12. It can be seen from the results that the rocks exhibit strong loading rate effects, although these rocks

show different degrees of loading rate sensitivity. The most likely reasons are differences in rock types, specimen sizes and confining pressure apparatus used in the triaxial compression test.

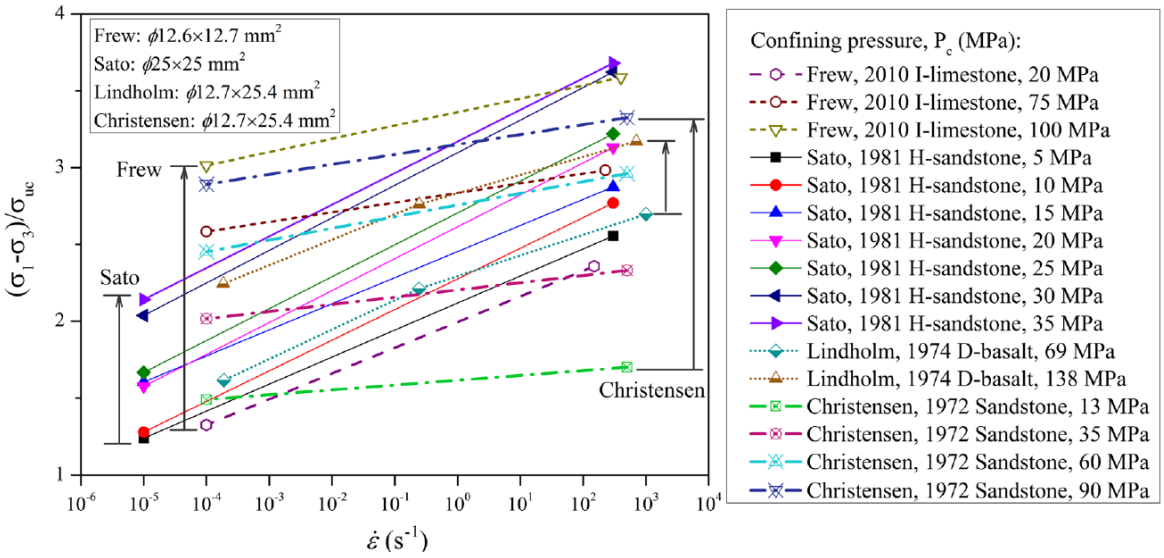

Figure 2.0–12. Normalised dynamic differential stress under different loading rates and confining pressure (Zhang and Zhao 2013).

- *Tensile tests*

Numerous dynamic tensile tests extended from the quasi-static tests have been developed, such as direct tensile tests (Asprone et al. 2009, Fuenkajorn and Klanphumeesri 2010), Brazilian disc tests (Dutta and Kim 1993, Dai and Xia 2010, Yan et al. 2011, Zhou et al. 2012), three-point bending tests (Zhao and Li 2000), semi-circular bending tests (Dai et al. 2008, Dai et al. 2013) and spalling tests (Klepaczko and Brara 2001, Kubota et al. 2008, Erzar and Forquin 2010). The last four groups of tests are indirect tensile tests. Experimental setups of the above-mentioned tensile tests are depicted in Figure 2.0–13. Compared with direct tensile tests, during which very slight misalignments can result in undesirable failure modes, indirect tensile tests are more popular for determining tensile strength at high loading rates due to the easier preparation and setup.

To investigate stress-strain relationships under dynamic tensile loadings, Asprone et al. (2009) conducted a series of direct tensile tests on Mediterranean natural stone under various high strain rates. The stress vs. crack opening displacement curves at different strain rates are plotted in Figure 2.0–14a. It can be observed that the peak stress and elastic stiffness of Mediterranean

stone increase as the strain rates increases. In contrast, the crack opening displacement corresponding to the peak stress reduces with increasing strain rates, indicating that the material assumes a more brittle behaviour at higher strain rates. When the specimen is subjected to strain rates from 10^{-5}/s to 10^{-1}/s, the responses of the specimen are very similar, except that a higher peak load is observed under the strain rate of 10^{-1}/s. However, the responses of the specimen are distinct when the strain rate is greater than 10^{-1}/s. The stiffness and peak load of the specimen under higher strain rates are much greater, indicating that more energy is required to initiate fracture at higher strain rates.

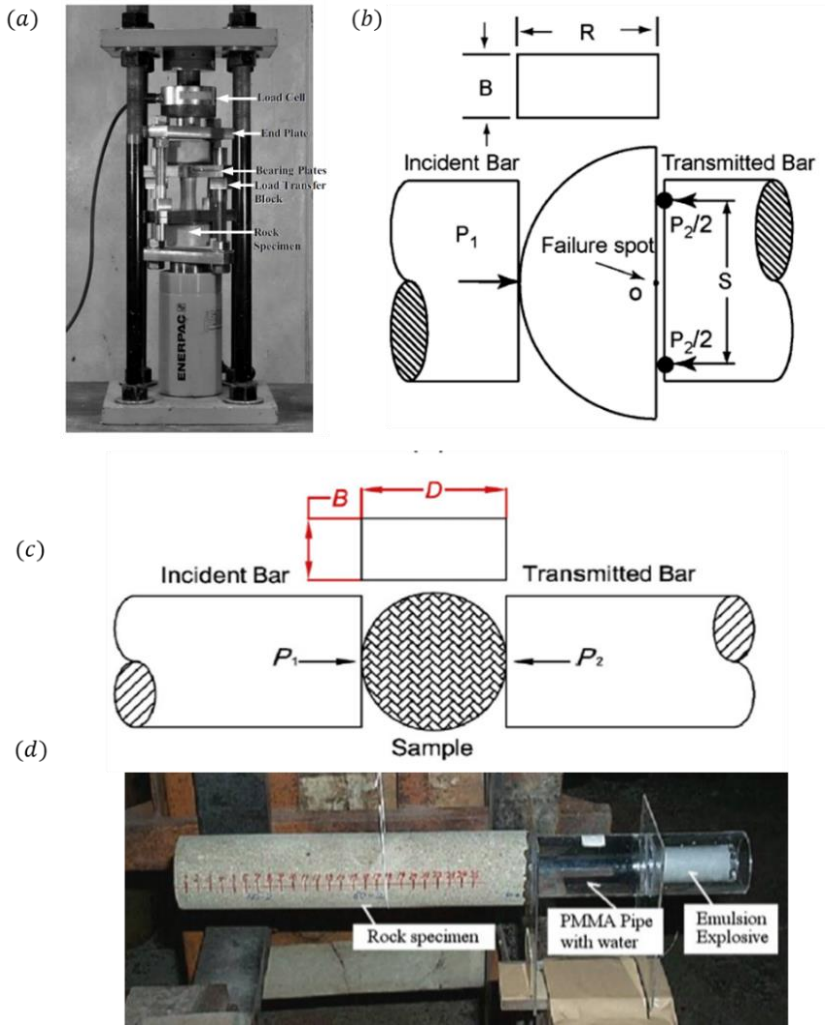

Figure 2.0–13. Dynamic tensile test setup: (a) Direct tensile test (Fuenkajorn and Klanphumeesri 2010);(b) Bending test (Dai et al. 2010); (c) Brazilian test (Yao et al. 2017); (d) Spalling test (Kubota et al. 2008).

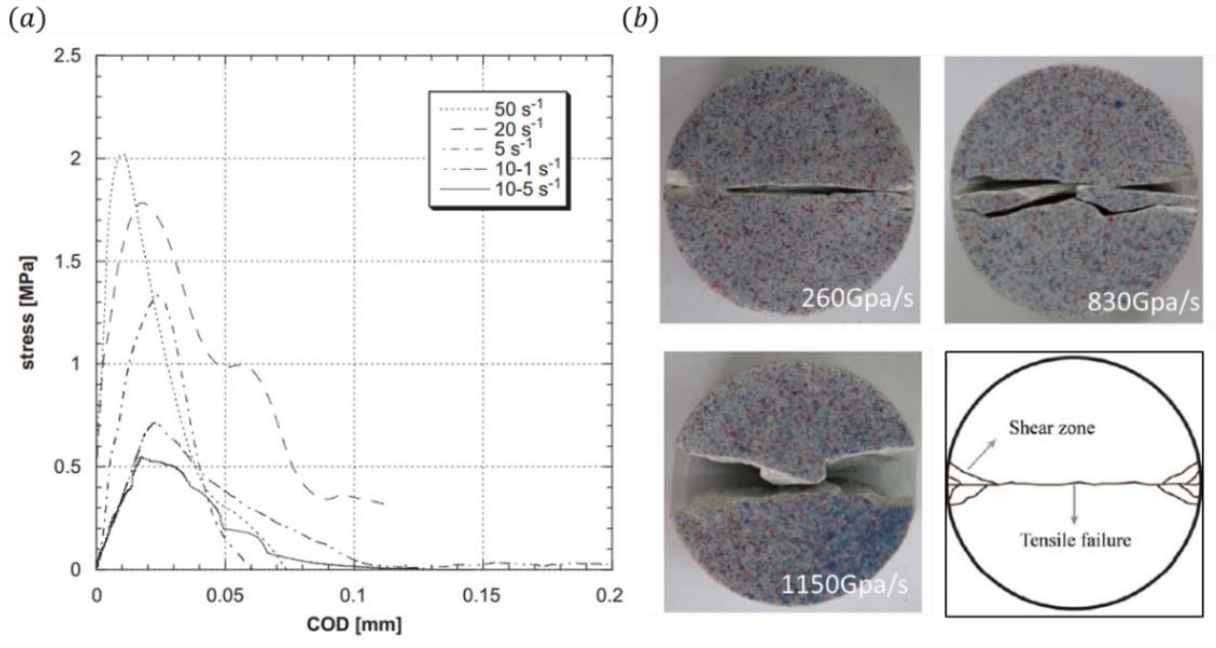

Figure 2.0–14. Rock responses under dynamic tensile tests:(a) stress-crack opening displacement curves in direct tensile tests performed by Asprone et al. (2009); (b) Final fracture patterns under different loading rates in Brazilian disc test conducted by Zhang and Zhao (2013).

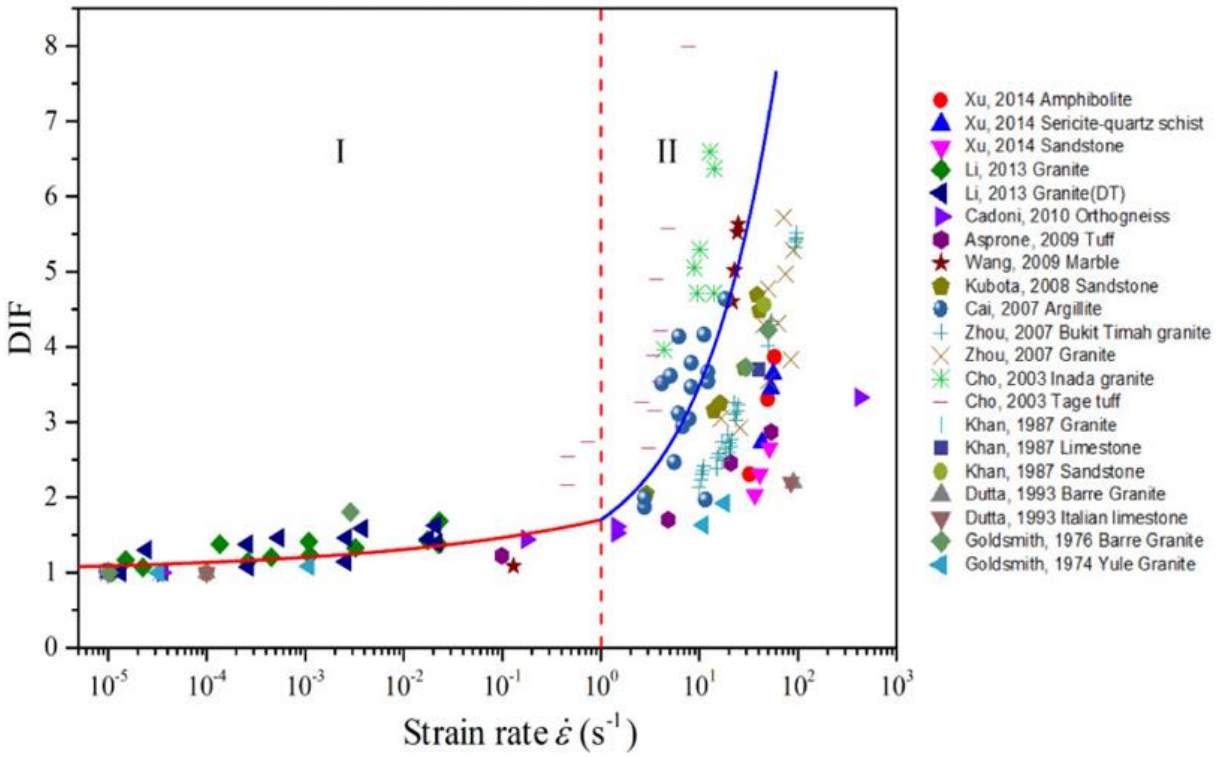

Figure 2.0–15. Normalised tensile strength with loading strain rates (Liu et al. 2018)

Figure 2.0–14b shows final fracture patterns of a Brazilian disc specimen under three different loading rates, obtained from Zhang and Zhao (2013). It can be seen that the fracture patterns of rocks are very different under different dynamic loading rates, although the main fracture orientation is parallel to the loading direction, dividing the specimen into two main pieces. Under a lower loading rate such as 260GPa/s, a thin fracture is formed in the middle of the specimen, while a large shear zone is observed under high loading rates. The extent of two shear failure zones at contact points of the disk depends on the loading rates. As the sensitivity of stress-strain curves and tensile strengths of rock to loading rates is well known, many researchers have summarised existing tensile experimental data and derived empirical expressions showing the evolution of dynamic tensile strength with strain rate. Figure 2.0–15 shows the normalised dynamic tensile strengths of different materials under a wide range of dynamic strain rates, as summarised by Liu et al. (2018). It can be seen from this figure that the tensile strength of rocks increases more rapidly when the strain rate is greater than 1/s. Therefore, the authors developed two exponent functions showing different degrees of sensitivity to tensile strength under two strain rate ranges, shown as:

$$DIF = \begin{cases} 1 + 0.7{\dot{\varepsilon}_t}^{0.18} & for\ \dot{\varepsilon} < 1/s \\ 1 + 0.7{\dot{\varepsilon}_t}^{0.55} & for\ \dot{\varepsilon} \geq 1/s \end{cases} \tag{2.16}$$

where DIF is the dynamic increase fracture, which is the ratio of dynamic tensile strength to static tensile strength.

- *Shear tests*

A torsional split Hopkinson bar (TSHB) system modified based on the traditional SHPB was developed and widely used for investigating the shear behaviour of rocks under dynamic loadings (Paterson and Olgaard 2000). In the TSHB test, dynamic torque produced by explosive loading or torsional deformation energy is applied to both ends of a cylindrical specimen (Goldsmith et al. 1976) or thin-walled tubes (Lipkin et al. 1979). The dynamic shear strength and strain rate of the test specimen can be easily calculated from the dynamic torque and the difference in angular velocity between the two ends of the specimen respectively. However, the complexity of specimen preparation and uncertainty of strain rate corresponding to failure strength make torque tests inefficient. Therefore, some other shear testing methods such as compression-shear tests (Rittel et al. 2002), direct shear-box tests (Barbero et al. 1996), punch tests (Yagiz 2009, Mishra and Basu 2012) and a split Hopkinson pressure shear bar (Zhao et al. 2011) have been developed.

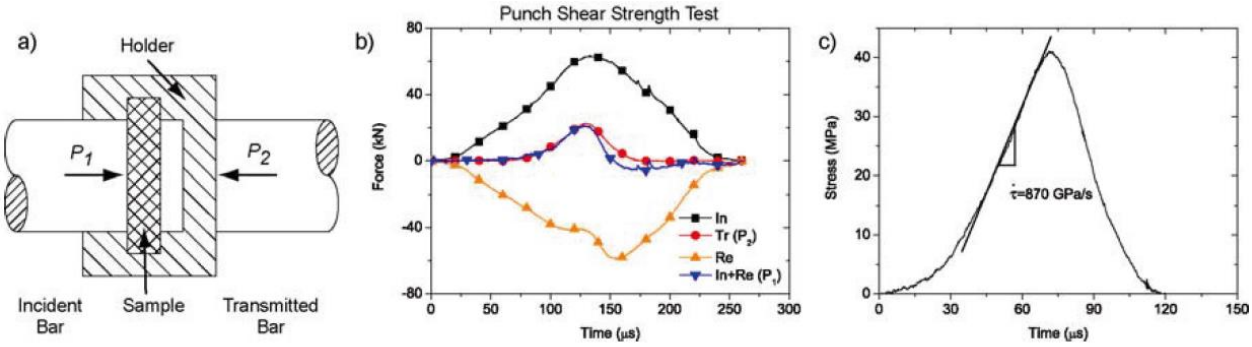

Figure 2.0–16. Punch shear strength tests in SHPB: (a) Schematic of the experiment; (b) Dynamic force equilibrium for a typical test; (c) Typical of stress-time curves in shear test(Huang et al. 2012).

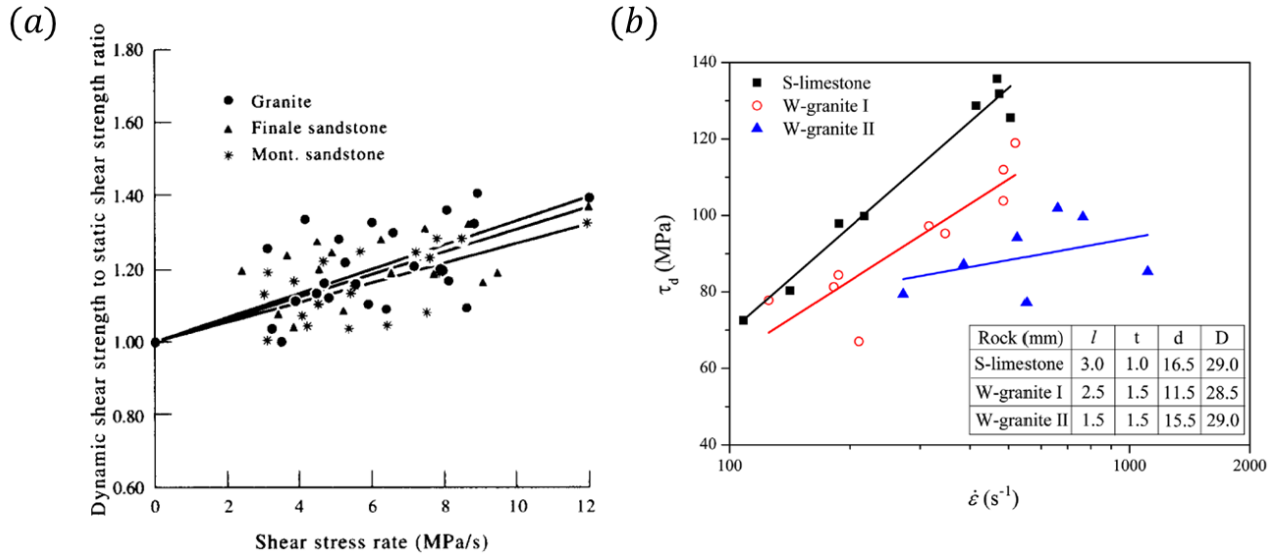

Figure 2.0–17. Shear test results (a) Normalised shear strengths with shear stress rates (Barbero et al. 1996); (b) shear strength and strain rate relationship under shear test (Lipkin et al. 1979).

Figure 2.0–16 shows a SHPB punch shear test on Longyou sandstone conducted by Huang et al. (2012). The schematic of the experiment setup is depicted in Figure 2.0–16a, while the red and blue lines in Figure 2.0–16b represent the forces applied on both ends of the specimen. A pulse-shaping technique was used in that study to minimise the inertia effect due to the mismatch between forces on both ends of the sample. Figure 2.0–16c shows a typical shear stress evolution under dynamic shear tests, in which the shear loading rate is determined as the slope of stress evolution curve. An increasing trend of punch shear stress was found in this study with the increasing shear loading rate. A similar experimental result was also obtained by Barbero et al. (1996), who conducted a series of direct shear tests on three different materials (granite, Finale sandstone, Mont sandstone) under different shear strain rates. Normalised

dynamic shear strengths with shear stress rates are plotted in Figure 2.0–17a. It can be seen that the normalised dynamic shear strengths of three rock materials under the same strain rate are similar and the shear strengths increase linearly with strain rates. The linear increasing trend of shear strength with increasing shear strain rate was also observed in the torque tests by Lipkin et al. (1979). In this work, thin-walled tubular specimens of Westerly granite and Solohofen sandstone were tested under different shear strain rates ranging from 100/s to 2000/s, with the result shown in Figure 2.0–17b. The sensitivity of specimen size to the shear strength of Westerly granite was also observed by comparing the results from Westerly granite with two different sizes in Figure 2.0–17b.

- *Rock fracture tests*

Besides rock strength tests, a number of rock fracture tests have also been conducted to analyse rock fracture processes under dynamic loadings. Through the tests, material dynamic parameters, such as fracture energy, fracture toughness and the average fracture velocity can be calculated. Existing studies focus mainly on the measurement of fracture toughness, including initiation fracture toughness and propagation fracture toughness. Most dynamic testing methods are extended from the static ones, and the normalised dynamic fracture toughness can be determined using the theory of quasi-static fracture mechanics, which is a direct measure of the stress state obtained from load transducers or pulses in the SHPB tests. Together with high-speed digital image correlation (DIC), the initiation and propagation of a crack can be recorded for calculating the time to fracture and the crack propagation velocity at different times. The most widely used core-based specimens for determining facture toughness under dynamic loadings are the chevron bend (CB) and short rod (SR) specimens method (Franklin et al. 1988, Zhang et al. 2000), cracked chevron notched Brazilian disc (CCNBD) specimen method (Dwivedi et al. 2000) and semicircular bending (SCB) method (Lim et al. 1993, Chen et al. 2009, Dai et al. 2010).

The dynamic initiation fracture toughness under pure mode I loading, denoted as K_{Id}, is determined by the time to fracture. In other words, the dynamic initiation fracture toughness for a loading rate is the fracture toughness when the fracture initiates, expressed as:

$$K_{Id}\left(\dot{K}_I^{dyn}\right) = K_I^{dyn}(t_f) \tag{2.17}$$

where $\dot{K}_I^{dyn} = K_{Id}/t_f$ is the loading rate and K_I^{dyn} is the stress intensity factor related to the specimen geometry and applied load.

Zhou et al. (2010) investigated the effects of loading rates on initiation fracture toughness by conducting a three-point bending experiment on Huanglong limestone. The results showed that when the loading rate was greater than a certain value, the fracture toughness of this type of rock increased markedly with an increase in loading rate. The same conclusion was also reached by Zhang et al. (1993) and Fengnian and Haijie (1998). Zhang and Zhao (2013) summarised the normalised dynamic initiation fracture toughness of different materials under a wide range of loading rates, depicted as Figure 2.0–18a. It can be seen from the figure that the normalised dynamic initiation fracture toughness increases slightly as the normalised loading rate increases from 10^3/s to 10^4/s. However, when the normalised loading rate continues to increase, all rock materials show a very strong rate effect on the dynamic initiation fracture toughness.

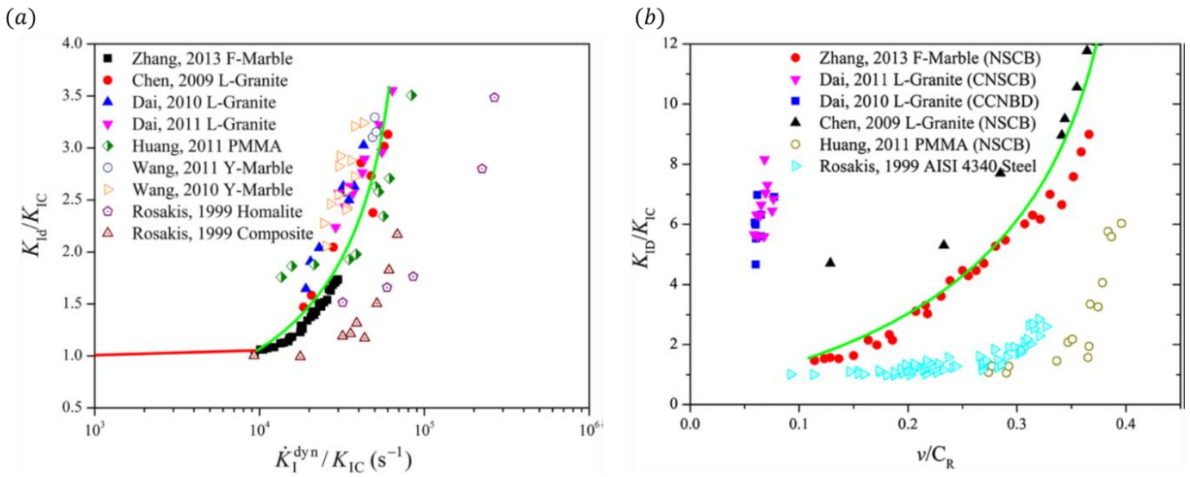

Figure 2.0–18. Dynamic fracture toughness with influencing factors: (a) Normalised dynamic initiation fracture toughness with loading rate; (b) Normalised dynamic initiation fracture toughness with crack propagation velocity for different materials.

The rate dependence of dynamic crack propagation toughness was also examined by Zhang and Zhao (2013), who plotted the normalised dynamic crack propagation toughness of different materials with the crack propagation velocity, presented in Figure 2.0–18b. The dynamic crack propagation could be obtained from experiment either by estimating the unit dissipated energy pertaining to the test specimen (Dai et al. 2011) or by measuring the crack propagation velocity through a chain of strain gauges positioned along the crack propagation path (Zhang and Zhao 2013). Although different materials show different degrees of rate-sensitivity, normalised dynamic crack propagation toughness depends highly on the crack propagation velocity. Apart

from the propagation velocity, the dynamic crack propagation toughness is also affected by some other factors such as acceleration and temperature. This is a possible reason why the result in Figure 2.0–18b shows such a big difference in the degree of rate sensitivity.

2.4. Numerical simulation of rock fracture

The computational modelling of rock fracture has also gained significant progress in the past few decades, with many studies focusing on the development of material constitutive models and numerical methods. On the constitutive modelling side, most existing constitutive models for rocks were developed based on classical plasticity and damage theories (Shao et al. 2003, Hu et al. 2010, Kolo et al. 2016). Constitutive models of this type are normally obtained by fitting the constitutive response with experiments. When considering loading rate effects, a similar calibration process is undertaken to consider the effect of loading rate on yielding strength or the yield function in plasticity or damage models (Bažant and Li 1997, Li and Bažant 1997, Zhao 2000, Zhou et al. 2005). Accordingly, these constitutive models are normally unable to provide accurate predictions of rock behaviour under loading rates which are outside the range of the calibration. Moreover, those models fail to account for the underlying mechanisms of strong localisation of deformation and fracture. In other words, these models describe the material behaviour from initial yield to complete fracture with a single stress-strain relationship, ignoring the strong gradient of strain due to localisation. As a consequence, despite the fact that they can reproduce results that please the eye for lab-scale experiments, they do not possess a scaling law to capture correctly the size-dependent behaviour due to localised failure.

Therefore, enhancements of such classical continuum constitutive models using smeared crack approach (Petersson 1981, De Borst 1987, Weihe et al. 1998, Hariri Ard et al. 2012) and nonlocal/gradient theories (Pijaudier-Cabot and Bažant 1987, Voyiadjis and Al-Rub 2005, Nguyen et al. 2015), the eXtended finite element method (Wells and Sluys 2001, Borst et al. 2006, Salimzadeh and Khalili 2015, Ferté et al. 2016, Dimitri et al. 2017), strong discontinuity approach (Oliver 1996, Dias-da-Costa et al. 2009, Dias-da-Costa et al. 2010, Dias‐da‐Costa et al. 2013, Bosco et al. 2015, Zhang and Zhuang 2018), enhanced assumed strain (Borja 2000, Motamedi et al. 2016, Reinoso et al. 2017) and double scale model (Nguyen et al. 2012, Nguyen et al. 2014, Nguyen et al. 2016, Nguyen et al. 2016) have been used as regularisation to resolve the issues. These constitutive models have their own advantages and limitations

when modelling rock fractures, which are comprehensively reviewed in Chapter 4 together with the key formulations.

The material constitutive model, once developed, is implemented in a numerical method to solve the equilibrium equation that governs the macro-behaviour of rock materials. Great efforts have been made to developing numerical methods for rock fractures. Research in this area can be divided into continuum-based, discontinuum-based and hybrid numerical approaches. Continuum-based methods can be further divided into mesh-based methods (e.g. the finite difference method, finite element method) and mesh-free methods (e.g. smoothed particle hydrodynamics). The dominant stream in discontinuum-based methods is that of the discrete element method (DEM), thanks to the strong feasibility of detaching new contacts during calculations. Depending to the solution algorithm used, the DEM can be divided into explicit formulation and implicit formulation. Hybrid methods that combine continuum-based and discontinuum-based methods have been developed for rock fracture mechanics in the last few decades. The main hybrid model types are the numerical manifold method (NMM) (Shi 1992) and the hybrid FEM/DEM method (Gui et al. 2015). In what follows, a detailed review of the popular numerical methods for simulating rock fracture is presented, with reference to their advantages and limitations. The existing knowledge gap in modelling rock fracture will be established from this review.

2.4.3. Continuum mesh-based method

- *Finite difference method*

The finite difference method (FDM) is the oldest numerical method for the numerical solution of the partial differential equations (PDEs). The basic concept of the FDM is to discretise the governing equations in the forms of PDEs by replacing the partial derivatives with the difference-defined spatial intervals in the coordinate directions (Wheel 1996). In conventional FDM, a rectangular grid of nodes is embedded and the FDM equation at the grid node can be expressed as combinations of function values at four adjacent nodes together with applied external forces, without any requirement for a trial or interpolation function. Therefore, implementation of the conventional FDM is very straightforward. However, the regular gird utilised in the conventional FDM limits its applicability to fractures, complex boundary conditions and material heterogeneity. To deal with this inherent deficiency, some improved techniques based on conventional FDM have been developed, such as the irregular mesh technique (Perrone and Kao 1975, Brighi et al. 1998) and the finite volume approach.

As a branch of FDM, the finite volume method (FVM) is also a direct approximation of the PDEs, but in the integral form (Jing 2003). FVM can overcome the numerical inflexibility of the grid generation and boundary conditions encountered in the FDM, showing great efficiency in memory and storage thanks to its localised formulation. In terms of computational solid mechanics, the finite volume method can be classified into two approaches: cell-centred (Demirdžić and Martinović 1993, Hattel and Hansen 1995) and vertex-based (Oñate et al. 1994, Taylor 1996). The cell-centred approach, based upon traditional FVM, has been successfully applied to small strain deformation (Wheel 1999) and stress-analysis of linear elastic and non-linear stress (Fryer et al. 1991). However, the cell-centred approximation has difficulty in prescribing boundary conditions when simulating problems with complex geometries or problems with indirect displacement-subjected boundaries, which constrains its application in rock fractures. Vertex-based FVM is the bridge between conventional FVM and traditional FE method. Like the FE method, the vertex-based approach employs shape functions to describe the variation of an independent variable, such as displacement, over an element and is therefore well suited to complex geometries (Bailey and Cross 1995).

In the last couple of decades, FDM/FVM has been successfully applied to fracture applications for investigating the mechanism of macroscopic fracturing processes. The examples are brittle fractures in heterogeneous rocks (Fang 2001), slope stability (Kourdey et al. 2001), coupled hydro-mechanical or THM processes (Garipov et al. 2016), dynamic fluid-structure interaction (Lv et al. 2007), and multiphase flow in fractured porous media (Hajibeygi et al. 2011). Although FVM was demonstrated to be a simple, straightforward, conservative and efficient approach due to its inherent iterative character, this method is still limited to small deformation and simple fracture applications.

- *Boundary element model*

Unlike FD methods, the boundary element method (BEM) seeks a weak solution at the global level through an integral statement, based on Betti's reciprocal theorem (Betti 1874) and Somigliana's identity (Somigliana 1885). Displacements and stresses of the computational domain can be evaluated by discretising the problem boundary with a finite number of boundary elements and then approximating the solution of functions locally of boundary elements by shape functions. The main advantage of the BEM over the FDM is its simpler mesh generation and greater accuracy if the same level of discretisation is used, thanks to its direct integral formulations. However, in BEM, fractures must be assumed to have two

opposite surfaces and singular tip elements must be used at the apex of the fracture tip, leading to mathematical degeneration in the numerical formulation (singular global stiffness matrices) if the same boundary conditions are specified at the two opposite fracture surfaces (Jing 2003).

To resolve this issue, some special techniques have been devised. Among these, the most popular are the subregion method proposed by Blandford et al. (1981) and the dual boundary element method proposed by Portela et al. (1992). In the subregion method, the computational domain is divided into multiple subdomains by fractures along their interfaces. In this case, the global stiffness matrices of opposing surfaces belong to different subdomains, thus solving the singularity issues of the global matrix. However, treatment will generates a much larger system of algebraic equation than necessary (Mi and Aliabadi 1992). Furthermore, this method requires a predefined fracturing path and growth rate for determination of the location and size of a subregion. These drawbacks constrain its application in rock fracture mechanics. As an alternative to the subregion method, the dual boundary element method could solve the singularity of the global matrix by implementing both displacement and traction boundary integral equations. The dual boundary element method combined with a maximum tensile stress failure criterion was developed by Chen et al. (1998) to predict crack initiation and propagation in a Brazilian disc shale specimen under a mixed-mode loading condition, as shown in Figure 2.0–19. The dual boundary element method has also been applied to predict dynamic stress intensity factors under mixed-mode conditions (Albuquerque et al. 2004, Garcia-Sanchez et al. 2007). Good agreement with experimental results was achieved, but this method is still limited to single or a couple of cracks.

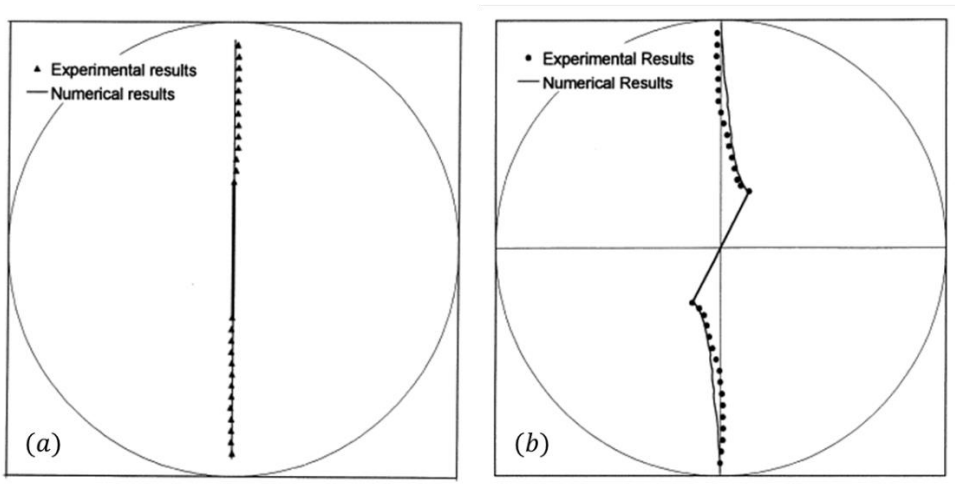

Figure 2.0–19. BEM simulation of fracture propagation in Brazilian disc test; (a) under mode I loading; (b) under mixed-mode loading (Chen et al. 1998).

Overall, despite successful applications of the BEM, prediction of the complex fracturing processes of rocks using the BEM is still very challenging. On the one hand, BEM is not very flexible in simulating material heterogeneity, because of the simple subdomain division and material non-linearity due to the presence of domain integrals (Jing 2003). On the other hand, complex numerical manipulations or remeshing are required to ensure that tip elements representing new fracture tips are added. Due to those limitations, fracture initiation and propagation of rock have not been widely simulated using BEM.

- *Extended finite element method*

The extended finite element method (XFEM) was first proposed by Belytschko and Black (1999). The basic idea of the XFEM is that an enriched shape function is added into the standard finite element discretisation via the partition of unity. The key advantage of this model is that it can simulate crack initiation and propagation without remeshing, thus providing an attractive way to investigate the fracture behaviour of solid materials. The XFEM has gained significant attention since its invention and many studies have been conducted applying this technique (Sukumar and Belytschko 2000, Bellec and Dolbow 2003, Mariano and Stazi 2004).

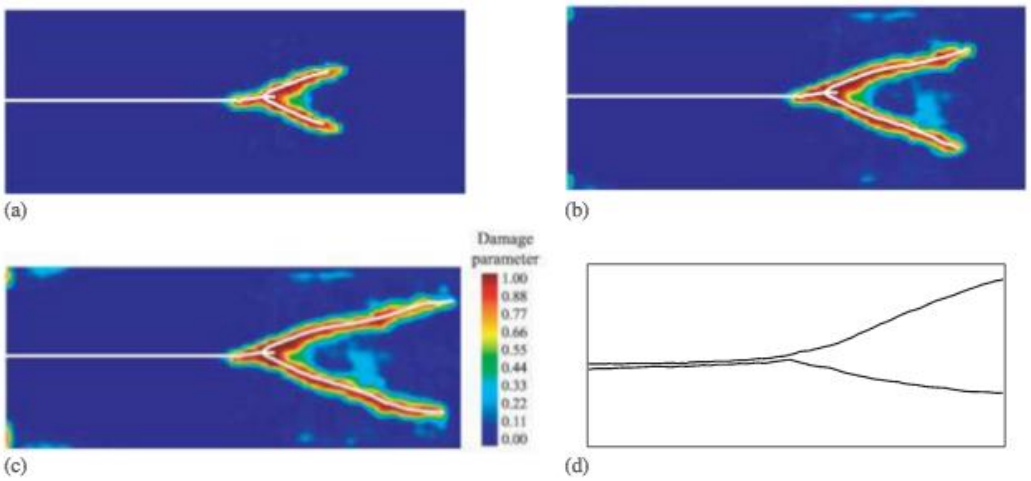

Figure 2.0–20. Crack branching simulation using XFEM: (a-c) fracture pattern at different time steps; (d) a sketch of the experiment paths

The XFEM has been mainly applied to problems involving crack growth of a single crack or a few cracks (Sukumar and Belytschko 2000) and crack nucleation (Bellec and Dolbow 2003, Mariano and Stazi 2004). Simulation of dynamic fracture was conducted by Belytschko et al. (2003) using the XFEM approach. A cohesive zone model was used to model the crack tip

behaviour and loss of the hyperbolicity criterion was applied to advance the crack. Song et al. (2006) introduced a new method for modelling arbitrary dynamic crack and shear band propagation by describing the discontinuity as superposed elements and phantom nodes. Figure 2.0–20 shows one numerical example of cracking propagation at different times. The results agree well with analytical solutions and numerical results reported by Belytschko et al. (2003).

Despite its robustness in capturing crack nucleation and propagation, the applications of XFEM are at present limited to models with few cracks. For problems involving a large number of cracks or multiple cracking networks, the application of the XFEM is challenging. Accordingly, application of the XFEM for large-scale geoengineering problems involving a large number of fractures is very difficult.

2.4.4. Continuum-based meshless method

Over the last few decades, a large family of meshless methods has been invented to eliminate the mesh-distortion issues in mesh-based continuum approaches which can be encountered during failure involving large deformation or fracture. In meshless methods, spatial differential equations for the whole problem domain are established without a predefined mesh for the domain discretization. Instead, the computational domain, as well as the boundaries, are represented by a set of arbitrarily distributed points. Thus, compared with mesh-based methods, meshless methods are more flexible in dealing with large-deformation problems.

Examples of meshless methods are smoothed particle hydrodynamics (SPH) (Monaghan 1997), material point methods (Sulsky et al. 1995), element-free Galerkin (EFG) method (Belytschko et al. 1994), meshless local Petrov-Galerkin (MLPG) method (Lin and Atluri 2001), cracking particles method (Rabczuk and Belytschko 2004) and particle finite element method – PFEM (Butler et al. 2007, Rodriguez et al. 2016, Rodríguez et al. 2017). Depending on the way they discretise governing equations, they can be divided into two categories: the strong-form formulation (e.g. SPH) and the weak form formulation (e.g. EFG). The weak-form methods are meshless only in terms of the particle approximation of field variables. However, to perform numerical integration over the problem domain, a background mesh must be adopted. Unlike the weak-form methods, the strong-form methods are truly meshless. In other words, they need no background mesh, during both numerical integration and approximation processes. They often use the Point Collocation Method to solve the governing PDEs and boundary conditions. Therefore, strong-form methods are more straightforward to implement and computationally cheaper than weak-form methods.

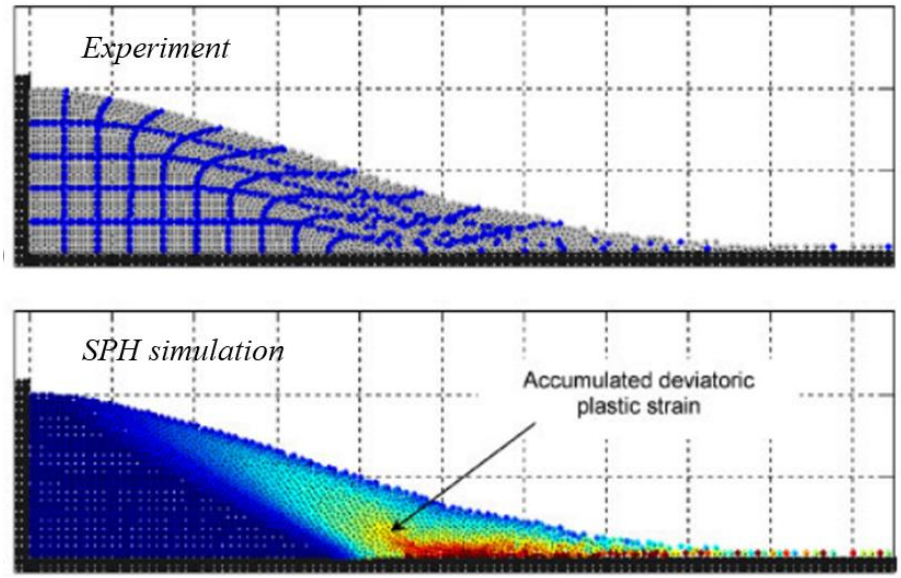

Figure 2.0–21. SPH simulation of non-cohesive soil failure in comparison with experimental results (Bui et al. 2008).

Among all the mesh-free methods, SPH is the oddest and a truly mesh-free technique that requires no background mesh for numerical integration of governing equations, thus avoiding some drawbacks associated with computational mesh, such as cell crossing in MPM (Zhang et al. 2011) or re-meshing in PFEM (Zhang et al. 2013). Originally developed by Gingold and Monaghan (1977) for astrophysical applications, SPH has since been successfully extended to other engineering applications such as fluid flow (Monaghan 1994, Chambon et al. 2011, Chen and Qiu 2011, Qu et al. 2013), friction stir welding (Pan et al. 2013), heat transfer (Cleary and Monaghan 1999), seepage through fixed porous media (Kermani and Qiu 2017) and failure of soils (Bui et al. 2007, Bui et al. 2008, Chen and Qiu 2011, Bui and Fukagawa 2013, Bui et al. 2014, Kermani and Qiu 2018, Sheikh and Qiu 2019). It can be seen from these examples, such as the soil failure simulation depicted in Figure 2.0–21, that SPH is a very attractive method for simulating large deformation in real-scale applications.

SPH has also been extended in the last decade to the simulation of fracturing problems which normally involve large displacement and even full detachment. For example, Das and Cleary (2010) investigated the fracture patterns of rock with different rock shapes under impact loading by using SPH with a continuum damage model. The result shows that SPH could handle very complex transient dynamic stress fields associated with collision and fracture. Compressive failure of heterogeneous rocks was also simulated under confining pressure by using SPH coupled with an elastoplastic damage model (Ma et al. 2011). Later, Douillet-

Grellier et al. (2016) applied SPH with the Druker-Prager and the Grady-Kipp damage model to simulate mixed-mode rock fractures. As it naturally keeps track of the free surface generated by fracturing, SPH allows the propagation of fracture and high-deformations of final fracture patterns without any issue like mesh-distortion in traditional mesh-based methods, thus is a good candidate in simulating rock fractures.

2.4.5. Discontinuum based numerical approaches

- *Discrete element method (DEM)*

Besides the classical continuum mechanics approach, the discrete element method is a powerful alternative for studying the fracture behaviour of quasi-brittle materials at high strain rates. In this method, the domain of interest is represented as an assemblage of separate blocks or particles. The contacts between these particles then need to be identified and kept updating during the simulation process. The discrete element method was first proposed by Cundall and Strack (1979) for studying granular materials, and it has subsequently been developed and applied to study the fracturing behaviour of rocks.

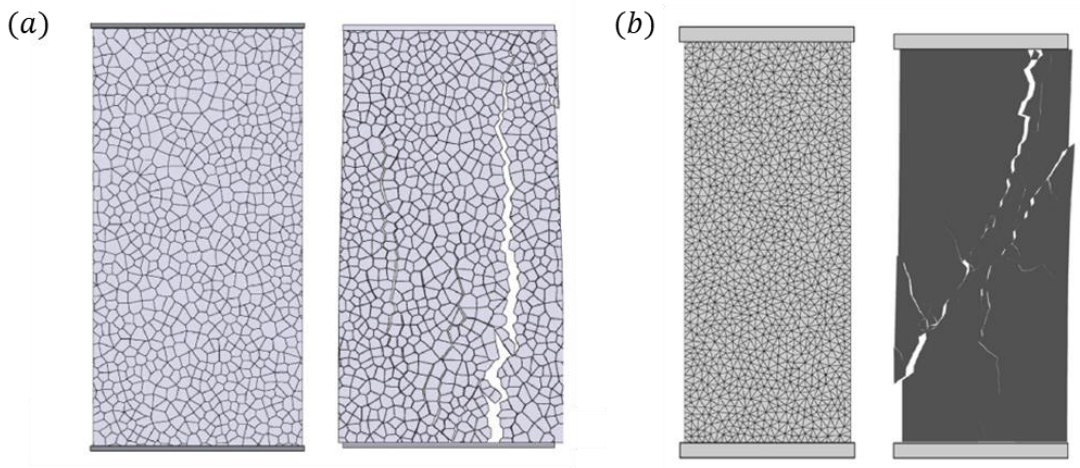

Figure 2.0–22. Uniaxial compression test using DEM: (a) Grain-based method (Kazerani and Zhao 2010); (b) Cohesive boundary approach (Kazerani et al. 2012).

The Universal Element Code (UDEC) and Particle Flow Code (PFC) are the two most widely used software packages that have been developed based on the discrete element concept. Rock fracture behaviour under quasi-static and dynamic loadings, either compression or tension, have been extensively studied using these software packages (Hentz et al. 2004). For example, a grain-based UDEC model was used by Christianson et al. (2006) to conduct numerical triaxial

testing of rock samples. Physical properties of rock material were obtained from these numerical experiments, providing better understanding of the behaviour of repository drifts. Yin and Zhao (2013) studied the bedding plane effect on the behaviour of an anisotropic rock under dynamic loads; Aliabadian et al. (2012) and Zhu (2013) studied rock fragmentation and wave propagation problems using UDEC; Kazerani et al. (2012) implemented a UDEC model where the rock material was represented as a collection of irregular-sized deformable triangles with cohesive boundaries controlling material fracture and fragmentation properties, as shown in Figure 2.0–22.

- *Discontinuous deformation analysis (DDA)*

The discontinuous deformation analysis (DDA), proposed by Shi (1992), is an implicit discrete element method. In DDA, a mechanical system under loading must move or deform in the direction which produces the minimum total energy of the whole energy. The minimisation of the system energy will produce an equation of motion, the same as that used in the FEM. DDA has been widely applied to capture failure along predefined structural planes in rock masses (Hatzor and Benary 1998, Bakun-Mazor et al. 2009, Hatzor et al. 2010). Subsequently, some techniques were developed to introduce fracturing capabilities into DDA, such as debonding of artificial block interfaces (Ke 1997), or subdividing the block into multiple sub-blocks (Koo and Chern 1997) once fracture is detected. DDA has also been successfully applied to simulate fracturing processes under blast loading (Mortazavi and Katsabanis 2001, Ning et al. 2011). However, DEM and DDA are not suitable for stress-strain analysis at the pre-failure stage. Moreover, these models consume much computational time, limited them to small-scale applications.

2.4.6. Coupled approaches

- *Hybrid FEM/DEM method*

Hybrid models have been widely used in rock engineering. One representative is the hybrid FEM/DEM method. The fundamental idea is that the finite element representation of the solid region is combined with progressive fracturing, which leads to the formation of discrete elements, thereby forming one or more deformable finite elements (Munjiza et al. 1995). This model has been widely and successfully applied to the simulation of fracturing processes such as complex rock mass behaviour in the close vicinity of excavations (Coggan et al. 2003), crack propagation under mixed-mode loading (Ariffin et al. 2006, Karami and Stead 2008), fracture

process associated with the block caving-induced step-path failure process (Vyazmensky et al. 2010) and dynamic failure of brittle rocks with a mixed model cohesive fracture model (Gui et al. 2016). A comparison of a notched semi-circular bending (NSCB) test between the hybrid FEM/DEM simulation and experiments is shown in Figure 2.0–23. The result demonstrates that the hybrid FEM/DEM is an appealing alternative numerical tool for small-scale rock mechanics applications. However, this method still requires the detection of new contacts and dealing with the interaction between discrete bodies, leading to extremely high computational cost when dealing with large-scale geotechnical applications. Furthermore, the method is highly sensitive to the initial mesh construction.

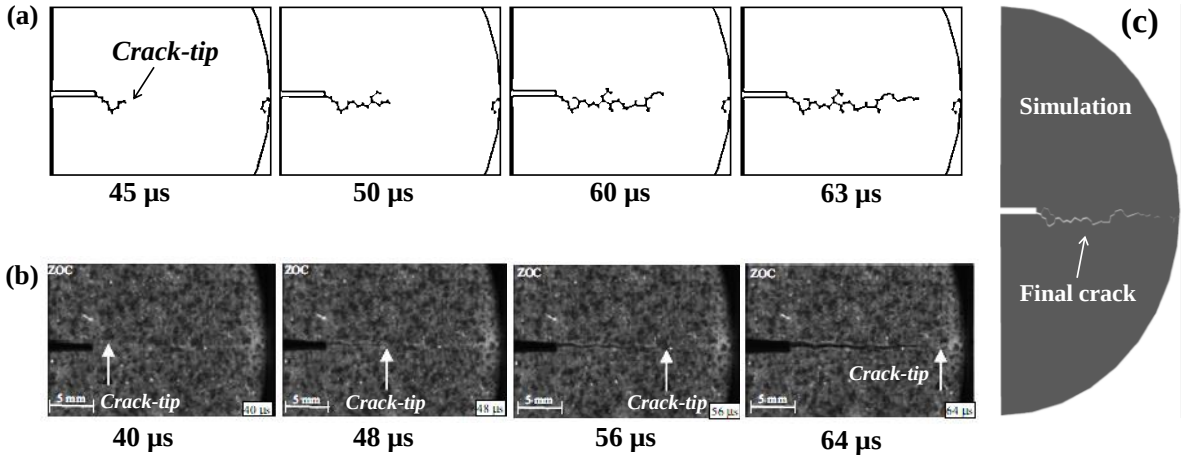

Figure 2.0–23. Crack-tip propagation process. (a) Hybrid FEM/DEM method; (b) experimental results (Gui et al. 2016)

- *Numerical manifold method (NMM)*

The numerical manifold method (NMM) was proposed by Shi (1992), combining the FEM and DDA into one framework. In the NMM, truncated discontinuous shape functions are applied to simulate fracture phenomena, and the continuum bodies, fracture bodies, as well as discrete blocks, are generally treated in the same way by these shape functions. NMMs have been applied to simulate multiple branched and intersecting cracks (Zhang et al. 2000, Zhang et al. 2007, Zhang et al. 2010), the dynamic friction mechanism of blocky rock systems (Ma et al. 2007a), dynamic nonlinear analysis of saturated porous media (Zhang and Zhou 2006), the shear response of heterogeneous rock joints (Ma et al. 2007b) and fracture progress simulations (Chiou et al. 2002, Chen et al. 2006). Figure 2.0–24 shows rock fracture under dynamic loading in the NMM framework by Chen et al. (2006). Based on the results, NMM is proved as promising in modelling large deformations and fracturing processes of transition from continua

to discontinua. However, implementation of the NMM for 3D simulation is still very difficult at present. Furthermore, the current NMM lacks large-scale computational capabilities due to its contact detection and modelling algorithm. When dealing with field-scale problems involving millions of particles with irregular shapes, NMM still faces the outstanding challenges of how to detect and represent the contact interaction between the particles and how to display results in a reasonable CPU time (Ma et al. 2010).

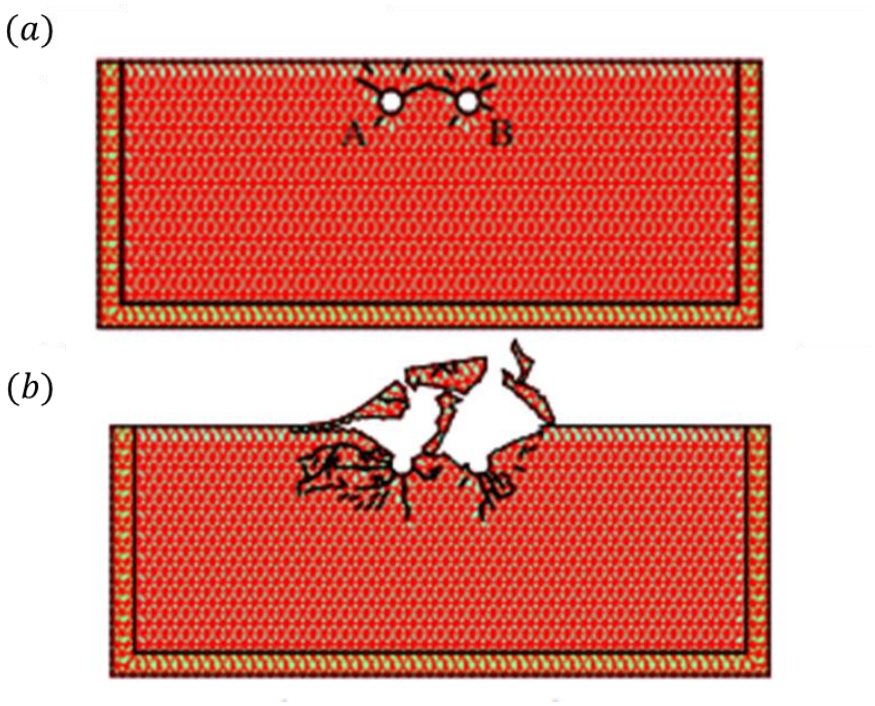

Figure 2.0–24. NMM simulation results of two-hole blasting (Chen et al. 2006).

- *Lattice spring model*

The idea of Lattice spring model (LSM) can be traced back to the work of Hrennikoff (1941), for simulating the problems of continuum elasticity with a fixed Poisson's ratio as 1/3. However, the original model suffers from the restriction of Poisson's ratio and the problem of parameter calibration. To resolve these shortcomings occurred in the original model, the distinct lattice spring model (DLSM) was developed by Zhao et al. (2011). In the DLSM, the computational domain is represented by a set of lattice points (or particles), between two of which are connected by a normal spring and a multibody shear spring. Different from DEM which requires the microscopic material parameters, macroscopic parameters obtained from

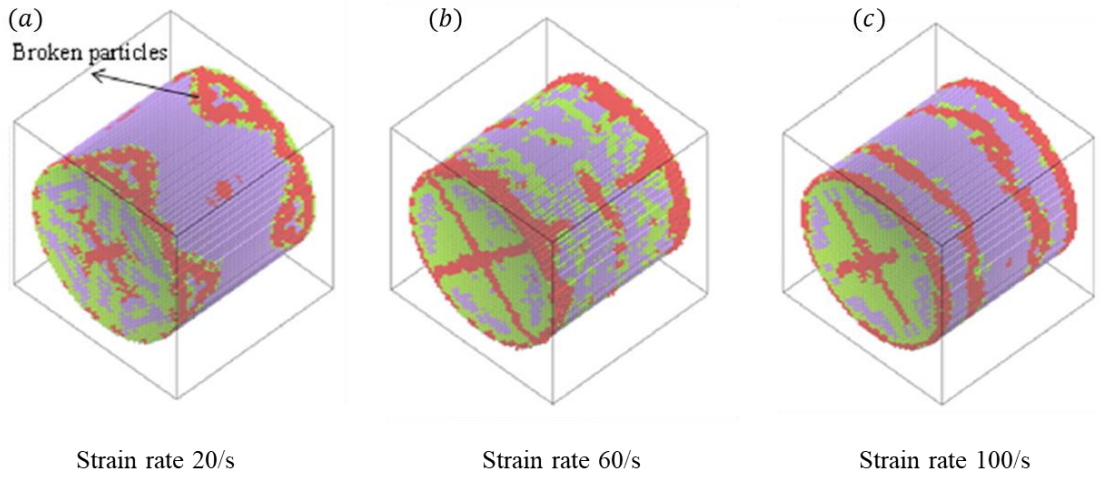

Figure 2.0–25. Failure of Gosford sandstone in uniaxial tensile tests using DLSM (Zhao et al. 2014).

the laboratory experiments can be directly used in the DLSM. In addition, as the stiffness matrix in DLSM is based on the local interaction between lattice points, and thus it does not require any global stiffness matrix in DEM. These two advantages give the DLSM great feasibility in simulating geotechnical problems such as failure of brittle materials (Kazerani et al. 2010, Zhao and Zhao 2010, Zhao et al. 2011, Zhao et al. 2013, Zhao et al. 2014), coupled fluid flow and deformation (Zhao and Khalili 2012), wave propagation (Zhu et al. 2011) and desiccation-induced soil cracking (Gui and Zhao 2015). Figure 2.0–25 shows failures of Gosford sandstone under different strain rates using DLSM with X-ray micro CT. The result clearly showed that DLSM could capture the strain rate dependency of the uniaxial tensile strength of the sandstone. Although its success in modelling large-deformation and complex fractures, DLSM is only suitable for modelling small scale problems due to the high computational cost. Therefore, the parallel DLSM (Zhao and Khalili 2012, Zhao et al. 2013) and the coupled approaches such as coupling between DLSM and NMM (Zhao et al. 2012) and coupling between DLSM and DDA (Zhao et al. 2016) were developed in past few years for reducing the computational time. However, a more complex constitutive model for bond springs and a more advanced representation technique in DLSM are still required for simulating size-dependent behaviour of rocks and solving real engineering problems (Zhao et al. 2012).

2.5. Summary of literature review

This literature review has highlighted a significant knowledge gap in the computational modelling of rock fractures. While most of the experimental data clearly demonstrates the time and length scales dependent behaviour of rock materials, computer modelling fails to capture

this behaviour. In particular, most existing material models for rocks are derived by fitting the mathematical formulation to certain experimental data conducted at a certain laboratory scale. These models may reproduce results that please the eye with the lab-scale experiment, but beyond this scale, their prediction is questionable due the lack of an embedded grain-scale mechanism and correct spatial scaling laws. Although many attempts have been undertaken to enhance the predictive capability of computer models, these approaches are still conducted on the same continuum basis, and thus they will lead to improved phenomenological responses but do not provide a model with any predictive capabilities.

Furthermore, there is a lack of a robust numerical tool capable of simulating rock fractures and analysing the complex fracture mechanics under various loading conditions. A discontinuum-based approach like the discrete element method has some advantages, thanks to its capability to handle large deformation and the meaningful descriptions of fracture and fragmentation processes from its use of force-displacement relationships in constitutive models for the discrete contacts (Gui et al. 2016, Nguyen et al. 2017, Nguyen et al. 2017). However, it requires very high computing power for detecting new contacts and dealing with the interactions between discrete bodies, thus limiting such methods to small-scale applications. Unlike discontinuum-based methods, continuum-based approaches have great feasibility for simulating large-scale problems, thanks to lumping all discrete fracture and fragmentation processes at a lower scale in a constitutive relationship describing the behaviour of a larger volume element. SPH shows great flexibility in dealing with complex fracture patterns and large deformations of rocks and has been successfully applied to solve rock fractures (Ma et al. 2011, Douillet-Grellier et al. 2016). However, those works fail to consider the size and rate dependence of rock fractures. This can be solved by developing appropriate constitutive models which can capture the experimentally observed rate effects and the energetic size effects due to strong strain gradients. As pointed out earlier by Van Mier (1986), post-peak behaviour must be described by a stress-displacement relationship, as the continuum assumption breaks down as soon as strong localisation of deformation occurs (Nguyen et al. 2014). Accordingly, further developments in terms of numerical method and constitutive models for this topic are needed to establish a robust way to predict rock fracture under both quasi-static and dynamic loading conditions.

Chapter 3

Smoothed Particle Hydrodynamics

3.1. Introduction

The previous chapter provided a detailed literature review of existing numerical methods for rock fracture problems under static and dynamic loadings. The mesh-free SPH method is preferred among all the existing numerical methods for fracture prediction problems for several reasons:

- SPH can naturally handle rock fractures involving extreme deformations and discontinuities without any mesh distortion, unlike traditional mesh-based methods such as FEM and DEM.
- SPH can model the disintegration of solids during developing fracture by virtue of its advantages in automatically handling free surface boundaries generated by fracture.
- SPH can predict complex fracture patterns without the restraint of an underlying grid in traditional mesh-based methods, as the fracture pattern in SPH is represented by a set of damaged SPH particles, each of which can possess fracture orientation.
- The time histories of all field variables in SPH are updated in a Lagrangian framework. The history-tracking ability of SPH helps establish a natural framework for predicting the initiation and propagation of fracture, compared with traditional Eulerian methods.
- SPH can handle the complex dynamic stress fields involving collisions and fractures, as SPH particles automatically exchange the variable history (e.g. stress, strain, velocity) with their surrounding particles as they move. Therefore, it can easily incorporate complex constitutive frameworks such as rate-dependent or size-dependent models for investigating the effect of loading and size on the fracture behaviour of rocks.

- In SPH, fracturing is driven by the stress-strain relationship. Therefore, damage evolution is easy to implement explicitly for representing the degree of fracture for each SPH particle.
- SPH is flexible in simulating large-scale real-life applications with reasonable computational cost.

On the basis of these advantages of SPH regarding rock fractures, the SPH method is adopted as the basic numerical framework in this study. In this chapter, the details of SPH methods are presented. First, the background of SPH is introduced briefly in Section 3.2, followed by the essential formulations of SPH in Section 3.3. Then SPH approximations regarding governing equations for rocks are derived in detail in Section 3.4. In Section 3.5, traditional time integration schemes for updating field variables are introduced. Some improvements to instabilities occurring in traditional SPH methods are explained in Section 3.6. Finally, some numerical results of elastic tests using two improved SPH methods are compared with the analytical solution or the traditional SPH to examine the stability of these two SPH frameworks in simulating elastic solids under different loading conditions.

3.2. Background of SPH

The SPH method was invented by Lucy (1977) and Gingold and Monaghan (1977) to solve astrophysical problems in three-dimensional open space. Since its invention, SPH has been widely extended to a range of applications such as elastic flow (Swegle 1992), response of material strength (Libersky and Petschek 1991, Libersky et al. 1993, Benz and Asphaug 1995), free surface fluid flows (Monaghan 1994), gravity currents (Monaghan 1995), low-Reynolds number viscous fluid flows (Takeda et al. 1994, Morris et al. 1997), underwater exploration (Swegle and Attaway 1995), incompressible fluid flows (Cummins and Rudman 1999, Shao and Lo 2003), heat transfer problems (Cleary and Monaghan 1999), friction stir welding (Pan et al. 2013), multi-phase flows (Monaghan and Kocharyan 1995, Monaghan 1997, Morris 2000), geophysical flows (Gutfraind and Savage 1998, Cleary and Prakash 2004) and turbulence flows (Monaghan 2002).

SPH has also been successfully applied to solid mechanics or solid-fluid interactions in engineering problems, due to its relatively strong ability in incorporating complex physical effects into the SPH formulations and handling large deformations. Those applications include large deformation and failure of geomaterials (Bui et al. 2007, Bui et al. 2008, Zhao et al. 2017), slope failures (Bui et al. 2011, Bui and Fukagawa 2013, Peng et al. 2016), granular flows and

landslides (Pastor et al. 2009, Nguyen et al. 2017), soil-structure interaction (Bui et al. 2008, Bui et al. 2014, Neto and Borja 2018), coupled soil-water problems (Bui 2007, Pastor et al. 2014, Zhang et al. 2016, Bui and Nguyen 2017), soil triaxial tests (Zhao et al. 2019) and rock fracture (Das and Cleary 2010, Ma et al. 2011, Douillet-Grellier et al. 2016).

3.3. Essential formulations of SPH

There are two main steps in deriving SPH formations. The first step is the integral approximation or so-called kernel approximation of field function, which is introduced in 3.3.1, and the second step is particle approximation, presented in 3.3.2. The last part of this section is the construction of kernel function.

3.3.1. Integral approximation

The concept of integral approximation of a function $f(\boldsymbol{x})$ starts from the following equation:

$$f(\boldsymbol{x}) = \int_{\Omega} f(\boldsymbol{x}')\,\delta(\boldsymbol{x}-\boldsymbol{x}')d\boldsymbol{x}' \tag{3.1}$$

where Ω is the volume of the integral that contains $\boldsymbol{x}$; $\delta(\boldsymbol{x}-\boldsymbol{x}')$ is the Dirac delta function (see Figure 3.0–1), the formulation of which is as follows:

$$\delta(\boldsymbol{x}-\boldsymbol{x}') = \begin{cases} 1 & \boldsymbol{x}=\boldsymbol{x}' \\ 0 & \boldsymbol{x}\neq\boldsymbol{x}' \end{cases} \tag{3.2}$$

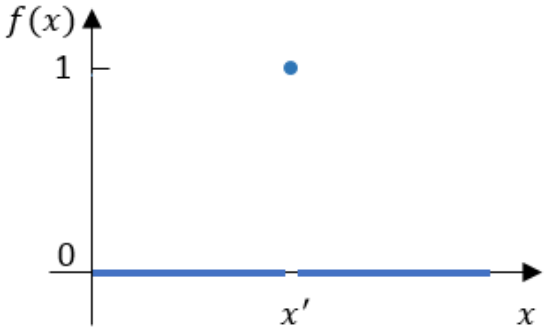

Figure 3.0–1. Dirac Delta Function

The Delta function kernel is then replaced by a smoothing function $W(\boldsymbol{x}-\boldsymbol{x}', h)$, and thus the function becomes:

$$f(\boldsymbol{x}) = \int_{\Omega} f(\boldsymbol{x}')\,W(\boldsymbol{x}-\boldsymbol{x}', h)d\boldsymbol{x}' \tag{3.3}$$

where W is the so-called smoothing kernel function, or kernel function for simplicity; h is the smoothing length defining the influence area of the smoothing function.

In SPH convention, the angle bracket <> is used to represent the kernel approximation operator and therefore equation (3.3) can be written as

$$< f(\boldsymbol{x}) >= \int_{\Omega} f(\boldsymbol{x}')\, W(\boldsymbol{x}-\boldsymbol{x}', h) d\boldsymbol{x}' \tag{3.4}$$

The approximation for the spatial derivative $\nabla \cdot f(\boldsymbol{x})$ is obtained by replacing $f(x)$ with $\nabla \cdot f(\boldsymbol{x})$ in equation (3.4):

$$< \nabla \cdot f(\boldsymbol{x}) >= \int_{\Omega} \nabla \cdot f(\boldsymbol{x})\, W(\boldsymbol{x}-\boldsymbol{x}', h) d\boldsymbol{x}' \tag{3.5}$$

$$< \nabla \cdot f(\boldsymbol{x}) >= \int_{\Omega} \nabla \cdot [f(\boldsymbol{x}')\, W(\boldsymbol{x}-\boldsymbol{x}', h)] dx' - \int_{\Omega} f(\boldsymbol{x}') \cdot \nabla W(\boldsymbol{x}-\boldsymbol{x}', h)] d\boldsymbol{x}' \tag{3.6}$$

$$< \nabla \cdot f(\boldsymbol{x}) >= \int_{\mathrm{S}} f(\boldsymbol{x}')\, W(\boldsymbol{x}-\boldsymbol{x}', h)] \cdot \vec{\boldsymbol{n}} dS - \int_{\Omega} f(\boldsymbol{x}') \cdot \nabla W(\boldsymbol{x}-\boldsymbol{x}', h)] d\boldsymbol{x}' \tag{3.7}$$

where $\nabla W(\boldsymbol{x}-\boldsymbol{x}', h) = \frac{\partial W(x-x', h)}{\partial \boldsymbol{x}'}$ is the derivative of the kernel function. For those particles whose support domain is inside the problem domain, the surface integral represented as the first term at the right of equation (3.7) is zero. Therefore, the above equation can be simplified as:

$$< \nabla \cdot f(\boldsymbol{x}) >= -\int_{\Omega} f(\boldsymbol{x}') \cdot \nabla W(\boldsymbol{x}-\boldsymbol{x}', h) d\boldsymbol{x}' \tag{3.8}$$

However, for particles whose support domain is truncated with the boundary, the surface integral is no longer zero, and improvements such as a corrective technique must be used to remedy the boundary deficiency, which is introduced later. From equation (3.8), it can be seen that the spatial gradient of a function through SPH integral approximation is determined from the values of the function together with the derivative of the smoothing function, rather than from the derivatives of the function itself.

3.3.2. Particle approximation

As the computational domain in SPH is discretised into a set of particles which carry all information concerning field variables (e.g. stress, density, velocity) and their derivatives, the continuous integral presentation cannot be directly applied to the particles. Therefore, a second step, particle approximation, is required, which converts the integral approximation of a function and its derivatives into discretised summations over the particles in the supporting domain (see Figure 3.0–2).

Therefore, the continuous integral approximation of a function shown as Equation (3.4) can be written in discretised forms as:

$$\langle f(\boldsymbol{x})\rangle = \int_{\Omega} f(\boldsymbol{x}')\, W(\boldsymbol{x}-\boldsymbol{x}', h)\, d\boldsymbol{x}'$$

$$= \sum_{j=1}^{N} f(\boldsymbol{x}_j) W(\boldsymbol{x}-\boldsymbol{x}_j, h)\, V_j$$

$$= \sum_{j=1}^{N} f(\boldsymbol{x}_j) W(\boldsymbol{x}-\boldsymbol{x}_j, h) \frac{1}{\rho_j}(\rho_j V_j)$$

$$\langle f(\boldsymbol{x}_i)\rangle = \sum_{j=1}^{N} \frac{m_j}{\rho_j} f(\boldsymbol{x}_j) W(\boldsymbol{x}-\boldsymbol{x}_j, h) \tag{3.10}$$

where $j = 1, 2, \ldots, N$ indicate particles within the support domain of particle i; m_j and ρ_j are respectively the mass and density of particle j. From equation (3.10), it can be seen that the value of a variable function at particle i is now expressed as the summation of the function values at its surrounding particles in the support domain of particle i with the kernel function.

Similarly, the particle approximation for the spatial derivative of a function becomes:

$$\langle \nabla \cdot f(\boldsymbol{x}_i)\rangle = -\sum_{j=1}^{N} \frac{m_j}{\rho_j} f(\boldsymbol{x}_j) \cdot \nabla_j W(x_i - x_j, h)$$

$$= \sum_{j=1}^{N} \frac{m_j}{\rho_j} f(\boldsymbol{x}_j) \cdot \nabla_i W(x_i - x_j, h) \tag{3.11}$$

where $\nabla_i W(x_i - x_j, h) = -\nabla_j W(x_i - x_j, h) = \frac{x_i - x_j}{r_{ij}} \frac{\partial W_{ij}}{\partial r_{ij}} = \frac{x_{ij}}{r_{ij}} \frac{\partial W_{ij}}{\partial r_{ij}}$. Equation (3.11) states that the value of the gradient of a variable function at particle i is represented as the summation of the function values at its surrounding particles in the support domain of particle i weighted by the gradient of kernel function with respect to particle i.

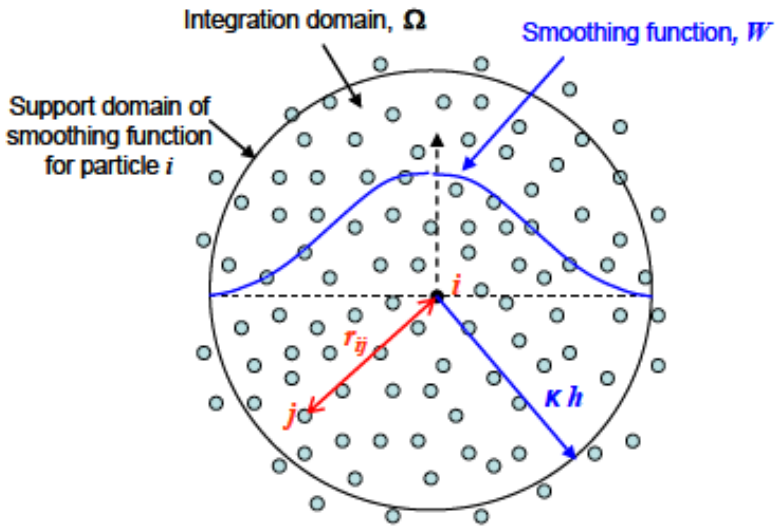

Figure 3.0–2. The basic idea of particle approximation of particle i with a compact supporting radius of κh .

3.3.3. Smoothing functions

Smoothing function plays a very important role in the SPH approximation as it can determine the accuracy of the function representation. Many different kernel functions have been presented in the literature for different applications. All kernel functions are constructed to satisfy certain requirements and only major ones are listed in this section. The first is the unity condition (normalisation condition), in which the integration of smoothing functions is equal to unity:

$$\int_{\Omega} W(x - x', h)dx' = 1 \tag{3.12}$$

The second condition is the Delta function property, which states that as the smoothing length approaches zero, the approximation value should be very close to the function value, which is represented as:

$$\lim_{h \to 0} W(x - x', h)dx' = \delta(x - x') \tag{3.13}$$

The third condition is the compact condition, defined as:

$$W(x - x', h)dx' = 0 \text{ when } |x - x'| > \kappa h \tag{3.14}$$

where κ defines the size of the influence area of the smoothing function.

Some other conditions exist such as positivity, symmetricity, decay and smoothness of smoothing kernel function. Detailed information for constructing a kernel function can be found in the work of Liu and Liu (2003). Any kernel functions satisfying those requirements can be applied in SPH. Some popular ones in the literature are listed next.

- *Gaussian kernel*

The Gaussian kernel is a good choice since it is very stable and accurate, originally used to simulate non-spherical stars (Gingold and Monaghan 1977). However, it can result in high computational cost since it requires a long distance for the kernel to approach zero, especially for high order derivatives of the function. The formulation of the Gaussian kernel is:

$$W(q, h) = \alpha_d e^{-q^2} \tag{3.15}$$

where α_d is $1/\pi^{1/2}h$, $1/\pi h^2$ and $1/\pi^{3/2}h^3$ in one-, two- and three-dimensional space respectively; and q is the normalized distance between particles i and particle j defined as $q = r/h$.

- *Quintic kernel*

Morris (1996) introduced a high-order spline kernel which is more stable than the Gaussian kernel. The formulation of Quintic kernel is:

$$w(q,h) = \alpha_d \times \begin{cases} (3-q)^5 - 6(2-q)^5 + 15(1-q)^5 & (0 \le q < 1) \\ (3-q)^5 - 6(2-q)^5 & (1 \le q < 2) \\ (3-q)^5 & (2 \le q < 3) \\ 0 & (q \ge 3) \end{cases} \tag{3.16}$$

where α_d is $120/h$, $7/478\pi h^2$ and $3/359\,\pi h^3$ in one-, two- and three-dimensional space respectively;

- *Cubic spline kernel*

The Cubic spline kernel, the most widely-used kernel function in the literature, was introduced by Monaghan and Lattanzio (1985) for astrophysical problems. The formulation of the cubic spline function is:

$$W(q,h) = \alpha_d \times \begin{cases} \frac{2}{3} - q^2 + \frac{1}{2}q^3 & (0 \le q < 1) \\ \frac{1}{6}(2-q)^3 & (1 \le q < 2) \\ 0 & (q \ge 2) \end{cases} \tag{3.17}$$

where α_d is $1/h$, $15/7\pi h^2$ and $3/2\,\pi h^3$ in one-, two- and three-dimensional space respectively. In this study, the Cubic spline kernel function is chosen for interpolations and the shape of this function and its derivative are illustrated in Figure 3.0–3.

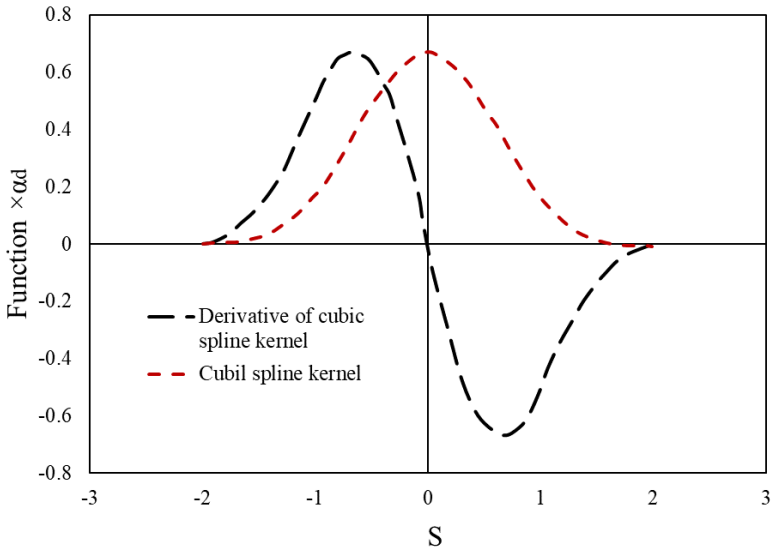

Figure 3.0–3. The cubic spline kernel and its first derivative.

3.4. SPH approximation of governing equations of rocks

3.4.1. Governing equations of rocks

The completed set of governing equations for rock consists of a mass conservation equation to describe the rate of change in density, a momentum conservation equation to describe the Lagrangian movement of rock material, and a constitutive relation to calculate stress from given strain increments. These equations can be written respectively as:

$$\frac{D\rho}{Dt} = -\rho\nabla \cdot \mathbf{v} \tag{3.18}$$

$$\frac{D\mathbf{v}}{Dt} = \frac{1}{\rho}\nabla \cdot \boldsymbol{\sigma} + \boldsymbol{b} \tag{3.19}$$

$$\frac{D\boldsymbol{\sigma}}{Dt} = \mathbf{D}_{ef} : \dot{\boldsymbol{\varepsilon}} \tag{3.20}$$

where ρ is the material density; $\mathbf{v}$ is the velocity vector; $\boldsymbol{\sigma}$ is the stress tensor; $\boldsymbol{b}$ is the vector component of acceleration due to external forces; $\mathbf{D}_{ef}$ is the material stiffness matrix;

$\dot{\boldsymbol{\varepsilon}}$ is the strain rate tensor, which can be calculated by velocity through a kinematic relation:

$$\dot{\boldsymbol{\varepsilon}} = [\nabla \cdot \mathbf{v} + (\nabla \cdot \mathbf{v})^{\mathrm{T}}]/2 \tag{3.21}$$

3.4.2. SPH approximation

To solve the continuity equation in SPH, the gradient of velocity for particle i ($\nabla \cdot \mathbf{v}$) must be approximated using equation (3.11), as follows:

$$\nabla \cdot \mathbf{v}_i = \sum_{j=1}^{N} \frac{m_j}{\rho_j} \mathbf{v}_j \cdot \nabla_i W(\boldsymbol{x_i} - \boldsymbol{x_j}, h) \tag{3.22}$$

However, the approximation will be more accurate when it involves the velocity difference between two interacting particles rather than using a single velocity of neighboring particles (Bui et al. 2008). To do this, the gradient of unity must be applied:

$$\frac{\partial 1}{\partial \boldsymbol{x}} = \sum_{j=1}^{N} \frac{m_j}{\rho_j} \nabla_i W\big(\boldsymbol{x_i} - \boldsymbol{x_j}, h\big) = 0 \tag{3.23}$$

By multiplying by $(-\mathbf{v}_i)$, equation (3.23) becomes:

$$\sum_{j=1}^{N} \frac{m_j}{\rho_j} (-\mathbf{v}_i) \nabla_i W\big(\boldsymbol{x_i} - \boldsymbol{x_j}, h\big) = 0 \tag{3.24}$$

Therefore, the gradient of velocity for particle i can be obtained by adding equation (3.22) to equation (3.24), leading to:

$$\nabla \cdot \mathbf{v}_i = \sum_{j=1}^{N} \frac{m_j}{\rho_j} \left(\mathbf{v}_j - \mathbf{v}_i\right) \cdot \nabla_i W(\boldsymbol{x_i} - \boldsymbol{x_j}, h) \tag{3.25}$$

Finally, the SPH approximation of governing equations can be now derived by combining equation (3.25) with equation (3.18) as:

$$\frac{\mathrm{D}\rho_i}{\mathrm{D}t} = \sum_{j=1}^{N} m_j \left(\mathbf{v}_i - \mathbf{v}_j\right) \cdot \nabla_i W(\boldsymbol{x_i} - \boldsymbol{x_j}, h) \tag{3.26}$$

The above equation states that the time rate of density for a particle can be approximated as the summation of the relative velocities between this particle and all the surrounding particles in the supporting domain weighted with the derivatives of the kernel function.

For the SPH approximation of the momentum equations, different transformations have been reported in the literature, which would lead to different discretised equation forms. One popular form of SPH particle discretisation for the momentum equation is similar to the SPH approximation for continuity equation. Directly applying the formulation of particle approximation (equation 3.11) to the right-hand side of equation (3.19) obtains:

$$\frac{\mathrm{D}\mathbf{v}_i}{\mathrm{D}t} = \frac{1}{\rho_j} \sum_{j=1}^{N} m_j \frac{\boldsymbol{\sigma}_j}{\rho_j} \cdot \nabla_i W(\boldsymbol{x_i} - \boldsymbol{x_j}, h) + \mathbf{b}_i \tag{3.27}$$

By adding the following gradient of unity with the stress:

$$\frac{\partial 1}{\partial \boldsymbol{x}} = \sum_{j=1}^{N} \frac{m_j}{\rho_j} \nabla_i W\left(\boldsymbol{x_i} - \boldsymbol{x_j}, h\right) = 0$$

$$\frac{\boldsymbol{\sigma}_i}{\rho_i} \sum_{j=1}^{N} \frac{m_j}{\rho_j} \nabla_i W\left(\boldsymbol{x_i} - \boldsymbol{x_j}, h\right) = 0 \tag{3.28}$$

the final SPH approximation of the momentum equation is

$$\frac{\mathrm{D}\mathbf{v}_i}{\mathrm{D}t} = \sum_{j=1}^{N} m_j \frac{\boldsymbol{\sigma}_i + \boldsymbol{\sigma}_j}{\rho_i \rho_j} \cdot \nabla_i W(\boldsymbol{x_i} - \boldsymbol{x_j}, h) + \mathbf{b}_i \tag{3.29}$$

This is one of the frequently used formulations of momentum evolution. The other popular one can be derived by first expanding the right-hand side of the momentum equation as follows:

$$\frac{1}{\rho} \nabla \cdot \boldsymbol{\sigma} = \nabla \cdot \left(\frac{\boldsymbol{\sigma}}{\rho}\right) + \frac{\boldsymbol{\sigma}}{\rho^2} \nabla \cdot \rho \tag{3.30}$$

By applying the SPH particle approximation to the gradient in above equation (3.30), the momentum equation (3.19) becomes:

$$\frac{\mathrm{D}\mathbf{v}_i}{\mathrm{D}t} = \sum_{j=1}^{N} \frac{m_j}{\rho_j} \frac{\boldsymbol{\sigma_j}}{\rho_j} \cdot \nabla_i W\left(\boldsymbol{x_i} - \boldsymbol{x_j}, h\right) + \frac{\boldsymbol{\sigma_i}}{{\rho_i}^2} \sum_{j=1}^{N} \frac{m_j}{\rho_j} \rho_j \cdot \nabla_i W(\boldsymbol{x_i} - \boldsymbol{x_j}, h)$$

$$\frac{\mathrm{D}\mathbf{v}_i}{\mathrm{D}t} = \sum_{j=1}^{N} m_j \left(\frac{\boldsymbol{\sigma_i}}{{\rho_i}^2} + \frac{\boldsymbol{\sigma_j}}{{\rho_j}^2}\right) \cdot \nabla_i W\left(\boldsymbol{x_i} - \boldsymbol{x_j}, h\right) \tag{3.31}$$

Both the approximations about the momentum equation shown in equation (3.29) and (3.31) conserve exactly linear and angular momentum and consequently reduce the error arising from the particle inconsistency problem.

Constitutive relation can be approximated through SPH particle approximation by substituting equations (3.25) and (3.21) into equation (3.20):

$$\frac{\mathrm{D}\boldsymbol{\sigma}_i}{\mathrm{D}t} = \mathbf{D}_{ef} : \left[\frac{1}{2} \sum_{j=1}^{N} \frac{m_j}{\rho_j} \left(\mathbf{v}_j - \mathbf{v}_i \right) \cdot \nabla W_{ij} + \frac{1}{2} \left(\sum_{j=1}^{N} \frac{m_j}{\rho_J} \left(\mathbf{v}_j - \mathbf{v}_i \right) \cdot \nabla W_{ij} \right)^T \right] \tag{3.32}$$

The above equation (3.32) states that the stress rate for a particle is related to the relative velocities between that particle and the surrounding particles, similar to the calculation of density rate. Therefore, once the material stiffness matrix $\mathbf{D}_{ef}$ is determined, the time rates of density, velocity and stress can be respectively calculated by equation (3.26), equation (3.29 or 3.31) and equation (3.32). How to determine the material stiffness matrix is introduced in the following sections of this thesis.

3.5. Time integration scheme

In order to solve the SPH equations in the form of ordinary differential equations, the field variables for each SPH particle must be integrated using a time integration scheme. In this section, four standard techniques, namely two-step Taylor, 2nd order Runge Kutta, 4th order Runge Kutta and second order accurate leapfrog, are introduced.

3.5.1. Taylor time integration scheme

In the Taylor time integration scheme, time discretisation of an unknown field variable $\boldsymbol{U}$ is achieved by means of a Taylor series expansion in the time of $\boldsymbol{U}$ up to the second order of accuracy:

$$\boldsymbol{U}^{n+1} = \boldsymbol{U}^n + \Delta t \frac{\partial \boldsymbol{U}}{\partial t}\bigg|^n + \frac{\Delta t^2}{2} \frac{\partial^2 \boldsymbol{U}}{\partial t^2}\bigg|^n + O(t^3) \tag{3.33}$$

where

$$\frac{\partial \boldsymbol{U}}{\partial t} = \nabla \boldsymbol{F} + \boldsymbol{S} \tag{3.34}$$

is the general formulation representing the governing equations of rocks (equations 3.18-3.21) in which $\boldsymbol{F}$ and $\boldsymbol{S}$ are the flex and source terms respectively.

The first order time derivative of $\boldsymbol{U}$ can be directly calculated using equation (3.34):

$$\left.\frac{\partial \boldsymbol{U}}{\partial t}\right|^{n} = (\boldsymbol{\nabla F} + \boldsymbol{S})^{n} \tag{3.35}$$

The second order time derivative of $\boldsymbol{U}$ can be obtained as:

$$\left.\frac{\partial^2 \boldsymbol{U}}{\partial t^2}\right|^{n} = \frac{\partial(\boldsymbol{\nabla F}+\boldsymbol{S})^{n}}{\partial t} = \left(\frac{\partial \boldsymbol{S}}{\partial t}\right)^{n} + \boldsymbol{\nabla}\left(\frac{\partial \boldsymbol{F}}{\partial t}\right)^{n} \tag{3.36}$$

In the first step, the variables of $\boldsymbol{U}$, $\boldsymbol{F}$ and $\boldsymbol{S}$ can be updated at an intermediate time $t^{n+1/2}$ by adopting the Taylor series expansion up to the first order

$$\boldsymbol{U}^{n+1/2} = \boldsymbol{U}^{n} + \frac{\Delta t}{2}\left.\frac{\partial \boldsymbol{U}}{\partial t}\right|^{n} = \boldsymbol{U}^{n} + \frac{\Delta t}{2}(\boldsymbol{\nabla F} + \boldsymbol{S})^{n} \tag{3.37a}$$

$$\boldsymbol{F}^{n+1/2} = \boldsymbol{F}^{n} + \frac{\Delta t}{2}\left.\frac{\partial \boldsymbol{F}}{\partial t}\right|^{n} \tag{3.37b}$$

$$\boldsymbol{S}^{n+1/2} = \boldsymbol{S}^{n} + \frac{\Delta t}{2}\left.\frac{\partial \boldsymbol{S}}{\partial t}\right|^{n} \tag{3.37c}$$

By substituting equation (3.37a-b) into equation (3.36), the second order time derivative of $\boldsymbol{U}$ can be written as the equation:

$$\left.\frac{\partial^2 \boldsymbol{U}}{\partial t^2}\right|^{n} = \frac{2}{\Delta t}\left(\left(\boldsymbol{S}^{n+1/2} - \boldsymbol{S}^{n}\right) + \boldsymbol{\nabla}(\boldsymbol{F}^{n+1/2} - \boldsymbol{F}^{n})\right) \tag{3.38}$$

Thus, in the second step, the unknown variable $\boldsymbol{U}^{n+1}$ can be updated by substituting equations (3.36) and (3.38) into the Taylor series expansion shown as equation (3.33):

$$\boldsymbol{U}^{n+1} = \boldsymbol{U}^{n} + \Delta t\left(\boldsymbol{F}^{n+\frac{1}{2}} + \boldsymbol{S}^{n+\frac{1}{2}}\right) = \boldsymbol{U}^{n} + \Delta t\left.\frac{\partial \boldsymbol{U}}{\partial t}\right|^{n+1/2} \tag{3.39}$$

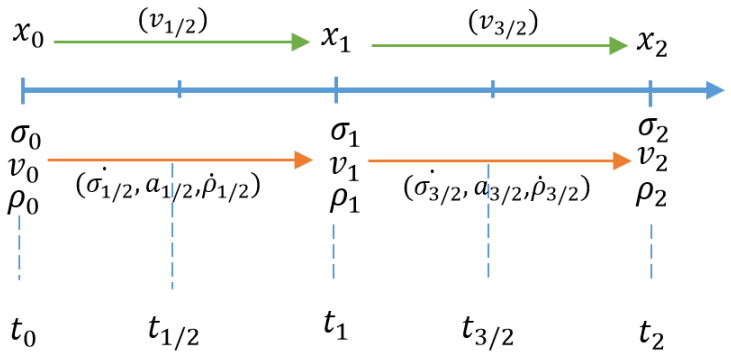

Figure 3.0–4. The procedure of the Taylor time integration scheme.

In summary, the Taylor time integration scheme consists of two steps (illustrated in Figure 3.0–4). In the first step, the field variables are updated at the intermediate time $t^{n+1/2}$ using the

time rates of field variables calculated at t^n; in the second step, the field variables at the full timestep are updated using the time rates obtained at $t^{n+1/2}$. This scheme is applied in the Taylor SPH method for exchanging and updating the information of two sets of particles, which is introduced later. The variable update using Taylor time integration scheme shown in

Table 3.0-1.

Table 3.0-1. Variable update algorithm using Taylor time integration scheme

First step:

- Calculate stress rate($\dot{\boldsymbol{\sigma}}_{\boldsymbol{n}}$), density rate($\dot{\boldsymbol{\rho}}_{\boldsymbol{n}}$) and acceleration($\boldsymbol{a_n}$) at $\boldsymbol{t^n}$;
- Calculate stress, density and velocity with half-timestep increments:

$$\boldsymbol{v_{n+1/2}} = \boldsymbol{v_n} + \Delta \boldsymbol{t/2} \times \boldsymbol{a_n}$$

$$\boldsymbol{\sigma_{n+1/2}} = \boldsymbol{\sigma_n} + \Delta \boldsymbol{t/2} \times \dot{\boldsymbol{\sigma}}_{\boldsymbol{n}}$$

$$\boldsymbol{\rho_{n+1/2}} = \boldsymbol{\rho_n} + \Delta \boldsymbol{t/2} \times \dot{\boldsymbol{\rho}}_{\boldsymbol{n}}$$

Second step:

- Calculate stress rate($\dot{\boldsymbol{\sigma}}_{\boldsymbol{n+1/2}}$), density rate($\dot{\boldsymbol{\rho}}_{\boldsymbol{n+1/2}}$) and acceleration($\boldsymbol{a_{n+1/2}}$) with half timestep increments;
- Calculate stress, density and velocity with full timestep increments;

$$\boldsymbol{v_{n+1}} = \boldsymbol{v_n} + \Delta \boldsymbol{t} \times \boldsymbol{a_{n+1/2}}$$

$$\boldsymbol{\sigma_{n+1}} = \boldsymbol{\sigma_n} + \Delta \boldsymbol{t} \times \dot{\boldsymbol{\sigma}}_{\boldsymbol{n+1/2}}$$

$$\boldsymbol{\rho_{n+1}} = \boldsymbol{\rho_n} + \Delta \boldsymbol{t} \times \dot{\boldsymbol{\rho}}_{\boldsymbol{n+1/2}}$$

- Calculate location with full timestep increments;

$$\boldsymbol{x_{n+1}} = \boldsymbol{x_n} + \Delta \boldsymbol{t} \times \boldsymbol{v_{n+1/2}}$$

3.5.2. 2nd-order Runge-Kutta method

The idea of Runge-Kutta methods is to evaluate the SPH governing equation in the forms of differential equations at several values in the intervals between t^n and t^{n+1}, and to combine them to obtain a high order approximation of the field variables. The second-order Runge-Kutta time integration scheme consists of two steps similar to the two-step Taylor scheme. In the Taylor SPH, the variable at t^{n+1} is calculated based on the time rate updated at half time-steps, while the field variable at t^{n+1} in the 2nd order Runge-Kutta scheme is updated due to the combined contribution of the time rates at t^n and t^{n+1}, as illustrated in Figure 3.0–5. The variable update using a second-order Runge-Kutta scheme in SPH is shown in Table 3.0-2.

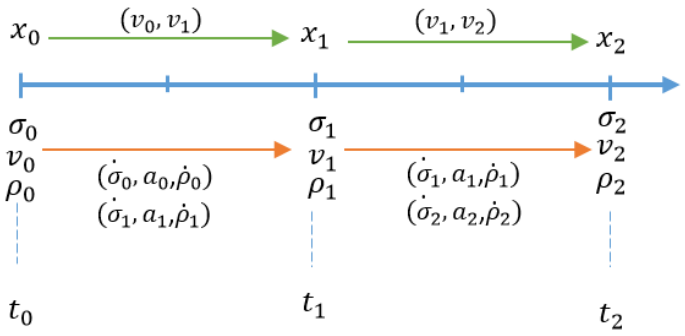

Figure 3.0–5. Procedure of second-order Runge-Kutta Method.

Table 3.0-2. Variable update algorithm using 2rd-order Runge-Kutta time integration scheme

First step:

- Calculate stress rate($\dot{\boldsymbol{\sigma}}_{\boldsymbol{n}}$), density rate($\dot{\boldsymbol{\rho}}_{\boldsymbol{n}}$) and acceleration($\boldsymbol{a_n}$) at $\boldsymbol{t^n}$;
- Calculate stress, density and velocity at full timestep increments;

$$\boldsymbol{v_{n+1}} = \boldsymbol{v_n} + \Delta \boldsymbol{t} \times \boldsymbol{a_n}$$

$$\boldsymbol{\sigma_{n+1}} = \boldsymbol{\sigma_n} + \Delta \boldsymbol{t} \times \dot{\boldsymbol{\sigma}}_{\boldsymbol{n}}$$

$$\boldsymbol{\rho_{n+1}} = \boldsymbol{\rho_n} + \Delta \boldsymbol{t} \times \dot{\boldsymbol{\rho}}_{\boldsymbol{n}}$$

Second step:

- Calculate stress rate($\dot{\boldsymbol{\sigma}}_{\boldsymbol{n+1}}$), density rate($\dot{\boldsymbol{\rho}}_{\boldsymbol{n+1}}$) and acceleration($\boldsymbol{a_{n+1}}$) at $\boldsymbol{t^{n+1}}$;
- Calculate stress, density and velocity at full timestep increments;

$$\boldsymbol{v_{n+1}} = \boldsymbol{v_n} + \Delta \boldsymbol{t}/\boldsymbol{2} \times (\boldsymbol{a_n} + \boldsymbol{a_{n+1}})$$

$$\boldsymbol{\sigma_{n+1}} = \boldsymbol{\sigma_n} + \Delta \boldsymbol{t}/\boldsymbol{2} \times (\dot{\boldsymbol{\sigma}}_{\boldsymbol{n}} + \dot{\boldsymbol{\sigma}}_{\boldsymbol{n+1}})$$

$$\boldsymbol{\rho_{n+1}} = \boldsymbol{\rho_n} + \Delta \boldsymbol{t}/\boldsymbol{2} \times (\dot{\boldsymbol{\rho}}_{\boldsymbol{n}} + \dot{\boldsymbol{\rho}}_{\boldsymbol{n+1}})$$

- Calculate location at full timestep increment;

$$\boldsymbol{x_{n+1}} = \boldsymbol{x_n} + \Delta \boldsymbol{t}/\boldsymbol{2} \times (\boldsymbol{v_n} + \boldsymbol{v_{n+1}})$$

3.5.3. 4th-order Runge-Kutta

In the 4th-order Runge-Kutta scheme, the field variable at t^{n+1} is updated using the value at t^n and the weighted average of four slope coefficients:

$$\boldsymbol{U}^{n+1} = \boldsymbol{U}^n + \frac{1}{6}(k_1 + 2k_2 + 2k_3 + k_4)\Delta t \tag{3.40}$$

where $k_1 = \frac{\partial \boldsymbol{U}}{\partial t}\Big|^n$ is the gradient of $\boldsymbol{U}^n$ at t^n; $k_2 = \frac{\partial \boldsymbol{U}}{\partial t}\Big|_{k1}$ is the gradient of $\boldsymbol{U}^{n+1/2}$ using the value $\boldsymbol{U}_{k1}^{n+1}$ calculated based on k_1; $k_3 = \frac{\partial \boldsymbol{U}}{\partial t}\Big|_{k2}$ is the gradient of $\boldsymbol{U}^{n+1/2}$ using the value

$\boldsymbol{U}_{k2}^{n+1/2}$ calculated based on k_2; $k_4 = \left.\frac{\partial \boldsymbol{U}}{\partial t}\right|_{k3}$ is the gradient of $\boldsymbol{U}^{n+1}$ using the value $\boldsymbol{U}_{k3}^{n+1}$ calculated based on k_3. Graphic descriptions of the slope estimates and variable updates in the 4th-order Runge-Kutta method are illustrated in Figure 3.0–6 and 3.Figure 3.0–7 respectively. In SPH applications, all field variables associated with governing equations can be updated by using the 4th-order Runge-Kutta following the algorithm shown in Table 3.0-3.

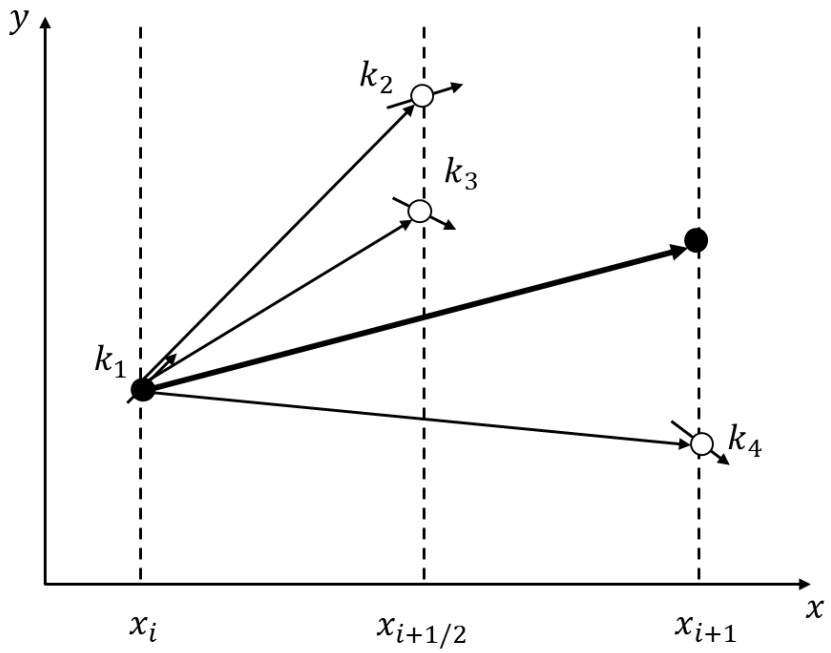

Figure 3.0–6. Graphical description of the slope estimates comprising the fourth-order Runge-Kutta method.

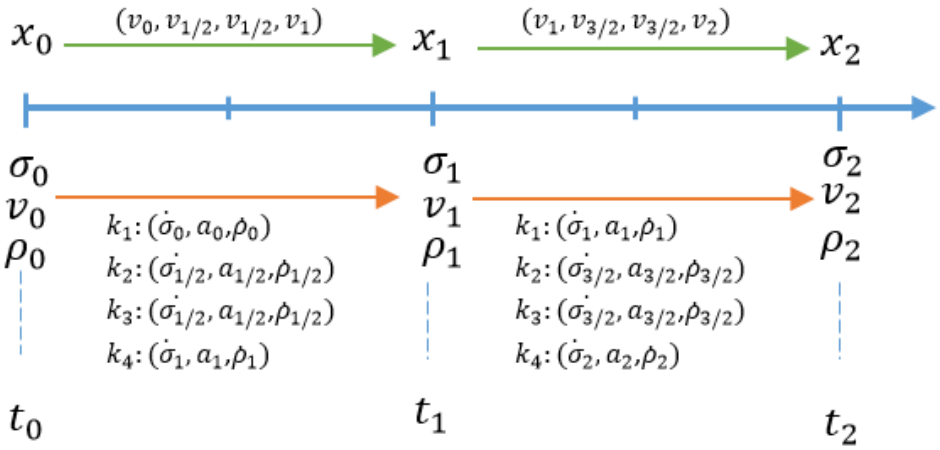

Figure 3.0–7. Procedure of the fourth-order Runge-Kutta Method

Table 3.0-3. Variable update algorithm using 4th-order Runge-Kutta time integration scheme

First step:

- Calculate stress rate ($\dot{\boldsymbol{\sigma}}^{(1)}$), density rate ($\dot{\boldsymbol{\rho}}^{(1)}$) and acceleration ($\boldsymbol{a}^{(1)}$);

$$\boldsymbol{k_1} = \dot{\boldsymbol{\sigma}}^{(1)}, \dot{\boldsymbol{\rho}}^{(1)}, \boldsymbol{a}^{(1)}$$

Second step:

- Calculate stress, density and velocity at half timestep increments;

$$\boldsymbol{v}_{\boldsymbol{n+1/2}}^{(1)} = \boldsymbol{v_n} + \Delta \boldsymbol{t/2} \times, \boldsymbol{a}^{(1)}$$

$$\boldsymbol{\sigma}_{\boldsymbol{n+1/2}}^{(1)} = \boldsymbol{\sigma_n} + \Delta \boldsymbol{t/2} \times \dot{\boldsymbol{\sigma}}^{(1)}$$

$$\boldsymbol{\rho}_{\boldsymbol{n+1/2}}^{(1)} = \boldsymbol{\rho_n} + \Delta \boldsymbol{t/2} \times \dot{\boldsymbol{\rho}}^{(1)}$$

- Calculate stress rate ($\dot{\boldsymbol{\sigma}}^{(2)}$), density rate ($\dot{\boldsymbol{\rho}}^{(2)}$) and acceleration ($\boldsymbol{a}^{(2)}$) using the updated variables;

$$\boldsymbol{k_2} = \dot{\boldsymbol{\sigma}}^{(2)}, \dot{\boldsymbol{\rho}}^{(2)}, \boldsymbol{a}^{(2)}$$

Third step:

- Calculate stress, density and velocity at half timestep increments using $\boldsymbol{k_2}$;

$$\boldsymbol{v}_{\boldsymbol{n+1/2}}^{(2)} = \boldsymbol{v_n} + \Delta \boldsymbol{t/2} \times \boldsymbol{a}^{(2)}$$

$$\boldsymbol{\sigma}_{\boldsymbol{n+1/2}}^{(2)} = \boldsymbol{\sigma_n} + \Delta \boldsymbol{t/2} \times \dot{\boldsymbol{\sigma}}^{(2)}$$

$$\boldsymbol{\rho}_{\boldsymbol{n+1/2}}^{(2)} = \boldsymbol{\rho_n} + \Delta \boldsymbol{t/2} \times \dot{\boldsymbol{\rho}}^{(2)}$$

- Calculate stress rate ($\dot{\boldsymbol{\sigma}}^{(3)}$), density rate ($\dot{\boldsymbol{\rho}}^{(3)}$) and acceleration ($\boldsymbol{a}^{(3)}$) using the updated variables;

$$\boldsymbol{k_3} = \dot{\boldsymbol{\sigma}}^{(3)}, \dot{\boldsymbol{\rho}}^{(3)}, \boldsymbol{a}^{(3)}$$

Fourth step:

- Calculate stress, density and velocity at half timestep increments using $\boldsymbol{k_3}$;

$$\boldsymbol{v}_{\boldsymbol{n+1/2}}^{(3)} = \boldsymbol{v_n} + \Delta \boldsymbol{t/2} \times \boldsymbol{a}^{(3)}$$

$$\boldsymbol{\sigma}_{\boldsymbol{n+1/2}}^{(3)} = \boldsymbol{\sigma_n} + \Delta \boldsymbol{t/2} \times \dot{\boldsymbol{\sigma}}^{(3)}$$

$$\boldsymbol{\rho}_{\boldsymbol{n+1/2}}^{(3)} = \boldsymbol{\rho_n} + \Delta \boldsymbol{t/2} \times \dot{\boldsymbol{\rho}}^{(3)}$$

- Calculate stress rate ($\dot{\boldsymbol{\sigma}}^{(4)}$), density rate ($\dot{\boldsymbol{\rho}}^{(4)}$) and acceleration ($\boldsymbol{a}^{(4)}$) using the updated variables;

$$\boldsymbol{k_4} = \dot{\boldsymbol{\sigma}}^{(4)}, \dot{\boldsymbol{\rho}}^{(4)}, \boldsymbol{a}^{(4)}$$

- Calculate stress, density and velocity at full timestep increments;

$$\boldsymbol{v_{n+1}} = \boldsymbol{v_n} + \Delta \boldsymbol{t/6} \times (\boldsymbol{a}^{(1)} + \boldsymbol{2a}^{(2)} + \boldsymbol{2a}^{(3)} + \boldsymbol{a}^{(4)})$$

$$\boldsymbol{\sigma_{n+1}} = \boldsymbol{\sigma_n} + \Delta \boldsymbol{t/6} \times (\dot{\boldsymbol{\sigma}}^{(1)} + \boldsymbol{2}\dot{\boldsymbol{\sigma}}^{(2)} + \boldsymbol{2}\dot{\boldsymbol{\sigma}}^{(3)} + \dot{\boldsymbol{\sigma}}^{(4)})$$

$$\boldsymbol{\rho_{n+1}} = \boldsymbol{\rho_n} + \Delta \boldsymbol{t/6} \times (\dot{\boldsymbol{\rho}}^{(1)} + \boldsymbol{2}\dot{\boldsymbol{\rho}}^{(2)} + \dot{\boldsymbol{\rho}}^{(3)} + \dot{\boldsymbol{\rho}}^{(4)})$$

- Calculate location at full timestep increments;

$$\boldsymbol{x_{n+1}} = \boldsymbol{x_n} + \Delta \boldsymbol{t} \times \boldsymbol{v_{n+1}}$$

3.5.4. LeapFrog time integration scheme

The LeapFrog integration scheme (LF) can help maintain a stable simulation solution with second-order accuracy while occupying a relatively amount of small computer memory (Bui et al. 2008). In the LF method, state variables of each SPH particle such as density, velocity and stress are updated at mid-steps in time, while their positions are updated at full timesteps. Hence, at the beginning of the computation, the state variables must be advanced to the mid-timestep using the equation:

$$\boldsymbol{U}^{1/2} = \boldsymbol{U}^{0} + \frac{\Delta t}{2}\frac{\partial \boldsymbol{U}}{\partial t}\Big|^{0} \tag{3.41}$$

Subsequently, the above state variables are updated with a full-time increment using the equation:

$$\boldsymbol{U}^{n+1/2} = \boldsymbol{U}^{n-1/2} + \Delta t\frac{\partial \boldsymbol{U}}{\partial t}\Big|^{n} \tag{3.42}$$

where $\frac{\partial \boldsymbol{U}}{\partial t}\Big|^{n}$ is the time rate of the variable by means of $\boldsymbol{U}^{n}$ calculated at timestep *n*, which is updated as follows:

$$\boldsymbol{U}^{n} = \boldsymbol{U}^{n-1/2} + \frac{\Delta t}{2}\frac{\partial \boldsymbol{U}}{\partial t}\Big|^{n} \tag{3.43}$$

Finally, the locations of particles are updated at a full timestep using the velocity at the mid timestep as follows:

$$\mathbf{x}_{n+1} = \mathbf{x}_{n} + \Delta t \times \mathbf{v}_{n+1/2} \tag{3.44}$$

To maintain the stability of the LF integration, the timestep Δt must satisfy a certain condition, which is proportional to the smoothing length (h) adopted in the computation. In this study, the timestep is determined by the condition:

$$\Delta t \leq C_{cour}(\frac{h}{c}) \tag{3.45}$$

where C_{cour} is the Courant number, which is chosen as 0.1; $c = \sqrt{E/\rho}$ is the speed of sound with E being the Young's modulus of the material. The updating process using the LF method is illustrated in Figure 3.0–8 and the variable updating algorithm using this method is detailed in Table 3.0-4.

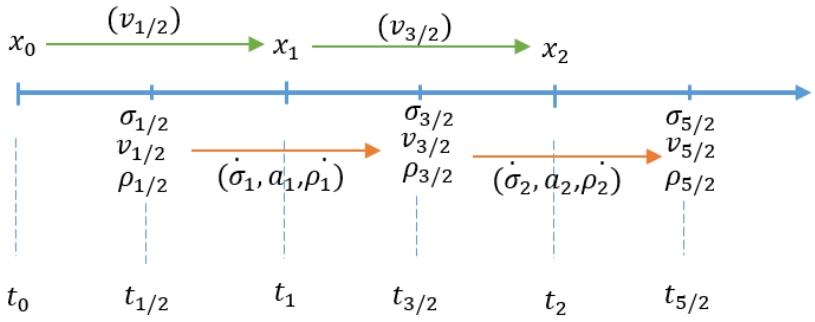

Figure 3.0–8. Procedure of LeapFrog Method

Table 3.0-4. Variable update algorithm using LeapFrog time integration scheme

Timestep from 0 to 1:

- Calculate stress rate($\dot{\boldsymbol{\sigma}}_{\boldsymbol{0}}$), density rate($\dot{\boldsymbol{\rho}}_{\boldsymbol{0}}$) and acceleration($\boldsymbol{a_0}$) at $\boldsymbol{t = 0}$;
- Calculate stress, density and velocity at half timestep increments;

$$\boldsymbol{v_{1/2} = v_0 + \Delta t/2 \times a_0}$$

$$\boldsymbol{\sigma_{1/2} = \sigma_0 + \Delta t/2 \times \dot{\sigma}_0}$$

$$\boldsymbol{\rho_{\frac{1}{2}} = \rho_0 + \frac{\Delta t}{2} \times \dot{\rho}_0}$$

- Calculate location at full timestep increment;

$$\boldsymbol{x_1 = x_1 + \Delta t \times v_{1/2}}$$

Timesteps from 1 to n:

- Calculate stress, density and velocity at half timestep increments;

$$\boldsymbol{v_n = v_{n-1/2} + \Delta t/2 \times a_{n-1}}$$

$$\boldsymbol{\sigma_n = \sigma_{n-1/2} + \Delta t/2 \times \dot{\sigma}_{n-1}}$$

$$\boldsymbol{\rho_n = \rho_{n-1/2} + \Delta t/2 \times \dot{\rho}_{n-1}}$$

- Calculate stress rate($\dot{\boldsymbol{\sigma}}_{\boldsymbol{n}}$), density rate($\dot{\boldsymbol{\rho}}_{\boldsymbol{n}}$) and acceleration($\boldsymbol{a_n}$) at itimestep = n;
- Calculate stress, density and velocity at full timestep increments;

$$\boldsymbol{v_{n+1/2} = v_{n-1/2} + \Delta t \times a_n}$$

$$\boldsymbol{\sigma_{n+1/2} = \sigma_{n-1/2} + \Delta t \times \dot{\sigma}_n}$$

$$\boldsymbol{\rho_{n+1/2} = \rho_{n-1/2} + \Delta t \times \dot{\rho}_n}$$

- Calculate location at full timestep increment;

$$\boldsymbol{x_{n+1} = x_n + \Delta t \times v_{n+1/2}}$$

3.6. Recent improvements on traditional SPH method

3.6.1. Artificial viscosity

SPH experiences numerical oscillation at shock front, which can result in unstable numerical solutions, especially when dealing with dynamic problems. That is because shocks propagating within the computational domain of SPH cannot smear out over a length scale sufficiently greater than the discretisation step (Bui et al. 2008). Therefore, a proper dissipative term 'artificial viscosity' is required for damping out the undesirable oscillation and thus stabilising the numerical domain. The term of artificial viscosity was introduced by VonNeumann and Richtmyer (1950), with the aim of smoothing shocks over a few resolution lengths. For SPH applications, the artificial viscosity term traditionally used is introduced into the momentum conservation equation shown in equation (3.29) as an artificial viscous pressure acting directly on the relative motions of the particles:

$$\frac{\mathrm{D}\mathbf{v}_i}{\mathrm{D}t} = \sum_{j=1}^{N} m_j \left(\frac{\boldsymbol{\sigma}_i + \boldsymbol{\sigma}_j}{\rho_i \rho_j} + \Pi_{ij} \right) \cdot \nabla_i W(\boldsymbol{x_i} - \boldsymbol{x_j}, h) + \mathbf{b}_i \tag{3.46}$$

where Π_{ij} is the artificial viscosity term. Several formulations for artificial viscosity have been derived and numerical examples showing the stability of numerical solutions have been greatly improved by incorporating this term into momentum conservation equations. Among those, that proposed by Monaghan and Gingold (1983) is the most widely used, written as:

$$\Pi_{ij} = \begin{cases} \frac{-\alpha_\Pi c_{ij} \phi_{ij} + \beta_\Pi \phi^2}{\rho_{ij}} & v_{ij} \cdot r_{ij} < 0 \\ 0 & v_{ij} \cdot r_{ij} \geq 0 \end{cases} \tag{3.47}$$

$$\text{where } \phi_{ij} = \frac{h_{ij} v_{ij} \cdot x_{ij}}{|x_{ij}|^2 + 0.01 h_{ij}^2}, \quad c_{ij} = \frac{c_i + c_j}{2}, \quad \rho_{ij} = \frac{\rho_i + \rho_j}{2} \tag{3.48}$$

$$h_{ij} = \frac{h_i + h_j}{2}, \quad x_{ij} = x_i - x_j, \quad v_{ij} = v_i - v_j \tag{3.49}$$

In the above equation, α_Π and β_Π are the parameters controlling the viscosity effect which can be either updated based on time and space during the calculation or predefined with a fixed value. The values of α_Π and β_Π are chosen according to specific applications. The density ρ_{ij} is an average value between particle i and j, c_{ij} is the sound speed in material, and the term $0.01h_{ij}^2$ is used to prevent numerical divergence when particles approach each other.

3.6.2. Tensile instability

It has been found that when a solid is in tension, the attraction between two SPH particles results in particle clumping, which is normally called tensile instability. This instability was first investigated by Swegle et al. (1995), who developed a simple criterion depending only on the sign of the product of the stress times the second derivative of the kernel function. Later, various countermeasures were introduced in the literature to eliminate tensile instability. Among these, the artificial stress method first proposed by Monaghan (2000) and Gray et al. (2001) is the most straightforward and effective in removing tensile instability in both non-cohesive and cohesive soils. The basic idea of this method is to introduce a repulsive force in a state of two neighbouring particles under tension. The closer the neighbouring particles, the greater is the repulsive force between them. Based on this idea, the SPH momentum balance in equation (3.46) should be further expanded as:

$$\frac{\mathrm{D}\mathbf{v}_i}{\mathrm{D}t} = \sum_{j=1}^{N} m_j \left(\frac{\boldsymbol{\sigma}_i + \boldsymbol{\sigma}_j}{\rho_i \rho_j} + \Pi_{ij} + f_{ij}^{n} (\boldsymbol{R_i} + \boldsymbol{R_j}) \right) \cdot \nabla_i W(\boldsymbol{x_i} - \boldsymbol{x_j}, h) + \mathbf{b}_i \tag{3.50}$$

where n is a state parameter dependent on the problem context. In geomechanical applications it was chosen as 2.55 in the work of Bui et al. (2008) and $\mathrm{f}_{\mathrm{ij}}^{\mathrm{n}}$ is the repulsive force term which can be specified as:

$$f_{ij}^{n} = \frac{W_{ij}}{W(\Delta x, h)} \tag{3.51}$$

The term of $W(\Delta x, h)$ is a constant with a non-evolving kernel function; dx is the initial particle spacing; $\boldsymbol{R_i}$ and $\boldsymbol{R_j}$ are the rotations of the local artificial stress tensor to their principal values, which are calculated from the stress state $\mathbf{R}_i'$ on the principal coordinate system subjected to tensile loading. The artificial stress $\mathbf{R}_i'$ on the principal coordinate system can be determined as follows (Gray et al. 2001):

$$\mathbf{R}_i' = \begin{cases} -\varepsilon \frac{\sigma_i'^{xx}}{\rho_i^2} & if\ \sigma_i'^{xx} > 0 \\ 0 & \text{otherwise} \end{cases} \tag{3.53}$$

where ε is a small constant parameter ranging from 0 to 1 and $\sigma_i'^{xx}$ is the diagonal stress tensor of particle i in the principal stress coordinate system (Gray et al. 2001). The constant parameter ε can be chosen based on the particular application.

3.6.3. Corrective SPH

The SPH approximation formulations described here can in principle achieve second order accuracy. But that is not always the case, especially when the material undergoes large deformation, which can lead to highly disordered particle configurations. The problem can be severe when the SPH particle comes close to the boundary where the kernel approximation is truncated by the boundary, although this is also an advantage of SPH that allows the method to automatically handle free surface boundary conditions in many applications (Zhao et al. 2019). To address this issue, certain remedies such as the corrective SPH technique were developed. The corrective SPH, originally developed by Chen et al. (1999), allows both the kernel and its gradient approximations to be corrected by means of the Taylor series expansion.

First, correction of the kernel is introduced by expanding the Taylor series for $f(\mathbf{x}')$, and multiplying both sides by a kernel function:

$$\int_\Omega f\left(\mathbf{x}'\right) W d\mathbf{x}' = f(\mathbf{x}) \int_{\boldsymbol{\Omega}} W d\boldsymbol{x}' + \left[\int_\Omega (\mathbf{x}' - \mathbf{x}) W d\mathbf{x}'\right] \frac{\partial f(\mathbf{x})}{\partial \mathbf{x}} + O(h^2) \tag{3.52}$$

where $W = W(x - x_i, h)$.

Neglecting the first derivative term in equation (3.52), the corrective kernel estimate is generated:

$$f(\mathbf{x}) = \frac{\int_\Omega f\left(\mathbf{x}'\right) W d\mathbf{x}'}{\int_{\boldsymbol{\Omega}} W d\boldsymbol{x}'} \tag{3.53}$$

The discretised form of equation (3.53) at a particle i can be written as:

$$f(\mathbf{x}_i) = \frac{\sum_{j=1}^{N} \frac{m_j}{\rho_j} f(\mathbf{x}_j) W}{\sum_{j=1}^{N} \frac{m_j}{\rho_j} W} \tag{3.54}$$

For SPH particles distant from the problem boundary, the summation of W over the supporting domain is equal to unity. In that case, equation (3.54) becomes the conventional kernel estimate. On the other hand, for SPH particles whose smoothing function W is truncated by the problem boundary, the summation of W over the supporting domain is less than one. This term will effectively reduce the boundary deficiency by enlarging the effect of the kernel estimate on those "near boundary "particles. As the discrete forms of derivatives of the governing equations all make use of the kernel gradient, correction of the kernel gradient is a key to improving the solution. The correction of the kernel gradient begins by rewriting the gradient of a field function $\nabla f(\mathbf{x})$ in the form:

$$f(\mathbf{x}) = \nabla f(\mathbf{x}) - f(\mathbf{x})\nabla 1 \tag{3.55}$$

Transforming Equation (3.55) into its continuous integral form results in:

$$< \nabla f(\mathbf{x}) >= -\int_{\Omega} f(\mathbf{x}')\,\nabla W d\mathbf{x}' + f(\mathbf{x})\int_{\boldsymbol{\Omega}} \nabla W d\mathbf{x}' \tag{3.56}$$

By applying the Taylor series expansion to $f(\mathbf{x}')$ up to second order accuracy, the first term on the right-hand side of Equation (3.56) becomes:

$$\int_{\Omega} f\left(\mathbf{x}'\right)\nabla W d\mathbf{x}' = f(\mathbf{x})\int_{\boldsymbol{\Omega}} \nabla W d\boldsymbol{x}' + \left[\int_{\Omega} (\mathbf{x}' - \mathbf{x})\nabla W d\mathbf{x}'\right]\frac{\partial f(\mathbf{x})}{\partial \mathbf{x}} + O(h^2) \tag{3.57}$$

Substituting Equation (3.57) into Equation (3.56) gives:

$$< \nabla f(\mathbf{x}) >= -\left[\int_{\Omega} (\mathbf{x}' - \mathbf{x})\nabla W d\mathbf{x}'\right]\frac{\partial f(\mathbf{x})}{\partial \mathbf{x}} + O(h^2) \tag{3.58}$$

The discrete form of Equation (3.58) at a particle i can be straightforwardly written as:

$$\nabla f(\mathbf{x}_i) = \left[\sum_{j=1}^{N} \frac{m_j}{\rho_j}(\mathbf{x}_j - \mathbf{x}_i)\nabla W_{ij}\right]\frac{\partial f(\mathbf{x})}{\partial \mathbf{x}_i} + O(h^2) \tag{3.59}$$

It can be seen from Equation (3.47) that the particle approximation for the gradient of a function can achieve second-order accuracy if and only if $\sum_{j=1}^{N} \frac{m_j}{\rho_j}(\mathbf{x}_j - \mathbf{x}_i)\nabla W_{ij} = \begin{pmatrix} 1 & 0 \\ 0 & 1 \end{pmatrix}$. However, this requirement cannot be always satisfied, especially when particles are located near the boundaries. This issue can be resolved by replacing the original kernel gradient ∇W_{ij} in Equation (3.59) by a corrective kernel gradient ∇W_{ij}^{C} as follows:

$$\nabla W_{ij}^{C} = \mathbf{L}(\mathbf{x}_i)\nabla W_{ij} \tag{3.60}$$

where the normalisation matrix $\mathbf{L}(\mathbf{x}_i)$ in 2D can be defined as:

$$\mathbf{L}(\mathbf{x}_i) = \begin{pmatrix} \sum_{j=1}^{N} \frac{m_j}{\rho_j}(x_j - x_i)\nabla_{x_i} W_{ij} & \sum_{j=1}^{N} \frac{m_j}{\rho_j}(x_j - x_i)\nabla_{y_i} W_{ij} \\ \sum_{j=1}^{N} \frac{m_j}{\rho_j}(y_j - y_i)\nabla_{x_i} W_{ij} & \sum_{j=1}^{N} \frac{m_j}{\rho_j}(y_j - y_i)\nabla_{y_i} W_{ij} \end{pmatrix}^{-1} \tag{3.61}$$

Figure 3.0–9 shows the performance of corrective SPH and standard SPH (or traditional SPH) for the approximation of $f(x) = x$ and $f(x) = x^2$, in comparison with the analytical solution. Figure 3.0–10 illustrates the SPH approximation of function $f(x) = x + y$ using traditional SPH and corrective SPH. It has been shown that boundary deficiency is clearly indicated in the result by using the traditional approximation. On the other hand, the accuracy of the SPH approximation with the corrective technique is quite remarkable in comparison with the analytical solution.

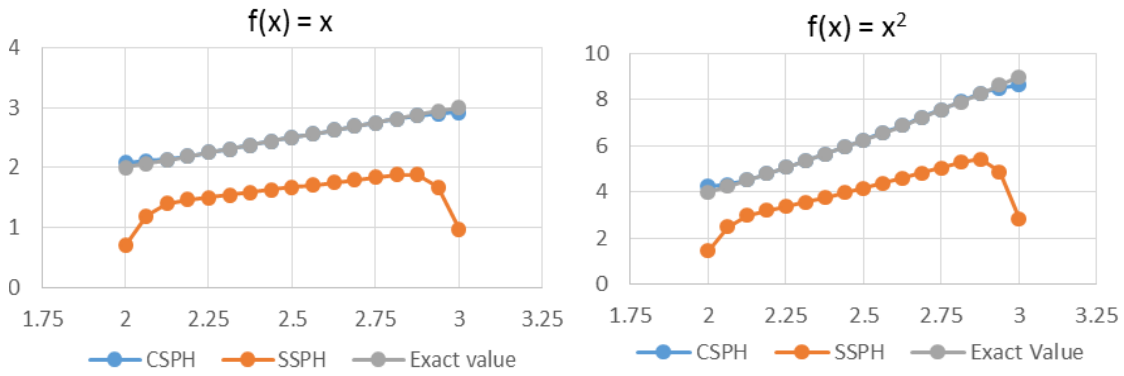

Figure 3.0–9. Performance of corrective SPH (CSPH) and standard SPH (SSPH) for $f(x) = x$ and $f(x) = x^2$ in comparison with analytical solution in 1D.

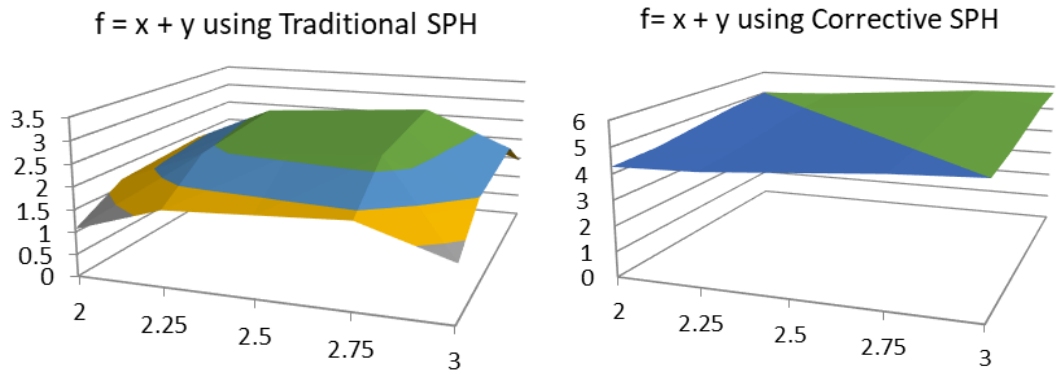

Figure 3.0–10. Performance of corrective SPH and traditional SPH (or SSPH) for $f(x) = x + y$ in 2D.

3.6.4. Stress points approach

It is known that the traditional SPH suffers from a zero-energy mode owing to the fact that both SPH approximations of a function and its derivative are evaluated at the same location. To avoid this problem, the concept of stress particles (or stress points) was introduced (Libersky et al. 1993, Dyka and Ingel 1995). In the approach of the SPH method with stress points, the computational domain is represented by two sets of particles (i.e. material and stress particles) as shown in Figure 3.0–11. These particles have their own field properties (such as density, velocity and stress) and move with their own motion equations. However, their field properties are exchanged when performing particle approximations to avoid issues associated with the zero-energy mode. In particular, the field approximations of material particles are applied on stress particles which are located within their influence domain. The same rule is applied when conducting particle approximations for stress particles. Nevertheless, the material is only

represented by material particles, and as a result, the total mass of the material is represented as:

$$M_{total} = \sum_{i=1}^{N} m_i \tag{3.62}$$

where N is the total number of material particles.

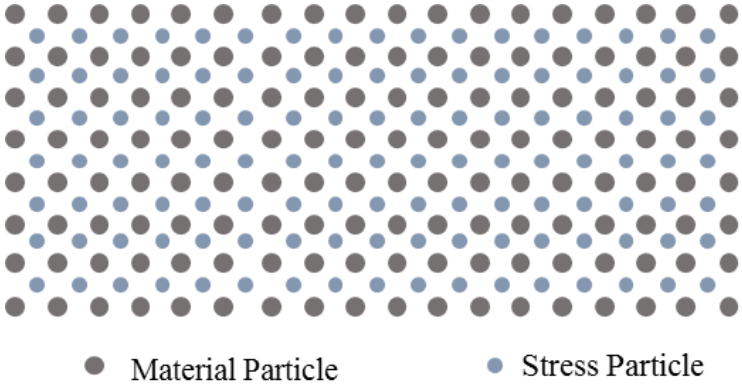

Figure 3.0–11. SPH particle arrangement of computational domain in the two-dimensional case.

3.7. Two-step Taylor SPH

In this section, an improved SPH model, the Taylor-SPH, proposed by Herreros and Mabssout (2011) is introduced for solving the inherent numerical drawbacks in traditional SPH such as tensile instability and particle inconsistency problems. In Taylor-SPH, the stress point method introduced in Section 3.6.4 is used to eliminate tensile instability and spurious zero-energy mode problems commonly observed in the original SPH method. The corrective smoothed particle method explained in Section 3.6.3 is also adopted to allow the method to fulfil the zero and first order completeness, thus enabling the derivatives of constant or linear fields to be reproduced exactly. Furthermore, to improve the numerical stability of the method, a two-step Taylor time discretisation scheme based on the Taylor series expansion is applied (Herreros and Mabssout 2011). The concept and algorithm of the Taylor time integration scheme were presented in Section 3.5.1. The combination of corrected SPH technique, stress point approach and Taylor time integration scheme provides an accurate and stable solution to solve the governing equations of rock.

In the Taylor SPH method, the calculation at each timestep is divided into two steps. In the first step, the normalisation formulation shown as equation (3.51) is used to approximate the field variables at stress particles at t^n through the surrounding material particles over the supporting domain. Then, the time rates of the field variables at stress particles at t^n are calculated using

corrective techniques (represented by equation 3.59-3.61). Finally, the variable values at stress particles at $t^{n+1/2}$ can easily be updated using equation 3.37. In the second step, the information of field variables is exchanged first from stress particles to material particles at $t^{n+1/2}$ using equation (3.51). Then the time rate of variables carried by material particles based on the value at $t^{n+1/2}$ are calculated, followed by the variable updating of material particles at t^{n+1} using equation (3.39). The detailed time integration algorithm and time rate calculation using the corrective techniques are presented in Table 3.0-5 and Table 3.0-6 respectively.

Table 3.0-5. Taylor SPH algorithm

First Step:

1. *Approximation of the vector of unknowns of stress points at time t_n:*

   Stress of stress points at t_n: $\sigma_s^n = \frac{\sum_{J=1}^{NP} \frac{m_J}{\rho_J} \sigma_{m_J}^n W_{IJ}}{\sum_{J=1}^{NP} \frac{m_J}{\rho_J} W_{IJ}}$

   Velocity of stress points at t_n: $v_s^n = \frac{\sum_{J=1}^{NP} \frac{m_J}{\rho_J} v_{m_J}^n W_{IJ}}{\sum_{J=1}^{NP} \frac{m_J}{\rho_J} W_{IJ}}$

   Strain of stress points at t_n (if needed): $\varepsilon_s^n = \frac{\sum_{J=1}^{NP} \frac{m_J}{\rho_J} \varepsilon_{m_J}^n W_{IJ}}{\sum_{J=1}^{NP} \frac{m_J}{\rho_J} W_{IJ}}$

   Note1: σ_s^n stands for the stress of stress points at time t_n and $\sigma_{m_J}^n$ stands for the stress of the jth material points.

2. *Calculation of strain rate ($\dot{\varepsilon}_s^n$), stress rate ($\dot{\sigma}_s^n$) and acceleration (a_s^n) of stress points (details are shown in Table 3.0-6)*

3. *Calculation of the vector of unknowns of stress points at time $t_{n+1/2}$:*

   Stress of stress points at $t_{n+1/2}$: $\sigma_s^{n+1/2} = \sigma_s^n + \frac{\Delta t}{2} \dot{\sigma}_s^n$

   Velocity of stress points at $t_{n+1/2}$: $v_s^{n+1/2} = v_s^n + \frac{\Delta t}{2} a_s^n$

Second Step:

1. *Approximation of the vector of unknowns of material points at the time $t_{n+1/2}$:*

   Stress of material points at $t_{n+1/2}$: $\sigma_m^{n+1/2} = \frac{\sum_{J=1}^{NP} \frac{m_J}{\rho_J} \sigma_s^{n+1/2}{}_J W_{IJ}}{\sum_{J=1}^{NP} \frac{m_J}{\rho_J} W_{IJ}}$

   Velocity of material points at $t_{n+1/2}$: $v_m^{n+1/2} = \frac{\sum_{J=1}^{NP} \frac{m_J}{\rho_J} v_s^{n+1/2}{}_J W_{IJ}}{\sum_{J=1}^{NP} \frac{m_J}{\rho_J} W_{IJ}}$

2. *Calculation of strain rate ($\dot{\varepsilon}_m^{n+1/2}$), stress rate ($\dot{\sigma}_m^{n+1/2}$) and acceleration ($a_m^{n+1/2}$) of material points (details are shown in Table 3.0-6)*

3. *Calculation of the vector of unknowns of material points at time t_{n+1}:*

	Stress of material points at t_{n+1}:	$\sigma_m^{n+1} = \sigma_m^n + \Delta t \times \dot{\sigma}_m^{n+1/2}$
	Velocity of material points at t_{n+1}: (Method 1)	$v_m^{n+1} = v_m^n + \Delta t \times a_m^{n+1/2}$
	Velocity of material points at t_{n+1}: (Method 2)	$v_m^{n+1} = 2v_m^{n+1/2} - v_m^n$
	Strain of material points at t_{n+1} (if needed):	$\varepsilon_m^{n+1} = \varepsilon_m^n + \Delta t \times \dot{\varepsilon}_m^{n+1/2}$
4.	*Calculation of position of material points:*	$X_m^{n+1} = X_m^n + \Delta t \times v_m^{n+1/2}$
5.	*Calculation of position of stress points:*	
	Method 1:	$X_s^{n+1} = X_s^n + \Delta t \times v_s^{n+1/2}$
	Method 2:	$X_s^{n+1} = \frac{1}{4}\sum_{J=1}^{4} X_m^{n+1}$

Table 3.0-6. Procedure to calculate stress rate, strain rate and acceleration.

General equation: (relating time rate of a function with the derivatives of another function)	$\dot{\varepsilon^{\alpha\beta}} = \frac{1}{2} \times (\frac{\partial v^\alpha}{\partial x^\beta} + \frac{\partial v^\beta}{\partial x^\alpha})$ $\dot{w^{\alpha\beta}} = \frac{1}{2} \times \left(\frac{\partial v^\alpha}{\partial x^\beta} - \frac{\partial v^\beta}{\partial x^\alpha}\right)$ $a^\alpha = \frac{1}{\rho} \times \frac{\partial \sigma^{\alpha\beta}}{\partial x^\beta}$ $\dot{\sigma^{\alpha\beta}} = D_e \dot{\varepsilon}^{\alpha\beta}$
General formula for calculation of derivative of a function (ϕ)	$\begin{pmatrix}\phi_{1,I}\\ \phi_{2,I}\end{pmatrix} = \begin{pmatrix}A_{11,I} & A_{12,I}\\ A_{21,I} & A_{22,I}\end{pmatrix}^{-1}\begin{pmatrix}F_{1,I}\\ F_{2,I}\end{pmatrix}$ where $\phi_{\alpha,I}$ is the particle approximation of the first derivative of ϕ with respect to dimension α; $A_{\alpha\beta,I} = \sum_{J=1}^{NP} \frac{m_J}{\rho_J}(x_{\alpha,J} - x_{\alpha,I}) W_{IJ,\beta}$; and $F_{\beta,I} = \sum_{J=1}^{NP} \frac{m_J}{\rho_J}(\phi(x_J) - \phi(x_I)) W_{IJ,\beta}$ Therefore, the particle approximation of the first derivative can be calculated by: $\left.\frac{\partial \phi}{\partial x_1}\right\|_I = {A_{11,I}}^{-1} \cdot \sum_{J=1}^{NP} \frac{m_J}{\rho_J}\left(\phi(x_J) - \phi(x_I)\right) W_{IJ,1} + {A_{12,I}}^{-1} \cdot \sum_{J=1}^{NP} \frac{m_J}{\rho_J}\left(\phi(x_J) - \phi(x_I)\right) W_{IJ,2}$ $\left.\frac{\partial \phi}{\partial x_2}\right\|_I = {A_{21,I}}^{-1} \cdot \sum_{J=1}^{NP} \frac{m_J}{\rho_J}\left(\phi(x_J) - \phi(x_I)\right) W_{IJ,1} + {A_{22,I}}^{-1} \cdot \sum_{J=1}^{NP} \frac{m_J}{\rho_J}\left(\phi(x_J) - \phi(x_I)\right) W_{IJ,2}$ where: $A_{11,I} = \sum_{J=1}^{NP} \frac{m_J}{\rho_J}(x_{1,J} - x_{1,I}) \frac{\partial W_{IJ}}{\partial x_1}$, $A_{12,I} = \sum_{J=1}^{NP} \frac{m_J}{\rho_J}(x_{2,J} - x_{2,I}) \frac{\partial W_{IJ}}{\partial x_1}$; $A_{21,I} = \sum_{J=1}^{NP} \frac{m_J}{\rho_J}(x_{1,J} - x_{1,I}) \frac{\partial W_{IJ}}{\partial x_2}$, $A_{22,I} = \sum_{J=1}^{NP} \frac{m_J}{\rho_J}(x_{2,J} - x_{2,I}) \frac{\partial W_{IJ}}{\partial x_2}$
Calculation of strain rate ($\dot{\varepsilon}$)	$\dot{\varepsilon_{11}} = \frac{1}{2} \times \left(\frac{\partial v_1}{\partial x_1} + \frac{\partial v_1}{\partial x_1}\right) = \frac{\partial v_1}{\partial x_1}$; $\dot{\varepsilon_{22}} = \frac{1}{2} \times \left(\frac{\partial v_2}{\partial x_2} + \frac{\partial v_2}{\partial x_2}\right) = \frac{\partial v_2}{\partial x_2}$ $\dot{\varepsilon_{12}} = \frac{1}{2} \times \left(\frac{\partial v_1}{\partial x_2} + \frac{\partial v_2}{\partial x_1}\right)$; $\dot{w_{12}} = \frac{1}{2} \times \left(\frac{\partial v_1}{\partial x_2} - \frac{\partial v_2}{\partial x^1}\right)$ where: $\frac{\partial v_{1,I}}{\partial x_1} = {A_{11,I}}^{-1} \cdot \sum_{J=1}^{NP} \frac{m_J}{\rho_J}\left(v_{1,J} - v_{1,I}\right) \frac{\partial W_{IJ}}{\partial x_1} + {A_{12,I}}^{-1} \cdot \sum_{J=1}^{NP} \frac{m_J}{\rho_J}\left(v_{1,J} - v_{1,I}\right) \frac{\partial W_{IJ}}{\partial x_2}$ $\frac{\partial v_{1,I}}{\partial x_2} = {A_{21,I}}^{-1} \cdot \sum_{J=1}^{NP} \frac{m_J}{\rho_J}\left(v_{1,J} - v_{1,I}\right) \frac{\partial W_{IJ}}{\partial x_1} + {A_{22,I}}^{-1} \cdot \sum_{J=1}^{NP} \frac{m_J}{\rho_J}\left(v_{1,J} - v_{1,I}\right) \frac{\partial W_{IJ}}{\partial x_2}$ $\frac{\partial v_{2,I}}{\partial x_1} = {A_{11,I}}^{-1} \cdot \sum_{J=1}^{NP} \frac{m_J}{\rho_J}\left(v_{2,J} - v_{2,I}\right) \frac{\partial W_{IJ}}{\partial x_1} + {A_{12,I}}^{-1} \cdot \sum_{J=1}^{NP} \frac{m_J}{\rho_J}\left(v_{2,J} - v_{2,I}\right) \frac{\partial W_{IJ}}{\partial x_2}$

Calculation of strain rate ($\dot{\varepsilon}$)	$\frac{\partial v_{2,I}}{\partial x_2} = {A_{21,I}}^{-1} \cdot \sum_{J=1}^{NP} \frac{m_J}{\rho_J}\left(v_{2,J} - v_{2,I}\right)\frac{\partial W_{IJ}}{\partial x_1} + {A_{22,I}}^{-1} \cdot \sum_{J=1}^{NP} \frac{m_J}{\rho_J}\left(v_{2,J} - v_{2,I}\right)\frac{\partial W_{IJ}}{\partial x_2}$
Calculation of acceleration (a)	$\frac{Dv_{1,I}}{Dt} = \frac{1}{\rho_I} \times \left(\frac{\partial \sigma_{11,I}}{\partial x_1} + \frac{\partial \sigma_{12,I}}{\partial x_2}\right)$; $\frac{Dv_2}{Dt} = \frac{1}{\rho_I} \times (\frac{\partial \sigma_{12,I}}{\partial x_1} + \frac{\partial \sigma_{22,I}}{\partial x_2})$ where: $\frac{\partial \sigma_{11,I}}{\partial x_1} = {A_{11,I}}^{-1} \cdot \sum_{J=1}^{NP} \frac{m_J}{\rho_J}\left(\sigma_{11,J} - \sigma_{11,I}\right)\frac{\partial W_{IJ}}{\partial x_1} + {A_{12,I}}^{-1} \cdot \sum_{J=1}^{NP} \frac{m_J}{\rho_J}\left(\sigma_{11,J} - \sigma_{11,I}\right)\frac{\partial W_{IJ}}{\partial x_2}$ $\frac{\partial \sigma_{11,I}}{\partial x_2} = {A_{21,I}}^{-1} \cdot \sum_{J=1}^{NP} \frac{m_J}{\rho_J}\left(\sigma_{11,J} - \sigma_{11,I}\right)\frac{\partial W_{IJ}}{\partial x_1} + {A_{22,I}}^{-1} \cdot \sum_{J=1}^{NP} \frac{m_J}{\rho_J}\left(\sigma_{11,J} - \sigma_{11,I}\right)\frac{\partial W_{IJ}}{\partial x_2}$ $\frac{\partial \sigma_{12,I}}{\partial x_1} = {A_{11,I}}^{-1} \cdot \sum_{J=1}^{NP} \frac{m_J}{\rho_J}\left(\sigma_{12,J} - \sigma_{12,I}\right)\frac{\partial W_{IJ}}{\partial x_1} + {A_{12,I}}^{-1} \cdot \sum_{J=1}^{NP} \frac{m_J}{\rho_J}\left(\sigma_{12,J} - \sigma_{12,I}\right)\frac{\partial W_{IJ}}{\partial x_2}$ $\frac{\partial \sigma_{12,I}}{\partial x_2} = {A_{21,I}}^{-1} \cdot \sum_{J=1}^{NP} \frac{m_J}{\rho_J}\left(\sigma_{12,J} - \sigma_{12,I}\right)\frac{\partial W_{IJ}}{\partial x_1} + {A_{22,I}}^{-1} \cdot \sum_{J=1}^{NP} \frac{m_J}{\rho_J}\left(\sigma_{12,J} - \sigma_{12,I}\right)\frac{\partial W_{IJ}}{\partial x_2}$ $\frac{\partial \sigma_{22,I}}{\partial x_1} = {A_{11,I}}^{-1} \cdot \sum_{J=1}^{NP} \frac{m_J}{\rho_J}\left(\sigma_{22,J} - \sigma_{22,I}\right)\frac{\partial W_{IJ}}{\partial x_1} + {A_{12,I}}^{-1} \cdot \sum_{J=1}^{NP} \frac{m_J}{\rho_J}\left(\sigma_{22,J} - \sigma_{22,I}\right)\frac{\partial W_{IJ}}{\partial x_2}$ $\frac{\partial \sigma_{22,I}}{\partial x_2} = {A_{21,I}}^{-1} \cdot \sum_{J=1}^{NP} \frac{m_J}{\rho_J}\left(\sigma_{22,J} - \sigma_{22,I}\right)\frac{\partial W_{IJ}}{\partial x_1} + {A_{22,I}}^{-1} \cdot \sum_{J=1}^{NP} \frac{m_J}{\rho_J}\left(\sigma_{22,J} - \sigma_{22,I}\right)\frac{\partial W_{IJ}}{\partial x_2}$
Calculation of strain rate ($\dot{\sigma}$)	Method 1: Using E and μ $\dot{\sigma^{\alpha\beta}} = D_e \dot{\varepsilon^{\alpha\beta}}$ where: $D_e = \frac{E}{(1+\mu)(1-2\mu)}\begin{pmatrix} 1-\mu & \mu & 0 & \mu \\ \mu & 1-\mu & 0 & \mu \\ 0 & 0 & 1-2\mu & 0 \\ \mu & \mu & 0 & 1-\mu \end{pmatrix} = \begin{pmatrix} D_{11} & D_{12} & D_{13} & D_{14} \\ D_{21} & D_{22} & D_{23} & D_{24} \\ D_{31} & D_{32} & D_{33} & D_{34} \\ D_{41} & D_{42} & D_{43} & D_{44} \end{pmatrix}$ Therefore, $\dot{\sigma_{11}} = D_{11}\dot{\varepsilon_{11}} + D_{12}\dot{\varepsilon_{22}}$; $\dot{\sigma_{22}} = D_{21}\dot{\varepsilon_{11}} + D_{22}\dot{\varepsilon_{22}}$; $\dot{\sigma_{12}} = D_{33}\dot{\varepsilon_{12}}$; $\dot{\sigma_{33}} = D_{41}\dot{\varepsilon_{11}} + D_{42}\dot{\varepsilon_{22}}$ Method 2: Using G and K $\dot{\sigma}_{\alpha\beta} = K\,\dot{\varepsilon_{kk}}\delta_{\alpha\beta} + 2G\,\dot{e_{\alpha\beta}}$ When dealing with large deformation, the Jaumann stress rate $\hat{\sigma}^{\dot{\alpha\beta}}$ is adopted to consider rotation: $\hat{\sigma}^{\dot{\alpha\beta}} = \sigma^{\dot{\alpha\beta}} - \sigma_{\alpha\gamma}\dot{\omega}_{\beta\gamma} - \sigma_{\gamma\beta}\dot{\omega}_{\alpha\gamma}$

3.8. SPH modelling of elastic solids

Based on the improvements in the numerical stability of the traditional SPH introduced in Section 3.6, two improved SPH methods were developed. The first method is the Taylor SPH presented in Section 3.7, which incorporates the stress particle approach corrective technique into the traditional SPH framework and discretises the governing equations using the two-step Taylor time integration. The second method is the traditional SPH with tensile instability treatment incorporating the corrective technique to achieve second order accuracy and introduces stabilised terms such as artificial viscosity and artificial stress to remove tensile instability. The built-in codes of these two improved SPH approaches were developed to provide a stable numerical platform in rock fracture simulation. In this section, two numerical tests are conducted, using the two improved SPH methods combined with the elastic constitutive model to examine the capability of these SPH methods to simulate elastic solids.

3.8.1. 1D shockwave test

A one-dimensional shockwave problem carried out by Dyka and Ingel (1995) is simulated. The purpose of this test is to verify the performance and accuracy of the Taylor-SPH framework. In this test, an elastic bar under constant tensile loading is considered as shown in Figure 3.0–12. The bar is 0.133m long with a unit cross-section. It is fixed at the left end and an instantaneous velocity ($v = 5\mathrm{m/s}$) is given to the right quarter of the bar. The linear elastic constitutive model is adopted and the model parameters are: Young's modulus $E = 200$ GPa; density $\rho = 7833\mathrm{kg/m^3}$.

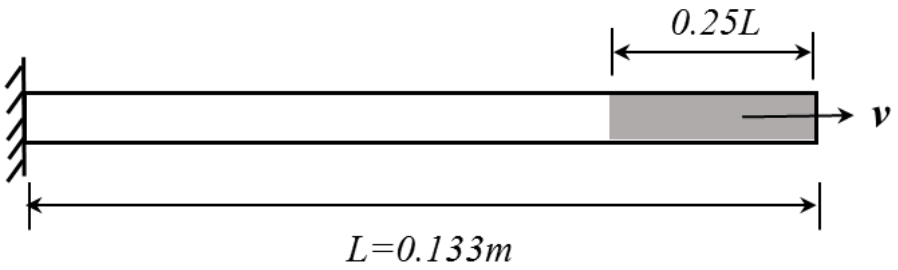

Figure 3.0–12. Geometry and boundary conditions of the 1D elastic bar.

In the Taylor SPH, the elastic bar is discretised by 41 material particles and 40 stress particles, which are arranged in a regular square lattice with the initial separation of dx = 0.00333m between two consecutive particles. The boundary conditions are: the velocity of the far left material particle is $v_1 = 0m/s$ and the stress of the far right material particle is $\sigma_{41} = 0$ Pa. Following the recommendation of Blanc and Pastor (2013) to improve the numerical stability of the Taylor-SPH model, the Courant number set to $C = 1$. The Courant number is defined as:

$$C = \frac{c_s \times dt}{dx} \tag{3.63}$$

where $c_s = E/\rho$ is the elastic wave speed, dt is the timestep and dx is the initial particle discretisation size.

For comparison, the traditional SPH is also applied to model the elastic response of a bar using the same constitutive model and material parameters. In total, 48 SPH particles are used for this simulation, 40 of which are used to form the elastic bar and the rest are used to provide the left fixed boundary by keeping their velocity at zero. The Courant number in the traditional SPH simulation is $C = 0.125$.

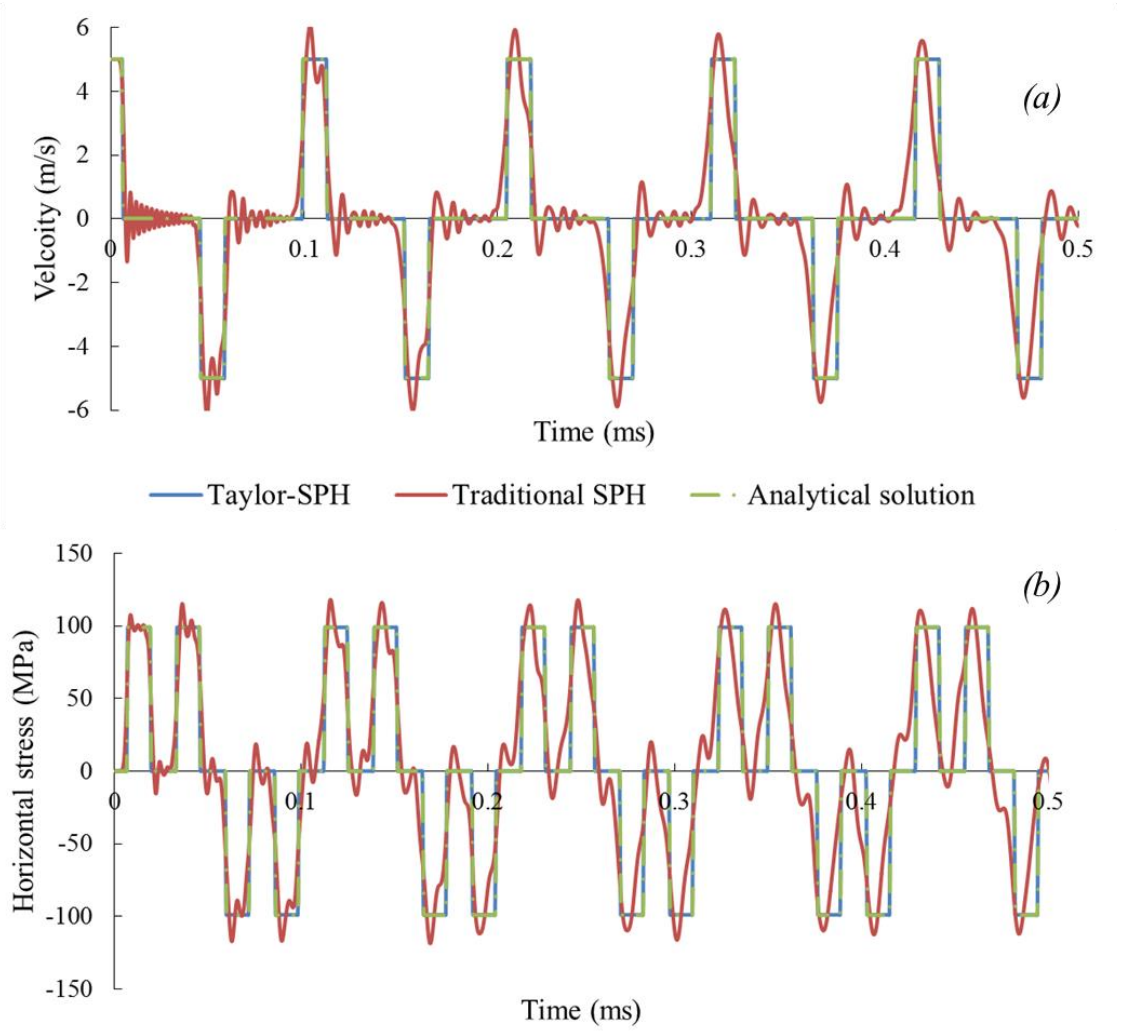

Figure 3.0–13. One-dimensional elastic bar test: (a). Velocity history of the right end of the bar; (b). Stress history for particles in the middle of the bar.

Figure 3.0–13(a) shows the velocity history of the SPH particle at the right end of the bar ($x = 0.133\text{m}$) using the Taylor and traditional SPH models, together with the analytical solution. As indicated in Figure 3.0–13(a), the results of the Taylor-SPH are in excellent agreement with the analytical solution. When the node at the right end of the bar is given an instant tensile loading, its velocity remains at 5m/s initially and decreases to 0. Then the node is under compression, and the velocity at this location immediately reduces to -5m/s. The observations can be extended to the stress history of a SPH particle located in the middle of the bar ($x = 0.0665\text{m}$), shown in Figure 3.0–13(b). As with the velocity history, good agreement between the Taylor-SPH results and the analytical solutions is achieved. The stress amplitude predicted by the Taylor-SPH is around 100MPa and remains unchanged with time, suggesting that the Taylor-SPH model is stable. On the other hand, the solutions of velocity and stress

predicted by the traditional SPH model, as illustrated in the same figure, show slightly larger amplitudes than those of the Taylor-SPH and analytical solutions. The solutions also show that the stress and velocity amplitudes in the traditional SPH model become smaller with time, suggesting that the energy in the traditional SPH model is not conservative. Furthermore, the numerical results predicted by the Taylor-SPH show less fluctuation than the traditional SPH solutions. This finding suggests that the Taylor-SPH model with stress particles is more stable than the traditional SPH model, despite its relatively complex formulations. Nevertheless, the above 1D elastic tension test demonstrates that the Taylor-SPH with chosen parameters can provide accurate numerical solutions.

3.8.2. 2D elastic cantilever test

A 2D elastic test of a cantilever beam is simulated to examine the capabilities of the Taylor SPH method and traditional SPH with the tensile instability treatment method in simulating 2D elastic problems. The bar's length is 0.2m and width is 0.02m as shown in Figure 3.0–14, and the vertical movement of the bar follows:

$$fx(x) = (\sinh kl + \sin kl) \times (\cosh kx - \cos kx) - ((\cosh kl + \cos kl)) \times (\sinh kx - \sin kx) \quad (3.64a)$$

$$fl = (\sinh kl + \sin kl) \times (\cosh kl - \cos kl) - ((\cosh kl + \cos kl)) \times (\sinh kl - \sin kl) \quad (3.64b)$$

$$v_y = V_f \times c \times fx(x)/fl \quad (3.64c)$$

where x is the horizontal distance from the right side of the fixed boundary; l is the total length of the beam, c is elastic wave speed, $V_f = 0.05$ and $k = 1.8751/l$ are the parameters defining the magnitude of vertical velocity.

The model parameters are: Young's modulus $E = 200Gpa$; Poisson ratio $v = 0.3$; density $\rho = 7.8kg/m^3$. The size of spatial discretisation in the Taylor SPH method is chosen as 1mm, resulting in 3061 materials particles and 2800 stress particles to form the beam and the left fixed boundary. The applied boundary conditions in Taylor SPH are as follows:

- Fixed left boundary, $v_x = v_y = 0$;
- At the right of the bar, $\sigma_{xx} = 0$, $\sigma_{xy} = 0$;
- At the top and bottom of the bar, $\sigma_{yy} = 0$, $\sigma_{xy} = 0$.

The elastic cantilever test is also simulated using the traditional SPH method with and without tensile instability treatment. The distance between two particles is adopted as 1mm, the same as the setting in Taylor SPH, thereby resulting in a total of 3061 particles representing the

computational domain. The velocities of the fixed boundary are set at zero, while the beam moves based on the equation (3.64c). The traditional SPH method can naturally deal with the free boundary surfaces, and thus it does not require any special treatment such as the settings in the Taylor SPH. For the simulation using the traditional SPH with tensile instability treatment, the constant parameters for the artificial viscosity are chosen to be 0.5 and 0 for the terms associated with the linear and quadratic of the velocity divergence respectively, while the constant parameter for the artificial stress is selected as 0.2.

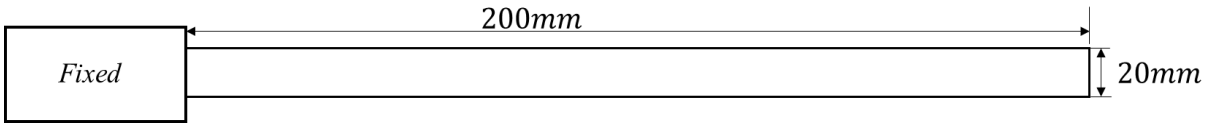

Figure 3.0–14. Configuration of 2D elastic test of a cantilever beam.

Figure 3.0–15 shows the simulation results using traditional SPH without any tensile instability treatment. The bar begins to curve upwards in Figure 3.0–15(a) and reaches the highest point in Figure 3.0–15(c), followed by downwards movement to Figure 3.0–15(d). It can be seen that the horizontal stress distribution in Figure 3.0–15(a) is quite smooth, whereas the results from Figure 3.0–15(b) show strong tensile instability. The detailed results of the horizontal stresses of SPH particles near the fixed boundary in stage c and d are also plotted in Figure 3.0–15, showing that the SPH particles clamp together, resulting in unrealistic stress distributions in the elastic material. Figure 3.0–16 and Figure 3.0–17 show the simulation results using the traditional SPH with tensile instability treatment and the Taylor SPH method respectively. It can be seen that the tensile instability is completely removed by using these two SPH methods. The clearer result of the horizontal stresses of the SPH particles using these two SPH methods can be also seen in Figure 3.0–16 and Figure 3.0–17 respectively. A very smoothed stress distribution is shown, without any particle clamping. In addition, the amplitudes of the elastic bar simulated by the two improved SPH methods are much higher compared with the result obtained using the traditional SPH without tensile instability treatment, indicating the energy conservation in the improved SPH methods. Overall, both the Taylor SPH and the traditional SPH with tensile instability treatment can solve the tensile instability and provide a stable solution for simulating rock fracture problems, in which tensile behaviour is of great importance.

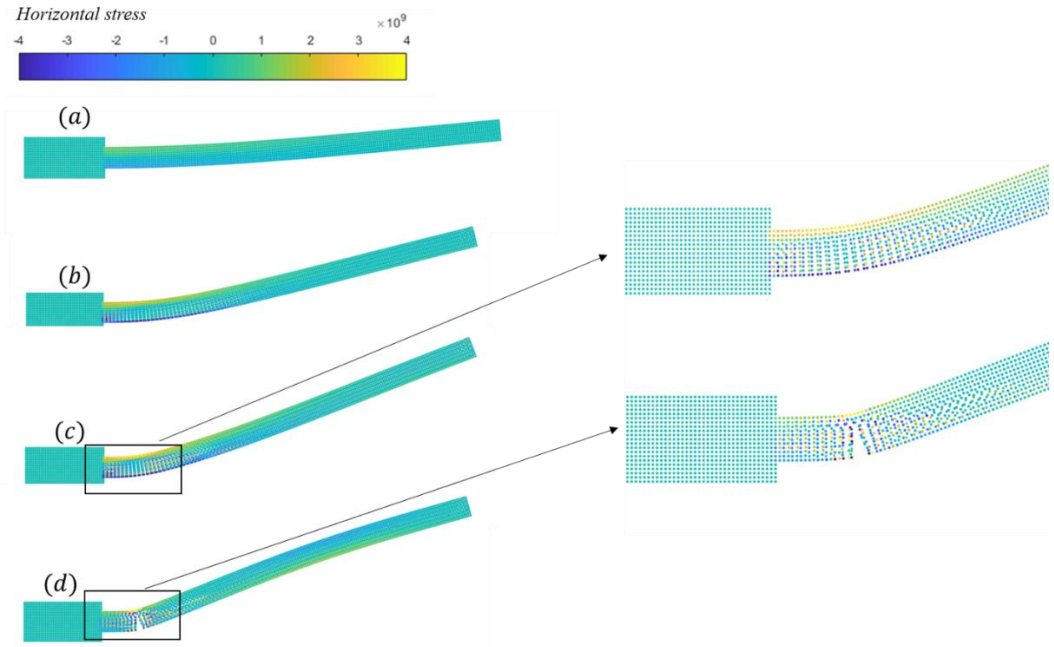

Figure 3.0–15. Result of traditional SPH without tensile instability treatment in elastic test of a cantilever beam.

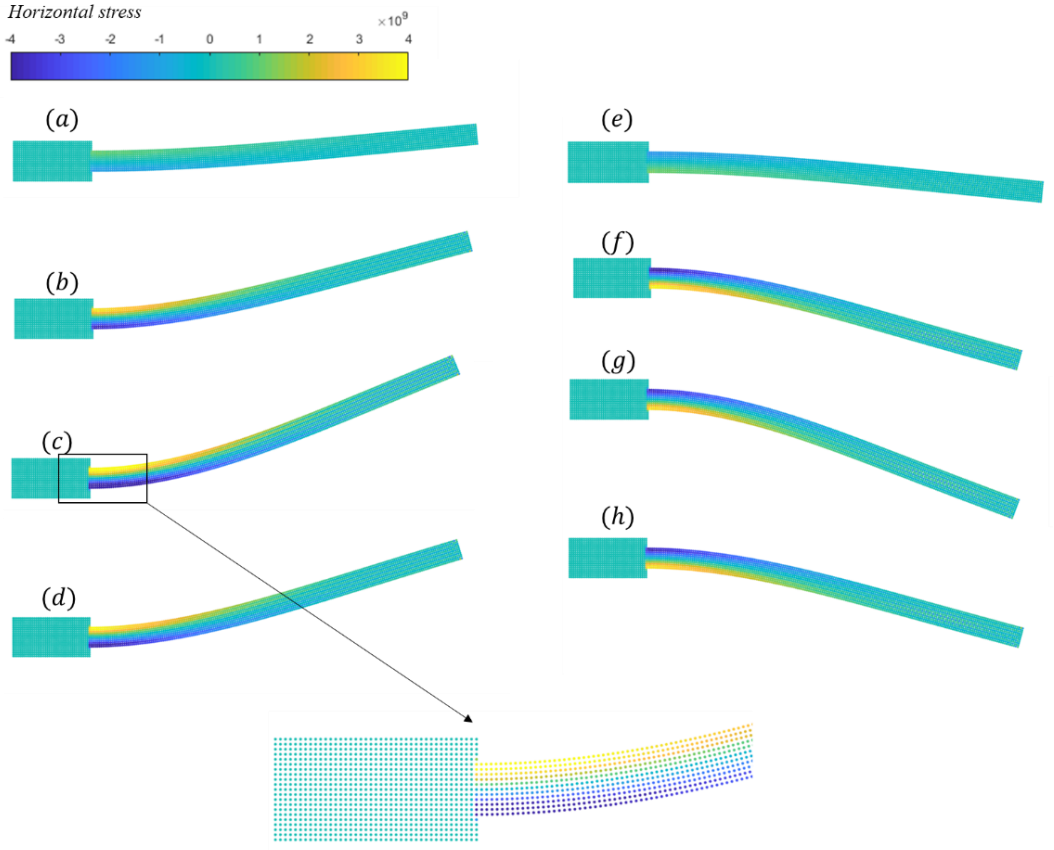

Figure 3.0–16. Result of traditional SPH with tensile instability treatment in elastic test of a cantilever beam.

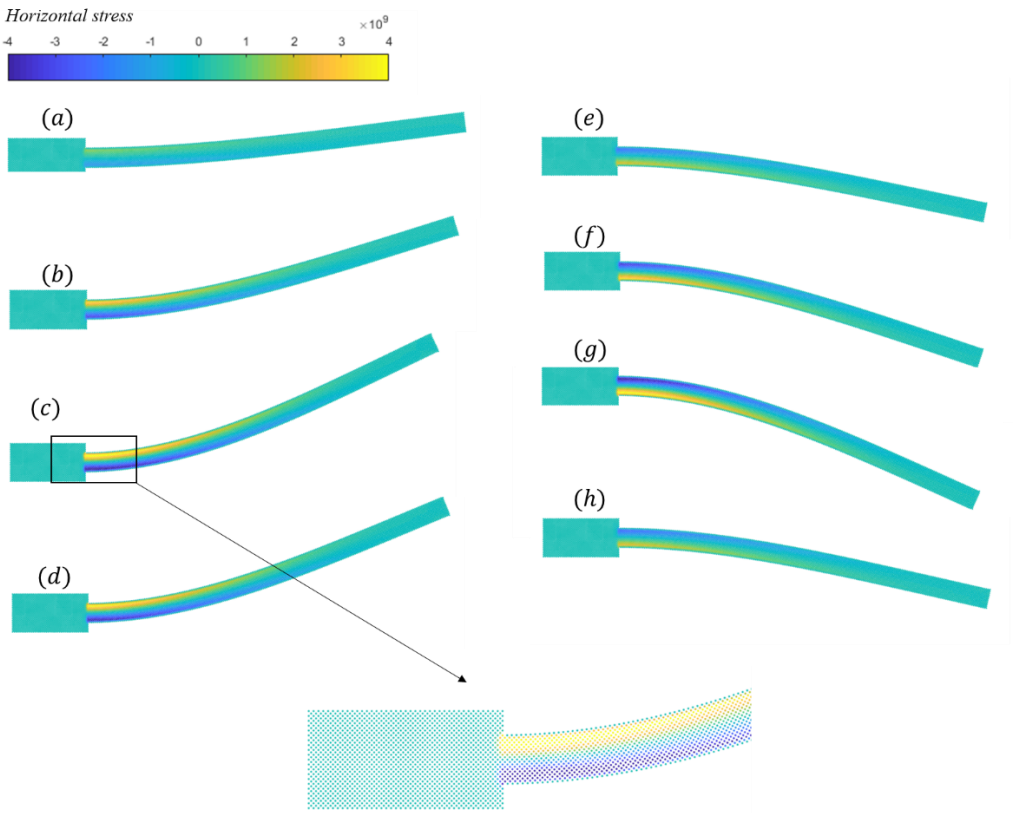

Figure 3.0–17. Result of Taylor SPH in elastic test of a cantilever beam.

3.9. Summary of different SPH versions

In this chapter, the basis of the SPH method was summarised with particular focus on the modelling of solid materials. Two stable SPH frameworks, the traditional SPH with tensile instability treatment and the Taylor SPH, were introduced and built-in codes for these two frameworks were developed for further simulation of rock fractures. The advantages and drawbacks of the two SPH frameworks are as follows:

- Complexity: The traditional SPH with tensile instability combines the traditional SPH approximation with stabilisation techniques (e.g. artificial stress and artificial viscosity). The simple LeapFrog time integration scheme is used, which keeps the implementation simple. On the other hand, the Taylor SPH, which combines the traditional SPH approximation, corrective technique and stress particle approach, employs two sets of particles with a two-step Taylor time integration scheme. Therefore, the Taylor SPH code is more complex to develop and implement.
- Stability in simulating tensile problems: In the traditional SPH with tensile instability treatment approach, the tensile instability can be removed by using the stabilised terms,

artificial viscosity and artificial stress, presented in Sections 3.6.1 and 3.6.2 respectively. Although the parameters in those stabilised terms must be chosen with care, the approach to resolving tensile instability is still very straightforward. With the Taylor SPH, tensile instability and spurious zero-energy mode problems can be automatically eliminated by using the stress particle approach. Therefore, both approaches can avoid tensile instability issues and provide a stable numerical solution for problems involving tensile loadings.

- Boundary condition treatment: In traditional SPH, boundary particles are adopted to simulate the boundary condition. The most common approach uses virtuals and ghost particles to respectively simulate non-slip and slip boundary conditions. And the stresses and velocities of all the boundary particles must be updated. An easier way to implement the boundary condition is to create three layers of real particles, whose field variables are updated in the same way as the particles which represent the problem domain. The Taylor SPH does not require extra SPH particles for generating boundary conditions. Instead, the boundary condition can be directly carried by the material particles which form the problem domain of a solid by using stress or velocity, thus it is much simpler than the traditional approach. However, the free surface boundaries in the Taylor SPH framework must be detected and updated at each calculation cycle, whereas the traditional SPH does not require special treatment of the free-surface boundary. Therefore, the traditional approach is computationally cheaper when dealing with complex fracture networks which involve a large number of fractures.
- Accuracy of the numerical result: It was proved by the example of a one-dimensional shockwave test in Section 3.8.1. that the result using Taylor SPH showed fewer frustrations and more energy conservation than the numerical solution using the traditional approach. Therefore, the Taylor SPH method can provide a more accurate solution than the traditional SPH due to its complex formulations. The Taylor SPH method would be a better choice when investigating the mechanical behaviour and fracturing processes of rocks with a couple of fractures; however, the traditional SPH with tensile treatment is preferred for handling complex problems involving multiple fracture networks with acceptable level of accuracy.

Chapter 4

Constitutive models for rock fractures

4.1. Introduction

Rock materials usually experience four stages during the loading process: a compaction stage, a quasilinear elastic stage, a yield stage and a failure stage. When there are some initial flaws, such as joints and cracks, within a rock mass, the rock mass will be densified during the very early loading stage. Although the macroscopic stress-strain responses of rocks under loading can be summarised into these four stages, the behaviour of rock materials under various loading conditions is very complex. For example, the mechanical properties and fracture behaviour of rocks are strongly affected by factors such as the loading/strain rate, specimen size, temperature and pressure, as addressed in Chapter 2. To model the abovementioned key features of rocks, a constitutive model that describes how materials respond to various loadings is required, with a robust and stable numerical approach as described in Chapter 3. Many constitutive models have been developed for modelling the behaviour of rock materials for various aspects of rock applications over the past few decades.

In this chapter, the popular constitutive models dedicated to rock modelling are reviewed, which are divided into two groups. The first group contains pure continuum models including elastoplastic models (Navarro et al. 2010, Pourhosseini and Shabanimashcool 2014, Chemenda and Mas 2016), elastic damage models (Cauvin and Testa 1999, Addessi et al. 2002, Maleki and Pouya 2010) and coupled elastoplastic damage models (Chiarelli et al. 2003, Shao et al. 2006, Chen et al. 2010, Pourhosseini and Shabanimashcool 2014, Zhang et al. 2016). Pure continuum models have been extensively proposed and applied in different rock problems, thanks to their simplicity in formulation, implementation and parameter identification. However, these models describe the material behaviour from initial yield to complete fracture with a single stress-strain relationship, ignoring the strong gradient of strain due to localisation.

As a consequence, despite the fact that they can reproduce results that please the eye for lab-scale experiments, they suffer from mesh dependence. Therefore enhancements to such classical continuum constitutive models using a smeared crack approach (Petersson 1981, De Borst 1987, Weihe et al. 1998, Hariri Ard et al. 2012) and nonlocal/gradient theories (Pijaudier-Cabot and Bažant 1987, Voyiadjis and Al-Rub 2005, Nguyen et al. 2015), the eXtended finite element method (Wells and Sluys 2001, Borst et al. 2006, Salimzadeh and Khalili 2015, Ferté et al. 2016, Dimitri et al. 2017), the strong discontinuity approach (Oliver 1996, Dias-da-Costa et al. 2009, Dias-da-Costa et al. 2010, Dias‐da‐Costa et al. 2013, Bosco et al. 2015, Zhang and Zhuang 2018), enhanced assumed strain (Borja 2000, Motamedi et al. 2016, Reinoso et al. 2017) and double-scale model (Nguyen et al. 2012, Nguyen et al. 2014, Nguyen et al. 2016, Nguyen et al. 2016) have been used for regularisation to resolve these issues. Among these advanced models, the smeared crack model, strong discontinuity model and double-scale model are reviewed as the group of enhancements to pure continuum models. After comprehensive revision of these existing constitutive models, a new size-dependent constitutive framework for rocks is described. The proposed constitutive model considers the RVE crossed by a fracture process zone, the behaviour of which is described by a cohesive fracture law. A length parameter is embedded in the constitutive relation for capturing the size-dependent behaviour of rocks. Detailed formulations and the algorithm of implementation are provided, following a validation test at the constitutive level.

4.2. Pure continuum models

4.2.1. Elastoplastic models

In elastoplastic models, the rock materials are considered to experience irreversible deformation, governed by the theory of plasticity during loading. Although many elastoplastic models have been developed for simulating different applications of rocks, the construction of all these models requires four steps. The first step is to decompose the rate of total strain into an elastic and a plastic part, expressed as:

$$\dot{\boldsymbol{\varepsilon}} = \dot{\boldsymbol{\varepsilon}}_{\mathrm{e}} + \dot{\boldsymbol{\varepsilon}}_{\mathrm{p}} \tag{4.1}$$

where $\dot{\boldsymbol{\varepsilon}}$, $\dot{\boldsymbol{\varepsilon}}_{\mathrm{e}}$ and $\dot{\boldsymbol{\varepsilon}}_{\mathrm{p}}$ represent the total strain rate tensor, elastic strain rate tensor and plastic strain tensor respectively.

The second step is to define a yield function denoted by f to determine whether the rock material has elastic or plastic regimes. Many yield functions have been proposed based on different considerations, which are introduced later in this section.

The third step is to define a plastic flow rule which can be associated or non-associated. The flow rule is used to determine the plastic strain rate tensor. The general expression of the plastic flow rule can be written as:

$$\dot{\boldsymbol{\varepsilon}}_{\mathrm{p}} = \dot{\lambda} \frac{\partial g(\boldsymbol{\sigma},\kappa)}{\partial \boldsymbol{\sigma}} \tag{4.2}$$

where $\dot{\lambda}$ is the rate of change of a plastic multiplier, the value of which is dependent on the state of stress and load history, $\boldsymbol{\sigma}$ is the stress tensor, g is the plastic potential function, which governs the evolution of the plastic strain. If an associated plastic flow rule is applied, the formulation of g is coincident with the yield function f. However, the associate plastic flow overestimates plastic volume expansion when modelling rock problems, so in this case non-associated plastic flow rule is more popular, in which the plastic potential function is formulated by modifying the yield function with one or more parameters in order to avoid excessive volume expansion. κ is the variable related to the stress tensor and plastic strain. This parameter controls the post-peak behaviour of the material, which can be perfect plastic, softening or hardening.

After determining the plastic strain based on the plastic flow, the last step is to calculate the stress rate using Hooke's law:

$$\dot{\boldsymbol{\sigma}} = \boldsymbol{C}\dot{\boldsymbol{\varepsilon}}_{\mathrm{e}} = \boldsymbol{C}(\dot{\boldsymbol{\varepsilon}} - \dot{\boldsymbol{\varepsilon}}_{\mathrm{p}}) \tag{4.3}$$

where $\boldsymbol{C}$ is the elastic stiffness matrix, which is controlled by the Young's modulus and Poisson's ratio. It can be seen that once the yield function is determined, the model can easily be developed by following these steps. Therefore, the emphasis of elastoplastic models is on the construction of yield criterion. Numerical yield criteria were developed last century for modelling rock failure (Broms 1966, Barron 1971, Franklin 1971, Miller and Cheatham Jr 1972, Brook 1979, Price and Farmer 1979, Yudhbir et al. 1983, Michelis and Brown 1986, Yumlu and Ozbay 1995, Sheorey 1997, Yu 2002, Yu et al. 2002, Huang and Gao 2004). Rahimi and Nygaard (2015) summarised the popular ones with their formulations as presented in Table 4.0-1. These yield criteria can be grouped either based on the number of model parameters (Chen and Han 2007) or based on the shape of the surface in the principal stress space (Yu et al. 2002).

Table 4.0-1. Summary of the yield criteria used for rock materials with their key formulations (Rahimi and Nygaard 2015).

Failure criteria	Governing equation
Mohr–Coulomb (MC)	$\sigma_1 = q\sigma_3 + C_0$
	$q = \frac{1+\sin\phi}{1-\sin\phi},\ C_0 = \frac{2c\cos\phi}{1-\sin\phi}$
Mogi–Coulomb (MG)	$\tau_{oct} = a + b\sigma_{m,2}$
	$a = \frac{2\sqrt{2}}{3}\frac{C_0}{q+1},\ b = \frac{2\sqrt{2}}{3}\frac{q-1}{q+1}$
Tresca (TR)	$\frac{(\sigma_1-\sigma_3)}{2} = c = \tau_{max},\ \frac{C_0}{2} = c$
Von Mises (VM)	$\sqrt{J_2} = \sqrt{\frac{(\sigma_1-\sigma_3)^2+(\sigma_2-\sigma_3)^2+(\sigma_1-\sigma_3)}{6}} = \frac{C_0}{3}$
Ins. Drucker–prager (IDP)	$\sqrt{J_2} = k + \alpha J_1$
	$\alpha = \frac{3\sin\phi}{\sqrt{9+3\sin\phi^2}},\ k = \frac{3C_0\cos\phi}{2\sqrt{q}\sqrt{9+3\sin\phi^2}}$
Cir. Drucker–prager (CDP)	$\sqrt{J_2} = k + \alpha J_1$
	$\alpha = \frac{\sqrt{3}(q-1)}{(2+q)},\ k = \frac{\sqrt{3}C_0}{2+q}$
Hoek–Brown (HB)	$\sigma_1 = \sigma_3 + \sqrt{mC_0\sigma_3 + sC_0^2}$
Modified Lade (ML)	$\frac{I_1^3}{I_3} = \eta_1 + 27$
	$S = \frac{c}{\tan\phi},\ \eta = \frac{4\tan^2\phi(9-7\sin\phi)}{(1-\sin\phi)}$
Modified Wiebols–Cook (MWC)	$\sqrt{J_2} = A + BJ_1 + CJ_1^2$
	$C = \frac{\sqrt{27}}{2C_1+(q-1)\sigma_3-C_0}\left(\frac{C_1+(q-1)\sigma_3-C_0}{2C_1+(2q-1)\sigma_3-C_0} - \frac{q-1}{q+2}\right)$
	$C_1 = (1+0.6\,\mu)C_0$
	$B = \frac{\sqrt{3}(q-1)}{q+2} - \frac{C}{3}[2C_0 + (q+2)\sigma_3]$
	$A = \frac{C_0}{\sqrt{3}} - \frac{C_0}{3}B - \frac{C_0^2}{9}C$
Griffith (GR)	$(\sigma_1-\sigma_3)^2 = 8T_0(\sigma_1+\sigma_3)$
	$\sigma_3 = -T_0\ if\ \sigma_1+3\sigma_3 < 0,\ T_0 = \frac{C_0}{8}$
Modified Griffith (MGR)	$\sigma_1[\sqrt{\mu^2+1}-\mu] - \sigma_3[\sqrt{\mu^2+1}+\mu] = 4T_0$
	$\frac{C_0}{T_0} = \frac{4}{\sqrt{\mu^2+1}-\mu}$
Murrell (MR)	$(\sigma_1-\sigma_3)^2 + (\sigma_1-\sigma_2)^2 + (\sigma_2-\sigma_3)^2 = 24T_0(\sigma_1+\sigma_2+\sigma_3)T_0 = \frac{C_0}{12}$
Stassi D'alia (SD)	

Among the criteria, the Tresca (Tresca 1864) and Von Mises (Mises 1913) criteria are the most classic pressure-independent models, initially developed for metallic materials, as shown in Figure 4.0–1. The shapes of both criteria are controlled only by the cohesion of the material, and thus are independent of pressure. When applied to model rock or rock-like materials, these models are normally used together with an extra tensile cut-off surface to capture tensile

failures (Feenstra and de Borst 1995). In addition, these models cannot reflect the different responses under different compressive hydrostatic pressures due to their insensitivity to pressure, and thus limiting their application to biaxial loading.

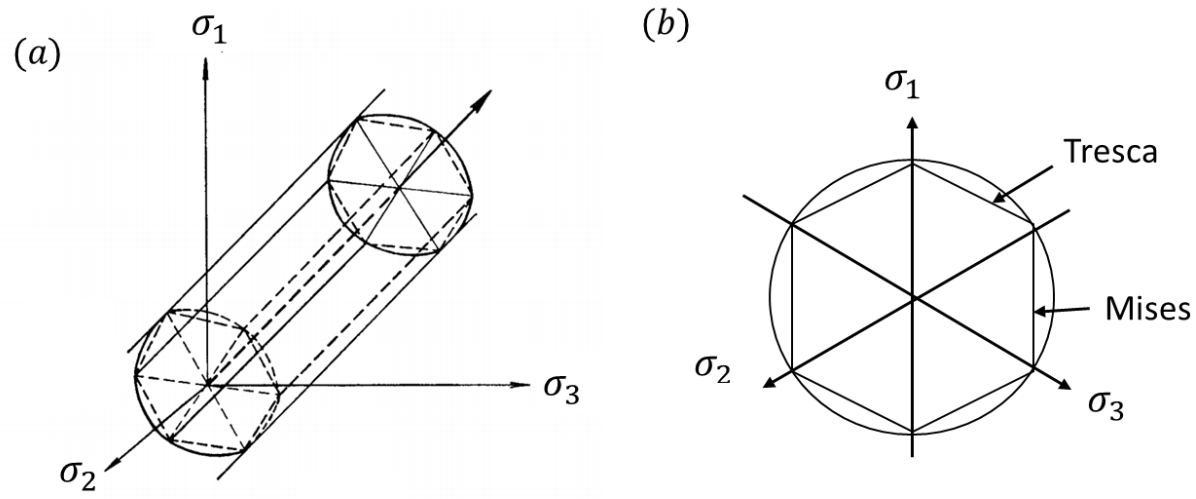

Figure 4.0–1. Shapes of the Tresca and Von Mises criteria: (a) in the three-dimensional stress space; (b) in an octahedral plane (Matsuoka and Nakai 1985).

To solve the problems of one parameter criteria such as Tresca and Von Mises, many pressure-dependent criteria have been developed, among which the Mohr-Coulomb and Dracker-Prager are the most widely used for modelling rock materials. The shapes of these two criteria are presented in Figure 4.0–2. Unlike the abovementioned one-parameter models, the shapes of the Mohr-Coulomb and Drucker-Prager models are controlled by two parameters, the cohesion and the friction angle of rocks, and furthermore these models can reflect pressure-dependent behaviour under compressive loading. Those two yield criteria have been successfully applied to analyse the strength of rock materials and capture shear bands in rocks (Singh et al. 1989, Borja et al. 2000, Zhao 2000, You 2009, Pan et al. 2012). However, Mohr Coulomb neglects the effect of intermediate principal stress and suffers from stress singularity in the vertex region. On the other hand, although the Drucker Prager avoids stress singularity by using the smooth curve, this criterion cannot reflect the experimentally-observed dependence of the Lode angle. In addition, those criteria in which shapes are linear and open fail to account for plastic deformation under pure compressive loading conditions, as there is no limit to the elastic zone on the negative part of the pressure axis. In this case, models that employ an open yield surface

cannot model compaction bands, which are the narrow zones of localised purely compressive deformation perpendicular to the most compressive principal stress in rocks.

In order to capture the compaction band, a cap on the existing yield surface such as Mohr Coulomb is required. The introduction of the cap allows the generation of inelastic volume deformation under purely hydrostatic conditions and reduction of the shear stress at yield with increasing mean compressive stress. After the first cap model invention by DiMaggio and Sandler (1971), this type of cap model has been widely used for porous rocks (Wong et al. 1992, Olsson 1999, Fossum and Fredrich 2000). The results through these studies showed that an elliptical cap is sufficient to describe the rock behaviour under pure compression and the onset of shear enhanced compaction in rocks. However, the interaction between two yield surfaces must be treated with care, otherwise it can result in an inaccurate solution. Apart from the introduction of a cap to the existing yield function, another alternative for modelling rock behaviour under compression is to develop a single closed yield surface. Closed yield criteria have been widely employed in many studies for modelling the compressive behaviour of porous materials (Antonellini et al. 1994, Cuss et al. 2003, Borja 2004, Borja and Aydin 2004). In those criteria, the yield surface is initially closed and gradually open towards the negative hydrostatic axis under loading, as illustrated in Figure 4.0–3. The nonlinear closed yield surface has been proved able to capture the process of how deformation bands (shear or compaction) grow and eventually fail to form through-going faults.

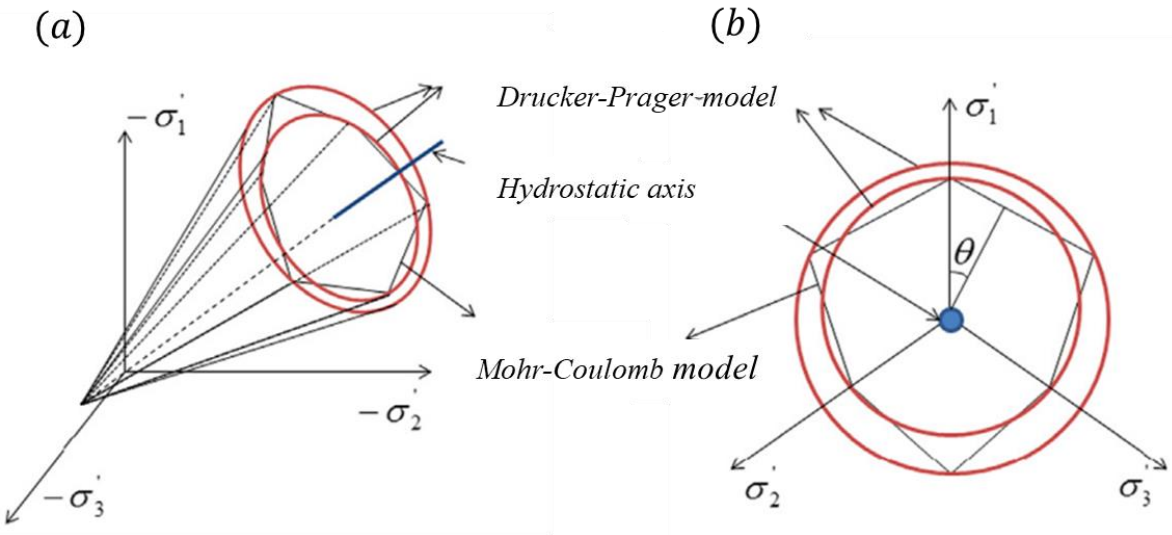

Figure 4.0–2. Shapes of Mohr-Coulomb and Drucker-Prager criteria: (a) in three-dimensional stress space; (b) in an octahedral plane (Kim and Moridis 2013)

Recently, more advanced yield functions have been proposed by calibrating with extensive experimental data under various loading conditions. For example, in the work by Chemenda and Mas (2016), Grassl et al. (2013), Paliwal et al. (2017) and Veiskarami and Tamizdoust (2017), the third stress invariant J_3 or alternatively the Lode angle parameter θ was introduced to the yield function for capturing the Lode angle dependency. Similarly, the first stress invariant I_1 or the hydrostatic pressure p was incorporated to reflect the pressure dependent behaviour under the compressive loading (Grassl and Jirásek 2006, Červenka and Papanikolaou 2008, Grassl et al. 2013, Paliwal et al. 2017). Detailed formulations of these yield functions are available in those references.

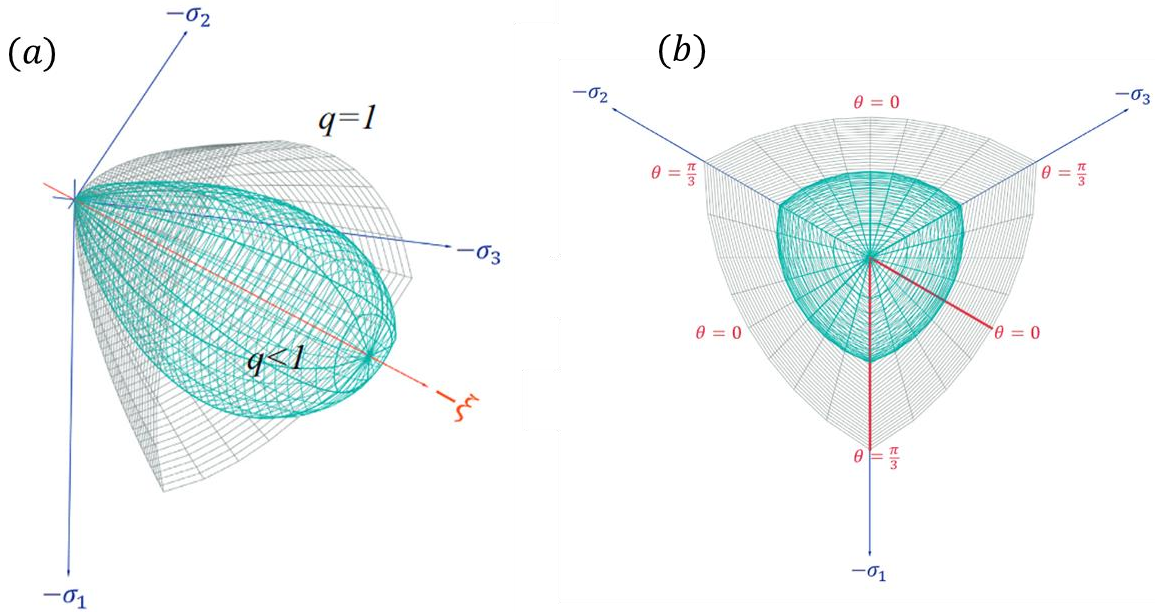

Figure 4.0–3. Shape of a closed cap model: (a) in the three-dimensional stress space; (b) in an octahedral plane (Paliwal et al. 2017).

Thanks to the simple concept, elastoplastic models are the most popular constitutive models which have been widely applied to modelling different rock applications. Although these models can capture well some material responses such as irreversible deformation and strain hardening/softening by choosing a suitable yield function and hardening/softening laws, elastoplastic models fail to take into account the stiffness reduction and high strain deformation in the fracture process zone during fracture-induced failures of rock. Thus these models are not favourable options for predicting fracture initiation and propagation and investigating the

underlying mechanism of rock fractures. Many advanced constitutive models have been developed by adding damage mechanics (Červenka and Papanikolaou 2008) or fracturing theory mechanics (Krätzig and Pölling 1998) into the existing elastoplastic framework for better modelling of rock fracture behaviour, as introduced later.

4.2.2. Elastic damage models

Unlike the elastoplastic models, elastic damage models based on continuum damage mechanics (CDM) can capture the stiffness degradation during the failure of rock materials due to the incorporation of the damage variable. In addition, simple damage models have been extensively used in structure analysis under monotonic loading thanks to their capability for reproducing the softening response of the material without requiring irreversible deformation. These are two key features of continuum damage mechanics over the theory of plasticity when modelling failure of rock materials. While the term "continuum damage mechanics" was apparently introduced by Janson and Hult (1977), the theory itself can be traced back to Kachanov (1958). After its invention, numerous elastic damage models which couple the elastic law with the continuum damage mechanics (CDM) emerged.

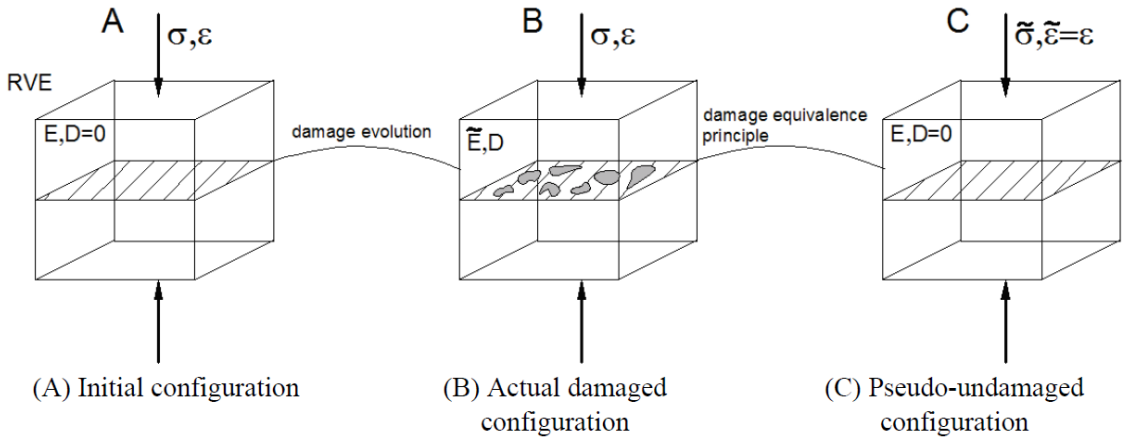

Figure 4.0–4. Concept of damage mechanics with scalar damage variable (Cieślik 2013)

The basic idea of continuum damage mechanics is to introduce damage variables to constitutive relations to characterise the material deterioration in a representative volume element (RVE) associated with the effective stress concept and the principle of equivalence. It is well known that damage in materials is a consequence of the growth and coalescence of microcracks or microvoids. Within the RVE, the discrete entities of damage at the microscopic level do not

appear explicitly but their effects are represented by means of macroscopic damage variables. The damage variable can be in the form of a scalar variable that describes the evolution of the isotropic material from an intact state to a fractured state (Cauvin and Testa 1999, Li and Ansari 1999, Addessi et al. 2002, Liu et al. 2016); on the other hand, it can be in the form of second or fourth rank tensor describing the different extents of stiffness degradation in multiple directions (Hayakawa and Murakami 1997, Swoboda and Yang 1999, Swoboda and Yang 1999, Shao and Rudnicki 2000, Shao et al. 2006, Maleki and Pouya 2010). Although the tensor representation of the damage variable is more accurate for capturing anisotropic damage, the scalar damage variable is more popular in the literature due to its simplicity in the formulation and numerical implementation.

Figure 4.0–4 shows the concept of an elastic damage model with a scalar damage variable. A representative volume element is under compressive loading. The RVE behaves elastically before the damage is identified, as shown in Figure 4.0–4a, by following Hooke's law:

$$\sigma = E\varepsilon \tag{4.4}$$

In Figure 4.0–4b, the cross section of the RVE (A) is divided into an undamaged area and a damaged area denoted asA_D, indicating the damage development in the RVE. Therefore, the damage variable can be defined as the ratio of the damaged area to the total area:

$$D = A_D/A \tag{4.5}$$

Consequently, the effective stress becomes:

$$\tilde{\sigma} = \frac{F}{\tilde{A}} = \frac{F}{A-A_D} = \frac{\sigma}{1-D} \tag{4.6}$$

The effective stress strain relationship representing the RVE in Figure 4.0–4c can be obtained using the strain equivalence hypothesis $\tilde{\varepsilon} = \varepsilon$ (Lemaitre, 1972):

$$\tilde{\sigma} = \frac{E\tilde{\varepsilon}}{1-D} \tag{4.7}$$

Similarly, the damaged RVE in Figure 4.0– 4c also can be described by the averaged stress-strain relationship as:

$$\sigma = (1-D)E\varepsilon \tag{4.8}$$

It can be seen that elastic damage models are formulated based on an elastic stress-strain law together with a damage variable D to characterise the material deterioration. Equation (4.8) can

be extended to express the stress-strain relationship of the RVE in two- or three-dimensional coordinate as:

$$\boldsymbol{\sigma} = (1 - D)\mathbf{C}\boldsymbol{\varepsilon} \tag{4.9}$$

Equation (4.9) is the basic formulation for all damage models, although they have different ways of defining the evolution of the damage variable. The choice of the damage variable and the evolution law for damage are the key steps in the development of damage models, many of which have appeared in the literature. The most popular approach is to describe the evolution of damage in rocks as a function of the effective stress or strain (Krajcinovic 1985, Simo and Ju 1987, Simo and Ju 1987, Mazars and Pijaudier-Cabot 1989, Reyes and Einstein 1991, Peerlings et al. 1996, Bonora 1997, Cauvin and Testa 1999, Peerlings 1999, Jirasek et al. 2004). As studies show that energy dissipation and damage are correlated in rock, another popular approach is to derive the damage evolution based on the basis of energy dissipation (Duyi and Zhenlin 2001, Fengnian et al. 2004, Xie et al. 2005, Peng et al. 2007, Wang et al. 2012). Some other studies relate the damage evolution to some material parameters of rock, such as joint spacing, Young's modulus, yield stress, wave velocity, and acoustic emission event count (Liu et al. 2016).

Overall, the density and orientation of microcracks can be represented in elastic damage models by using internal variables such as a scalar variable for isotropic damage, second and fourth rank tensors to describe anisotropic damage. The results from numerous studies show that these models successfully account for the reduction of stiffness and the macroscopic stress-strain responses of brittle rock deformation under both tensile and compressive loading conditions. However, some of the concepts and parameters involved in these models are not clearly related to physical mechanisms (Shao et al. 2006). Moreover, these models fail to take into account some key macroscopic features of the material behaviour, such as Lode-angle dependency, mixed mode and size effect. Importantly, these models assume that all energy dissipates due only to the damage mechanics, and thus cannot capture the irreversible strains of the materials under loading. These drawbacks of elastic damage models limit their applications in modelling mixed-mode rock fracture problems or problems related to the unloading-reloading cycle.

4.2.3. Coupled elastoplastic damage models

It has been found through numerical experiments that in most rock materials, plastic deformation is generally coupled with damage due to the growth of microcracks (Niandou 1994). This induced damage is the main mechanism which results in the material softening.

Therefore, for the coupling between damage and plasticity, as illustrated in Figure 4.0–5, it is necessary to take into account both stiffness degradation and irreversible strain during the course of loading. Owing to this advantage, numerous coupled elastoplastic damage models have been developed (Chiarelli et al. 2003, Shao et al. 2006, Chen et al. 2010, Pourhosseini and Shabanimashcool 2014, Zhang et al. 2016). In those coupling models, the total strain rate ($\dot{\boldsymbol{\varepsilon}}$) is decomposed into an elastic part ($\dot{\boldsymbol{\varepsilon}}_{\mathrm{e}}$) and a plastic part ($\dot{\boldsymbol{\varepsilon}}_{\mathrm{p}}$), as in elastoplastic models:

$$\dot{\boldsymbol{\varepsilon}} = \dot{\boldsymbol{\varepsilon}}_{\mathrm{e}} + \dot{\boldsymbol{\varepsilon}}_{\mathrm{p}} \tag{4.10}$$

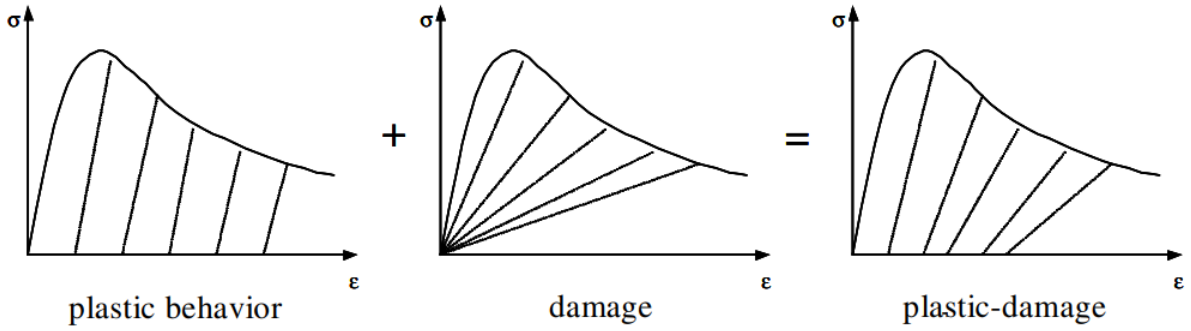

Figure 4.0–5. Basic idea of elastoplastic damage models (Tao and Phillips 2005)

Apart from the strain decomposition, two separate loading functions are required to respectively control the evolution of plastic strain ($\dot{\boldsymbol{\varepsilon}}_{\mathrm{p}}$) and damage variable ($D$). The plastic strain rate is characterised through determination of the plastic yield function or plastic potential function, while the damage evolution can be derived by a damaged surface (Yazdani and Schreyer 1990, Shao et al. 2006) or a function of internal variables such as plastic strain and material strengths (Salari et al. 2004, Grassl et al. 2013). The plastic strain and damage variable are coupled through the final stress-strain relationship, the general formulation of which can be written as:

$$\dot{\boldsymbol{\sigma}} = (1 - D)\, \boldsymbol{C}\dot{\boldsymbol{\varepsilon}}_{\mathrm{e}} = (1 - D)\boldsymbol{C}(\dot{\boldsymbol{\varepsilon}} - \dot{\boldsymbol{\varepsilon}}_{\mathrm{p}}) \tag{4.11}$$

The basic framework for coupled elastoplastic damage models has been comprehensively introduced by Shao et al. (2006), Chiarelli et al. (2003) and Mohamad-Hussein and Shao (2007). In these studies, the mechanics of plastic flow and damage evolution are also discussed based on the experimental observations. Coupled elastoplastic damage models were first proposed and used in modelling semi-brittle rocks such as argillite (Jia et al. 2007, Chen et al.

2010) and claystone (Chiarelli et al. 2003). Then, more coupled elastoplastic damage models were developed to describe the mechanical behaviour of brittle rocks (Zhou et al. 2011, Chen et al. 2015). The results showed that these models could capture the plastic hardening effect in the pre-peak regime, thanks to the employment of plasticity, and rapid damage degradations in elastic stiffness and yield strength in the post-peak regime, thanks to the employment of damage mechanics.

Although the coupled elastoplastic damage models have achieved considerable success in modelling brittle rocks, they fail to take into account another important feature in brittle rocks, which is time-dependent deformation. In the previous models, the elastic and plastic deformation are both instantaneous (practically in a very short time), and therefore these models are not suitable for modelling long-term (or creep) plastic responses due to the effect of material viscosity. Although it was found that creep deformation is essentially related to sub-critical propagation of microcracks, viscoplastic models which introduced a viscosity coefficient into the constitutive relation at the RVE level are the most popular methods for the modelling of creep deformation (Lemaitre and Chaboche 1994). Many viscoplastic models have been developed for rocks for long-term safety analysis (Cristescu 1986, Cristescu 1994, Dahou et al. 1995, Jin and Cristescu 1998, Maranini and Yamaguchi 2001). In the following part of this section, a coupled elastoplastic and viscoplastic damage model proposed by Zhou et al. (2008) is briefly introduced. In their work, the rock material is assumed to experience simultaneous instantaneous plastic deformation ($\dot{\boldsymbol{\varepsilon}}_{\mathrm{p}}$) and time-dependent plastic deformation denoted as $\dot{\boldsymbol{\varepsilon}}_{\mathrm{vp}}$. In this case, the total strain rate is decomposed into three parts as:

$$\dot{\boldsymbol{\varepsilon}} = \dot{\boldsymbol{\varepsilon}}_{\mathrm{e}} + \dot{\boldsymbol{\varepsilon}}_{\mathrm{p}} + \dot{\boldsymbol{\varepsilon}}_{\mathrm{vp}} \tag{4.12}$$

The general form of the stress-strain relationship can be written as:

$$\dot{\boldsymbol{\sigma}} = \mathbf{K}\dot{\boldsymbol{\varepsilon}}_{\mathrm{e}}\delta + 2\mathbf{G}\dot{\mathbf{e}}_{\mathrm{e}} \tag{4.13}$$

where **K** and **G** are the bulk modulus and shear modulus respectively, both of which can be calculated based on the Young's modulus and Poisson's ratio of material.

A nonlinear plastic yield function and plastic potential, together with the non-associated flow rule for determining the instantaneous plastic deformation, are respectively expressed as:

$$f_p(\boldsymbol{\sigma}, \alpha_p) = q - g(\theta)\alpha_p(\gamma_p)R_c\sqrt{A\left(C_s + \frac{p}{R_c}\right)} \tag{4.14a}$$

$$Q_p(\boldsymbol{\sigma}, \alpha_p) = q - g(\theta)(\alpha_p - \beta_p)(p + C_s R_c) \tag{4.14b}$$

$$\dot{\boldsymbol{\varepsilon}}_{\mathrm{p}} = \lambda_p \frac{\partial Q_p(\boldsymbol{\sigma},\alpha_p)}{\partial \boldsymbol{\sigma}} \tag{4.14c}$$

where p, q and θ are the mean stress, stress deviator and Lode's angle respectively; C_s is the parameter representing the coefficient of material cohesion; A defines the internal friction coefficient of the failure surface; R_c is a normalised coefficient related to the uniaxial compression strength; $g(\theta)$ is a function related to the Lode's angle for describing the dependency of the yield function on the Lode's angle; β_p defines the transition point from the compressibility zone ($\alpha_p < \beta_p$) to the dilatancy zone ($\alpha_p > \beta_p$) in which the plastic hardening α_p is a function of the equivalent plastic shear strain γ_p, expressed as:

$$\alpha_p(\gamma_p) = \alpha_p^0 + (1 - \alpha_p^0)\frac{\gamma_p}{B+\gamma_p} \tag{4.15a}$$

$$\dot{\gamma}_p = \sqrt{\frac{2}{3}\dot{e}_p\dot{e}_p} + \sqrt{\frac{2}{3}\dot{e}_{vp}\dot{e}_{vp}} \tag{4.15b}$$

The plastic hardening function in Equation (4.15a) is used to model the hardening behaviour of quasi-brittle materials, where the parameter B controls the rate of plastic hardening and $\dot{e}_p$ and $\dot{e}_{vp}$ are respectively the plastic and viscoplastic deviatoric strains.

In order to model the time-dependent behaviour of rocks, a viscoplastic yield function, a viscoplastic potential and a viscoplastic flow rule are also required to control the evolution of viscoplastic deformation, shown as:

$$f_{vp}(\boldsymbol{\sigma}, \alpha_p) = q - g(\theta)\alpha_{vp}(\gamma_p)R_c\sqrt{A\left(C_s + \frac{p}{R_c}\right)} \tag{4.16a}$$

$$Q_{vp}(\boldsymbol{\sigma}, \alpha_p) = q - g(\theta)(\alpha_{vp} - \beta_p)(p + C_s R_c) \tag{4.16b}$$

$$\dot{\boldsymbol{\varepsilon}}_{\mathrm{vp}} = \gamma(T)\left\langle\frac{f_{vp}(\boldsymbol{\sigma},\alpha_p)}{R_c}\right\rangle^N \frac{\partial Q_p(\boldsymbol{\sigma},\alpha_p)}{\partial \boldsymbol{\sigma}} \tag{4.16c}$$

where $\alpha_{vp}(\gamma_p)$ defines the current internal friction coefficient of the viscoplastic loading surface, expressed as:

$$\alpha_{vp}(\gamma_p) = \alpha_p^0 + (1 - \alpha_{vp}^0)\frac{\gamma_p}{B_{vp}+\gamma_p} \tag{4.17}$$

The value of $\alpha_{vp}(\gamma_p)$ must be less than the value of $\alpha_p(\gamma_p)$, as viscoplastic deformation always lags behind instantaneous plastic deformation.

Finally, a damage variable (ω) is introduced to model the degradation of elastic properties and plastic deformation. As it was found through mechanical analysis that induced damage mainly

affects the shear modulus of the material, a linear relationship between shear modulus and damage variable was proposed in this work, expressed as:

$$\mathbf{G}(\omega) = \mathbf{G}_0(1 - \alpha_2\omega) \tag{4.18}$$

The shear modulus in Equation (4.13) is replaced by the new damage-dependent shear modulus $G(\omega)$ to reflect the stiffness degradation due to damage. Furthermore, the damage variable is also introduced into the expressions of hardening laws in Equations (4.15a) and (4.17). They are now expressed as:

$$\hat{\alpha}_p(\gamma_p, \omega) = (1 - \omega)\alpha_p(\gamma_p) \tag{4.19a}$$

$$\hat{\alpha}_{vp}(\gamma_p, \omega) = (1 - \omega)\alpha_{vp}(\gamma_p) \tag{4.19b}$$

where the damage variable ω can be calculated using the following damage function:

$$f_\omega(\omega, \xi_\omega) = \omega - \left[1 - \frac{(1-A_1)\xi_\omega^0}{\xi_\omega} + \frac{A_1}{\exp\left(B_1(\xi_\omega - \xi_\omega^0)\right)}\right] \leq 0 \tag{4.20}$$

This model shows a good example of coupling both time-independent and time-dependent plastic deformation with induced damage by the growth of microcracks. Similar coupled elastoplastic and viscoplastic damage models have been proposed by Chen et al. (2015), Souley et al. (2011) and Dufour et al. (2012), to list just a few. Overall, the use of coupled elastoplastic damage models with or without consideration of long-term deformation could lead to a more realistic result for capturing the macroscopic behaviour of rock, such as the stiffness reduction and irreversible deformation, compared with the damage models and elastoplastic models. However, the deformation in the abovementioned models is assumed to be homogeneous over a unit volume, thereby neglecting the existence of a high gradient of deformation across the localisation band during the nonlinear phases of rock fractures. In addition, those models fail to account for the characteristics of the localisation zone such as size, fracture orientation and evolution of inelastic behaviour, together with the material behaviour outside the zone. As a consequence, the localisation of deformation in classical models depends highly on the resolution of discretisation, which is also called mesh-dependence.

4.3. Enhancements to pure continuum models

As discussed in the previous sections, models based on the continuum mechanics fail to take into account the material behaviour and the size of the FPZ in rocks, thereby suffering from mesh-dependency of the numerical solutions. To solve this problem, some enhancements have been employed at the constitutive level, such as the smeared crack model, strong discontinuity

model and double-scale model. In these models, the quantities charactering the behaviour of the localisation zone are taken into account, thus helping to remove mesh-dependency and hence enabling proper capturing of the failure behaviour of the materials. In the following part of this section, the concepts of these enhanced models are introduced, together with their strengths and limitations.

4.3.1. Smeared crack model

The origins of the smeared cracked approach can trace back to the sixties of the last century in the study of prestressed concrete pressure vessels (Rashid 1968). Despite its successful implementation in FE codes, it was found that the total dissipated energy of this model is proportional to the mesh size during the cracking process. This lack of objectivity also implies that the dissipated energy vanishes if an infinitesimally small mesh size is used, which is not physically correct. Furthermore, the original approach still suffers from mesh size dependence in localisation problems. Those problems were solved by Bažant and Oh (1983), who proposed a crack band model in the context of continuum mechanics. The basic idea of this model is to simulate fracture opening in rock and concrete as a blunt smeared crack band in which the material undergoes progressive micro-cracking. A loss of rigidity is introduced in the direction perpendicular to the direction of maximum tensile stress. In the crack band, a triaxial stress-strain relationship involves strain-softening which is controlled by fracture energy, strength limitation and width of the crack band (normally five times the grain size of material). However, the crack band model proposed by Bažant and Oh (1983) is limited to simulating pure mode I tensile failure.

Later, a number of smeared crack approaches were developed for simulating mixed-mode failure, ranging from fixed single to fixed multi-directional and rotating crack approaches. The distinctions among them are how often the orientation of the crack is updated and how many cracks are assumed in the RVE. Detailed formulations for the fixed single smeared crack model can be found in the work of De Borst and Nauta (1985) and Rots et al. (1985), while detailed formulations for the fixed multi-directional and rotating crack approaches can be found in the studies of Gouveia et al. (2008), Pimanmas and Maekawa (2001), Jirásek and Zimmermann (1998), Jirásek and Zimmermann (1998), Ardebili et al. (2012),and Broujerdian and Kazemi (2010), to list a few. Next, the concept of the fixed single smeared crack model together with key formulations is introduced, as fixed multi-directional and rotating smeared crack approaches are also developed based on the same framework.

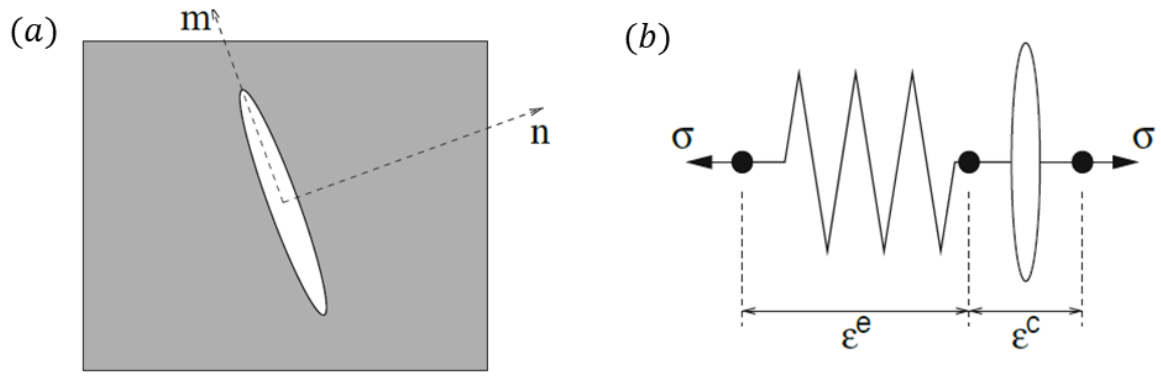

Figure 4.0–6. The concept of the smeared crack model: (a) A smeared crack band within the RVE; (b) Schematic representation of strain decomposition in smeared crack models (Jirásek 2011)

In the fixed single smeared crack model, the RVE is considered as an equivalent anisotropic continuum with degraded material properties in the direction normal to the crack orientation (Figure 4.0–6a). The crack orientation is kept fixed once the crack plane initiates. As the crack is represented continuously and no strong discontinuity is formed, remeshing is not needed. Similar to plasticity, the smeared crack model decomposes the total strain into an elastic part ($\dot{\boldsymbol{\varepsilon}}_{\mathrm{e}}$) and an inelastic part, which is specifically called the crack strain in smeared crack model ($\dot{\boldsymbol{\varepsilon}}_{\mathrm{c}}$):

$$\dot{\boldsymbol{\varepsilon}} = \dot{\boldsymbol{\varepsilon}}_{\mathrm{e}} + \dot{\boldsymbol{\varepsilon}}_{\mathrm{c}} \tag{4.13}$$

where the elastic strain follows the elastic Hook's law shown as:

$$\dot{\boldsymbol{\sigma}} = \boldsymbol{C}\dot{\boldsymbol{\varepsilon}}_{\mathrm{e}} = \boldsymbol{C}(\dot{\boldsymbol{\varepsilon}} - \dot{\boldsymbol{\varepsilon}}_{\mathrm{c}}) \tag{4.14}$$

It can be seen from Equations (4.13-4.14) that the final stress-strain relationship can be obtained once the crack strain is determined. The material is assumed to be homogeneous initially; therefore the crack strain vanishes and the overall material response is linear elastic. Once the crack is initiated when the stress state reaches the strength envelope, the crack strain develops within the smeared crack band. It is noted that the crack strain $\dot{\boldsymbol{\varepsilon}}_{\mathrm{c}}$ is defined in the global coordinate, which can be related to the local crack strain ($\dot{\boldsymbol{e}}_{\mathrm{c}}$) as:

$$\dot{\boldsymbol{\varepsilon}}_{\mathrm{c}} = \boldsymbol{N}\dot{\boldsymbol{e}}_{\mathrm{c}} \tag{4.15}$$

where $\boldsymbol{N}$ is a transformation matrix that reflects the orientation of the crack; $\dot{\boldsymbol{e}}_{\mathrm{c}} = [\dot{e}_c^n \quad \dot{e}_c^s]^T$ have two components for two-dimensional problems: normal crack strain $\dot{e}_c^n$ and shear crack strain $\dot{e}_c^s$. Similarly, the traction tensor across the crack in the local coordinate can be calculated from the stress tensor in the global coordinate using the same transformation matrix, as:

$$\dot{\boldsymbol{t}}_c = \boldsymbol{N}^{\boldsymbol{T}}\dot{\boldsymbol{\sigma}} \tag{4.16}$$

Instead of postulating a yield function and a flow rule, the inelastic strain due to crack opening is related directly to the traction transmitted across the fracture plane using a traction-strain relation. The general form of a traction-strain relation is expressed as:

$$\dot{\boldsymbol{t}}_c = \boldsymbol{D}_c\dot{\boldsymbol{e}}_{\mathrm{c}} \tag{4.17}$$

Using Equations (4.13-4.17), the final constitutive relation for a single crack model is:

$$\boldsymbol{C}\dot{\boldsymbol{\sigma}} = [\boldsymbol{C} - \boldsymbol{N}[\boldsymbol{D}_c + \boldsymbol{N}^{\boldsymbol{T}}\boldsymbol{C}\boldsymbol{N}]^{-\mathbf{1}}\boldsymbol{N}^{\boldsymbol{T}}\boldsymbol{C}]\dot{\boldsymbol{\varepsilon}} \tag{4.18}$$

The spurious mesh dependency on the structural load-deformation responses can be eliminated in smeared crack models by introducing the width of the localisation zone that is related to the adopted finite element size into the constitutive relation. The relation between the width of localisation zone and the mesh size is normally determined by trial-and-error fitting of experimental results. The width of the localisation zone can also be related to the orientation of the crack, the characteristics of the finite element interpolation functions or damage variables, depending on the choice of smeared crack approach.

Introduction of the width of the localisation zone can be achieved by incorporating a localisation limiter that imposes a certain size of the localisation zone into the overall stress-strain law as a material parameter (Bažant and Lin 1988, Strömberg and Ristinmaa 1996, Jirásek and Zimmermann 1998). Another approach introduces a length parameter called the equivalent element size into the traction-crack strain law in the local coordinate (Bažant and Oh 1983, Rots 1988, Oliver 1989). In that case, the slope of the curve representing inelastic softening behaviour can be adjusted based on the choice of the equivalent element size. In both cases, the mesh dependency occurring in traditional continuum models is overcome by artificially scaling the model parameters with the resolution of the discretisation so that the correct amount of energy dissipation can be reproduced (Burnett and Schreyer 2019). However, this artificial scaling can lead to questions about the physical meaning of the approach, as well as stability issues (snap-back) encountered when the resolution of the discretisation cannot be sufficiently small, especially in modelling large-scale problems (Jirásek and Bažant 1995). Furthermore, although smeared crack models can alleviate mesh size dependence, these models in the finite element framework suffer from mesh alignment sensitivity, which means that the orientation of the discretisation determines the orientation of the smeared crack (Rabczuk 2013). Some remedies, such as a transition from the rotating crack model to a scalar damage

model proposed by Jirásek and Zimmermann (1998), must be applied to avoid the mesh alignment sensitivity.

4.3.2. Strong discontinuity model

Unlike the smeared crack models in which an average stress-strain relation is specified based on the requirement for correct fracture energy dissipation within a smeared crack band of a certain thickness, the strong discontinuity models enrich the finite elements with additional degrees of freedom representing the displacement jump across a strong discontinuity, as depicted in Figure 4.0–7. The formulations of enrichment are development locally at the element level, thus keeping the number of degrees of freedom constant (Dias-da-Costa et al. 2010). Thanks to its efficiency in modelling of strain localisation problems, many approaches have been developed based on the strong discontinuity concept (Oliver 1996, Oliver et al. 1999, Dias-da-Costa et al. 2009, Dias-da-Costa et al. 2010, Dias‐da‐Costa et al. 2013, Bosco et al. 2015, Zhang and Zhuang 2018).

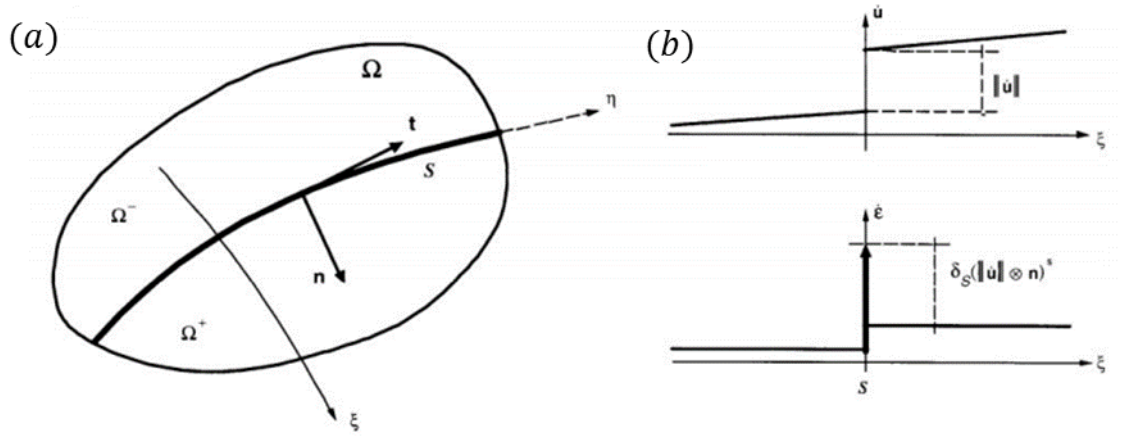

Figure 4.0–7. Basic idea of strong discontinuity models: (a) A strong discontinuity zone embedded in RVE; (b) The displacement jump across the strong discontinuity zone (Oliver et al. 1999).

The most general expression of a displacement field exhibiting strong discontinuities along a discontinuity path S can be written as:

$$\dot{\boldsymbol{u}}(\boldsymbol{x},t) = \dot{\bar{\boldsymbol{u}}}(\boldsymbol{x},t) + H_s(\boldsymbol{x})[\![\dot{\boldsymbol{u}}]\!](\boldsymbol{x},t) \tag{4.19}$$

where $\boldsymbol{x}$ and t denote the material coordinates and time respectively; $H_s(\boldsymbol{x})$ is the Heaviside function ($H_s(\boldsymbol{x}) = 1 \forall x \in \Omega^+$ and $H_s(\boldsymbol{x}) = 0 \forall x \in \Omega^-$); $\dot{\bar{\boldsymbol{u}}}(\boldsymbol{x},t)$ is the rate of the regular part

of the displacement field; $[\![\dot{\boldsymbol{u}}]\!](\boldsymbol{x},t)$ is the rate of a displacement jump function. The rate of the corresponding strain can be obtained through the rate of the displacement jump function as:

$$\dot{\boldsymbol{\varepsilon}}(\boldsymbol{x},t)=\nabla^{s}\dot{\boldsymbol{u}}=\underbrace{\nabla^{s}\dot{\bar{\boldsymbol{u}}}+H_{s}(\boldsymbol{x}\nabla^{s}[\![\dot{\boldsymbol{u}}]\!]}_{\dot{\bar{\boldsymbol{\varepsilon}}}}+\delta_{s}([\![\dot{\boldsymbol{u}}]\!]\otimes\boldsymbol{n})^{s}=\dot{\bar{\boldsymbol{\varepsilon}}}+\delta_{s}([\![\dot{\boldsymbol{u}}]\!]\otimes\boldsymbol{n})^{s} \tag{4.20}$$

where $\dot{\bar{\boldsymbol{\varepsilon}}}$ is the rate of the regular part of the strain field; δ_s is the Dirac line delta function along S satisfying:

$$\int_{\Omega}\ \delta_{s}\varphi_{0}\,d\Omega=\int_{s}\ \ \varphi_{0}d\Gamma\ \forall\ \varphi_{0}\in C_{0}^{\infty}(\Omega) \tag{4.21}$$

The concept of strong discontinuity can be applied to any standard constitutive model. To be more specific, the regular part of the strain field $\left(\dot{\bar{\boldsymbol{\varepsilon}}}\right)$ can be described by the standard constitutive models such as elastic damage models (Oliyer 1995, Oliver 1996, Oliver et al. 1999, Dias-da-Costa et al. 2009, Dias-da-Costa et al. 2010) and elastoplastic models (Oliver 1996, Feist and Hofstetter 2006), while the local displacement jump ($[\![\dot{\boldsymbol{u}}]\!]$) across a discontinuity that is disconnected from the bulk continuum behaviour is calculated through a local formulation at the element level. To ensure that the constitutive equations of these models successfully embed the unbound strain field in Equation (4.20), three conditions must be imposed. The first is stress boundedness, which means that the stress field is bounded everywhere in Ω. The second condition is traction vector continuity, which means that the traction vector is continuous across the discontinuity surface S all the time. The traction vector continuity can be obtained from the balance laws or from equilibrium conditions across the discontinuity surface expressed as:

$$\dot{\boldsymbol{\sigma}}_{\Omega\backslash s}\big|_{x\in S}\cdot\boldsymbol{n}=\dot{\boldsymbol{\sigma}}_{s}\cdot\boldsymbol{n} \tag{4.22}$$

The third condition is identification of the normal, which means that the normal vector $\boldsymbol{n}$ of the discontinuity surface S is provided by the stress field when the discontinuity initiates under a certain condition.

The strong discontinuity approach introduces a kinetic state of strong discontinuity characterised by a discontinuous displacement field across a discontinuity surface with the constitutive relation, without requiring additional degrees of freedom. Thus it can capture the propagation process of cracks and mechanical responses of rock materials efficiently. This enrichment, together with a standard continuum constitutive model, also enable the strong discontinuity approach to capture both the deformation due to opening/shearing across a

discontinuity and the shrinking of the elastic bulk. Importantly, the concept of a regularised softening parameter is incorporated in the constitutive relations to solve the problem of infinite strains and Dirac-delta functions. This softening parameter, which is made dependent on a length scale parameter, helps to avoid mesh-size and mesh-alignment dependencies and stress locking issues (Oliver 1996, Dias-da-Costa et al. 2010, Zhang and Zhuang 2018). However, this model requires the finite element mesh to be finer than the physical width of the localisation zone (Sluys and Berends 1998). Therefore, very fine meshes are required to obtained an accurate strain profile within the discontinuity.

4.3.3. Double-scale constitutive framework

The double-scale model was originally developed by Nguyen et al. (2012), Nguyen et al. (2014) for modelling strain localisation problems. This model was then extended to predict the onset and orientation of localisation bands (Le et al. 2018, Le et al. 2019, Le et al. 2020), Lode-angle dependence of geomaterial (Le et al. 2020) and the size-dependent behaviour of soils (Nguyen et al. 2016, Phan et al. 2017). Unlike traditional constitutive models, which are defined over a unit volume where deformation is assumed homogeneous, the double-scale model is formulated over a volume element comprising two different regions (a localised zone and surrounding bulk) for describing the high strain deformation within a localised zone as shown in Figure 4.0–8a. Figure 4.0–10b shows the general stress-strain responses of the material inside and outside the localised zone in the double-scale model. The material is initially treated in a classical way using a classical continuum constitutive model when localised failure is detected, e.g. via the loss of positive definiteness of the determinant of the acoustic tensor. After that, the material behaviour inside and outside the localised zone is distinct, following different constitutive laws. The interaction between the inside and outside materials is then linked by a traction continuity condition across the localised zone, resulting in the averaged macroscopic stress-strain relation of the RVE that represents the combined behaviour of the localised and outside bulk materials. The details of derivation of this model are as follows.

First, definition of total strain rate tensor $\dot{\boldsymbol{\varepsilon}}$ across the volume element is required. As the volume element is viewed as an elastic bulk crossed by a localised zone, the total strain rate is contributed by both parts. Using mixed theory, the volume averaged total strain rate tensor can be expressed as:

$$\dot{\boldsymbol{\varepsilon}} = \eta \dot{\boldsymbol{\varepsilon}}_{\mathrm{in}} + (1-\eta)\dot{\boldsymbol{\varepsilon}}_{\mathrm{out}} \tag{4.23}$$

where $\dot{\boldsymbol{\varepsilon}}_{\text{out}}$ and $\dot{\boldsymbol{\varepsilon}}_{\text{in}}$ represent the strain rate tensors outside and inside the localised zone respectively; and $\eta = \Omega_i/\Omega = h/H$ is the volume fraction of the localised zone. Given the localised zone is very thin but finite, the strain rate tensor in it can be described as (Vardoulakis et al. 1978, Kolymbas 2009):

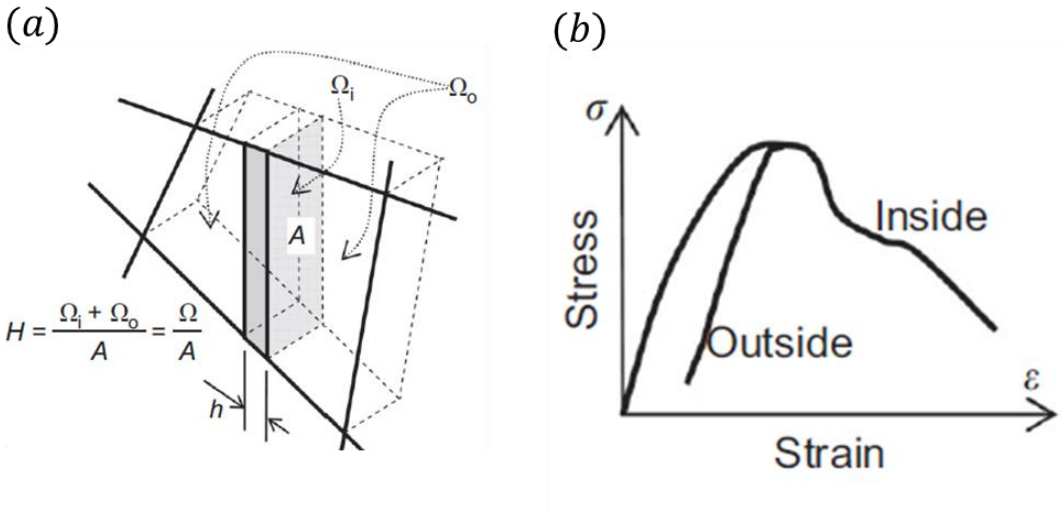

Figure 4.0–8. Double-scale model: (a) Numerical discretisation and localisation zone; (b) Material responses inside and outside the localisation zone

$$\dot{\boldsymbol{\varepsilon}}_{\text{in}} \approx \frac{1}{h}(\boldsymbol{n} \otimes [\![\dot{\boldsymbol{u}}]\!])^{sym} \tag{4.24}$$

where n is the normal vector of the localised zone and $[\![\dot{\boldsymbol{u}}]\!]$ denotes the relative velocity jump between opposite sides of the localization band.

The inelastic behaviour inside the localisation zone and elastic behaviour outside the localisation zone can be respectively written as:

$$\dot{\boldsymbol{\sigma}}_{\text{in}} = \boldsymbol{a}_{\text{i}}^{T} : \dot{\boldsymbol{\varepsilon}}_{\text{i}} \tag{4.25}$$

$$\dot{\boldsymbol{\sigma}}_{\text{out}} = \boldsymbol{a}_{o} : \dot{\boldsymbol{\varepsilon}}_{\text{out}} \tag{4.26}$$

where $\boldsymbol{a}_{\text{i}}^{T}$ is the tangent stiffness, and $\boldsymbol{a}_{o}$ is the elastic tangent stiffness.

The inside and outside material are connected through the continuity of traction across the boundary of the localisation band:

$$(\dot{\boldsymbol{\sigma}}_{\text{out}} - \dot{\boldsymbol{\sigma}}_{\text{in}}) \cdot \mathbf{n} = 0 \tag{4.27}$$

Combining equations (4.23-4.26), the traction continuity expressed in Equation (4.29) can be rewritten as:

$$\frac{1}{1-\eta}\boldsymbol{a}_o:\left(\dot{\boldsymbol{\varepsilon}}-\frac{\eta}{h}(\boldsymbol{n}\otimes[\![\dot{\boldsymbol{u}}]\!])^{sym}\right)\cdot\mathbf{n}=(\boldsymbol{a}_{\mathrm{i}}^{T}:\frac{1}{h}(\boldsymbol{n}\otimes[\![\dot{\boldsymbol{u}}]\!])^{sym})\cdot\mathbf{n} \tag{4.28}$$

Rearranging the above equation leads to:

$$(\boldsymbol{a}_o:\dot{\boldsymbol{\varepsilon}})\cdot\mathbf{n}=(\frac{1}{H}\boldsymbol{A}_0+\frac{(1-\eta)}{h}\boldsymbol{A}_{\mathrm{i}}^{T})\cdot[\![\dot{\boldsymbol{u}}]\!] \tag{4.29}$$

where $\boldsymbol{A}_{\mathrm{i}}^{T}=\mathbf{n}\cdot\boldsymbol{a}_{\mathrm{i}}^{T}\cdot\mathbf{n}$ and $\boldsymbol{A}_0=\mathbf{n}\cdot\boldsymbol{a}_o\cdot\mathbf{n}$ are the acoustic tensors controlling the behaviour of material inside and outside the localisation band respectively. Therefore, the rate of displacement jump $[\![\dot{\boldsymbol{u}}]\!]$ can be calculated from the input strain rate as:

$$[\![\dot{\boldsymbol{u}}]\!]=(\frac{1}{H}\boldsymbol{A}_0+\frac{(1-\eta)}{h}\boldsymbol{A}_{\mathrm{i}}^{T})^{-1}\cdot(\boldsymbol{a}_o:\dot{\boldsymbol{\varepsilon}})\cdot\mathbf{n}=\mathbf{C}^{-1}\cdot(\boldsymbol{a}_o:\dot{\boldsymbol{\varepsilon}})\cdot\mathbf{n} \tag{4.30}$$

The final constitutive relation can be derived by combining Equations (4.30) and (4.24):

$$\dot{\boldsymbol{\sigma}}=\frac{1}{1-\eta}\boldsymbol{a}_o:\left[\dot{\boldsymbol{\varepsilon}}-\frac{1}{H}\left(\boldsymbol{n}\otimes(\mathbf{C}^{-1}\cdot(\boldsymbol{a}_o:\dot{\boldsymbol{\varepsilon}})\cdot\mathbf{n})\right)\right] \tag{4.31}$$

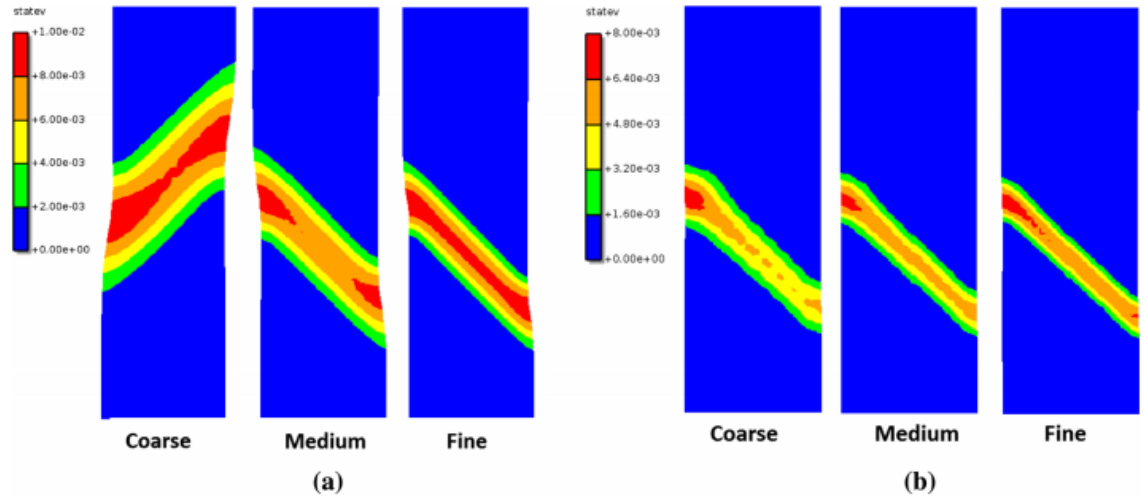

Figure 4.0–9. The development of shear bands in two-dimensional tension tests: (a) using the classical approach;(b) using double-scale model (Nguyen et al. 2016).

Figure 4.0–9 shows the numerical result of the shear bands in two-dimensional tension tests using a double-scale approach in comparsion with the result using a classical approach. Three spatial discretisation sizes were adopted to examine the mesh sensitivity of both approaches. It can be seen from Figure 4.0–9 that the double-scale model correctly captures the shear failure

thanks to the anisotropy introduced by the oriented localisation zone and the use of coupled stresses inside and outside the localisation zone. Furthermore, the double-scale approach considers the relative size of the localisation zone and the surrounding bulk, leading to a length parameter embedded in the final constitutive model. Therefore, the numerical solution using this approach does not suffer from any of the mesh dependency issues occurring in the classical approach.

4.4. Summary of existing constitutive models

Simple models, such as the elastoplastic models, elastic damage models and coupled elastoplastic damage models, can provide satisfactory numerical solutions in specific cases, but they fail to capture both irreversible deformation and stiffness degradation, which are key features of the macroscopic behaviour of rocks. To solve this problem, new pure continuum models formed by coupling elastoplastic with damage models were proposed. While they worked well for some applications, the deformation in these models is assumed homogeneous over a unit volume, thereby neglecting the existence of the high gradient of deformation across the localisation band during the nonlinear phases of rock fractures. Therefore, the accuracy of those models in capturing the post-localisation behaviour and size effects due to localisation beyond the onset of localised failure is still questionable. In addition, the models fail to account for the relative size between the fracture process zone and surrounding bulk together with some characteristics of the fracture process zone such as fracture orientation and evolution of inelastic behaviour. Therefore, those models suffer from the mesh dependency issues of the numerical solutions.

To resolve those issues, some enhancements have been employed at the constitutive level by introducing an internal length that acts as a localisation limiter into constitutive equations such as the smeared crack model, strong discontinuity approach and double-scale framework. The smeared crack model is a continuum approach in which crack bands are smeared over a certain thickness within the finite element. To characterise the behaviour of smeared crack bands, the crack strain is linked to the displacement jump in the local coordinate and some length parameter over which this displacement jump is distributed. The introduction of such characteristic length allows modelling of cracks without suffering from any mesh dependency. While the smeared crack model works well for some applications, this model experiences mesh alignment sensitivity and snap-back instability when a coarse mesh is used. With a different line of approach to capture localised failures, the strong discontinuity approach based on discretisation-based enhancements does not require the extra global degree of freedom for

capturing localisation behaviour, due to its local enhancement of the extra strain field. However, the strong discontinuity approach requires the finite element mesh to be finer than the physical width of localisation. Since the thickness of the localisation zone for rock fracture problems is very small, a very high resolution of discretisation is required in such models, making the analysis computationally expensive. The last constitutive approach reviewed in this chapter is the double-scale approach, in which the constitutive relation is developed based on a thermodynamics framework with the employment of an additional kinematic and a corresponding length scale to describe the localised failure of materials. The material behaviour of both the localisation zone and the surrounding bulk, as well as the relative sizes, are considered. Therefore, the double-scale approach can capture size-dependent behaviour naturally without suffering from mesh dependency. More importantly, the approach is formulated in a very generic form, which allows any suitable law to be incorporated for the behaviour of the localisation band. Furthermore, this approach also can be applied easily to any continuum-based numerical framework. Based on these advantages, the double-scale approach is adopted in this study as the basis of the proposed model for rock fracture analysis. Three key further improvements are needed for the development of a reliable and robust constitutive model that includes both intrinsic spatial and temporal scales. First, a new size-dependent constitutive model with an embedded mode I cohesive facture law is developed for modelling fracture behaviour and its size dependency of rocks under pure mode I loading conditions. The concept and detailed formulations of the size dependent constitutive model for rocks are introduced in Section 4.5 and the implementation in rock fracture applications is presented in Chapter 5. The size dependent constitutive model presented in Chapter 6 is further developed by incorporating a mixed-mode cohesive fracture law in order to describe mixed-mode failure of the fracture process zone. Finally, the rate effect is incorporated in the mixed-mode continuum constitutive model for dynamic rock fracture analysis, which is introduced in Chapter 7.

4.5. A new continuum constitutive model with embedded mode I cohesive fracture law for rocks

4.5.1. Model formulation

The idea of the continuum constitutive model is presented in Figure 4.0–10. The unit volume is crossed by a very thin fracture process zone with the width of h. In this figure, H is the representative size of the volume element (Ω), defined as $H = \Omega/A$, with A being the fracture

surface and $\boldsymbol{n}$ the vector normal to the fracture plane. Once fracture is triggered, that is, when the fracture criterion is met, the behaviour of the RVE is bifurcated into two different parts: the material inside the fracture process zone undergoes inelastic deformation governed by a cohesive fracture law while that outside the fracture process zone (i.e. bulk materials) unloads and, for rock fracture modelling, can be reasonably assumed to be elastic.

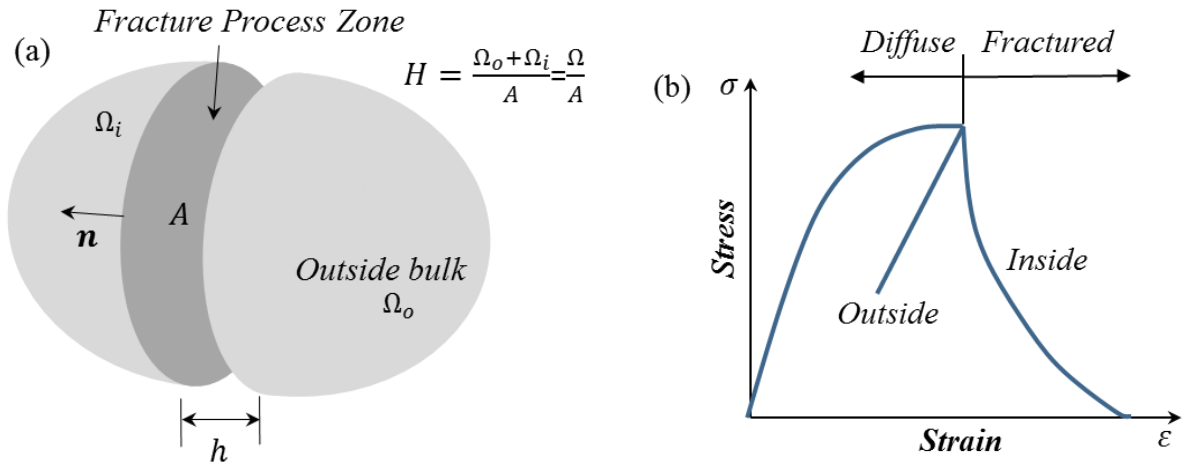

Figure 4.0–10. A size-dependent constitutive model: (a) Fracture process zone surrounded by an elastic bulk; (b) Corresponding stress-strain responses inside and outside the fracture process zone.

Similar to the double-scale model, the total strain rate comprises strains inside and outside the fracture process zone, expressed as:

$$\dot{\boldsymbol{\varepsilon}} = \eta \dot{\boldsymbol{\varepsilon}}_{\text{in}} + (1-\eta)\dot{\boldsymbol{\varepsilon}}_{\text{out}} \tag{4.32}$$

where the strain rate tensor inside the fracture zone is described as:

$$\dot{\boldsymbol{\varepsilon}}_{\text{in}} \approx \frac{1}{h}(\boldsymbol{n} \otimes [\![\dot{\boldsymbol{u}}]\!])^{sym} \tag{4.33}$$

where $\boldsymbol{n}$ is the normal vector of the fracture zone and $[\![\dot{\boldsymbol{u}}]\!]$ denotes the relative velocity jump across the fracture zone, which can be written in the three-dimensional case as follows:

$$\boldsymbol{n} = [n_x \quad n_y \quad n_z]^T, \quad [\![\dot{\boldsymbol{u}}]\!] = [\dot{u}_x \quad \dot{u}_y \quad \dot{u}_z]^T \tag{4.34}$$

with n_x, n_y and n_z being the cosines of the unit vector of the normal vector in the global coordinate system. The normal vector is calculated based on the maximum principal stress and remains unchanged once fracture is triggered. Inclusion of the normal vector in the constitutive model enables the model to capture anisotropy due to the appearance of fracture.

By applying the Hill-Mandel condition (Hill, 1963), which states that the virtual work produced by the averaged stress and its corresponding averaged strain is equal to the volume-averaged work produced by stresses and strains inside and outside of the fracture process zone, we have:

$$\boldsymbol{\sigma}: \dot{\boldsymbol{\varepsilon}} = (1-\eta)\boldsymbol{\sigma}_{\text{out}}: \dot{\boldsymbol{\varepsilon}}_{\text{out}} + \eta\boldsymbol{\sigma}_{\text{in}}: \dot{\boldsymbol{\varepsilon}}_{\text{in}} \tag{4.35}$$

where $\boldsymbol{\sigma}$ is the averaged macrosopic stress; $\boldsymbol{\sigma}_{\text{out}}$ and $\boldsymbol{\sigma}_{\text{in}}$ denote the stresses inside and outside of the fracture zone. By substituting Equations (4.32-4.33) into Equation (4.35), the following equation can be obtained after some rearrangement:

$$\frac{\eta}{h}(\boldsymbol{\sigma}\cdot\boldsymbol{n} - \boldsymbol{t}_{\text{in}}) \cdot [\![\dot{\boldsymbol{u}}]\!] + (1-\eta)(\boldsymbol{\sigma} - \boldsymbol{\sigma}_{\text{out}}) : \dot{\boldsymbol{\varepsilon}}_{\text{out}} = 0 \tag{4.36}$$

where $\boldsymbol{t}_{in} = \boldsymbol{\sigma}_{in}\cdot\boldsymbol{n}$ is the traction generated by the stress inside the fracture process zone. The above condition needs to be satisfied for any values of the velocity jump and strain rate, leading to:

$$\boldsymbol{t}_{\text{in}} = \boldsymbol{\sigma}\cdot\boldsymbol{n} \qquad \text{and} \qquad \boldsymbol{\sigma} = \boldsymbol{\sigma}_{\text{out}} \tag{4.37}$$

It can be seen from the above equation that the averaged macroscopic stress coincides with the stress outside the fracture process zone. Assuming an elastic response of the bulk material outside the fracture process zone, $\dot{\boldsymbol{\sigma}}_{\text{out}} = \boldsymbol{a}_o : \dot{\boldsymbol{\varepsilon}}_{\text{out}}$, where $\boldsymbol{a}_o$ denotes the elastic tangent stiffness, and combining Equations (4.32-4.33) and (4.37), the following macroscopic stress can be derived:

$$\dot{\boldsymbol{\sigma}} = \dot{\boldsymbol{\sigma}}_{\text{out}} = \frac{1}{(1-\eta)}\boldsymbol{a}_o : \left(\dot{\boldsymbol{\varepsilon}} - \frac{\eta}{h}(\boldsymbol{n}\otimes[\![\dot{\boldsymbol{u}}]\!])^{sym}\right) \tag{4.38}$$

For rock fracturing problems, the fracture process zone can be viewed as a fracture plane in 3D and a fracture line in 2D whose thickness is very small ($h \to 0$). In such cases, $\eta \approx 0$ and the above macroscopic stress-strain relation can be further simplified to:

$$\dot{\boldsymbol{\sigma}} = \dot{\boldsymbol{\sigma}}_{\text{out}} = \boldsymbol{a}_o : \left(\dot{\boldsymbol{\varepsilon}} - \frac{1}{H}(\boldsymbol{n}\otimes[\![\dot{\boldsymbol{u}}]\!])^{sym}\right) \tag{4.39}$$

To complete the above macroscopic stress-strain relation, one needs to define the constitutive relationship across the fracture plane that involves velocity jump $[\![\dot{\boldsymbol{u}}]\!]$ and traction rate $\dot{\boldsymbol{t}}_{in}$. This can be achieved by adopting any existing cohesive fracture law that relates tractions and displacement jumps across the fracture plane. In this work, two types of cohesive fracture law (i.e. linear or exponential cohesive fracture laws) are investigated and the general form of these models can be written as follows:

$$\dot{\boldsymbol{t}}_{\text{in}} = \boldsymbol{K}\cdot[\![\dot{\boldsymbol{u}}]\!] \tag{4.40}$$

where $\boldsymbol{K}$ is the tangent stiffness of the cohesive fracture zone written in the global coordinate system.

Using Equation (4.37), $\boldsymbol{t}_{\text{in}} = \boldsymbol{\sigma} \cdot \boldsymbol{n}$, for continuity of traction across the boundary of the fracture process zone, and the constitutive relationships (4.39) and (4.40), we have:

$$\boldsymbol{K} \cdot [\![\dot{\boldsymbol{u}}]\!] = \dot{\boldsymbol{\sigma}} \cdot \boldsymbol{n} = \boldsymbol{a}_o : \left(\dot{\boldsymbol{\varepsilon}} - \frac{1}{H} (\boldsymbol{n} \otimes [\![\dot{\boldsymbol{u}}]\!])^{sym} \right) \cdot \boldsymbol{n} \tag{4.41}$$

From this equation, the velocity jump across the fracture plane can be obtained as:

$$[\![\dot{\boldsymbol{u}}]\!] = \left[\frac{1}{H} (\boldsymbol{n} \cdot \boldsymbol{a}_o \cdot \boldsymbol{n}) + \boldsymbol{K} \right]^{-1} \cdot (\boldsymbol{a}_o : \dot{\boldsymbol{\varepsilon}}) \cdot \boldsymbol{n} = \boldsymbol{C}^{-1} \cdot (\boldsymbol{a}_o : \dot{\boldsymbol{\varepsilon}}) \cdot \boldsymbol{n} \tag{4.42}$$

Finally, by substituting Equation (4.42) into Eq. (4.39), the following macroscopic stress-strain relation can be obtained:

$$\dot{\boldsymbol{\sigma}} = \boldsymbol{a}_o : \left(\dot{\boldsymbol{\varepsilon}} - \frac{1}{H} [\boldsymbol{n} \otimes (\boldsymbol{C}^{-1} \cdot (\boldsymbol{a}_o : \dot{\boldsymbol{\varepsilon}}) \cdot \boldsymbol{n})]^{sym} \right) \tag{4.43}$$

We noted that the above macro stress-strain formulation, which is the simplified version of the more generic stress-strain relation described in Equation (4.43), shares some similarities in the general form of the expression with that proposed by Pietruszczak and Mroz (1981), Pietruszczak and Niu (1993), Pietruszczak and Xu (1995), Haghighat and Pietruszczak (2015), Pietruszczak and Haghighat (2015). However, in this work, which is derived from a double-scale constitutive framework (Nguyen et al. 2012, Nguyen et al. 2014, Nguyen et al. 2016), the static constraint (4.37) appears naturally as a consequence of the work balance Equation (4.36) and the kinematic enrichments (4.32-4.33). In other words, supplying the enrichment based on the observed mechanisms of localised failure followed by the application of the work balance, Equation (4.35) naturally leads to other static conditions to complete the model descriptions. This systematic approach is advocated, as it can naturally result in homogenised constitutive equations involving the responses and sizes of all phases, not only in the context of localised failure (Nguyen et al. 2016) but also in the context of homogenisation and nonlinear constitutive modelling of multi-phase materials (Vu et al. 2017). In addition, the similarities in enriching the kinematics of constitutive descriptions (this work, and that by Pietruszczak and co-authors referred to above) or discretization schemes (such as the enhanced strain by Larsson et al. (1996), Oliver (1996), Borja (2000)) and eXtended Finite Elements by Wells and Sluys (2001), Samaniego and Belytschko (2005), Sanborn and Prévost (2011)), are very common in most (if not all) enhancements to deal with localised failure. However, the constitutive

enrichments are independent of the discretisation and hence can be readily applied to mesh-free numerical approaches like the SPH used in this study.

Thus far, the constitutive model has been described in the global coordinate system, which defines the full macroscopic averaged stress and strain tensors of the volume element, including the cohesive law described the relationship between $\dot{\boldsymbol{t}}_{\text{in}}$ and $[\![\dot{\boldsymbol{u}}]\!]$ in Equation (4.40). To obtain the explicit form of the cohesive law in the global coordinate system, it is necessary to specify the corresponding cohesive law in the local coordinate system (i.e. across the fracture plane). In this work, the cohesive law in the local coordinate system is defined as:

$$\dot{\boldsymbol{t}}_{cr} = \boldsymbol{K}_{cr}[\![\dot{\boldsymbol{u}}]\!]_{cr} \tag{4.44}$$

where the subscript *cr* denotes quantities that are defined in the local coordinate system. The local tangent stiffness ($\boldsymbol{K}_{cr}$) can be obtained by rotating the global stiffness ($\boldsymbol{K}$) to the local coordinate system and vice-versa, using the equation:

$$\boldsymbol{K} = \boldsymbol{R}^T \boldsymbol{K}_{cr} \boldsymbol{R} \tag{4.45}$$

where $\boldsymbol{R}$ is the rotational matrix from the global to local coordinate systems, defined as:

$$\boldsymbol{R} = \begin{bmatrix} n_x & n_y & n_z \\ m_x & m_y & m_z \\ l_x & l_y & l_z \end{bmatrix} \tag{4.46}$$

with n_i, m_i and l_i ("i" stands for x, y, z) being cosines of the unit normal vectors in the global coordinate system, respectively.

As discussed, any existing cohesive fracture law can be incorporated in the current constitutive model, i.e. via Equation (4.44). For the purpose of simplifying the numerical development as the first step to demonstrating the proposed SPH framework with embedded cohesive fracture, only mode-I cohesive fracture is considered in this study. Nevertheless, mixed-mode cohesive fracture laws such as those recently developed by (Gui et al. 2015, Nguyen et al. 2017, Nguyen et al. 2017) can be incorporated into the current proposed framework. The incorporation of these generic fracture laws makes the framework possible for modelling more complex fracture problems accounting for both tensile and shear cracks, volumetric dilatancy in compression regime and multiple fractures.

For pure mode-I loading, fracture is mainly governed by two rock properties: fracture toughness (G_f) and initial tensile strength (σ_{t0}). A yield criterion is required to determine

whether the material is elastic or inelastic and to calculate the evolution of traction during loading or unloading, as follows:

$$y = t_{cr1} - \sigma_t \tag{4.47}$$

where t_{cr1} is the normal traction in the local coordinate and σ_t is the tensile strength of the cohesive fracture law. The normal traction-separation can be modelled using either the linear or exponential cohesive fracture law, as shown in Figure 4.0–11.

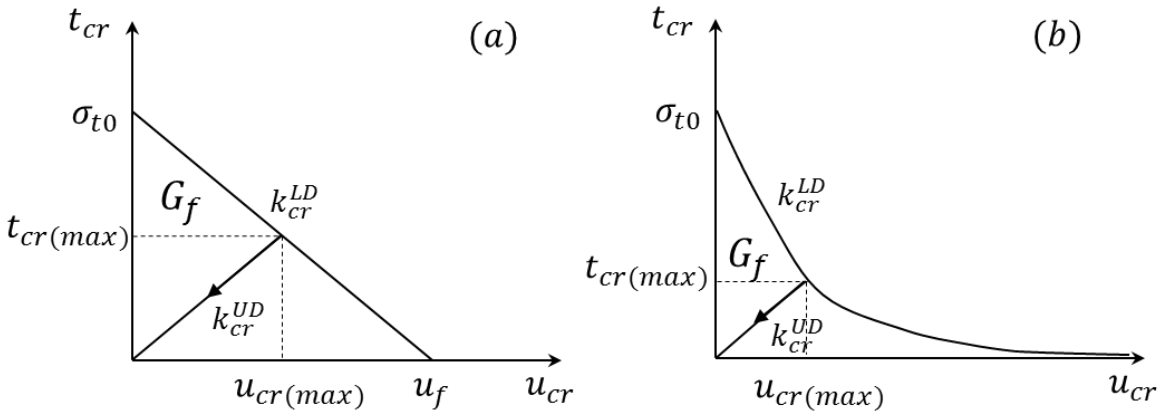

Figure 4.0–11. Concept of cohesive fracture law: (a) linear; (b) exponential.

In the linear cohesive fracture law (Figure 4.0–11a), the loading tangent stiffness k_{cr}^{LD} and ultimate cracking opening (u_{cr}^{f}) are linked through the equation:

$$k_{cr}^{LD} = -\frac{\sigma_{t0}}{u_{cr}^{f}} \quad \text{and} \quad u_{cr}^{f} = \frac{2G_f}{\sigma_{t0}} \tag{4.48}$$

For the exponential cohesive fracture law (Figure 4.0–11b), the ultimate crack opening (u_{cr}^{f}) is infinite and the loading tangent stiffness k_{cr}^{LD} is an exponential function of the displacement jump, as:

$$k_{cr}^{LD} = -\frac{{\sigma_{t0}}^2}{G_f}\exp\left(-\frac{\sigma_{t0}}{G_f}u_{cr}\right) \tag{4.49}$$

Accordingly, during the inelastic loading stage, the local tangent stiffness matrix is defined as:

$$\boldsymbol{K}_{cr}^{LD} = \begin{bmatrix} k_{cr}^{LD} & 0 & 0 \\ 0 & 0 & 0 \\ 0 & 0 & 0 \end{bmatrix} \tag{4.50}$$

On the other hand, for the unloading stage, the local tangent stiffness matrix takes the form:

$$\boldsymbol{K}_{cr}^{UD} = \begin{bmatrix} \frac{t_{cr}^{max}}{u_{cr}^{max}} & 0 & 0 \\ 0 & 0 & 0 \\ 0 & 0 & 0 \end{bmatrix} \tag{4.51}$$

where u_{cr}^{max} is the maximum displacement jump at the point of unloading and t_{cr}^{max} is the corresponding traction (see Figure 4.0–11 for illustration).

As the fracture develops, the tensile strength gradually degrades to zero. This can be achieved by adopting the following traction laws for the linear and exponential cases, respectively:

Linear: $$\sigma_t = \sigma_{t0}(1 - \frac{u_{cr}}{u_{cr}^f}) \tag{4.52a}$$

Exponential: $$\sigma_t = \sigma_{t0} exp(-\frac{\sigma_{t0}}{G_f} u_{cr}) \tag{4.52b}$$

Finally, to visualize the evolution of damage, the following damage variable is defined:

$$D = 1 - \frac{\sigma_t}{\sigma_{t0}} \tag{4.53}$$

The numerical implementation of the proposed continuum constitutive model with an embedded cohesive fracture zone is presented in **Algorithm 4.1**.

Algorithm 4.1: Explicit stress update input $\Delta\boldsymbol{\varepsilon}$, output $\Delta\boldsymbol{\sigma}$ (matrix-vector form)

1. Calculate trial stress: $\boldsymbol{\sigma}_{trial}^{n+1} = \boldsymbol{\sigma}^n + \Delta\boldsymbol{\sigma}^{tiral} = \boldsymbol{\sigma}^n + \boldsymbol{a}_0\Delta\boldsymbol{\varepsilon}$
2. If $D = 0$: un-cracked state
3. Calculate normal vector $\boldsymbol{n}$ and rotation matrix $\boldsymbol{R}$
4. Calculate trial tractions in the local coordinate: $\boldsymbol{t}_{\boldsymbol{cr}(\boldsymbol{trial})}^{\boldsymbol{n+1}} = \boldsymbol{R}\boldsymbol{n}^T\boldsymbol{\sigma}_{trial}^{n+1}$
5. If $y > 0$: inelastic loading
6. Calculate $\boldsymbol{C}$: $\boldsymbol{C} = \frac{1}{H}\boldsymbol{n}^T\boldsymbol{a}_0\boldsymbol{n} + \boldsymbol{R}^T\boldsymbol{K}_{cr}^{LD}\boldsymbol{R}$
7. Go to line 19
8. End
9. Else: elastic loading
10. Update final stress increment: $\Delta\boldsymbol{\sigma} = \Delta\boldsymbol{\sigma}^{tiral}$
11. Endif
12. Elseif $D \neq 0$: crack occurs
13. Calculate trial tractions in the local coordinate: $\boldsymbol{t}_{\boldsymbol{cr}(\boldsymbol{trial})}^{\boldsymbol{n+1}} = \boldsymbol{R}\boldsymbol{n}^T\boldsymbol{\sigma}_{trial}^{n+1}$
14. If $y < 0$: elastic unloading

15. Calculate $\boldsymbol{C}$: $\boldsymbol{C} = \frac{1}{H}\boldsymbol{n}^T\boldsymbol{a}_0\boldsymbol{n} + \boldsymbol{R}^T\boldsymbol{K}_{cr}^{UD}\boldsymbol{R}$

16. Else: inelastic loading

17. Calculate $\boldsymbol{C}$: $\boldsymbol{C} = \frac{1}{H}\boldsymbol{n}^T\boldsymbol{a}_0\boldsymbol{n} + \boldsymbol{R}^T\boldsymbol{K}_{cr}^{LD}\boldsymbol{R}$

18. Endif

19. Calculate the increment of displacement jump in the global coordinate:

$$\Delta\boldsymbol{u} = \boldsymbol{C}^{-1}\boldsymbol{n}^T\boldsymbol{a}_0\Delta\boldsymbol{\varepsilon}$$

20. Calculate the increment of displacement jump in the local coordinate:

$$\Delta\boldsymbol{u}_{cr} = \boldsymbol{R}\Delta\boldsymbol{u}$$

21. Update the local displacement: $\boldsymbol{u}_{cr}^{n+1} = \boldsymbol{u}_{cr}^{n} + \Delta\boldsymbol{u}_{cr}$

22. Update the tensile strength and damage variable:

$$\sigma_t = \sigma_{t0}(1 - u_{cr}^{n+1}/u_{cr}^{f}) \quad \text{or} \quad \sigma_t = \sigma_{t0}exp(-\frac{\sigma_{t0}}{G_f}u_{cr}^{n+1})$$

$$D^{n+1} = 1 - \sigma_t/\sigma_{t0}$$

23. Calculate final stress increment: $\Delta\boldsymbol{\sigma} = \boldsymbol{a}_0(\Delta\boldsymbol{\varepsilon} - \frac{1}{H}\boldsymbol{n}\Delta\boldsymbol{u})$

24. Endif

4.5.2. Constitutive model behaviour

In this section, the behaviour of the proposed continuum constitutive model with embedded cohesive fracture laws (i.e. linear and exponential) at the element level is examined by comparing model responses against analytical solutions. In the tests, a constant strain increment of 10^{-5} is imposed on a RVE to provide tensile loading and the characteristic length (H) is varied to investigate its effect on the model response. The material properties are: Young's modulus $E = 45$ GPa, tensile strength $f_t = 2.9$ MPa, and fracture energy $G_f = 47.17$ Nm/m^2. In this pure mode-I case, it is straightforward to see that the local traction and global traction coincide.

The responses of the proposed constitutive model with embedded linear and exponential cohesive fracture laws are illustrated in Figure 4.0–12 and Figure 4.0–13, respectively. For each case, the macroscopic averaged stress-strain relationship, local traction-displacement curve, and responses of tensile strength and damage variable with displacement jump are plotted in (a)–(d), respectively, together with analytical solutions. The macro-constitutive behaviour under loading cases (Figure 4.0–12a & Figure 4.0–13a) can be divided into two phases: linearity and then bifurcation. During the first stage, the macro-averaged stress

increases linearly with the corresponding strain and its response is controlled only by Young's modulus (E) for the one-dimensional case. The local tractions (Figure 4.0–12b & Figure 4.0–13b) also increase with the macro-averaged stresses while the displacement jumps remain zero, suggesting that the fracture has not yet been detected. Meanwhile, the tensile strength and damage variable remain unchanged.

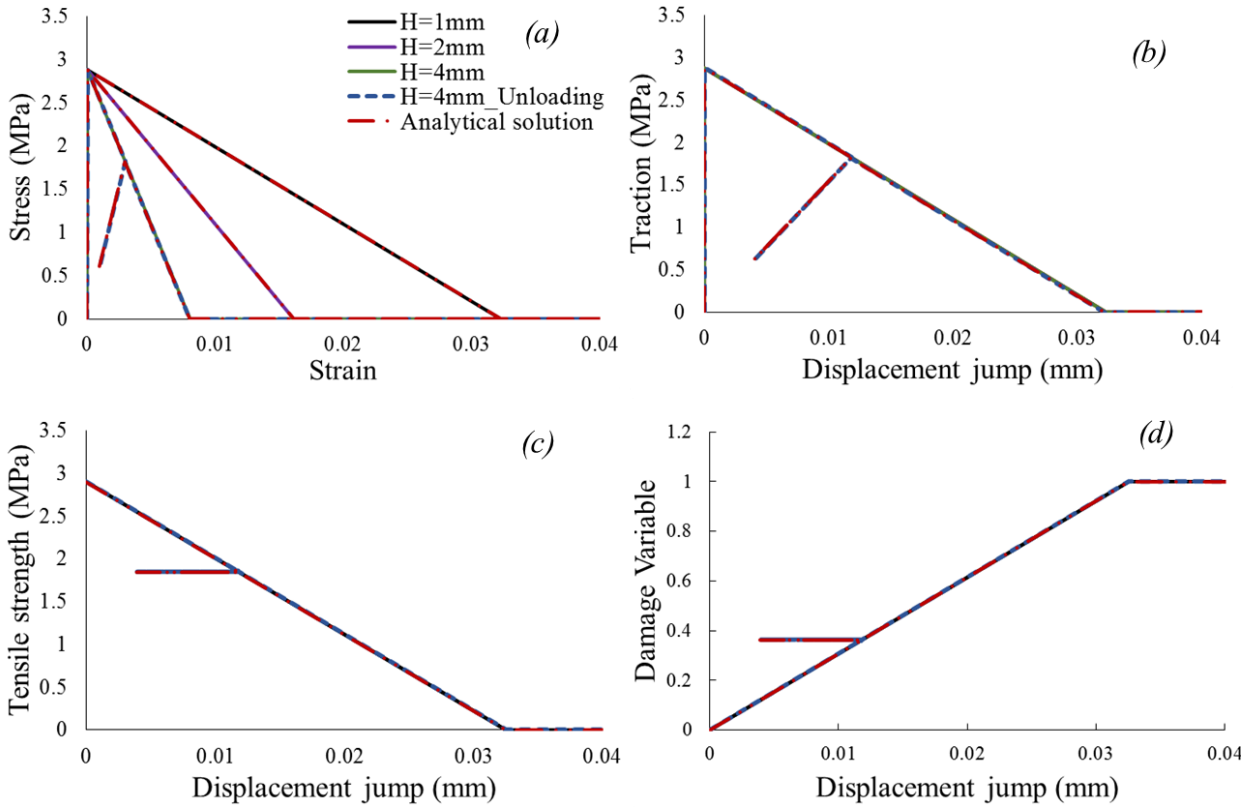

Figure 4.0–12. Constitutive model with embedded linear cohesive fracture law: (a) average stress-strain relationship; (b) traction-displacement curve; (c) tensile strength-displacement jump curve; (d) damage variable-displacement curve.

In the second stage, where the fracture (or bifurcation) is initiated, the macro-averaged stresses in both cases (i.e. the linear and exponential cohesive laws) decrease with the loading, indicating that the material undergoes softening behaviour which is controlled by the fracture energy (G_f), tensile strength (σ_t) and characteristic length (H). With variation of the characteristic length (H), the macro-averaged stress-strain curves of the proposed model also change, as illustrated in Figure 4.0–12(a) and Figure 4.0–13(a). This suggests that the proposed model scales with the size of the volume element and thus can capture well the size-dependent

behaviour due to localised failure. Once fracture is detected, the traction decreases with the increase in the displacement jump. The traction-displacement curves are the same for different characteristic lengths (*H*) as shown in Figure 4.0–12(b) and Figure 4.0–13(b), indicating that the behaviour of the cohesive fracture zone is independent of the characteristic length. Similar to the response to traction, the tensile strength reduces to zero with the increase in the displacement jump (Figure 4.0–12c & Figure 4.0–13c). Figure 4.0–12(d) and Figure 4.0–13(d) show the evolution of damage variables with the displacement jumps. The damage variable increases from 0 to 1 for both linear and exponential cases.

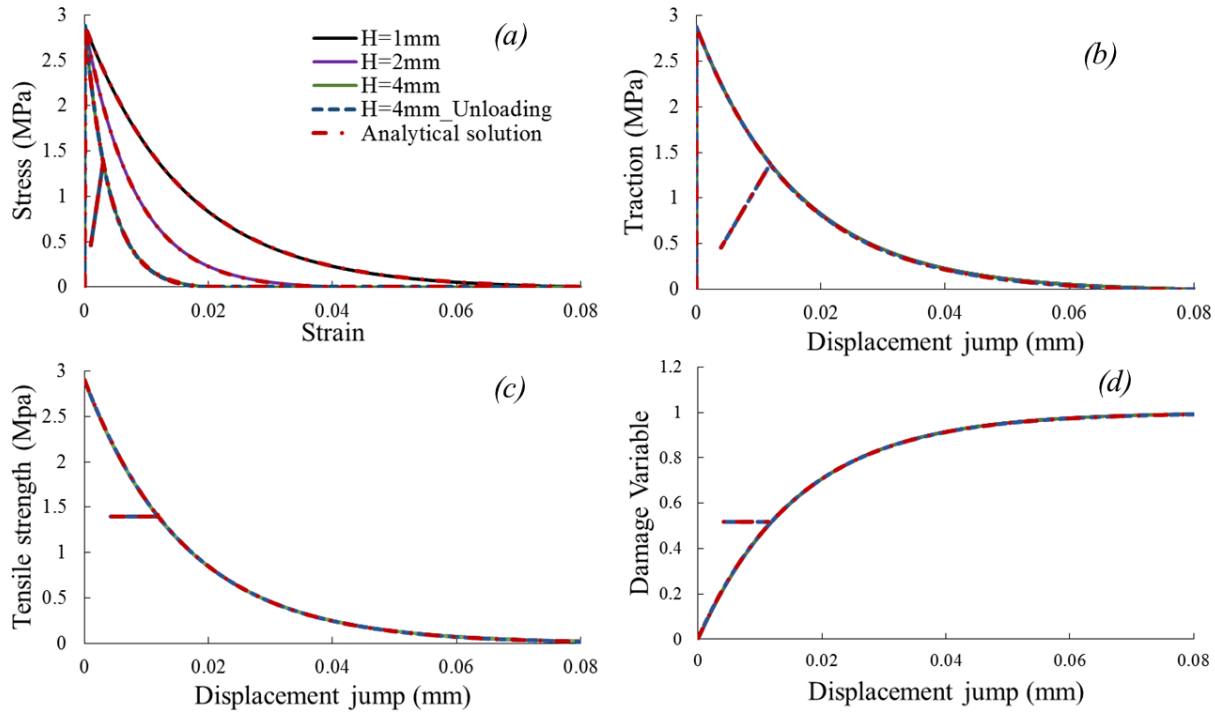

Figure 4.0–13. Constitutive model with embedded exponential cohesive fracture law: (a) average stress-strain relationship; (b) traction-displacement curve; (c) tensile strength-displacement jump curve; (d) damage variable-displacement curve

The constitutive responses under unloading cases are also plotted to illustrate the model's performance, as illustrated in Figure 4.0–12 and Figure 4.0–13, in which the unloading elastic stiffness replaces the inelastic tangent stiffness to control the unloading behaviour. It can be seen that the macro-averaged stress and local traction reduce with strain and displacement jump upon unloading. The unloading curves pass the original point in both the stress-strain and traction-displacement jump curves (Figure 4.0–12a-b & Figure 4.0–13a-b). Accordingly, the

values of tensile strength and damage variable remain unchanged with the decreasing separation (Figure 4.0–12c-d & Figure 4.0–13c-d). All the results predicted by the model agree well with the analytical solutions, demonstrating the validity of the proposed constitutive model and numerical implementation algorithm.

4.6. Conclusions

In this chapter, a detailed review of existing continuum constitutive models was presented. Based on the descriptions of the existing models, together with their advantages and limitations, a new continuum constitutive model for rock was developed in this work based on the double-scale model. Unlike the double-scale model for modelling strain localisation problems, the proposed continuum constitutive model was proposed for rock fracture problems by combining the double-scale model with a cohesive fracture law used to describe the material behaviour within the fracture process zone. The new continuum constitutive framework has the following features: (i) the behaviour and size of the inside and outside of the fracture process zone can be reflected under a rigorous model framework; (ii) a local cohesive fracture law, either rate sensitive or insensitive and either pure mode I or mixed mode, can be easily introduced to describe the behaviour of the fracture process zone; and (iii) a length parameter is embedded in the stress-strain relationship for natural capture of size dependency. The model behaviour of the continuum constitutive model with embedded mode I cohesive fracture law was examined at the constitutive level by comparing the results with the analytical solution. The results showed that the constitutive model is size-dependent at the constitutive level, thanks to the characteristic length scale parameter introduced into the model. The proposed constitutive model will be incorporated into the SPH framework for simulating mode I failure of rocks and size-dependent behaviour.

Chapter 5

Taylor-SPH modelling of rock fracture and its size dependence under pure mode I loading

5.1. Introduction

In this section, rock fracture and its size dependence under pure mode I loading are simulated by a new computational approach combining the SPH and a constitutive model that possesses an intrinsic length scale. In particular, a continuum-based size-dependent constitutive model with an embedded fracture process zone described by a cohesive model is developed for modelling strain localisation in geomaterials. A length scale is introduced into the constitutive equations to describe the scale effect commonly observed in localised failure of geomaterials. The constitutive model is then employed in a mesh-free Taylor Smooth Particle Hydrodynamics (Taylor-SPH) framework to produce a new computational tool for rock fracture modelling. The key feature of the proposed numerical framework is its ability to describe fracture geometry by a set of Lagrangian particles, which carry fracture information such as damage evolution and fracture orientation, thus bypassing the need to represent the fracture's topology and fracture orientation.

This section is organised as follows. The key formulations of the Taylor-SPH framework are listed in Section 5.2 to provide a background for the introduction of particle behaviour with an embedded crack in Section 5.3. This includes both formulation and corresponding implementation algorithms, followed by verification of the implementation in Section 5.4. demonstrating the key features and potentials of the proposed framework. To test the capability of this computational framework for simulating rock fracture behaviour, two mode-I numerical fracture tests including a Brazilian-disc test and a semicircular bending test are performed in Section 5.5. The mesh dependency on the simulation solution is also examined. Section 5.6. shows two numerical examples of size-dependent behaviour of rocks compared with experimental results.

5.2. SPH framework formulation for simulating rock fracture

In this section, the key general formulations of the Taylor-SPH framework are presented to provide a platform for incorporation of the size-dependent constitutive model with an embedded fracture process zone simulating rock fractures. For detailed formulation, readers can refer to Section 3.7.

5.2.1. Governing equations of rock materials

The dynamic behaviour of rock materials can be described by three governing equations: mass conservation, momentum conservation and a stress-strain relationship, as follows:

$$\frac{d\rho}{dt} = -\rho\nabla\cdot\mathbf{v} \tag{5.1}$$

$$\frac{d\mathbf{v}}{dt} = \frac{1}{\rho}\nabla\cdot\boldsymbol{\sigma} + \boldsymbol{b} \tag{5.2}$$

$$\frac{d\boldsymbol{\sigma}}{dt} = \mathbf{D}_{ef}:\dot{\boldsymbol{\varepsilon}} \tag{5.3}$$

where ρ is the material density; $\mathbf{v}$ is the velocity vector; $\boldsymbol{\sigma}$ is the stress tensor; $\boldsymbol{b}$ is the vector component of acceleration due to external forces; $\dot{\boldsymbol{\varepsilon}}$ is the strain rate tensor, which can be calculated by velocity through a kinematic relation $\dot{\boldsymbol{\varepsilon}} = [\nabla\cdot\mathbf{v} + (\nabla\cdot\mathbf{v})^{\mathrm{T}}]/2$; $\mathbf{D}_{ef}$ is the material stiffness matrix; and d/dt is the material derivative defined as:

$$\frac{d}{dt} = \frac{\partial}{\partial t} + (\mathbf{v}\cdot\nabla) \tag{5.4}$$

with $\partial/\partial t$ and $\mathbf{v}\cdot\nabla$ being the local and convective derivative terms, respectively.

For simplicity, the density is assumed to be constant throughout the computation. Thus, only Equations (5.2) and (5.3) need to be solved in this work. Furthermore, because the governing equations are solved in the Lagrangian SPH framework, the convective terms in Equations (5.2) and (5.3) vanish and the equations can be rewritten as follows:

$$\frac{\partial\mathbf{v}}{\partial t} = \frac{1}{\rho}\nabla\cdot\boldsymbol{\sigma} + \boldsymbol{b} \tag{5.5}$$

$$\frac{\partial\boldsymbol{\sigma}}{\partial t} = \mathbf{D}_{ef}:\dot{\boldsymbol{\varepsilon}} \tag{5.6}$$

To complete these governing equations, a constitutive model is needed to calculate the material stiffness matrix and this is detailed in Section 5.3.

5.2.2. Time discretisation of governing equations

The time discretisation of Equations (5.5) and (5.6) is carried out using a two-step Taylor time discretisation scheme by means of a Taylor series expansion proposed by Mabssout and Herreros (2013). Accordingly, the unknown velocity ($\mathbf{v}$) and stress ($\boldsymbol{\sigma}$) can be calculated by applying the Taylor series expansion up to the second order as follows:

$$\mathbf{v}^{n+1} = \mathbf{v}^n + \Delta t \left.\frac{\partial \mathbf{v}}{\partial t}\right|^n + \frac{\Delta t^2}{2} \left.\frac{\partial^2 \mathbf{v}}{\partial t^2}\right|^n + O(\Delta t)^3 \tag{5.7a}$$

$$\boldsymbol{\sigma}^{n+1} = \boldsymbol{\sigma}^n + \Delta t \left.\frac{\partial \boldsymbol{\sigma}}{\partial t}\right|^n + \frac{\Delta t^2}{2} \left.\frac{\partial^2 \boldsymbol{\sigma}}{\partial t^2}\right|^n + O(\Delta t)^3 \tag{5.7b}$$

where Δt is the time increment and $\mathbf{v}^n$ and $\boldsymbol{\sigma}^n$ are the velocity and stress vectors at time t^n, respectively.

The first-order time derivative of velocity and stress in Equations (5.7a) and (7.7b) can be calculated using Equations (5.5) and (5.6), respectively:

$$\left.\frac{\partial \mathbf{v}}{\partial t}\right|^n = \left(\frac{1}{\rho}\nabla \cdot \boldsymbol{\sigma} + \boldsymbol{b}\right)^n \tag{5.8a}$$

$$\left.\frac{\partial \boldsymbol{\sigma}}{\partial t}\right|^n = (\mathbf{D}_{ef} : \dot{\boldsymbol{\varepsilon}})^n \tag{5.8b}$$

The second-order time derivative of velocity and stress in Equations (5.7a) and (5.7b) can be obtained by taking the time derivative of Equations (5.8a) and (5.8b) respectively, leading to:

$$\left.\frac{\partial^2 \mathbf{v}}{\partial t^2}\right|^n = \frac{\partial}{\partial t}\left(\frac{1}{\rho}\nabla \cdot \boldsymbol{\sigma} + \boldsymbol{b}\right)^n = \frac{1}{\rho}\nabla \cdot \left(\frac{\partial \boldsymbol{\sigma}}{\partial t}\right)^n \tag{5.9a}$$

$$\left.\frac{\partial^2 \boldsymbol{\sigma}}{\partial t^2}\right|^n = \frac{\partial}{\partial t}\left(\mathbf{D}_{ef} : \dot{\boldsymbol{\varepsilon}}\right)^n = \mathbf{D}_{ef}^n : \left(\frac{\partial \dot{\boldsymbol{\varepsilon}}}{\partial t}\right)^n \tag{5.9b}$$

To calculate the first-order time derivatives of stress and strain rate tensors in Equations (5.8a) and (5.8b), the Taylor series expansions of $\boldsymbol{\sigma}$ and $\dot{\boldsymbol{\varepsilon}}$ up to the first order are applied:

$$\boldsymbol{\sigma}^{n+1/2} = \boldsymbol{\sigma}^n + \frac{\Delta t}{2}\left(\frac{\partial \boldsymbol{\sigma}}{\partial t}\right)^n + O(\Delta t)^2 \tag{5.10a}$$

$$\dot{\boldsymbol{\varepsilon}}^{n+1/2} = \dot{\boldsymbol{\varepsilon}}^n + \frac{\Delta t}{2}\left(\frac{\partial \dot{\boldsymbol{\varepsilon}}}{\partial t}\right)^n + O(\Delta t)^2 \tag{5.10b}$$

By ignoring the last term in Equations (5.10a) and (5.10b), the first-order time derivatives of stress, external force and strain rate at time step n can be computed by:

$$\left(\frac{\partial \boldsymbol{\sigma}}{\partial t}\right)^n = \frac{2}{\Delta t}\left(\boldsymbol{\sigma}^{n+1/2} - \boldsymbol{\sigma}^n\right) \tag{5.11a}$$

$$\left(\frac{\partial \dot{\boldsymbol{\varepsilon}}}{\partial t}\right)^n = \frac{2}{\Delta t}\left(\dot{\boldsymbol{\varepsilon}}^{n+1/2} - \dot{\boldsymbol{\varepsilon}}^n\right) \tag{5.11b}$$

where all the unknown variables at time step $t^{n+1/2}$, including the strain rate tensor $\dot{\boldsymbol{\varepsilon}}^{n+1/2}$ which is calculated from the velocity $\mathbf{v}^{n+1/2}$, can be estimated by applying Taylor series expansions, leading to:

$$\boldsymbol{\sigma}^{n+1/2} = \boldsymbol{\sigma}^n + \frac{\Delta t}{2}\frac{\partial \boldsymbol{\sigma}}{\partial t}\Big|^n = \boldsymbol{\sigma}^n + \frac{\Delta t}{2}(\mathbf{D}_{ef}:\dot{\boldsymbol{\varepsilon}})^n \tag{5.12a}$$

$$\mathbf{v}^{n+1/2} = \mathbf{v}^n + \frac{\Delta t}{2}\frac{\partial \mathbf{v}}{\partial t}\Big|^n = \mathbf{v}^n + \frac{\Delta t}{2}\left(\frac{1}{\rho}\nabla\cdot\boldsymbol{\sigma} + \boldsymbol{b}\right)^n \tag{5.12b}$$

$$\dot{\boldsymbol{\varepsilon}}^{n+1/2} = \frac{1}{2}\left[\nabla\cdot\mathbf{v}^{n+1/2} + (\nabla\cdot\mathbf{v}^{n+1/2})^{\mathrm{T}}\right] \tag{5.12c}$$

By substituting Equations (5.11a) and (5.11b) into Equations (5.9a) and (5.9b), then Equations (5.8a) and (5.8b) into Equations (5.7a) and (5.7b), respectively, and ignoring the last terms in Equation (5.7), the velocity and stress at time t^{n+1} are calculated as follows:

$$\mathbf{v}^{n+1} = \mathbf{v}^n + \Delta t\left(\frac{1}{\rho}\nabla\cdot\boldsymbol{\sigma} + \boldsymbol{b}\right)^{n+1/2} \tag{5.13a}$$

$$\boldsymbol{\sigma}^{n+1} = \boldsymbol{\sigma}^n + \Delta t\left(\mathbf{D}_{ef}:\dot{\boldsymbol{\varepsilon}}\right)^{n+1/2} \tag{5.13b}$$

Finally, the displacement of particles is updated using the following equation:

$$\mathbf{x}^{n+1} = \mathbf{x}^n + \mathbf{v}^{n+1/2}\,\Delta t \tag{5.14}$$

where the velocity at time step $t^{n+1/2}$ is calculated from Equation (5.12b).

5.2.3. Spatial discretisation by corrective SPH

The corrective SPH method is used to perform the spatial discretisation of the divergent terms. Detailed descriptions of the corrected SPH method were well explained in section 3.6, thus are not repeated here. The final SPH approximations of a function and its derivatives using the corrective technique can be represented as:

$$< f(x_i) >= \sum_{j=1}^{N}\frac{m_j}{\rho_j} f(x_j)\widetilde{W}(x - x_j, h) \tag{5.15}$$

$$< \nabla\cdot f(x_i) >= \sum_{j=1}^{N}\frac{m_j}{\rho_j}\left(f(x_j) - f(x_i)\right)\cdot\widetilde{\nabla}_i W(x_i - x_j, h) \tag{5.16}$$

where $\widetilde{W}$ and $\widetilde{\nabla}_i W$ are the corrected kernel function and its gradient, which are defined as follows, respectively:

$$\widetilde{W}(x-x_j,h)=\frac{W(x-x_j,h)}{\sum_{j=1}^{N}\frac{m_j}{\rho_j}W(x-x_j,h)} \tag{5.17}$$

$$\widetilde{\nabla}_i W(x_i-x_j,h)=\frac{\nabla_i W(x_i-x_j,h)}{\sum_{j=1}^{N}\frac{m_j}{\rho_j}(\boldsymbol{x}_i-\boldsymbol{x}_j)\otimes\nabla_i W(x_i-x_j,h)} \tag{5.18}$$

5.2.4. Taylor-SPH discretisation of governing equations

In the Taylor SPH, the stress point approach is used to minimize the zero-energy mode occurring in the traditional SPH. Therefore, the computational domain in the Taylor SPH is represented by two sets of particles (i.e. material and stress particles). All the particles can carry their own properties and move based on the governing equation. All the field variables and their derivatives of material particles are approximated based on the stress particles, and vice versa. Finally, combining the above stress particle approach, the corrective SPH approximation with the two-step Taylor scheme, the time discretisation of Equations (5.5) and (5.6) is performed in two steps:

First step: The velocities and stresses of stress particles at the half time step $t^{n+1/2}$ are first calculated by Equations (5.12a) and (5.12b):

$$\mathbf{v}_s^{n+1/2}=\mathbf{v}_s^n+\frac{\Delta t}{2}\left(\sum_{m=1}^{N}\frac{m_m}{\rho_m\rho_s}(\boldsymbol{\sigma}_m-\boldsymbol{\sigma}_s)^n\cdot\widetilde{\nabla}_s W_{sm})+\boldsymbol{b}_s^n\right) \tag{5.19a}$$

$$\boldsymbol{\sigma}_s^{n+1/2}=\boldsymbol{\sigma}_s^n+\frac{\Delta t}{2}\left(\mathbf{D}_{ef}:\dot{\boldsymbol{\varepsilon}}_s\right)^n \tag{5.19b}$$

where subscripts *s* and *m* refer to stress and material particles, respectively; and the velocity, stresses and strain rate of stress particles at time step n can be calculated by the following SPH approximations, respectively:

$$\mathbf{v}_s^n=\sum_{m=1}^{N}\left(\frac{m_s}{\rho_s}\mathbf{v}_m^n\widetilde{W}_{sm}\right) \tag{5.20a}$$

$$\boldsymbol{\sigma}_s^n=\sum_{m=1}^{N}\left(\frac{m_s}{\rho_s}\boldsymbol{\sigma}_m^n\widetilde{W}_{sm}\right) \tag{5.20b}$$

$$\dot{\varepsilon}_s^n=\frac{1}{2}\sum_{m=1}^{N}\left[\frac{m_m}{\rho_m}(\boldsymbol{v}_m-\boldsymbol{v}_s)^n\cdot\widetilde{\nabla}_s W_{sm}\right] \tag{5.20c}$$

Second step: The velocities and stresses of material particles at time $t^{n+1/2}$ are then calculated from those of stress particles using Equation (15):

$$\mathbf{v}_m^{n+1/2}=\sum_{s=1}^{N}\left(\frac{m_s}{\rho_s}\mathbf{v}_s^{n+1/2}\widetilde{W}_{ms}\right) \tag{5.21a}$$

$$\boldsymbol{\sigma}_m^{n+1/2}=\sum_{s=1}^{N}\left(\frac{m_s}{\rho_s}\boldsymbol{\sigma}_s^{n+1/2}\widetilde{W}_{ms}\right) \tag{5.21b}$$

Next, the velocities and stresses of material particles at time step t^{n+1} are calculated using Equations (5.13a) and (5.13b):

$$\mathbf{v}_m^{n+1} = \mathbf{v}_m^n + \Delta t \left(\sum_{s=1}^{N} \frac{m_s}{\rho_s \rho_m} (\boldsymbol{\sigma}_s - \boldsymbol{\sigma}_m)^{n+1/2} \cdot \widetilde{\nabla}_m W_{ms} \right) + \boldsymbol{b}_m^{n+1/2} \right) \tag{5.22b}$$

$$\boldsymbol{\sigma}_m^{n+1} = \boldsymbol{\sigma}_m^n + \Delta t \left(\mathbf{D}_{ef} : \dot{\boldsymbol{\varepsilon}}_m \right)^{n+1/2} \tag{5.22b}$$

where the strain rate of material particles at time step $n + 1/2$ can be computed by:

$$\dot{\varepsilon}_m^{n+1/2} = \frac{1}{2} \sum_{s=1}^{N} \left[\frac{m_s}{\rho_s} (\boldsymbol{v}_s - \boldsymbol{v}_m)^{n+1/2} \cdot \tilde{\nabla}_m W_{ms} \right] \tag{5.23}$$

Finally, the displacements of both stress and material particles are updated using Equation (5.14) as follows:

$$\mathbf{x}_{\boldsymbol{m}}^{n+1} = \mathbf{x}_m^n + \mathbf{v}_m^{n+1/2} \, \Delta t \tag{5.24a}$$

$$\mathbf{x}_s^{n+1} = \mathbf{x}_s^n + \mathbf{v}_s^{n+1/2} \, \Delta t \tag{5.24b}$$

The combination of the corrective SPH technique, stress point approach and Taylor time integration scheme provides an accurate and stable solution to solve the governing equations of rock. Moreover, unlike the standard SPH approach in which extra boundary particles are used to reinforce boundary conditions, boundary conditions in the current SPH approach are applied directly to all particles located on the boundaries, with predefined values of stress and velocity.

5.3. Size-dependent constitutive framework

The continuum constitutive model with embedded mode I cohesive fracture law proposed in Chapter 4 is adopted in this work. The proposed constitutive model enables to distinguish the responses of the material inside and outside the fracture process zone under tensile loading conditions, therefore it can realistically reflect the high strain deformation within the process fracture zone. This model also possesses a length parameter embedded in the final constitutive relation for capturing the size dependency of rock fractures without any ad hoc treatment. The detailed formulations have been comprehensively explained in Chapter 3, and thus only key formulations are presented in this section. The macro stress strain relationship of a representative volume element (RVE) for rocks is expressed as:

$$\dot{\boldsymbol{\sigma}} = \boldsymbol{a}_o : \left(\dot{\boldsymbol{\varepsilon}} - \frac{1}{H} [\boldsymbol{n} \otimes (\boldsymbol{C}^{-1} \cdot (\boldsymbol{a}_o : \dot{\boldsymbol{\varepsilon}}) \cdot \boldsymbol{n})]^{sym} \right) \tag{5.25}$$

where

$$\boldsymbol{C} = \left[\frac{1}{H}(\boldsymbol{n} \cdot \boldsymbol{a}_o \cdot \boldsymbol{n}) + \boldsymbol{K}\right] \tag{5.26}$$

It can be seen that once the global stiffness $\boldsymbol{K}$ is determined, the constitutive relation of rocks can be easily calculated. The global stiffness can be determined by a simple cohesive fracture law with a matrix rotation process shown as:

$$\dot{\boldsymbol{t}}_{cr} = \boldsymbol{K}_{cr}[\![\dot{\boldsymbol{u}}]\!]_{cr} \tag{5.27a}$$

$$\boldsymbol{K} = \boldsymbol{R}^T \boldsymbol{K}_{cr} \boldsymbol{R} \tag{5.27b}$$

In this work, linear and exponential cohesive fracture law have been proposed for determining the evolution of tensile strength, and the parameters controlling the shapes of those models are respectively represented as:

Linear: $$k_{cr}^{LD} = -\frac{\sigma_{t0}}{u_{cr}^f} \quad \text{and} \quad u_{cr}^f = \frac{2G_f}{\sigma_{t0}} \tag{5.28a}$$

Exponential: $$k_{cr}^{LD} = -\frac{{\sigma_{t0}}^2}{G_f}\exp(-\frac{\sigma_{t0}}{G_f}u_{cr}) \tag{5.28b}$$

In addition, an evolution of the damage variable is required, which is defined as:

$$D = 1 - \frac{\sigma_t}{\sigma_{t0}} \tag{5.29}$$

where σ_t is the tensile strength, which is gradually degraded depending on the extent of fracture development. The strength degradation can be described by linear and exponential traction laws, respectively expressed as:

Linear: $$\sigma_t = \sigma_{t0}(1 - \frac{u_{cr}}{u_{cr}^f}) \tag{5.30a}$$

Exponential: $$\sigma_t = \sigma_{t0} exp(-\frac{\sigma_{t0}}{G_f}u_{cr}) \tag{5.30b}$$

It is noted that the above constitutive model is derived based on the small strain theory and thus could not achieve the incremental objectivity of stress and strain measures when solving large deformations. To mitigate this problem, this study adopts the Jaumann stress rate of the Cauchy stress tensor $\boldsymbol{\sigma}$ when updating the proposed constitutive model (Bui et al. 2008). The combination of this constitutive model with the SPH method, whose governing equations are solved within the updated-Lagrangian framework, also helps to improve the incremental objectivity of stress and strain measures. Nevertheless, we acknowledge that full incremental objectivity can still not be achieved with the above numerical framework. However, the

inaccuracy caused by the lack of incremental objectivity is not significant as very small time steps are also applied in the explicitly updated Lagrangian procedure. These issues have been well addressed in the previous works of Bui et al. (2008) and Nguyen et al. (2017) and proved that error is negligible when comparing our SPH solutions with FEM and experiments for large deformation problems.

5.4. Verification of proposed coupling numerical framework

A tension test conducted by Wu (2017) is carried out in this section. The purpose of this test is to verify the performance of the proposed numerical framework in one and two dimensions. The geometry and boundary conditions of this test are shown in Figure 5.0–1. For the one-dimensional case, the bar is 200mm long with a unit cross-section, while the two-dimensional bar is 200mm long and 20mm wide. The bar is fixed at the left end and tensile loading is applied at the right end of the bar. The stress and displacement of nodes at the right end of the bar are recorded during the simulation.

In this test, three different particle discretisation sizes (i.e. the initial space between two consecutive particles) are used: *dx* = 2mm, 4mm and 5mm. The numbers of material particles and stress particles used for different particle discretisation sizes are listed in Table 5.0-1. The proposed constitutive model with both linear and exponential cohesive fracture law is adopted. The material properties are: Young's modulus $E = 30\text{Gpa}$, Poisson's ratio $v = 0.2$, Courant number $C = 1$, and fracture energy $G_f = 120\text{Nm/m}^2$, tensile strength $f_t = 3\text{Mpa}$. The stress and displacement of the particles located at the right end are recorded during the test and compared with analytical solutions which can be directly obtained based on the formulations provided by Wu (2011). In these simulations, the value of *H* is taken to be the same as the particle discretisation size (*dx*). Boundary conditions for the 1D case are:

- Velocity of the left end node is $v_x = 0\ \text{mm/s}$
- Velocity of the right end node is $v_x = 0.5\text{mm/s}$.

For the 2D case, the applied boundary conditions are:

- Velocity of the right end nodes are $v_x = 0, v_y = 0.5\text{mm}/s$;
- Velocity of the left end nodes are $v_x = 0, v_y = 0$;
- Free-stress boundary conditions at the top and bottom: $\sigma_{yy} = 0\ , \sigma_{xy} = 0$.

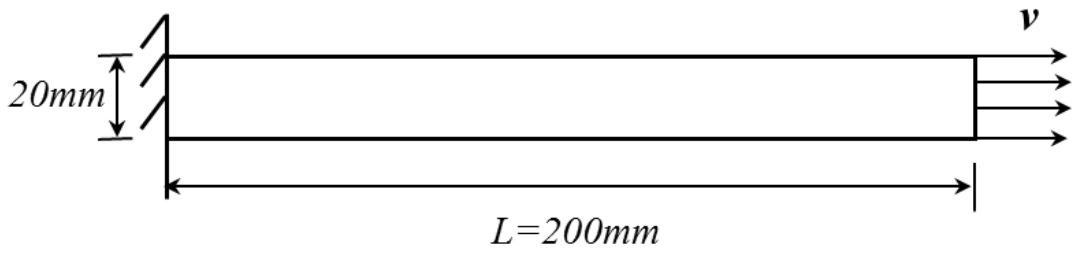

Figure 5.0–1. 2D tension test of proposed numerical framework.

Table 5.0-1. Numbers of material and stress particles for different particle discretisation sizes.

Tests	*dx = 0.25mm*		*dx = 0.125mm*		*dx = 0.0625mm*	
	Material	*Stress*	*Material*	*Stress*	*Material*	*Stress*
1D	41	40	81	80	161	160
2D	533	480	2025	1920	7889	7680

Figure 5.0–2 presents a comparison of the stress-displacement curves between simulation results using three different particle discretisation sizes (i.e. initial spacing between particles) and analytical solutions for the one-dimensional case. The simulation results match the analytical solutions well for both linear and exponential cohesive fracture laws. In both cases, the stress increases linearly with the displacement before reaching 3 MPa. After this point, the softening behaviour in stress is seen with the increasing displacement and the stresses reduce to zero at full damage. It can also be observed that the stress-displacement curves are the same regardless of the particle discretisation size. This suggests that the proposed numerical approach is independent of the spatial discretisation (or mesh-independent). Figure 5.0–3 shows the relationship between horizontal stress and displacement in the two-dimensional case. As in the 1D case, the horizontal stress shows a linear increase with the corresponding displacement until reaching around 3MPa. The tangent stiffness, i.e. the slope between stress and displacement in 2D, is found to be slightly greater than that in 1D, which can be attributed to the influence of Poisson's ratio. The softening behaviour also occurs after the peak stress and the horizontal stress reduces to zero at full damage. Numerical solutions are also

independent of the size of domain discretisation. For both cases, the localisation band formed at the boundary edge.

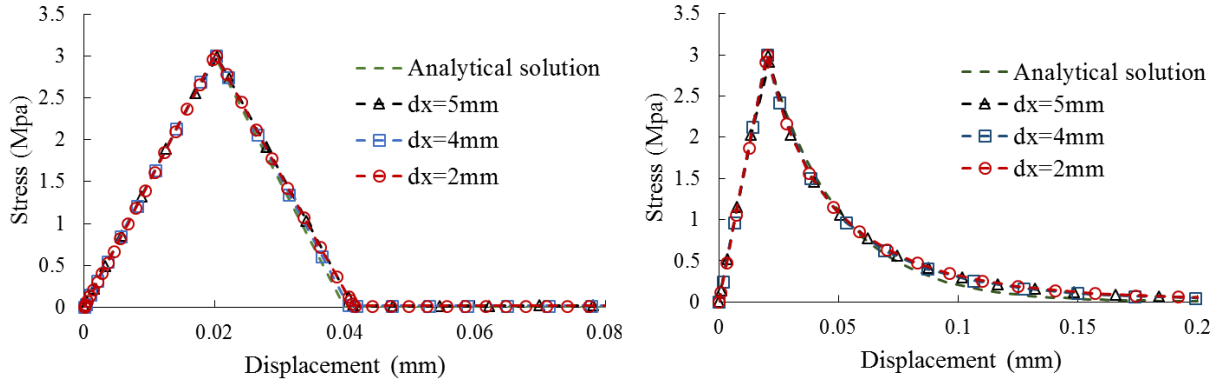

Figure 5.0–2. Stress-displacement relationship for one-dimensional tensile test: linear cohesive fracture law (left); exponential cohesive fracture law (right).

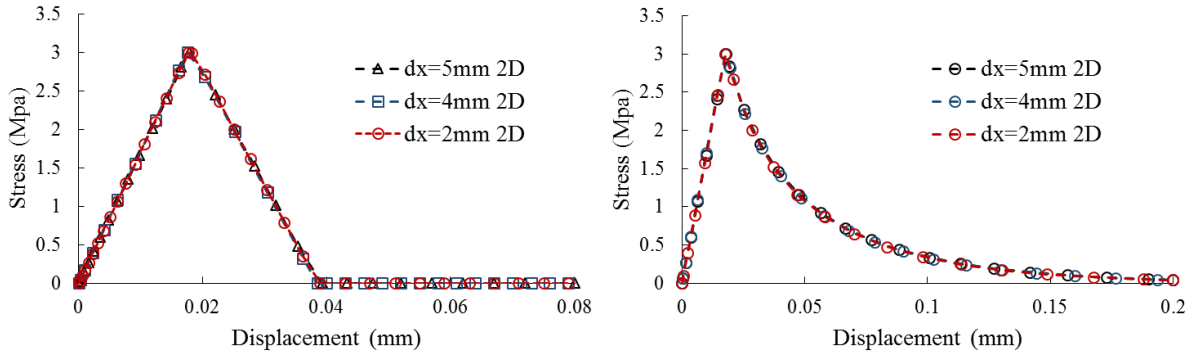

Figure 5.0–3. Horizontal stress-displacement relationship for two-dimensional tensile test: linear cohesive fracture law (left); exponential cohesive fracture law (right).

5.5. Mode I rock fracture applications

In this section, two laboratory tests, the Brazilian disc test and the semi-circular bending test, are simulated using the proposed numerical approach. The simulation results are then compared with those of experiments to demonstrate the predictive capability of the proposed coupling of Taylor-SPH and the continuum constitutive model with an embedded cohesive fracture process zone in predicting the mode-I fracture behaviour of rock and rock-like materials. In all examples, the linear cohesive law is adopted and the smoothing length (h) is chosen to be $h = 1.2dx$ with dx being the initial spacing between two consecutive SPH particles. The

characterised length (H) of the constitutive model is chosen to be the same as the spatial discretisation dx. All numerical tests are performed in the plane stress condition.

5.5.1. Brazilian disc test

In the first numerical application, the Brazilian disc (BD) test for Gosford sandstone conducted by Gui et al. (2015) is simulated. The experimental specimen has dimensions of 50mm in diameter and 25mm in height and is subjected to a constant vertical loading velocity as shown in Figure 5.0–4. The material properties of Gosford sandstone reported in Gui et al. (2015) are Young's modulus E = 4 GPa, Poisson's ratio $\mu = 0.25$, tensile strength $f_t = 4$ MPa, fracture energy $G_f = 20\ \mathrm{Nm/m^2}$. The same material properties for Gosford sandstone reported by Gui et al. (2015) are adopted in the SPH simulations except for the elastic Young's modulus, which is taken to be E = 3.43 GPa to fit the experimental and numerical results for the load-displacement curve at the initial elastic loading stage. The numerical tests using both the SPH method and the FEM could not achieve the same elastic behaviour of the load-displacement curve in the experiment if E = 4 GPa is adopted. Moreover, the selection of E = 3.43 GPa is reasonable as the elastic Young's modulus of Gosford sandstone varies significantly in the literature. For instance, Zhao et al. (2014) reported the value of 2.5 GPa while Hagan (1992) provided a range of 3.6 GPa to 9 GPa for Gosford sandstone.

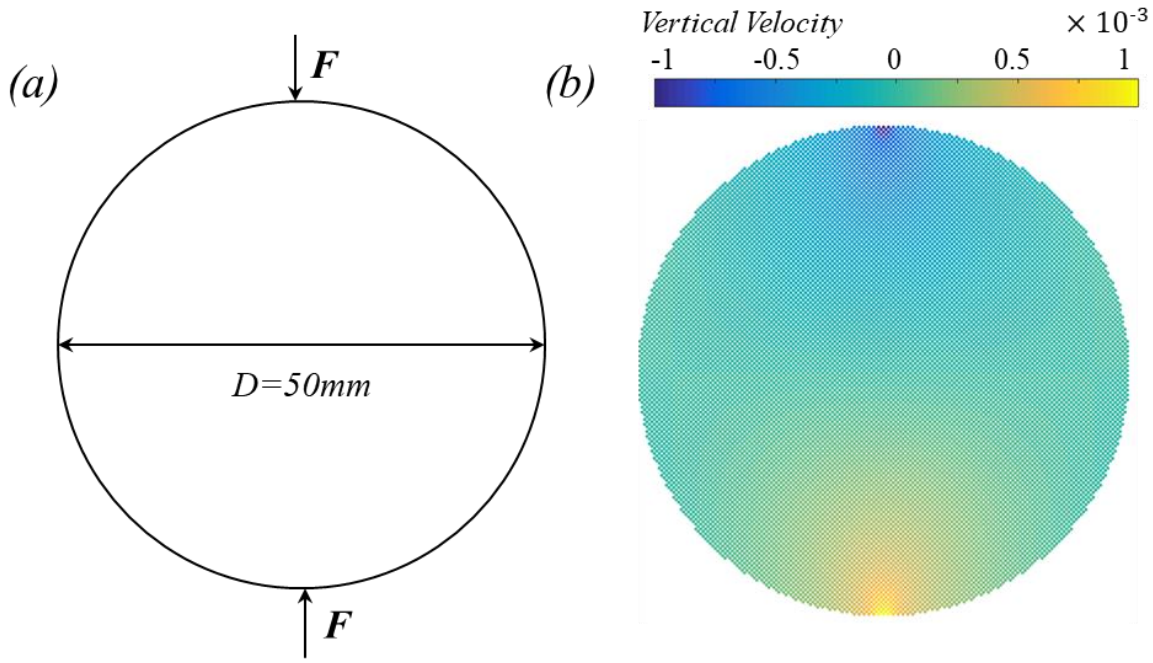

Figure 5.0–4. Setup of Brazilian test: (a) Geometry and boundary conditions, (b) Loading condition in Taylor SPH

Table 5.0-2. Loading rates in the Brazilian test (dx = 0.5mm)

Velocity (mm/s)	*Equivalent strain rate (s^{-1})*	*Notes*
0.5	0.01	within quasi-static loading range
1	0.02	
2	0.04	
5	0.1	upper bound of the range
10	0.2	outside the range
12.5	0.25	
15	0.3	

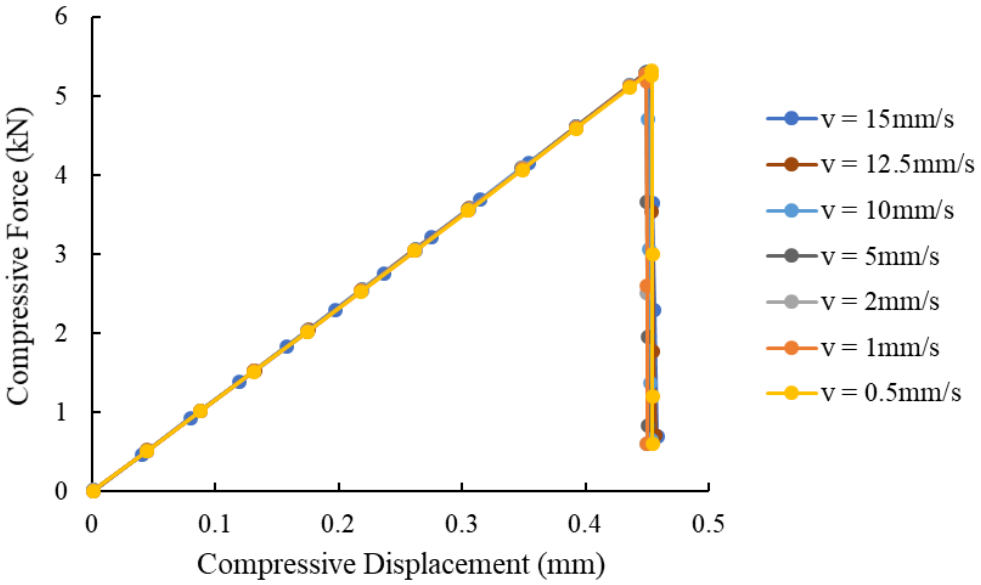

Figure 5.0–5. Compressive force-displacement curves obtained from the Brazilian test subject to a wide range of loading velocities (dx = 0.5m)

In the SPH simulation, the numerical specimen is analysed using three different particle discretisation sizes of 0.25mm, 0.5mm and 1mm, resulting in 63277 particles (31649 material particles), 15965 particles (7989 material particles) and 3996 particles (1998 material particles), respectively. The influence of the loading rate is also investigated by conducting tests with different loading velocities, listed in

Table 5.0-2. The compressive force and displacement curves corresponding to those velocities are plotted in Figure 5.0–5. Unlike the three-point bending test, the model response in Brazilian test shows that it is insensitive to loading rate, even with velocities that are outside the quasi-static range. Therefore, the velocity value of 1mm/s, corresponding to a strain rate of $0.02s^{-1}$, is applied to material particles at the top and bottom ends of the sample for simulating the point load. The detailed boundary conditions for the SPH simulations are summarised as follows:

- At the bottom end, the vertical velocity component of the loading particles is imposed, $v_x = 0, v_y = 1\ \mathrm{mm/s}$;
- At the top end, the vertical velocity component of the loading particles is imposed, $v_x = 0, v_y = -1\ \mathrm{mm/s}$;
- On the surface boundary surrounding the disc, $\sigma_{xx} = 0,\ \sigma_{yy} = 0,\ \sigma_{xy} = 0$.

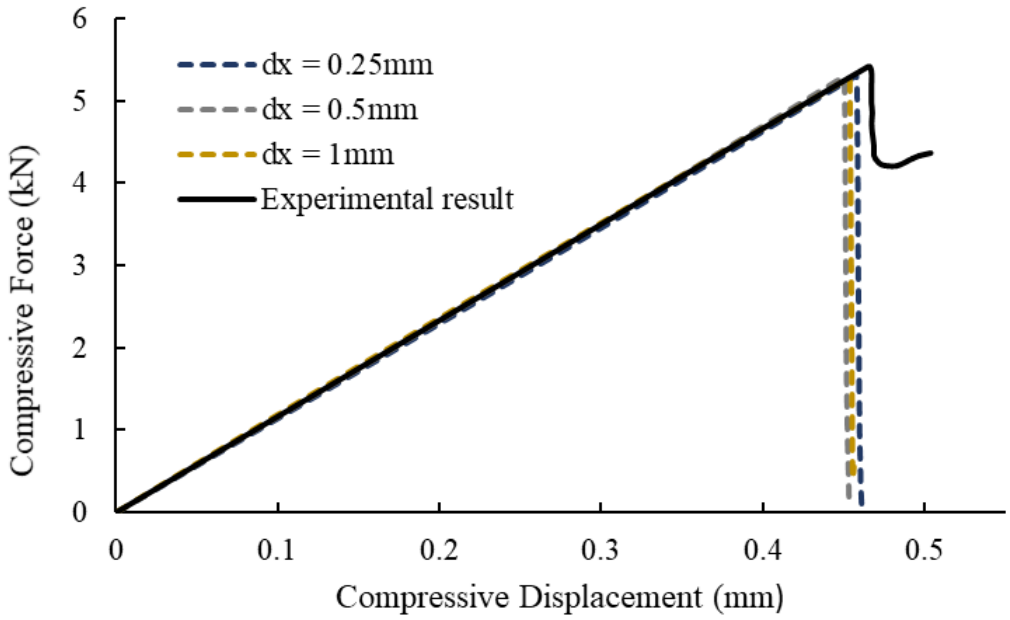

Figure 5.0–6. Compressive force and displacement of the Brazilian disc test.

Figure 5.0–6 shows a comparison between the SPH simulation and experiment for the load-displacement curve. It can be seen that the proposed SPH model captures well the overall response of the load-displacement curve in the experiment. The force increases linearly before reaching the peak load and this process is controlled mainly by the elastic properties of the rock (i.e. Young's modulus and Poisson's ratio). After reaching the peak load, the force-

displacement curves drop dramatically, indicating that the Gosford sandstone is highly brittle. Nevertheless, the SPH model slightly underestimates the peak load of the experiment and further investigation is required to confirm this difference. The results of the load-displacement curve using different particle discretisation sizes are also plotted in Figure 5.0–6. Although there are some minor differences among three cases, the general responses of the load-displacement curves are similar, suggesting that the proposed numerical modelling framework is insensitive to spatial discretisation (or the initial space between two consecutive particles).

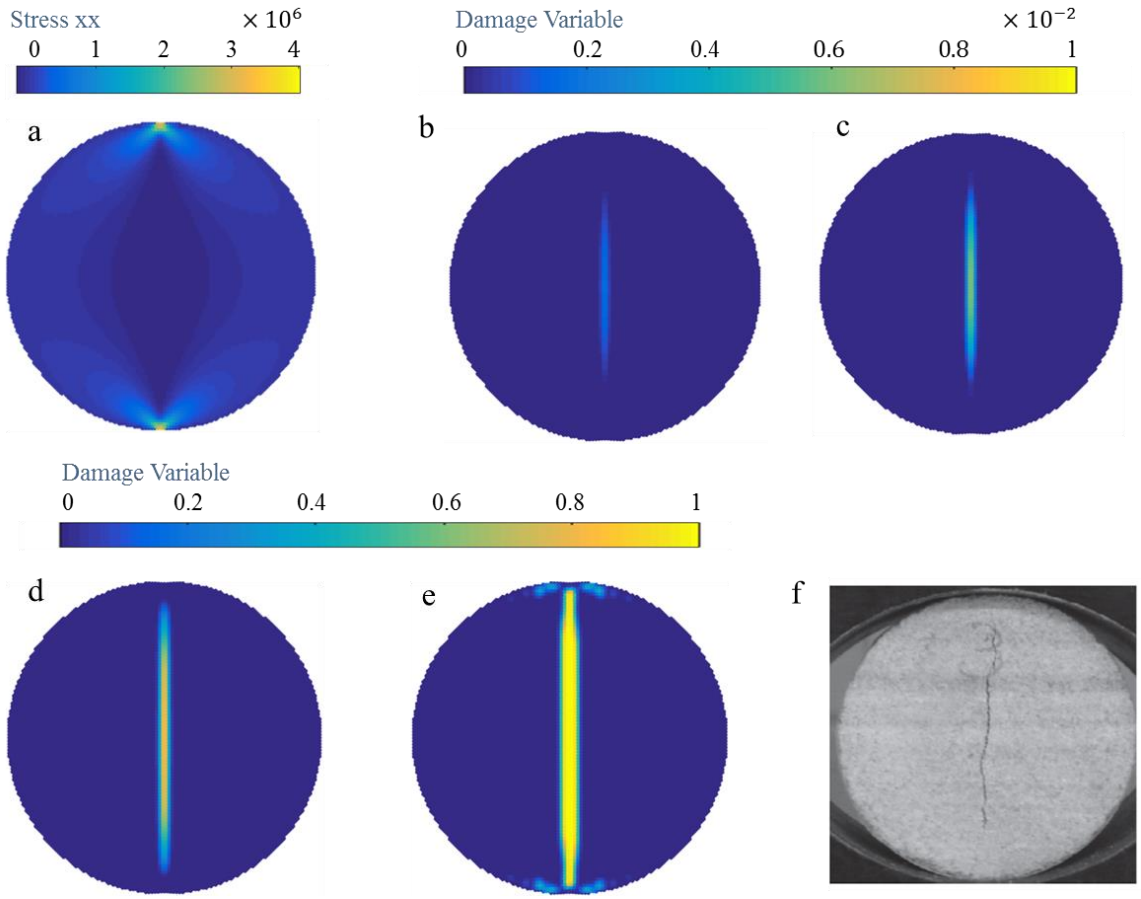

Figure 5.0–7. Comparison between SPH simulation and experiment: (a) Horizontal stress profile before fracture; (b-e) Fracture initiation and propagation; (f) Final fracture pattern from the experiment (Gui et al. 2015)

The failure process of the Brazilian disk is shown in Figure 5.0–7 compared to the final failure pattern obtained from the experiment. The horizontal stress distribution within the numerical specimen before the crack initiates is illustrated in Figure 5.17a, indicating that the tensile stress concentrates in the middle of the disc. The initiation and development of the crack in the

simulation are shown in the subsequent figures (Figure 5.0–7b-e). A crack initiates at the centre of the disc when the induced tensile stress at that point exceeds the tensile strength of the rock (Figure 5.0–7b). It then propagates along the centre line toward the top and bottom ends of the specimen, and eventually splits the specimen into two equal halves (Figure 5.0–7c-d). The final fracture pattern obtained from the simulation (Figure 5.0–7e) is similar to that observed in the experiment (Figure 5.0–7f), demonstrating the potential of the proposed SPH computational framework in modelling brittle fracture.

5.5.2. Semicircular Bending Test

To further examine the predictive capability of the proposed model in simulating mode-I rock fracture behaviour, a semicircular bending experiment as performed by Lim et al. (1993) on Johnstone is conducted. The aim of this numerical test is to demonstrate the predictive capability of the proposed approach to capture the influences of notch length and span on the mode-I normalised stress intensity factor (Y_I), which is calculated as follows:

$$Y_I = \frac{K_I}{\sigma_0\sqrt{\pi a}} \tag{53}$$

where K_I mode I stress instensity factor, $\sigma_0 = \frac{P}{2rt}$ is normalised stress, P is applied load and t is specimen thickness.

Figure 5.0–8 shows the experimental and numerical setup of the notched semicircular disk. The specimen is supported by two rollers located at the bottom end and loads by another roller placed at the top end. The distance between two rollers at the bottom end ($2s$) is $0.5r$, $0.61r$ and $0.8r$, with r being the radius of the specimen. A vertical notch is created in the middle of the bottom end of the sample with the length (a) of $0.1r$, $0.2r$, $0.3r$, $0.4r$, $0.5r$, $0.61r$, $0.7r$ and $0.8r$. In some cases, $a = 0.67r$ is also adopted in the experiment. The material properties are Young's modulus E = 400 MPa, Poisson's ratio $\mu = 0.25$, tensile strength $f_t = 0.6$ MPa, and mode I fracture toughness $K_{Ic} = 2.15\ \text{MPa}\sqrt{\text{mm}}$.

In SPH simulations, the semicircular numerical specimen is generated using 4009 material and 3952 stress particles with an initial particle spacing of 0.95mm. It is noted that these particle numbers might be slightly changed with different notch lengths. The vertical loading is simulated by applying a downward vertical velocity of 2mm/s on loading particles located at the top end of the sample, which gives a corresponding quasi-static strain rate of 0.042s^{-1}. The boundary conditions used in the semicircular bending test are summarised as follows:

- At the location of rollers at the bottom end, the vertical motions of particles are fixed, thus $v_y = 0$ and $\sigma_{xy} = 0$;
- At the top end, the vertical velocity component is imposed to loading particles, $v_x = 0$ and $v_y = -2\ mm/s$;
- On other free-stress boundary surfaces of the specimen, $\sigma_{xx} = 0$, $\sigma_{yy} = 0$ and $\sigma_{xy} = 0$.

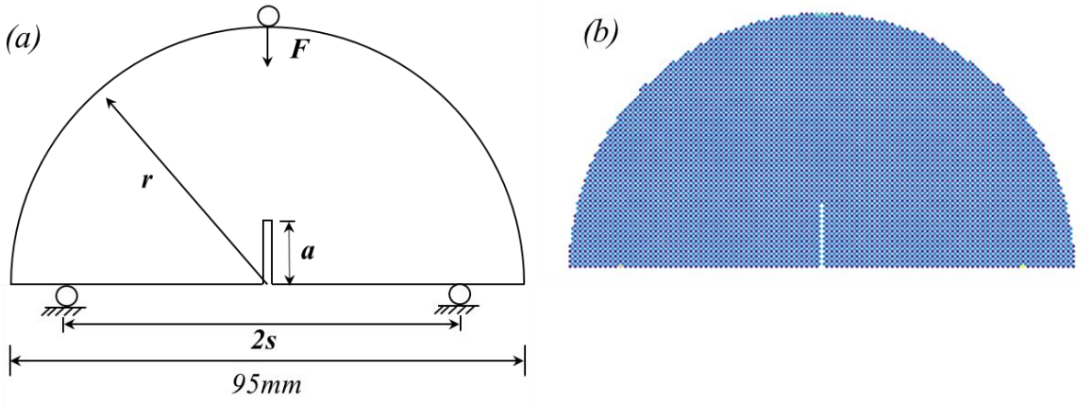

Figure 5.0–8. Geometry and boundary conditions in the semicircular bending test

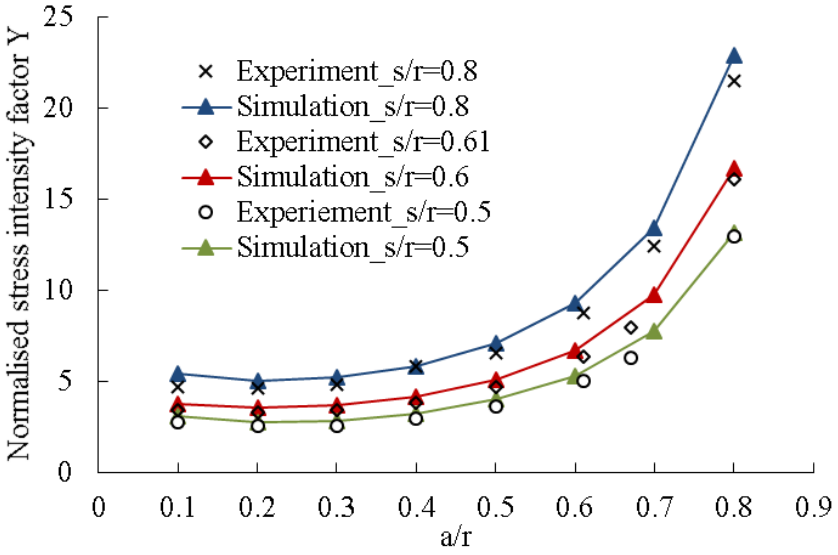

Figure 5.0–9. Variation of normalised stress intensity factor in semicircular bending test

Figure 5.0–9 shows a comparison between experiments and simulation for the normalised stress intensity factor with respect to different notch lengths and spans. It can be seen that the

numerical approach captures very well the variation trend of the normalised stress intensity factor with respect to different notch lengths and the numerical results are in excellent agreement with those obtained experimentally. There is an increasing trend in the normalised stress intensity factor with the notch length for the same sample span size, although this variation seems to be negligible for ratios of notch length-to-radius of less than 0.3. The shorter span size results in lower values of normalised stress intensity factor for the same notch length-to-radius ratio.

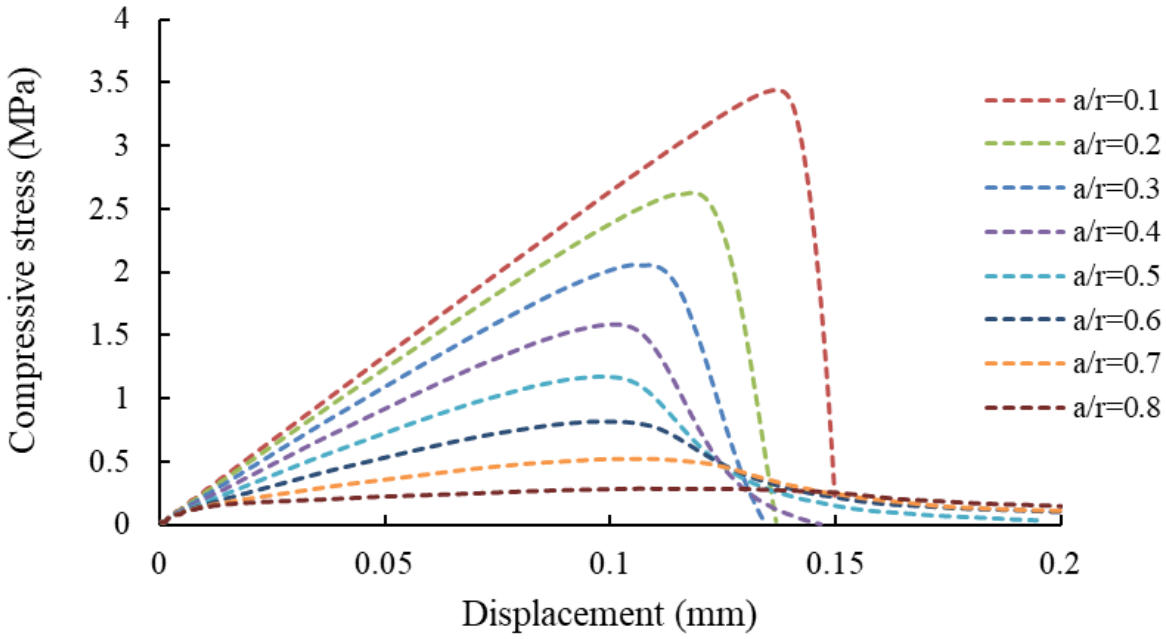

Figure 5.0–10. Compressive stress and displacement relationship for s/r=0.8

The typical stress-displacement curves obtained in the numerical specimen of $s/r = 0.8$, 0.6 and 0.5 for different length-to-radius ratios of the notch are respectively presented in Figure 5.0–10, Figure 5.0–11 and Figure 5.0–12. The stress-displacement curves are shown to undergo the same elastic behaviour prior to the initiation of fracture, while significant deviation of the curves is observed after the crack is initiated (i.e. after the yielding point). The peak stresses are shown to increase with the reduction in notch length, while the softening portion of the stress-displacement curves is extended with increasing notch length. These observations are reasonable, in the sense that both the peak stress and the softening portion of the stress-displacement curve are associated with the ligament length $(r - a)$, which defines the amount

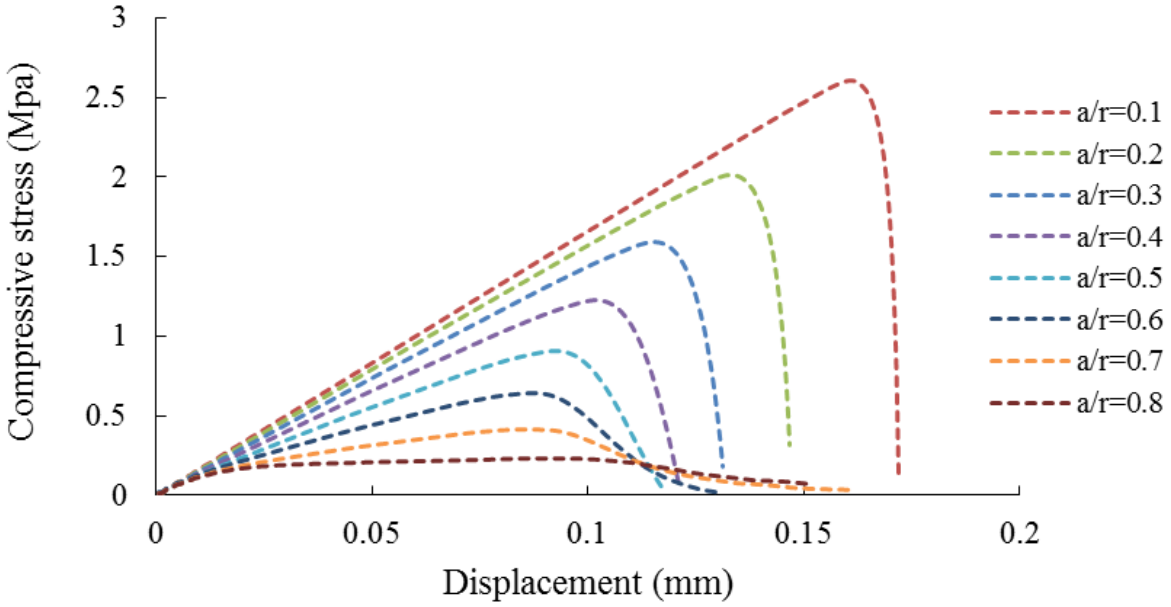

Figure 5.0–11. Compressive stress and displacement relationship for s/r=0.6

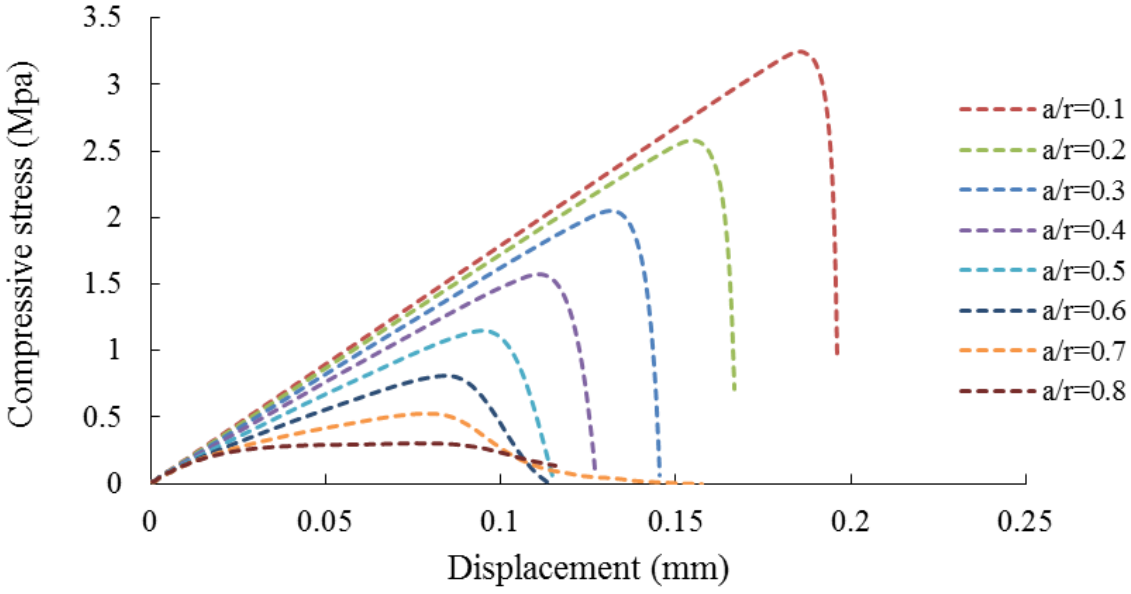

Figure 5.0–12. Compressive stress and displacement relationship for s/r=0.5

of work required to grow crack in a specimen (Bažant and Kazemi 1991). The RILEM method reported by Bažant and Kazemi (1991) gave a positive correlation between peak stress and length of ligament under the condition that the fracture energy is unchanged. As the notch length in the specimen decreases, the effective area of the fractured ligament increases.

Consequently, more work is required to grow crack, and samples with a shorter notch can carry higher loads. On the other hand, as the notch length increases, the fractured ligament area decreases. To ensure that the fracture energy of the material is the same, the work required to grow crack must reduce, thus the peak stress decreases and the softening portion of the stress-displacement curve increases.

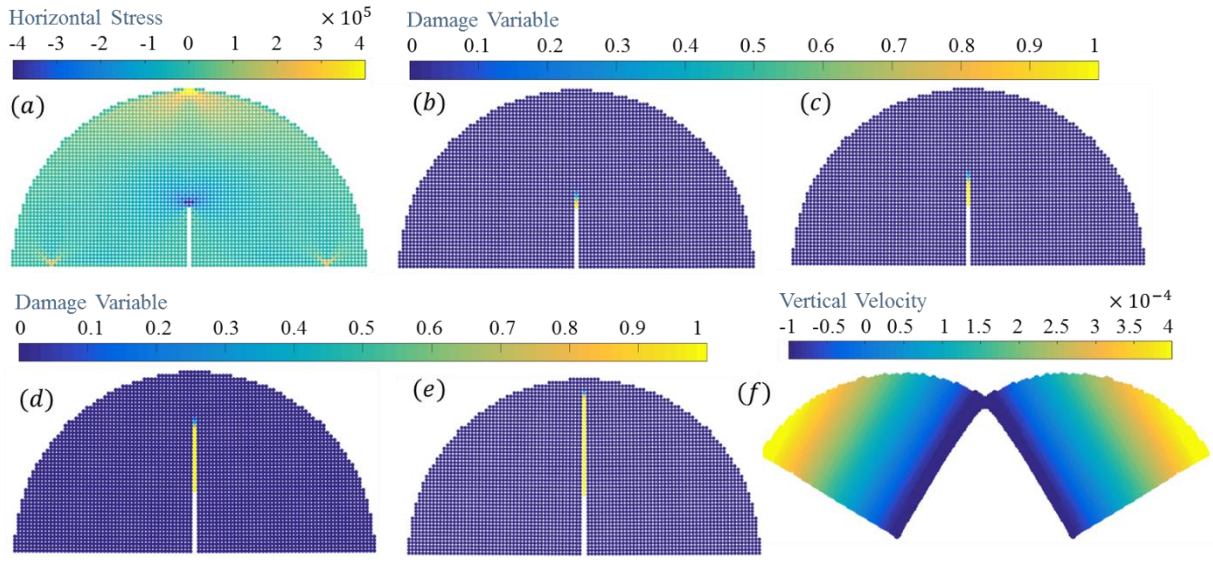

Figure 5.0–13. SPH simulations of Johnstone fracture in semicircular bending test: (a) Horizontal stress profile before fracture; (b-e) Progressive development of fracture; (f) Final failure pattern through vertical velocity profile.

Figure 5.0–13 shows a typical SPH simulation of Johnstone fracture in the semicircular bending test. The span and notch lengths of the numerical sample in this test are $0.8r$ and $0.35r$, respectively. As indicated in Figure 5.0–13a, particles near the notch tip experience tensile stresses prior to the initiation of fracture. Subsequently, the fracture initiates at the notch tip and propagates toward the loading points (Figure 5.0–13b-d), as illustrated through the progressive development of the damage variable in the numerical specimen. A set of damaged particles forms a vertical fracture geometry in the middle of the sample, as shown in Figure 5.0–13e. The vertical velocity profile at the final stage is also plotted in Figure 5.0–13f, showing that the numerical sample is split into two halves, which is consistent with experimental results commonly observed in the literature.

5.6. Size-dependent applications of rocks

In this section, a series of three-point bending tests and direct tensile tests are conducted under pure mode I loading conditions to examine the capability of the SPH framework in capturing size effects on rock fractures. The manner of setting the model parameter (such as smoothing length, cohesive fracture law) is as the same as that in Brazilian test and semicircular bending test, thus not repeated here.

5.6.1. Three-point bending test

In this first application, a series of experimental tests carried out by Bellego et al. (2000) on three-point bending beams are numerically analysed. Figure 5.0–14a shows the experimental setup of the notched mortar beams of different heights of W = 80mm, 160mm and 320mm, length $L = 4W$ and thickness B = 40mm. A vertical notch is created at the bottom middle span with the ratio of the notch to height (a/W) equal to 0.1. During the experiment, the beam is supported by two steel rollers placed at the distance of $S = 3W$, and loaded by another steel roller located on its top mid-span. The material properties obtained from the experiment are: Young's modulus E=45 GPa, Poisson's ratio $\mu = 0.24$, tensile strength $f_t = 2.9$MPa, fracture energy $G_f = 47.17\ \mathrm{Nm/m^2}$.

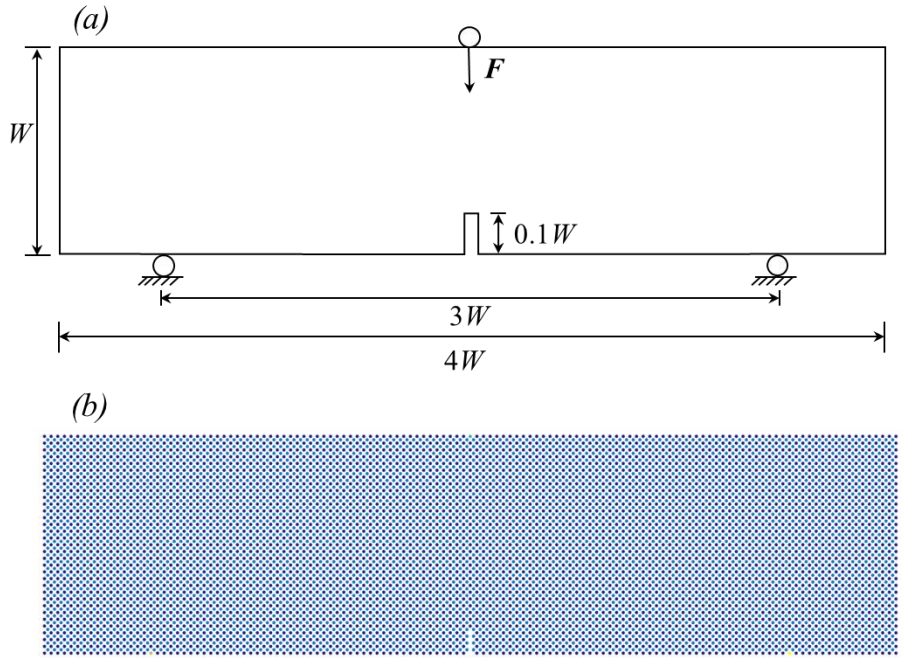

Figure 5.0–14. Setup of three-point bending test: (a) Geometry and boundary conditions, (b) Particle arrangement in Taylor-SPH

In the Taylor-SPH simulations, the notched mortar beams of different sizes are created using material and stress particles as shown in Figure 5.0–14b. Three beams of different sizes (W = 80mm, 160mm and 320mm) are analysed using the same spatial discretisation size of dx = 5mm. Furthermore, to investigate the influence of spatial discretisation on numerical solutions, the smallest beam size (W = 80mm) is further analysed using two smaller particle discretisation sizes of dx = 1mm and 2.5mm. The number of SPH particles corresponding to different beam sizes and domain discretisation is summarised in Table 5.0-3.

Table 5.0-3. Particle numbers for beams of different sizes and discretisation

Testing cases / *Particle type*	*Small size*			*Medium size*	*Large size*
	dx = 1mm	*dx = 2.5mm*	*dx = 5mm*	*dx = 5mm*	*dx = 5mm*
Material particles	25993	4253	1103	4253	16698
Stress particles	25584	4096	1024	4096	16384

The compressive force and displacement of the loading particle located at the top mid-span of the numerical sample are recorded during the simulation and compared with experimental results obtained from the literature. Unlike the experimental tests, which are notch-opening controlled, a direct velocity control is applied on the top mid-span of the beam to simulate a point loading. This approach is considered appropriate since the response of the sample does not exhibit snap-back. However, the loading velocity must be chosen with care to ensure that the numerical results are insensitive to loading, given the fact that SPH is a fully dynamic model, the results of which are highly sensitive to loading velocity. This can be achieved by selecting appropriate loading speeds to ensure that they are within a quasi-static range, i.e. the strain rate of $0.00001s^{-1}$ to $0.1s^{-1}$ (Zhang and Zhao 2014). To demonstrate this, a series of tests using the smallest specimen under a wide range of loading velocities are conducted.

Table 5.0-4 lists the applied loading velocities and the corresponding strain rates and Figure 5.0–15 shows the corresponding force-deflection curves subjected to those loading velocities. The results confirm that the model response is not very sensitive to the loading rate if the loading velocity is chosen to be small enough within the quasi-static range, and higher loading

velocities lead to rate dependent behaviour. Therefore, the loading velocity of 1mm/s is adopted in this test to speed the computational time. In the meantime, a ramp loading type is also used to reduce dynamic effects due to load suddenly applied to the specimen. In summary, the boundary conditions for this test are as follows:

- At the location of bottom rollers, the vertical motion of particles is fixed, thus $v_y = 0,\ \sigma_{xy} = 0$;
- In the top middle of the beam, the vertical velocity component of the loading nodes is imposed, $v_x = 0, v_y = -1\ \mathrm{mm/s}$;
- On free-surface boundaries surrounding the beam, $\sigma_{xx} = 0,\ \sigma_{yy} = 0,\ \sigma_{xy} = 0$.

Table 5.0-4. Loading rates in three-point bending test (dx = 5mm)

Velocity(mm/s)	*Equivalent strain rate (s^{-1})*	*Notes*
0.01	0.000125	within quasi-static loading range
0.05	0.000625	
0.1	0.00125	
0.25	0.003125	
0.5	0.00625	
1	0.0125	
4	0.05	
8	0.1	upper bound of the range
16	0.2	outside the range

Figure 5.0–16 shows a comparison of the load-deflection curves between the experiments and SPH simulations for three different beam sizes. It can be seen that the numerical results agree well with their experimental counterparts and the scale-dependent behaviour is also well captured by the simulation. In all cases, the applied forces undergo three distinct stages: linear elastic until reaching the yielding stresses, then hardening responses up to the peak failure stress and finally softening behaviour until the sample completely fails. The peak loads predicted by the simulations are very close to those obtained from the experiments. For the largest specimen

size (W = 320mm), the simulation slightly under-predicts the experiment result. However, the predicted peak load is still within the range of peak values (850-1010N) reported by Le Bellégo et al. (2003).

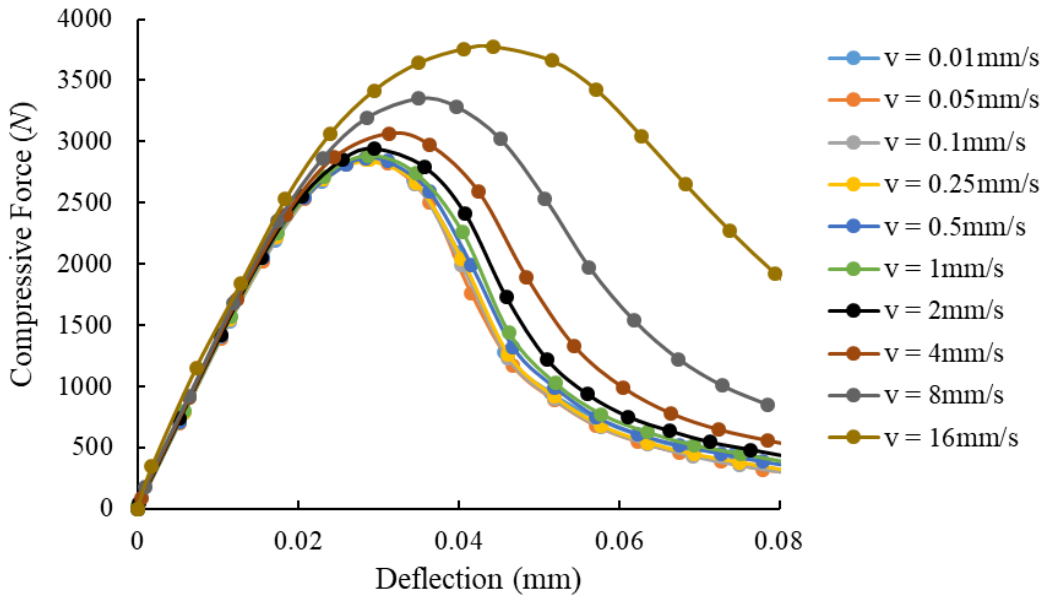

Figure 5.0–15. Load-deflection curves obtained from the three-point bending test for the small specimen subjected to a wide range of loading velocities (dx = 5mm)

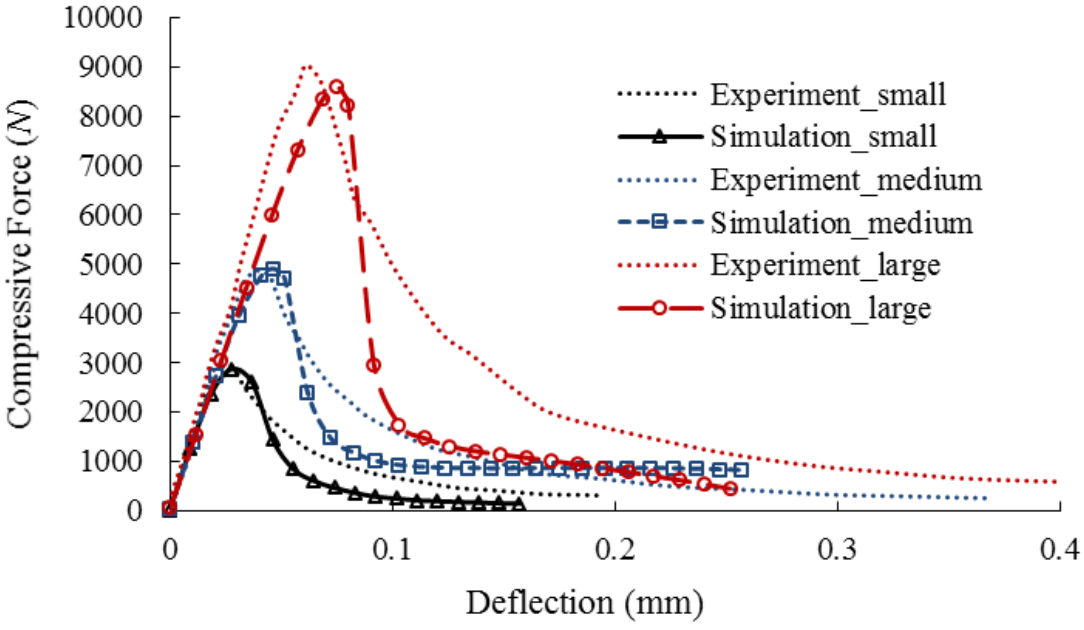

Figure 5.0–16. Force-deflection responses of three different beam sizes

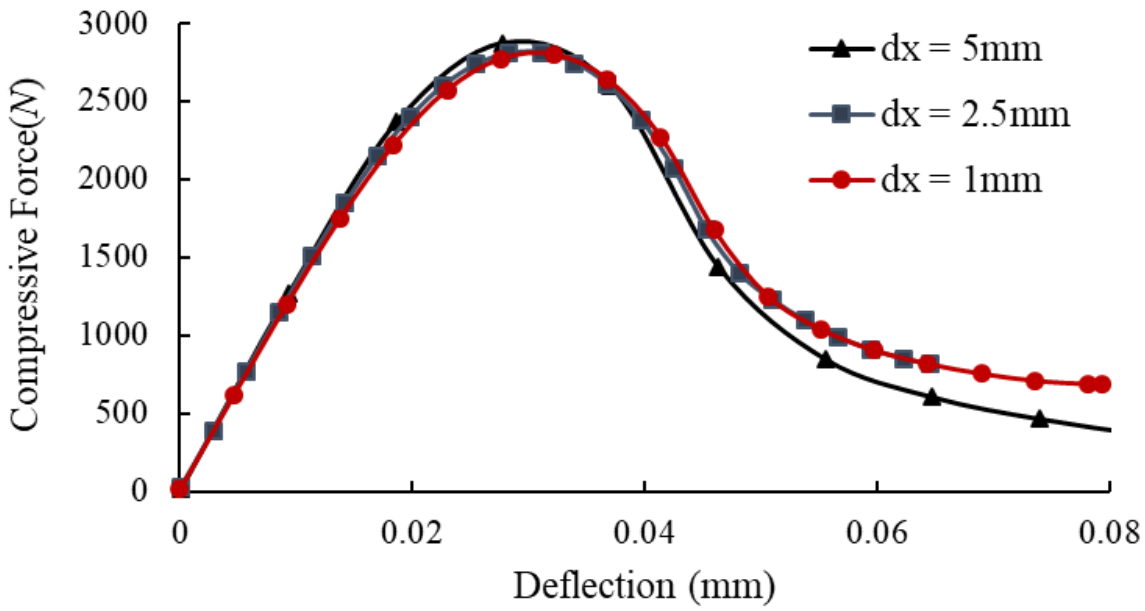

Figure 5.0–17. Force-deflection responses for different spatial discretisation (small beam).

Figure 5.0–17 shows the compressive force and deflection responses of the smallest beam size using three different spatial discretisations. It can be seen that the proposed numerical approach shows convergence with respect to the refinement of the discretisation, and the numerical results are quite consistent with respect to different particle discretisation sizes, thanks to the inclusion of the characteristic length (*H*) in the constitutive model. Figure 5.0–18 illustrates the progressive development of cracking patterns (i.e. via damage evolution and vertical velocity profile) of the smallest beam size using the spatial discretisation of 2.5mm. The corresponding force-deflections of Figure 5.0–18(a) to Figure 5.0–18(e) are marked in Figure 5.0–17. At the initial elastic stage (point *a* in Figure 5.0–17), the horizontal stress distribution is shown in Figure 5.0–18(a_1), indicating that the tensile stress is concentrated near the notch tip prior to the failure of the specimen. The tensile stress continues to develop until the crack is initiated at the notch tip of the specimen as indicated in Figure 5.0–18b_1, which corresponds to the yielding point (*b*) in the load-deflection curve in Figure 5.0–17. The applied force reaches its peak at point *c* in Figure 5.0–17 when the damage propagates to around half the specimen height, as illustrated in Figure 5.0–18c_2. After this point, the specimen reaches the post-peak failure stage where the crack accelerates toward the top mid-span of the specimen, forming a vertical fracture pattern (Figure 5.0–18d_1-e_1). The vertical velocity profile during the test is

also plotted in Figure 5.0–18(a_2-e_2). The numerical results indicate that particles at the middle of the beam move downward while those at the two sides of the beam move upward, which is consistent with observations from the experiments. The results also demonstrate the capability of SPH in simulating large displacement and separation of the numerical samples at their final stages of failure as shown in Figure 5.0–18(e_2), which is difficult for mesh-based methods due to mesh constraints although the initial fracture process can be predicted.

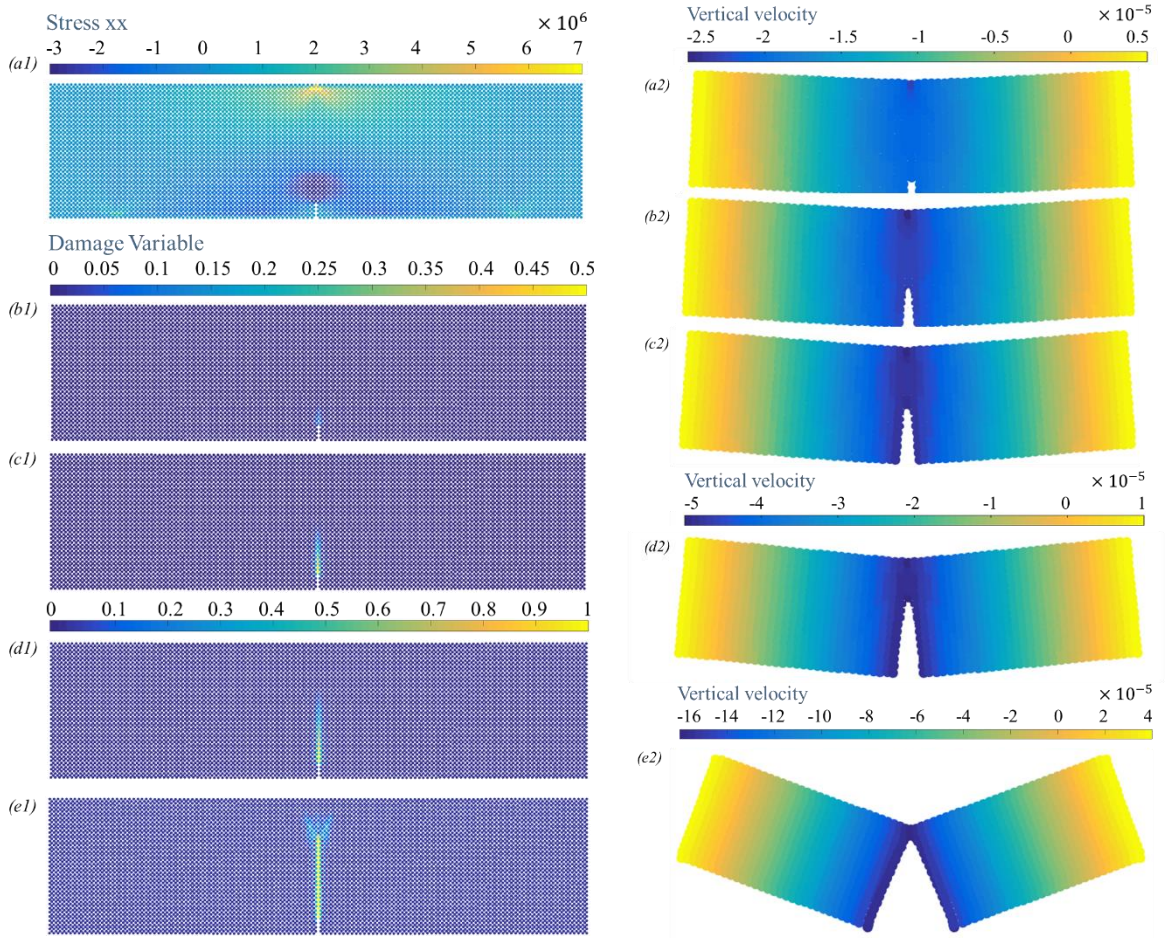

Figure 5.0–18. Progressive failure of the beam specimen in SPH simulation.

5.6.2. Tensile test

In the final example, simulation of the uniaxial tension experiments carried out by Van Vliet and Van Mier (2000) on concrete is conducted to validate the performance of the proposed numerical framework. Figure 5.0–19 shows the experimental and numerical setup of the dog-bone specimen. The dimensions of the specimen are length 1.5D, width D and 0.6D for

maximum and minimum cross sections; and thickness 100mm. Three specimens of different sizes (Size A-C) are created to examine the size-dependent behaviour of rock fracture, and their corresponding dimensions are summarised in Table 5.0-5. In the experiment, a uniaxial tensile force is applied to both ends of the specimen with eccentricity from the vertical axis of symmetry $e = D/50$. The material properties of the concrete are (Vořechovský and Sadílek 2008): Young's modulus $E = 36.95GPa$, Poisson's ratio $v = 0.2$, tensile strength $f_t = 3.2\ MPa$, fracture energy $G_F = 200Nm$.

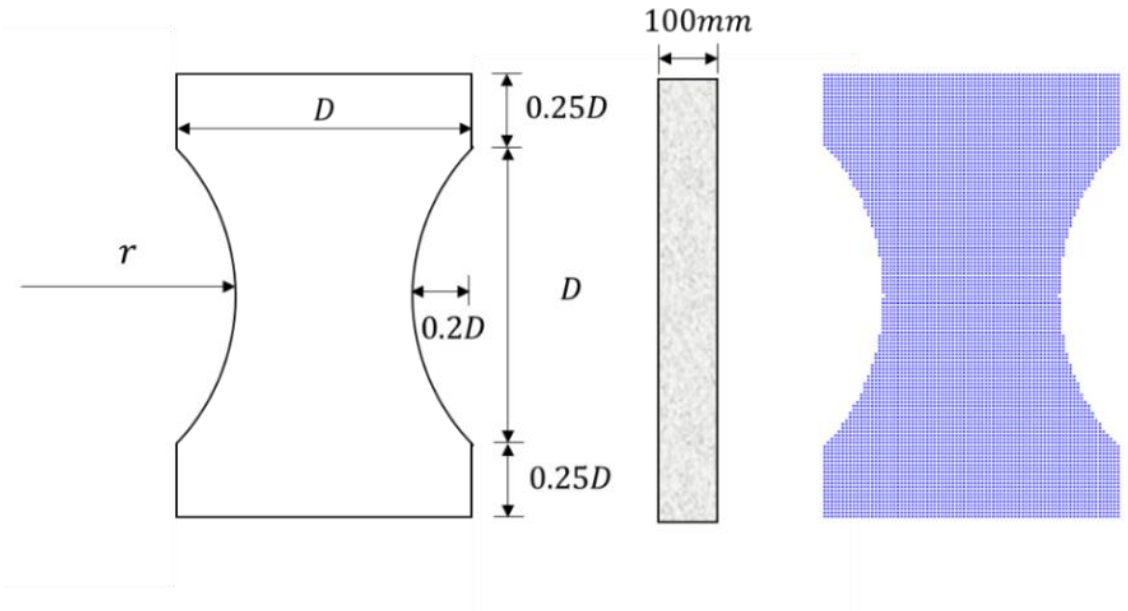

Figure 5.0–19. Geometry and boundary conditions of the tension test.

Table 5.0-5. Specimen dimensions and numbers of SPH particles for specimens of different sizes

Size	***D (mm)***	***r (mm)***	***Material particle***	***Stress particle***
A	50	36.25	522	492
B	100	72.5	2028	1960
C	200	145	7935	7808

In the SPH simulation, the concrete specimens are created by a set of material and stress particles, the numbers of which corresponding to different specimen sizes are summarised in Table 5.0-5. Three specimens of different sizes (Size A-C) are modelled using the same particle

discretisation size of dx=2.5mm. A simplified boundary condition is applied in the SPH simulation, in which a constant vertical velocity is applied to all particles located at both ends of the specimen to provide uniform tensile loading. The detailed boundary conditions in the Taylor SPH simulation are summarised as follows:

1) At the bottom end, a vertical velocity component is imposed, $v_y = -2\mathrm{m}m/s,\ \sigma_{xx} = 0$;

2) At the top end, a vertical velocity component is imposed, $v_y = 2\mathrm{m}m/s, \sigma_{xx} = 0$;

3) At other boundary surfaces of the specimen, $\sigma_{xx} = 0,\ \sigma_{yy} = 0,\ \sigma_{xy} = 0$.

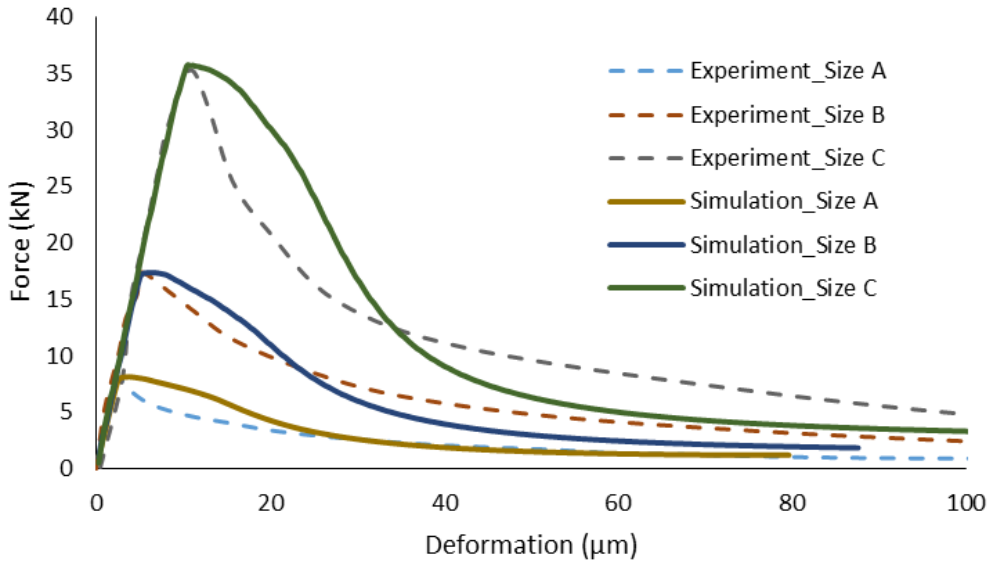

Figure 5.0–20. Tensile force-deformation curve of tension test.

Figure 5.0–20 shows a comparison of the tensile load-displacement curves between SPH simulations and the experiments for three specimens of different sizes. It can be seen the proposed numerical framework successfully predicts the overall response of the load-displacement curves in the experiment and captures well the size-dependent behaviour in the uniaxial tensile test. It is noted here that the same spatial discretisation size is applied for all specimens of different sizes to avoid the influence of spatial discretisation on the rock fracture behaviour. However, it was also proved that this numerical framework is insensitive to spatial discretisation in the previous simulations. The behaviours of the specimen in the uniaxial tensile test can be distinguished by two different stages: elastic linearity and softening failure. In the first stage, the tensile force increases linearly with the increment of displacement until reaching the peak force. The tangent stiffness in all force-displacement curves of different

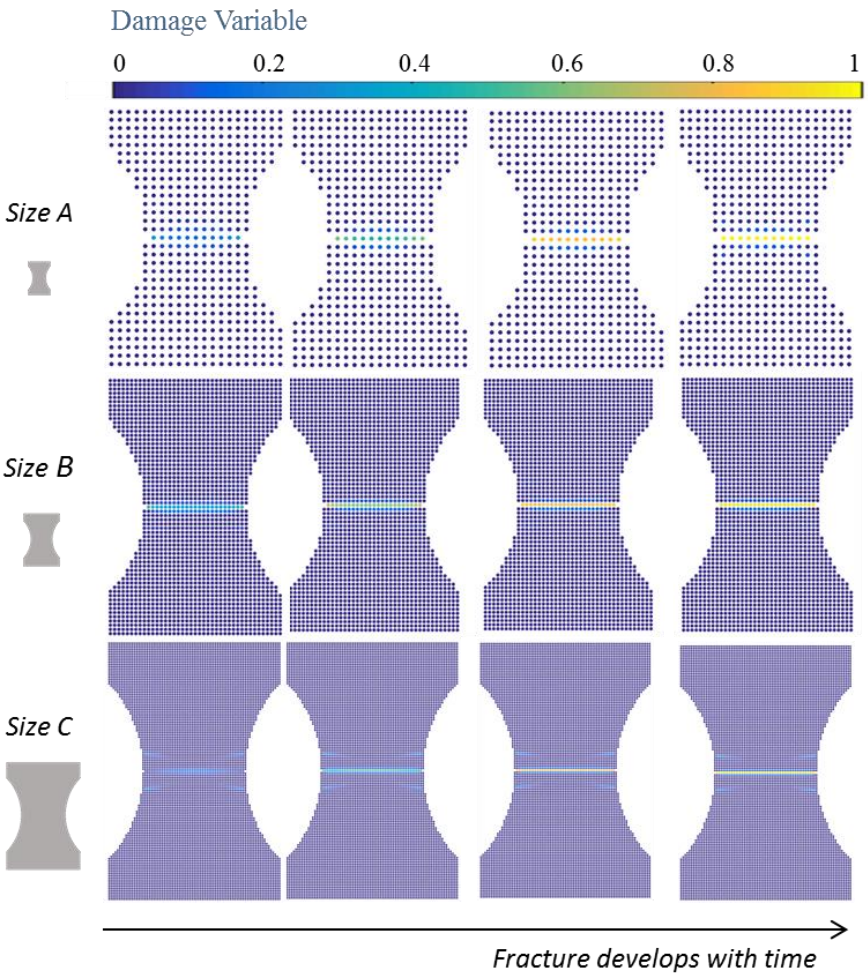

Figure 5.0–21. Profile of damage variable in tension test for three specimens of different sizes

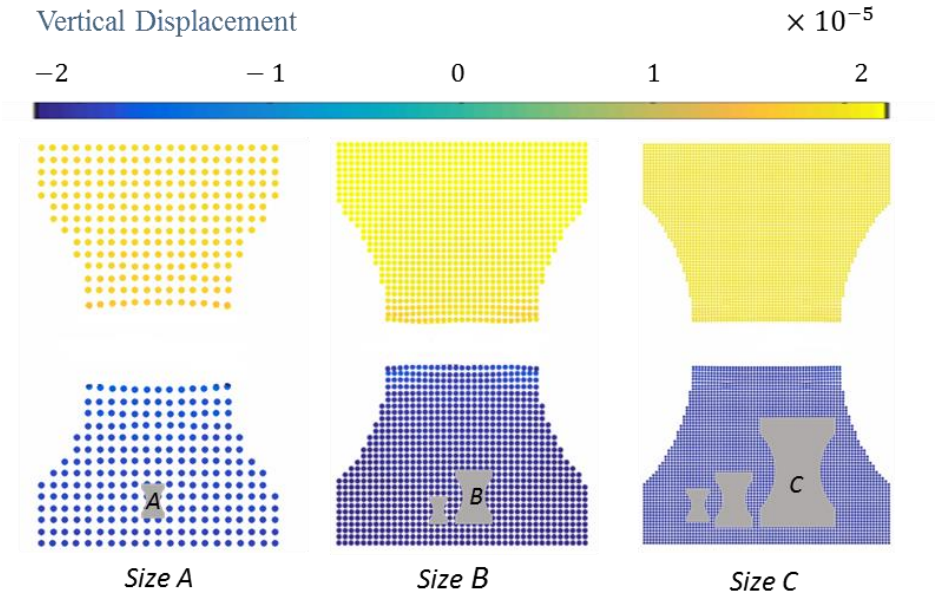

Figure 5.0–22. Profile of vertical displacement in the tension test for three specimens of different sizes.

specimens is the same because of the same parameter input, such as Young's modulus and Poisson's ratio. Then, the specimens experience softening behaviour in which the force decreases with the increment in displacement. The experimental results show a steeper softening response than those observed in the simulations, indicating a more brittle behaviour of rock fracture. A possible reason is the different boundary settings between the SPH simulation and the experiment. Nevertheless, SPH is well able to predict the peak loads of all the specimens obtained in the experiment, suggesting the potential of this framework for capturing the size-dependent behaviour of rock fracture.

Figure 5.0–21 illustrates the progressive development of the damage variable and the fracture patterns of different specimens (A-C) in the SPH simulations. A set of damaged particles forms the fracture geometry of the specimen. It can be seen from the figure that fracture initiates in the middle of the specimens, which is the location of the minimum cross-section, and finally a horizontal fracture pattern is formed in the same location. The vertical velocities for these three specimens of different sizes at the final stage are also plotted Figure 5.0–22. The numerical results indicate that SPH particles at the lower part of specimens move downward while those at the upper part move upward with the same velocity value. The specimens finally split into two equal pieces.

5.7. Conclusions

In this section, a new numerical framework that combines the Taylor SPH method with a new continuum constitutive model with an embedded fracture process zone is developed to enhance the predictive capability of existing computational tools for modelling mode-I rock fracture behaviour. The proposed numerical framework is considered unique for the following reasons:

i) The proposed numerical framework that combines the advantages of SPH and a generic continuum constitutive model with an embedded cohesive fracture is the first rigorous SPH framework to model rock fracture featuring an intrinsic length scale. The approach is therefore scale-dependent, insensitive to spatial discretisation (or mesh independent) and can handle fracture detachment. Furthermore, because the fracture geometry is represented by a set of damaged particles over which the fracture plane is defined and can have any orientation depending on the stress condition, the proposed approach is in principle capable of dealing with complex crack patterns.

ii) Originating from the generic double-scale continuum constitutive framework, the constitutive model in this study was derived by supplying kinematic enrichments based on

observed mechanisms of localised failure followed by the application of the work balance. The approach naturally leads to a scale-dependent constitutive model with an embedded fracture process zone. No ad hoc treatments or regularisations are needed, facilitating its implementation in the SPH. The model tests demonstrate that this approach works well at both material and structural levels.

iii) The proposed scale-dependent numerical framework is capable of accommodating existing cohesive fracture laws and thus can be used for a wide range of fracturing applications involving different types of material. Since the model's formulations are derived for general 3D conditions, it can also be straightforwardly extended to full three-dimensional conditions for large-scale practical applications across disciplines.

The proposed numerical framework was first verified against analytical solutions for one- and two-dimensional tests. It was then used to analyse four laboratory tests, the Brazilian disc test, semicircular bending test, three-point bending test and direct tensile test, and numerical results were compared with their experimental counterparts. Very good agreement with analytical solutions and experimental results was achieved, suggesting that the proposed approach is capable of accurately predicting the mode-I fracturing behaviour. This work provides a fundamental basis bridging the constitutive and structural aspects, via a length scale directly obtained from the particle size, for further developments in SPH towards better modelling of fracture and fragmentation.

Chapter 6

Cracking SPH Particle Framework for Modelling of Mixed-Mode Rock Fracture

6.1. Introduction

In the previous chapter, a novel numerical framework based on the Taylor SPH method was developed for simulating pure mode I rock fractures by incorporating a new continuum size-dependent constitutive model with an embedded cohesive fracture process zone (FPZ). The results demonstrated the capability of the numerical framework to capture the experimentally observed size-dependent behaviour of rock fracture under pure mode I loading conditions. Thanks to the characteristic length scale embedded in the constitutive model, the proposed numerical framework was independent of the spatial discretisation of the computational domain (or mesh independent). This success, as a proof of concept, demonstrated the capabilities and potentials of the SPH with a FPZ idealised as a cohesive model embedded in the particles to capture rock fracture and fragmentation. However, the previous work utilised a mode I constitutive model and thus could only capture mode I rock fracture SPH. Furthermore, the Taylor SPH method employs two sets of particles with a two-step Taylor time integration scheme and requires special treatments for free-surface boundary conditions, resulting in a relatively complex model for simulating rock fracture problems. Further work is required to improve the constitutive model as well as to simplify the Taylor-SPH method to capture rock fracture and fragmentation under mixed-mode loading conditions.

In this study, the SPH-based numerical framework introduced in Chapter 5 to model pure mode I rock fracture is further developed to fully capture rock fracture under mixed-mode loading conditions. However, unlike the previous work, the conventional SPH framework with tensile instability treatment (Bui et al. 2008) instead of the Taylor-SPH method is adopted in this study.

The key advantages of this approach include: i) it does not require an extra set of stress particles; this, in principle, can reduce the overall computational cost, and ii) it does not require any prescribed stress boundary condition on the free surface, thus is more computationally efficient to handle complex applications. In conjunction with the conventional SPH framework, a size-dependent constitutive model with an embedded mixed-mode cohesive fracture is employed for describing the stress states of rock under a wide range of loading conditions. Unlike the previous work which focused on the pure mode I fracture, the FPZ in this study is described by a mixed-mode cohesive fracture law to capture the plastic and damage evolutions of material under various loading conditions. The combination of these two approaches enables the proposed numerical framework to represent fracture geometries by a set of damaged SPH particles, each of which possesses its own FPZ with arbitrary orientations, therefore can naturally capture complex fracture patterns without any predefined topology. The rest of chapter is organised as follows. The general SPH framework for simulating rock materials is briefly presented in Section 6.2. The concept of a size-dependent constitutive model and details of model formulations are then explained in Section 6.3. This is followed by an implicit implementation algorithm of the constitutive model and demonstrations of model behaviour at the constitutive level under complex loading conditions in Section 6.4. Section 6.5 presents three applications to examine the model's capability in predicting mixed-mode rock fractures. Finally, the conclusion drawn from this study is summarised in Section 6.6.

6.2. Traditional SPH approximation of governing equations of rocks

As stated in the introduction, the traditional SPH with tensile instability treatment has been adopted for simulating mixed-mode rock fractures. A corrective technique has also been applied to resolve the general problems of particle deficiency at the boundaries in the traditional SPH. As the details of SPH approximation and the corrective technique were explained in Chapter 3, only key formulations are given next, starting with the governing equations of rocks:

$$\frac{\mathrm{D}\rho}{\mathrm{D}t} = -\rho\nabla\cdot\mathbf{v} \tag{6.1a}$$

$$\frac{\mathrm{D}\mathbf{v}}{\mathrm{D}t} = \frac{1}{\rho}\nabla\cdot\boldsymbol{\sigma} + \mathbf{b} \tag{6.1b}$$

$$\frac{\mathrm{D}\boldsymbol{\sigma}}{\mathrm{D}t} = \mathbf{D}_{ef}:\dot{\boldsymbol{\varepsilon}} \tag{6.1c}$$

where ρ is the material density; $\mathbf{v}$ is the velocity vector; $\boldsymbol{\sigma}$ is the stress tensor; $\mathbf{b}$ is the vector component of acceleration due to external forces; $\mathbf{D}_{ef}$ is the material stiffness matrix;

$\mathrm{D}(\cdot\ )/\mathrm{D}t$ is the material derivative and $\dot{\boldsymbol{\varepsilon}}$ is the strain rate tensor, which can be calculated by velocity through the kinematic relation:

$$\dot{\boldsymbol{\varepsilon}} = [\nabla \cdot \mathbf{v} + (\nabla \cdot \mathbf{v})^{\mathrm{T}}]/2 \tag{6.2}$$

The kernel approximation of a field function $f(x)$ and its spatial derivatives $\nabla f(x)$ are presented as

$$< f(\mathbf{x}) >= \int_{\Omega} f(\mathbf{x}')\, W(\mathbf{x}-\mathbf{x}', h) d\mathbf{x}' \tag{6.3a}$$

$$< \nabla f(\mathbf{x}) >= -\int_{\Omega} f(\mathbf{x}') \cdot \nabla W(\mathbf{x}-\mathbf{x}', h) d\mathbf{x}' \tag{6.3b}$$

where $W(\mathbf{x}-\mathbf{x}', h)$ is the smoothing function, h is the smoothing length defined as an effective domain Ω of the smoothing function; $\nabla W(\mathbf{x}-\mathbf{x}', h)$ is the derivative of W with respect to $\mathbf{x}'$.

In SPH particle approximation, the integral equations, i.e. equations (6.3a) and (6.3b), are discretised into forms of summation over all particles $\boldsymbol{x}_j$ located within the support domain of a given particle at $\boldsymbol{x}_i$, shown as:

$$f(\mathbf{x}_i) = \sum_{j=1}^{N} \frac{m_j}{\rho_j} f(\mathbf{x}_j) W_{ij} \tag{6.4a}$$

$$\nabla f(\mathbf{x}_i) = \sum_{j=1}^{N} \frac{m_j}{\rho_j} f(\mathbf{x}_j) \cdot \nabla W_{ij} \tag{6.4b}$$

where $W_{ij} = W(|\mathbf{x}_i - \mathbf{x}_j|, h))$ and $\nabla W_{ij} = \left(\frac{\mathbf{x}_i - \mathbf{x}_j}{|\mathbf{r}|}\right) \frac{\partial W_{ij}}{\partial r}$

with ∇W_{ij} denoting the gradient of the kernel function W_{ij} evaluated at the location $\mathbf{x}_i$; $|\mathbf{r}| = |\mathbf{x}_i - \mathbf{x}_j|$ is the relative distance between particles i and j; N is the total number of neighbouring particles of i within its supporting domain; and m_j/ρ_j is the volume of particle j.

As the discrete forms of derivatives of the governing equations all make use of the kernel gradient, the next step is to apply a corrective technique to the gradient approximation of SPH. The final corrected gradient approximation is written as:

$$\nabla f(\mathbf{x}_i) = \sum_{j=1}^{N} \frac{m_j}{\rho_j} f(\mathbf{x}_j) \cdot \nabla W_{ij}^{C}(\mathbf{x}_i - \mathbf{x}_j', h) \tag{6.5}$$

where $$\nabla W_{ij}^{C} = \mathbf{L}(\mathbf{x}_i) \nabla W_{ij} \tag{6.6}$$

with the normalisation matrix $\mathbf{L}(\mathbf{x}_i)$ defined as:

$$\mathbf{L}(\mathbf{x}_i) = \begin{pmatrix} \sum_{j=1}^{N} \frac{m_j}{\rho_j}(x_j - x_i)\nabla_{x_i} W_{ij} & \sum_{j=1}^{N} \frac{m_j}{\rho_j}(x_j - x_i)\nabla_{y_i} W_{ij} \\ \sum_{j=1}^{N} \frac{m_j}{\rho_j}(y_j - y_i)\nabla_{x_i} W_{ij} & \sum_{j=1}^{N} \frac{m_j}{\rho_j}(y_j - y_i)\nabla_{y_i} W_{ij} \end{pmatrix}^{-1} \tag{6.7}$$

Finally, the governing equations of rocks in equation (6.1-6.2) can be rewritten as the corrective SPH approximation forms:

$$\frac{\mathrm{D}\rho_i}{\mathrm{D}t} = \sum_{j=1}^{N} m_j(\mathbf{v}_i - \mathbf{v}_j) \cdot \nabla W_{ij}^C \tag{6.8}$$

$$\frac{\mathrm{D}\mathbf{v}_i}{\mathrm{D}t} = \sum_{j=1}^{N} m_j \left(\frac{\boldsymbol{\sigma}_i + \boldsymbol{\sigma}_j}{\rho_i \rho_j} + C_{ij}\right) \cdot \nabla W_{ij}^C + \mathbf{b}_i \tag{6.9}$$

$$\frac{\mathrm{D}\boldsymbol{\sigma}_i}{\mathrm{D}t} = \mathbf{D}_{ef} : \left[\frac{1}{2}\sum_{j=1}^{N} \frac{m_j}{\rho_j}(\mathbf{v}_j - \mathbf{v}_i) \cdot \nabla W_{ij}^C + \frac{1}{2}\left(\sum_{j=1}^{N} \frac{m_j}{\rho_j}(\mathbf{v}_j - \mathbf{v}_i) \cdot \nabla W_{ij}^C\right)^T\right] \tag{6.10}$$

where $\mathbf{C}_{ij}$ is a stabilisation term consisting of artificial viscosity and artificial stress (Bui et al. 2008). The artificial viscosity is proportional to the sound speed of a material and acts as a damping term to regularise stress fluctuation, while the artificial stress is usually utilised to prevent particles clumping under tensile stress. Examples of large-scale slope failure in (Bui et al. 2008, Bui et al. 2011) demonstrated that the tensile instability problem could be completely removed by adding a stabilisation term. In this study, the artificial viscosity is the only used stabilisation term used to regularise the strong shockwave propagation in hard rocks. This is because the sound speed propagating in hard rocks is often much faster than that in soft rocks, or in other words, the elastic Young's modulus of hard rocks is often very large. This results in a greater influence of artificial viscosity in the momentum equation and thus mitigation of the tensile instability problem. However, when it comes to examples related to soft rocks, both the artificial viscosity and artificial stress must be adopted, because the artificial viscosity is not sufficient to mitigate the tensile instability problem. The inclusion of artificial stress helps to prevent particles from coming closer by applying a repulsive force between neighbouring particles when they are subjected to tensile loading. The constant parameters for the artificial viscosity in this study are chosen as 0.5 and 0 for the terms associated with the linear and quadratic in the velocity divergence, respectively; the constant parameter for the artificial stress is selected as 0.2.

6.3. A mixed-mode continuum constitutive model for rock fracture

In this study, the double scale model developed by Nguyen et al. (2012), Nguyen et al. (2014) is adopted for mixed-mode rock fracture applications, due to its advantage of insensitivity to

discretisation compared to other models. This model was employed with success in the SPH for simulating rock fracture under pure mode I loading, introduced in Chapter 5. Now, the model is extended to mixed-mode fracture problems of rocks by introducing a new mixed-mode cohesive fracture law into a double-scale model to capture post-localisation behaviour of material within the FPZ in mixed-mode tests. The final constitutive relationship between macro stress rate and macro strain rate in the double scale model is expressed as:

$$\dot{\boldsymbol{\sigma}} = \dot{\boldsymbol{\sigma}}_{out} = \mathbf{a}_0 \left(\dot{\boldsymbol{\varepsilon}} - \frac{1}{H} \mathbf{n} [\![\dot{\mathbf{u}}]\!] \right) \tag{6.11}$$

where the rate of displacement jump $[\![\dot{\mathbf{u}}]\!]$ can be calculated by an elastic stiffness matrix $\mathbf{a}_0$ and the tangent cohesive stiffness $\mathbf{K}^t$ in cohesive fracture law:

$$[\![\dot{\mathbf{u}}]\!] = \left(\frac{1}{H} \mathbf{n}^T \mathbf{a}_0 \mathbf{n} + \mathbf{K}^t \right)^{-1} \mathbf{n}^T \mathbf{a}_0 \dot{\boldsymbol{\varepsilon}} = \mathbf{C}^{-1} \mathbf{n}^T \mathbf{a}_0 \dot{\boldsymbol{\varepsilon}} \tag{6.12}$$

It can be seen from equations (6.11-6.12) that the overall stress-strain relationship takes into account the corresponding responses of material both inside and outside the FPZ. A length scale parameter *H* is also embedded in the final formulation, giving the model capability of capturing the size-dependent behaviour of rocks at the constitutive level. Moreover, the double scale model has high feasibility for incorporating any cohesive fracture law for material inside FPZ. An example for one of those models is introduced next.

6.3.1. Mixed-mode cohesive fracture law

A mixed-mode cohesive fracture law coupling damage mechanics and plasticity theory is employed in this study to describe the behaviour of rock material inside a FPZ. The cohesive law relates the tractions ($\mathbf{t}_c$) and the corresponding displacement jumps ($\mathbf{u}_c$) across two faces of the FPZ. For notational simplicity, subscript *c* is reserved in this study for all variables in the local coordinate system, representing the local behaviour of material inside the FPZ, while subscripts n and s denote normal and shear directions, respectively. The incremental displacement jump ($d\mathbf{u}_c$) can be partitioned into elastic ($d\mathbf{u}_c^e$) and inelastic $\left(d\mathbf{u}_c^p\right)$ parts, standing for reversible and irreversible displacements, respectively:

$$d\mathbf{u}_c = d\mathbf{u}_c^e + d\mathbf{u}_c^p \tag{6.13}$$

The traction state of material in FPZ can be calculated by the elastic displacement jump as:

$$d\mathbf{t}_c = \mathbf{P}\mathbf{K}_{c0}^s d\mathbf{u}_c^e \tag{6.14}$$

with

$$\mathbf{K}_{c0}^{s} = \begin{bmatrix} K_n & 0 \\ 0 & K_s \end{bmatrix} \tag{6.15}$$

$$\mathbf{P} = \begin{cases} \begin{bmatrix} 1-D & 0 \\ 0 & 1-D \end{bmatrix} & when\ t_{c(n)} \geq 0 \\ \begin{bmatrix} 1 & 0 \\ 0 & 1-D \end{bmatrix} & when\ t_{c(n)} < 0 \end{cases} \tag{6.16}$$

where $\mathbf{K}_c^s = \mathbf{P}\mathbf{K}_{c0}^s$ is the secant stiffness matrix of the cohesive fracture zone; $\mathbf{K}_{c0}^s$ denotes the elastic secant stiffness matrix of the cohesive fracture zone; $\mathbf{P}$ is a parameter matrix with respect to normal traction $t_{c(n)}$. The inclusion of $\mathbf{P}$ allows the cohesive model to account for different effects of damage on the tractions under compression and tensional conditions. D is the damage variable characterising the degradation of material strength due to fracture. When D is zero, the material is elastic, and the material is fully damaged when D approaches unity. Thus, the evolution of damage variable D is expressed as an exponential function of the accumulated inelastic displacement jump, written as:

$$D = \max\left(D_{pre}, 1 - e^{-(\frac{u_n^p}{\delta_0} + \frac{u_s^p}{\delta_0})}\right) \tag{6.17}$$

where D_{pre} is the damage variable in the previous step, δ_0 is the displacement jump corresponding to the peak normal traction, u_n^p and u_s^p are respectively normal and shear inelastic displacement jumps, which are introduced later. Unlike the linear or exponential softening law described in previous work in which the damage variable is calculated based only on the degraded tensile strength, the incorporation of both normal and shear inelastic displacement jumps into the evolution of damage variable gives the model the capability of capturing material failure under both tensile and shear loading.

Provided that the traction-displacement jump relationship and the evolution of damage variable are determined, a failure function is required to cater for the combined influence of normal and shear tractions. To be specific, the failure function is employed to determine whether material is within elastic or plastic-damage regimes and then to compute the current traction states depending on different cases. In this study, a modified form of the Mohr-Coulomb failure criterion is adopted to represent failure states, expressed as:

$$f(t_n, t_s, D) = {t_s}^2 - 2c_0(1-D)\tan\phi\,(\sigma_{t0}(1-D) - t_n) - \tan^2\phi\,({t_n}^2 - (\sigma_{t0}(1-D))^2) \tag{6.18}$$

where ϕ is the friction angle of material; c_0 and σ_{t0} represent the initial cohesion and tensile strength, which are the controlling variables for the tensile loading and shear loading respectively. Those three values are unchanged during the calculation process, but the

geometry of the yield function changes with the evolution of damage variable D, as illustrated in Figure 6.0–1.

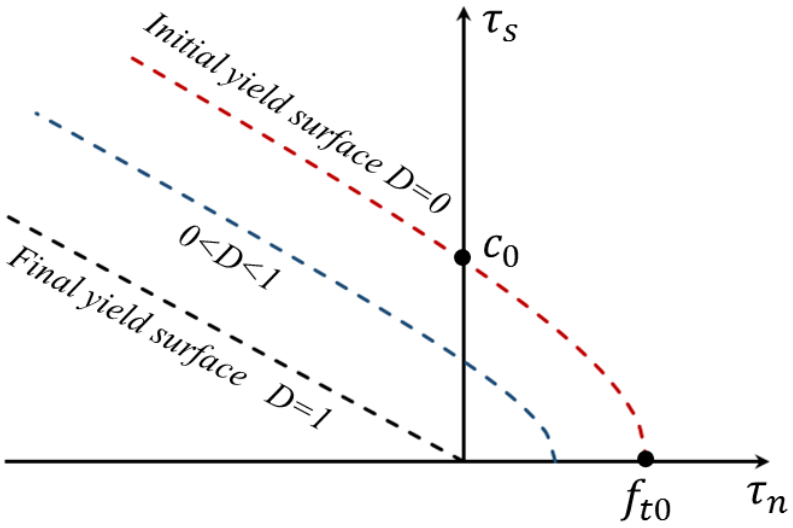

Figure 6.0–1. Illustration of the shrinking of yield function against the evolution of the damage variable.

A non-associated plastic potential is also used in this study, which takes into account the effect of dilatancy angle, the formulation of which is written as:

$$g(t_n, t_s, D) = {t_s}^2 - 2c_0(1-D)\tan\psi\,(\sigma_{t0}(1-D) - t_n) - \tan^2\psi\,({t_n}^2 - (\sigma_{t0}(1-D))^2) \quad (6.19)$$

where ψ is the dilatancy angle of material. The incremental plastic displacement jump can be computed by the non-associated flow rule as:

$$d\boldsymbol{u}_{\mathrm{c}}^{\mathrm{p}} = d\lambda \frac{\partial g}{\partial \boldsymbol{t}_{\mathrm{c}}} \quad (6.20)$$

where $d\lambda$ is the plastic multiplier, which is a non-negative and can be determined based on the current traction state and the loading history.

In the above cohesive fracture model there is a set of constitutive parameters, including an elastic secant stiffness $\mathbf{K}_{c0}^{s}$ consisting of normal stiffness K_n and shear stiffness K_s, a parameter δ_0 controlling the evolution of damage, and shear strength parameters such as initial tensile strength σ_{t0}, initial cohesion c_0, friction angle ϕ and dilatancy angle ψ. The normal stiffness K_n stands for the initial elastic stiffness of material in the FPZ, which can thus be calculated by $K_n = E/h$, where h is the thickness of the FPZ. As already mentioned, the FPZ of rock is

regarded as having zero-thickness, thus the value of the normal elastic stiffness K_n approaches infinity. As a result, K_n is selected to be a few orders of magnitude larger than E for numerical simulation. The shear stiffness K_s is the elastic stiffness in the pure shear test and can be computed from the experiment. Since the present model focuses mainly on rock failure under pure mode I and mixed tensile-shear loading, the shear stiffness K_s is simply selected to be a similar order of magnitude to Young's modulus *E*. Another key parameter to be determined is δ_0, which controls softening behaviour in the cohesive fracture model. The value of δ_0 must be satisfied with the requirement that the area under the traction curve is equal to the input fracture energy, that is $\int_0^{u_f} t_n du_n = G_{fI}$, depicted in Figure 6.0–2. Other material parameters (σ_{t0}, c_0, ϕ, ψ) can be estimated from certain laboratory experiments (e.g. uniaxial compression, shear and triaxial tests) and those values are directly used in our simulation tests.

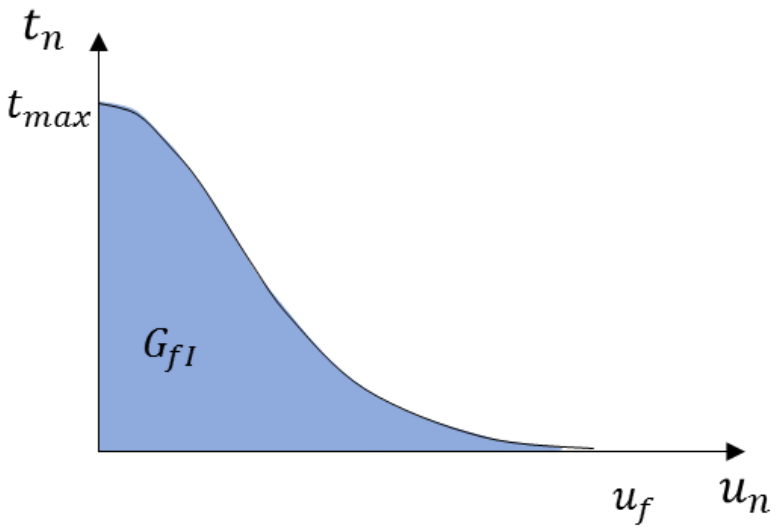

Figure 6.0–2. Determination of model parameters in traction-displacement jump curves

6.3.2. Stress return algorithm of cohesive fracture law

An appropriate numerical algorithm is required to correctly update tractions from a given displacement jump. In this work, a semi-implicit stress return algorithm is adopted. Given an incremental displacement jump $\mathrm{d}\mathbf{u}_\mathrm{c}$, the predictor traction $\mathbf{t}_\mathrm{c}^{\mathrm{trial}}$ can be calculated using Equation (6.14). The trial yield function f^{trial} based on the elastic traction predictor is then computed using Equation (6.18). If the trial yield function $f^{trial} < 0$, no further action is

required and the trial traction is accepted as correct. In contrast, if the trial traction $f^{trial} \geq 0$, the correct stress can be calculated using the Taylor expansion of the yield function, written as:

$$f = f^{trial} + \frac{\partial f}{\partial \mathbf{t}_c}^T \frac{\partial \mathbf{t}_c}{\partial \mathbf{u}_c^p} d\mathbf{u}_c^p + \frac{\partial f}{\partial \mathbf{t}_c}^T \frac{\partial \mathbf{t}_c}{\partial D} dD + \frac{\partial f}{\partial D} dD = 0 \tag{6.21}$$

where dD can be expressed as a function of $d\lambda$ based on the Equations (6.17) and (6.20):

$$dD = \frac{\partial D}{\partial u_n^p} du_n^p + \frac{\partial D}{\partial u_s^p} du_s^p = d\lambda \left(\frac{\partial D}{\partial u_n^p} \frac{\partial g}{\partial t_n} + \frac{\partial D}{\partial u_s^p} \frac{\partial g}{\partial t_s} \right) = d\lambda R \tag{6.22}$$

Substituting Equations (6.22) and (6.20) into equation (6.21), the plastic multiplier $d\lambda$ is calculated as:

$$d\lambda = \frac{-f^{trial}}{\frac{\partial f}{\partial \mathbf{t}_c}^T \frac{\partial \mathbf{t}_c}{\partial \mathbf{u}_c^p} \frac{\partial g}{\partial \mathbf{t}_c} + \frac{\partial f}{\partial \mathbf{t}_c}^T \frac{\partial \mathbf{t}_c}{\partial D} R + \frac{\partial f}{\partial D} R} \tag{6.23}$$

Once $d\lambda$ is determined, the change of damage variable dD and the increment of plastic displacement jump $d\mathbf{u}_c^p$ can be calculated accordingly by solving equations (6.22) and (6.20). Finally, the corrected traction is returned using the following equation as:

$$\mathbf{t}_c = \mathbf{t}_c^{trial} + \frac{\partial \mathbf{t}_c}{\partial \mathbf{u}_c^p} d\mathbf{u}_c^p + \frac{\partial \mathbf{t}_c}{\partial D} dD \tag{6.24}$$

The stress return algorithm of the cohesive fracture law is summarised in Algorithm 6.1.

Algorithm 6.1: Stress return algorithm of cohesive fracture law

Input value: $\Delta \mathbf{u}_c^{trial}$*; Output value:* $\Delta \mathbf{t}_c$

1. Calculate trial local traction increment: $\Delta \mathbf{t}_c^{trial} = \mathbf{P}\mathbf{K}_{c0}^s \Delta \mathbf{u}_c^{trial}$
2. Calculate trial yielding surface:
   $f^{trial} = \left({t_{s1}}^{trial^2} + {t_{s2}}^{trial^2} \right) - 2c_0(1-D)\tan\phi \left(\sigma_{t0}(1-D) - {t_n}^{trial} \right) - \tan^2\phi \left({t_n}^{trial^2} - (\sigma_{t0}(1-D))^2 \right)$
3. If $f^{trial} < 0$ then
4. $\Delta \mathbf{t}_c = \mathbf{t}_c^{trial}, \Delta D = 0, \Delta \mathbf{u}_c^p = 0$
5. else
6. Calculate $\Delta\lambda$: $\Delta\lambda = \frac{-f^{trial}}{\frac{\partial f}{\partial \mathbf{t}_c}^T \frac{\partial \mathbf{t}_c}{\partial \mathbf{u}_c^p} \frac{\partial g}{\partial \mathbf{t}_c} + \frac{\partial f}{\partial \mathbf{t}_c}^T \frac{\partial \mathbf{t}_c}{\partial D} R + \frac{\partial f}{\partial D} R}$
7. Calculate increment of local plastic displacement jump $\Delta \mathbf{u}_c^p = \Delta\lambda \frac{\partial g}{\partial \mathbf{t}_c}$
8. Calculate increment of damage variable: $\Delta D = \Delta\lambda R$
9. Calculate increment of traction: $\Delta \mathbf{t}_c = \Delta \mathbf{t}_c^{trial} + \frac{\partial \mathbf{t}_c}{\partial \mathbf{u}_c^p} \Delta \mathbf{u}_c^p + \frac{\partial \mathbf{t}_c}{\partial D} \Delta D$
10. Endif
11. Update local plastic displacement jump, damage variable

$$D = D + \Delta D;\ \mathbf{u}_c^p = \mathbf{u}_c^p + \Delta \mathbf{u}_c^p$$

6.4. Implicit algorithm of continuum constitutive model

After the introduction of key formulations of the double scale framework and the cohesive fracture law, the criteria for determining fracture initiation and orientation are first explained in this section. Then an implicit algorithm for stress updating based on traction continuity condition is presented, followed by its performance at the constitutive level at the end of this section.

6.4.1. Fracture initiation and its orientation

As stated in Section 3, the material is initially treated as homogeneous and elastic until the local fracture is triggered, after which the response of the material bifurcates into two different branches for material inside and outside FPZ, respectively. Therefore, an important question now is how to detect the correct onset of fracture and also determine the associated orientation of the fracture plane. In this study, a scanning technique is used in which the local tractions of all possible fracture orientations $\mathbf{n}$ varying from 0° to 180° are calculated as follows:

$$\mathbf{t}_c = \mathbf{R}\mathbf{n}^T\boldsymbol{\sigma} \tag{6.25}$$

Then, the yield function value $f(t_n, t_s, D)$ corresponding to each traction is calculated. Fracture initiates when a traction state (t_n^*, t_s^*) at any rotational plane gives the maximum positive yield function $f(t_n^*, t_s^*, D)$ in equation (6.18). Once fracture is triggered, scanning is stopped and the fracture orientation is saved for the rest of the calculation.

6.4.2. Implicit stress-return algorithm for the traction-continuity condition

Beyond the onset of fracture, the homogeneity of material is lost and the responses of material inside and outside FPZ at the given strain increment will be different. Those two responses are coupled via the traction continuity across the boundaries of the FPZ. Thus, a stress return mapping algorithm is required for the constitutive model to track the evolution of two distinct material responses, with the traction continuity condition guaranteed at the same time. In this study, the implicit algorithm proposed by Nguyen et al. (2016) is adopted, beginning with calculation of the elastic displacement jump increment $d\mathbf{u}_c^{\text{trial}}$ from the input of the strain increment $\mathrm{d}\boldsymbol{\varepsilon}$ based on the assumption that the material is under elastic behaviour:

$$d\mathbf{u}^{trial} = (\frac{1}{H}\mathbf{n}^T\mathbf{a}_0\mathbf{n} + \mathbf{R}^T\mathbf{K}_c^s\mathbf{R})^{-1}\mathbf{n}^T\mathbf{a}_0\mathrm{d}\boldsymbol{\varepsilon} \tag{6.26}$$

The trial macro stress $\boldsymbol{\sigma}^{trial}$ and trial local traction $\mathbf{t}_c^{trial}$ can be then calculated from $\mathrm{d}\mathbf{u}^{trial}$ using Equations (6.11) and (6.25), respectively. The local trial traction $\mathbf{t}_c^{trial}$ is then substituted

back to the yield function f^{trial} as formulated in Equation (6.18). If $f^{trial} < 0$, the assumption of elasticity is correct and all variables at the new state are updated elastically. Otherwise, the material is under inelastic loading and the stress return algorithm in Section 6.3.2 needs to be applied to calculate the corrected traction vectors $\mathbf{t}_c$. In that case, the traction continuity, $\mathbf{n}^T\,\boldsymbol{\sigma} - \mathbf{t}_{in} = \mathbf{0}$ where $\mathbf{t}_{in} = \mathbf{R}^T\,\mathbf{t}_c$ is not met, thus an iteration process is required to satisfy the condition, starting with calculation of the traction residual across FPZ as:

$$\mathbf{r} = \mathbf{n}^T\boldsymbol{\sigma} - \mathbf{t}_{in} \tag{6.27}$$

Thus, the first order Taylor expansion at the new state in terms of traction residual can be expressed as:

$$\mathbf{r}^{new} = \mathbf{r}^{old} + \mathbf{n}^T\delta\boldsymbol{\sigma} - \delta\mathbf{t}_{in} = \mathbf{r}^{old} - \frac{1}{H}\mathbf{n}^T\mathbf{a}_0\mathbf{n}\delta\mathbf{u} - \mathbf{K}^t\delta\mathbf{u} \tag{6.28}$$

where $\delta\boldsymbol{\sigma}$ and $\delta\mathbf{t}_{in}$ are the iterative macro-stress and the iterative inside traction in the global coordinate in the new state, calculated by the equations:

$$\delta\boldsymbol{\sigma} = -\frac{1}{H}\mathbf{n}^T\mathbf{a}_0\mathbf{n}\delta\mathbf{u} \tag{6.29}$$

$$\delta\mathbf{t}_{in} = \mathbf{K}^t\delta\mathbf{u} \tag{6.30}$$

where $\mathbf{K}^t$ is the tangent stiffness of the cohesive fracture law which is introduced in the next section. It should be noted here that the iterative strain $\delta\boldsymbol{\varepsilon}$ is neglected in Equation (6.29) as it was considered during the calculation of trial stress before performing the iteration process. By enforcing the requirement $\mathbf{r}^{new} = 0$ and combining Equations (6.28-6.30), the iterative displacement jump $\delta\mathbf{u}$ can be solved as:

$$\delta\mathbf{u} = \left(\frac{1}{H}\mathbf{R}\mathbf{n}^T\mathbf{a}_0\mathbf{n} + \mathbf{R}^T\mathbf{K}_c^t\mathbf{R}\right)^{-1}\mathbf{r}^{old} \tag{6.31}$$

Once $\delta\mathbf{u}$ has been computed, the iterative stress can be calculated based on Equation (6.29). In the meantime, the iterative traction in the local coordinate $\delta\mathbf{t}_c$ can be obtained from $\delta\mathbf{u}_c$ following a stress-return algorithm (Algorithm 1). The iteration process as described will keep repeating until the traction residual $\mathbf{r}$ meets the convergence criterion:

$$\frac{\|\mathbf{r}^{old}\|}{\|\mathbf{n}^T\boldsymbol{\sigma}_0\|} \leq \text{TOLERANCE} \tag{6.32}$$

where TOLERANCE is a very small value and is set as 10^{-4} in this study.

6.4.3. Calculation of tangent stiffness of cohesive fracture law

To complete the implicit algorithm, the tangent stiffness $\mathbf{K}_c^t$ of the cohesive fracture law appearing in Equation (6.31) must be calculated explicitly for each iteration step. It can be achieved by using the consistency condition with respect to yield function f:

$$df = \frac{\partial f}{\partial \mathbf{t}_c} \mathrm{d}\mathbf{t}_c + \frac{\partial f}{\partial D} dD = 0 \tag{6.33}$$

As the local traction $\mathbf{t}_c$ is a function of the displacement jump, plastic displacement jump and damage variable, the incremental form of local traction can be expressed as:

$$d\mathbf{t}_c = \frac{\partial \mathbf{t}_c}{\partial \mathbf{u}_c} d\mathbf{u}_c + \frac{\partial \mathbf{t}_c}{\partial \mathbf{u}_c^p} d\mathbf{u}_c^p + \frac{\partial \mathbf{t}_c}{\partial D} dD \tag{6.34}$$

Substituting Equations (6.20), (6.22) and (6.34) into Equation (6.33) and solving the equation obtained for $d\lambda$ leads to:

$$d\lambda = \frac{-\frac{\partial f}{\partial \mathbf{t}_c}\frac{\partial \mathbf{t}_c}{\partial \mathbf{u}_c}}{\frac{\partial f}{\partial \mathbf{t}_c}\frac{\partial g}{\partial \mathbf{t}_c}\frac{\partial \mathbf{t}_c}{\partial \mathbf{u}_c^p} + \frac{\partial f}{\partial \mathbf{t}_c}\frac{\partial \mathbf{t}_c}{\partial D}R + \frac{\partial y}{\partial D}R} d\mathbf{u}_c = \mathbf{M} d\mathbf{u}_c \tag{6.35}$$

where $\mathbf{M}$ is a one by three matrix.

By combining Equations (6.34-6.35), the increment of local traction can be written as:

$$d\mathbf{t}_c = \left(\frac{\partial \mathbf{t}_c}{\partial \mathbf{u}_c} + \frac{\partial \mathbf{t}_c}{\partial \mathbf{u}_c^p}\frac{\partial g}{\partial \mathbf{t}_c}\mathbf{M} + R\mathbf{M} \right) d\mathbf{u}_c \tag{6.36}$$

where the tangent stiffness $\mathbf{K}_c^t$ of the cohesive fracture law in the loading case is formulated as:

$$\mathbf{K}_c^t = \frac{\partial \mathbf{t}_c}{\partial \mathbf{u}_c} + \frac{\partial \mathbf{t}_c}{\partial \mathbf{u}_c^p}\frac{\partial g}{\partial \mathbf{t}_c}\mathbf{M} + R\frac{\partial \mathbf{t}_c}{\partial D}\mathbf{M} \tag{6.37}$$

6.4.4. Summary of the implicit algorithm of the constitutive model

This section presents the summary of the implicit algorithm for stress update and all other internal variables from the input of strain increment, shown as Algorithm 6.2. This implicit algorithm includes all the loading scenarios from the elastic stage to final failure stage.

Algorithm 6.2: Implicit algorithm of double-scale model

Input value: $\Delta\boldsymbol{\varepsilon}$*; Output value:* $\Delta\boldsymbol{\sigma}$

1. Initial value: $para = 0, D = 0$;
2. Update strain for $t = N + 1$, $\boldsymbol{\varepsilon}^{N+1} = \boldsymbol{\varepsilon}^{N} + \Delta\boldsymbol{\varepsilon}$;
3. **If ($para = 0$) then** *% Haven't cracked*
4. Calculate elastic trial stress $\boldsymbol{\sigma}^{trial}$ for $t = N + 1$;
5. Scan and find possible fracture plane;
6. Calculate trial traction in global coordinate: $\mathbf{t}^{trial} = \mathbf{n}^{T}\,\boldsymbol{\sigma}^{trial}$;
7. Calculate trial traction in local coordinate: $\mathbf{t}_c^{trial} = \mathbf{R}\mathbf{t}^{trial}$;
8. Calculate maximum failure function:

$$f_{max} = \left({t_{s1}}^{trial^2} + {t_{s2}}^{trial^2}\right) - 2c_0(1-D)\tan\phi\left(\sigma_{t0}(1-D) - {t_n}^{trial}\right) - \tan^2\phi\left({t_n}^{trial^2} - (\sigma_{t0}(1-D))^2\right)$$

9. If ($f_{max} < 0$) then
10. Update stress and all the internal variables:

$$D^{N+1} = D^{N}, \boldsymbol{\sigma}^{N+1} = \boldsymbol{\sigma}^{trial}$$

11. Elseif ($f_{max} \geq 0$) then *% first crack*
12. $Para = 1$
13. Record normal vector $\mathbf{n}$ and rotation matrix $\mathbf{R}$
14. Go to *line 17*
15. Endif
16. **Elseif ($para = 1$) then** *% Already cracked*
17. Calculate increment of trial displacement jump in global coordinate:

$$\Delta\mathbf{u}^{trial} = \left(\frac{1}{H}\mathbf{n}^{T}\mathbf{a}_0\mathbf{n} + \mathbf{R}^{\mathrm{T}}\mathbf{K}_c^{s}\mathbf{R}\right)^{-1}\mathbf{n}^{T}\mathbf{a}_0\Delta\boldsymbol{\varepsilon} = \mathbf{C}^{-1}\mathbf{n}^{T}\mathbf{a}_0\Delta\boldsymbol{\varepsilon}$$

18. Calculate increment of displacement jump in local coordinate: $\Delta\mathbf{u}_c^{trial} = \mathbf{R}\Delta\mathbf{u}$
19. Calculate trial stress increment:$\Delta\boldsymbol{\sigma} = \mathbf{a}_0 : \left(\Delta\boldsymbol{\varepsilon} - \frac{1}{H}\mathbf{n}^{T}\Delta\mathbf{u}\right)$
20. Update trial stress for $t = N + 1$: $\boldsymbol{\sigma}^{trial} = \boldsymbol{\sigma}^{N} + \Delta\boldsymbol{\sigma}$
21. Calculate trial traction in local coordinate $\mathbf{t}_c^{trial} = \mathbf{t}_c^{N} + \mathbf{R}\mathbf{n}^{T}\Delta\boldsymbol{\sigma}$
22. Calculate failure function:

$$f = \left({t_{s1}}^{trial^2} + {t_{s2}}^{trial^2}\right) - 2c_0(1-D)\tan\phi\left(\sigma_{t0}(1-D) - {t_n}^{trial}\right) - \tan^2\phi\left({t_n}^{trial^2} - (\sigma_{t0}(1-D))^2\right)$$

23. If ($f \leq 0$) then *% elastic unloading/reloading*
24. Update stress and all the internal variables:

$$D^{N+1} = D^{N}, \boldsymbol{\sigma}^{N+1} = \boldsymbol{\sigma}^{trial}, \mathbf{t}^{N+1} = \mathbf{t}^{trial}, \mathbf{t}_c^{N+1} = \mathbf{t}_c^{trial}$$

25. Elseif ($f > 0$) then *% inelastic loading*
26. Calculate $\Delta\mathbf{t}_c$ from $\Delta\mathbf{u}_c^{trial}$ following the procedure starting at step 6 in Algorithm 1;
27. Update traction $\mathbf{t}_c = \mathbf{t}_c^{N} + \Delta\mathbf{t}_c$ and calculate residual $\mathbf{r} = \mathbf{n}^{T}\boldsymbol{\sigma}^{trial} - \mathbf{R}^{T}\mathbf{t}_c$;
28. While $\|\mathbf{r}\| \geq$ TOLERANCE
29. Calculate $\mathbf{K}_c^{t}$ with the new updated internal variable;
30. Calculate residual displacement in global coordinate:$\delta\mathbf{u} = \left(\frac{1}{H}\mathbf{n}^{T}\mathbf{a}_0\mathbf{n} + \mathbf{R}^{T}\mathbf{K}_c^{t}\mathbf{R}\right)^{-1}\mathbf{r}$;
31. Calculate residual displacement in local coordinate: $\delta\mathbf{u}_c = \mathbf{R}\delta\mathbf{u}$;

Algorithm 6.2: Implicit algorithm of double-scale model (continued)

32. Calculate $\delta\mathbf{t}_c$ from $\delta\mathbf{u}_c$ following the procedure starting at step 6 in Algorithm 1;
33. Calculate $\delta\boldsymbol{\sigma} = -\frac{1}{H}\mathbf{a}_0\mathbf{n}\delta\mathbf{u}$;
34. Update $\boldsymbol{\sigma} = \boldsymbol{\sigma} + \delta\boldsymbol{\sigma}$; $\mathbf{t}_c = \mathbf{t}_c + \delta\mathbf{t}_c$; $\mathbf{u}_c = \mathbf{u}_c + \delta\mathbf{u}_c$;
35. Calculate residual $\mathbf{r} = \mathbf{n}^T\boldsymbol{\sigma} - \mathbf{R}^T\mathbf{t}_c$
36. Endwhile
37. Endif

Endif

6.4.5. Constitutive behaviour of mixed-mode model

After introduction of the algorithm of the double-scale constitutive model with an embedded mixed-mode cohesive FPZ, an element test under complex loading conditions is performed to illustrate the constitutive response of the model. In this test, a representative volume element (RVE) with the length of 4mm made from a soft rock so-called Johnstone is employed. The mechanical properties of this rock are taken from the experiment of Lim (1993) and listed in Table 6.0-1. Four different loading conditions are applied to the RVE for examining model behaviour at different loading stages, namely (1) loading under pure mode I; (2) loading under mixed-mode; (3) unloading; and (4) reloading under mixed-mode condition, as illustrated in Figure 6.0–3. In the first loading stage, a constant strain increment $\Delta\varepsilon_{xx} = 3 \times 10^{-7}$ in the horizontal direction is applied to the element. During this stage, the fracture is initiated and the element experiences softening behaviour. In the second loading stage, the element undergoes mixed-mode loading, achieved by adding a constant shear strain increment $\Delta\varepsilon_{xy} = 15 \times 10^{-7}$ to the element. The behaviour of the element under unloading and reloading conditions is examined in Stage 3 and Stage 4, respectively.

The responses of the constitutive model with the mixed-mode cohesive fracture law are demonstrated in Figure 6.0–4. In this figure, the model's behaviour at the macroscopic level is illustrated by the stress-strain relationships in the *xx* and *xy* directions (Figure 6.0–4a-b), while the local traction-displacement jump relationships in the normal and shear directions represent the corresponding responses of material in the FPZ under different loading conditions (Figure 6.0–4c-d). At the beginning of the test (i.e. Stage 1), the pure mode-I behaviour of Johnstone is observed, in which σ_{xx} increases linearly with its corresponding strain ε_{xx}. Meanwhile, the

local traction in the normal direction t_n increases without any development in the normal displacement jump. This is due to the fact that the element is under homogeneous deformation without any fracture detected inside the element. The element deforms elastically until the initiation of fracture where the state of local traction reaches its yield surface. Beyond the onset of fracture, the normal traction t_n decreases with the increase of the normal displacement jump u_n, which is controlled by its cohesive fracture parameters such as fracture energy and its damage evolution law. Meanwhile, σ_{xx} at the macroscopic scale reduces as the tensile loading continues, indicating a softening response from the material. Both macro-stress in the *xy* direction σ_{xy} and shear traction in the local coordinate t_s remain zero, owing to the pure Mode I loading condition.

Table 6.0-1. Material properties of Johnstone

Material properties of soft rock	
Young's Modulus (E)	0.4GPa
Poisson's ratio (v)	0.25
Density (ρ)	1.54g/cm^3
Tensile strength (f_t)	0.6MPa
Cohesion (c)	1.0MPa
Friction angle (φ)	33°
Dilation angle (ψ)	4°
Mode I fracture toughness (K_{Ic})	$2.15\text{MPa}/\sqrt{\text{mm}}$
Mode II fracture toughness (K_{IIc})	$1.05\text{MPa}/\sqrt{\text{mm}}$
Peak displacement (δ_0)	18μm
Secant normal stiffness (K_{n0})	$1.d13\text{Pa/m}$
Secant shear stiffness (K_{s0})	$1.d11\text{Pa/m}$

In the second stage, where an additional strain increment ε_{xy} is applied to provide a shear force on the element, the material undergoes softening behaviour under the mixed-mode loading condition. In that case, the shear traction starts to develop with an increase in its corresponding displacement jump, while the normal traction continues to reduce with a steeper slope. For each step, the tractions are corrected in order to locate exactly on the yield surface which is changed

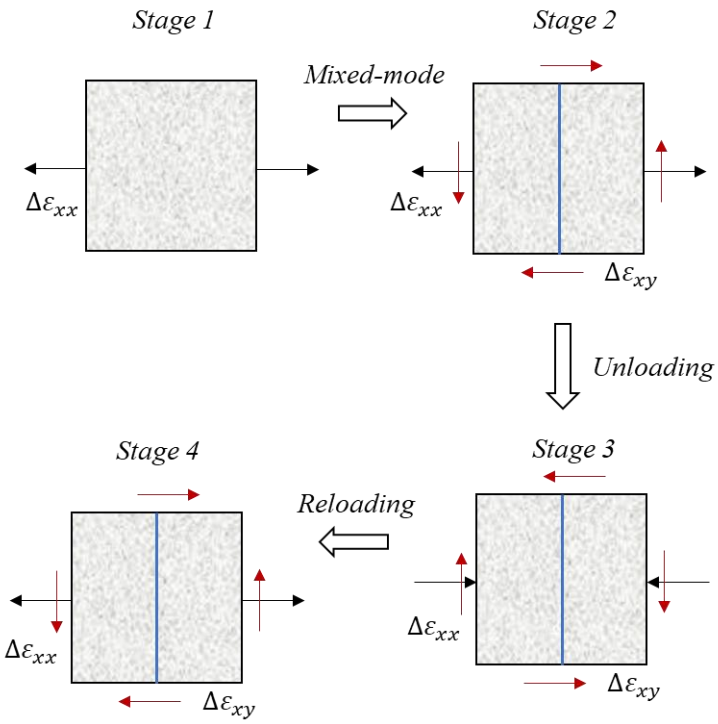

Figure 6.0–3. Loading paths for illustration of constitutive behaviour

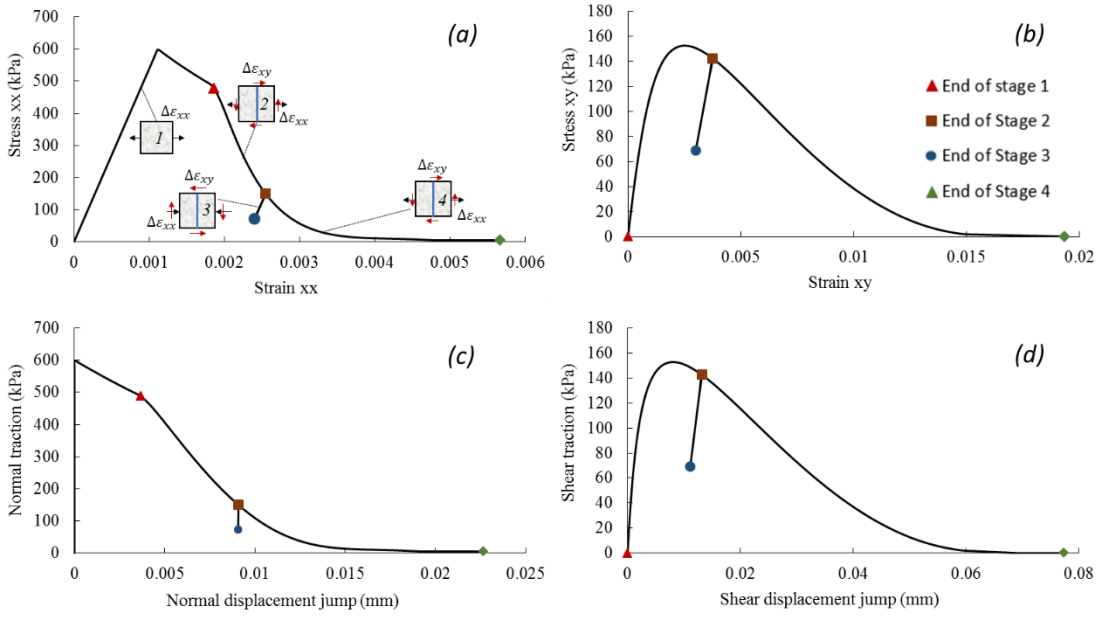

Figure 6.0–4. Constitutive behaviour of constitutive model for different loading scenarios. (a) Stress-strain relationship in xx direction; (b) Stress-strain relationship in xy direction; (c) Traction-displacement jump relationship in normal direction; (d) Traction-displacement jump relationship in shear direction

with the damage variable. The macro behaviour of the material is similar to the local behaviour of material in the FPZ, suggesting that the softening behaviour of the element is mainly controlled by the material behaviour in the FPZ where the fracture dissipation takes place. The constitutive responses under unloading and reloading are also tested in the third and last stages, respectively. During the unloading stage, the material both inside and outside FPZ behaves elastically. In that case, all macro-stress and local tractions are reducing with corresponding strains and displacement jumps until the end of Stage 3. Then those stresses and tractions increase linearly at the beginning of Stage 4, following the same stress path as that of the unloading stage until reaching to the point where the unloading starts. Beyond that point, the material undergoes softening behaviour again under the mixed-mode tensile-shear loading.

6.5. Experimental validation and application

After examining model behaviour under mixed-mode loading conditions at constitutive level, the mixed-mode constitutive model is implemented into traditional SPH framework for rock fracture applications. In this approach, one SPH particle is regarded as one representative volume element and the stress evolution of each SPH particle under various loading conditions is described by the above mixed-mode constitutive law. Once the fracture is initiated, a fracture plane at arbitrary orientation is formed within the SPH particle and the SPH starts to damage. With the increasing strain, the overall stresses for the damaged SPH particle reduce, the connection of the damage SPH with its surrounding SPH particles will be weakened, thereby resulting in the separation of two damaged SPH particles. Finally, as many damaged SPH particles are formed, the fracture geometries in the proposed numerical framework are represented by a set of damaged SPH particles, each of which possesses its own FPZ with arbitrary orientations, and the full detachment (or separation) of the specimen is formed due to the separation of adjacent SPH particles. In this section, three validation tests are conducted and their simulation results are compared with experimental results for examining the capability of the proposed SPH framework in simulating mixed-mode rock fractures.

6.5.1. Three-point bending test

In the first validation, the three-point bending test conducted by Bellego et al. (2000) is simulated to demonstrate the mesh-insensitivity of the constitutive model. This test was also used in Chapter 5 to examine the capability of the Taylor SPH framework associated with the pure mode I constitutive model. Unlike the previous work in Chapter 5 which required an additional set of stress-points and a Taylor time integration scheme to stabilise the numerical

solution, this work employs the conventional SPH with the standard Leap-Frog time integration scheme to re-simulate this test. Figure 6.0–5 shows the geometry and boundary conditions of the specimen and the corresponding setup in the SPH model. The dimensions of the notched beam are width W = 80mm, length L = 320mm, thickness B = 40mm and notch length b = 8mm. The beam is supported by two steel rollers 240mm apart and loaded by another steel roller located on top of the mid-span. The material properties obtained from the experiment are listed in Table 6.0-2. It is noted here that the cohesion and mode II fracture energy are not specified in the experiment; thus, in this study, the cohesion (c) is assumed to be the same as the tensile strength (f_t) and the mode II fracture energy (G_{II}) is equal to the mode I fracture energy (G_I). The typical friction angle $\varphi = 37°$ is selected from Fujita (1998) and the dilation angle $\psi = 5°$ is assumed in this test. The selection of dilation angle has little effect on the simulation result.

With the aim of examining the influence of spatial discretisation on the numerical solutions, three different particle discretisation sizes ($dx = dy =$ 4mm, 3mm and 2mm) are used to generate the computational domain in SPH simulation. The numbers of SPH particles corresponding to these discretisations are 1378, 3021 and 6598, repectively. The length parameter (H) in the constitutive model is equal to the corresponding particle discretisation size

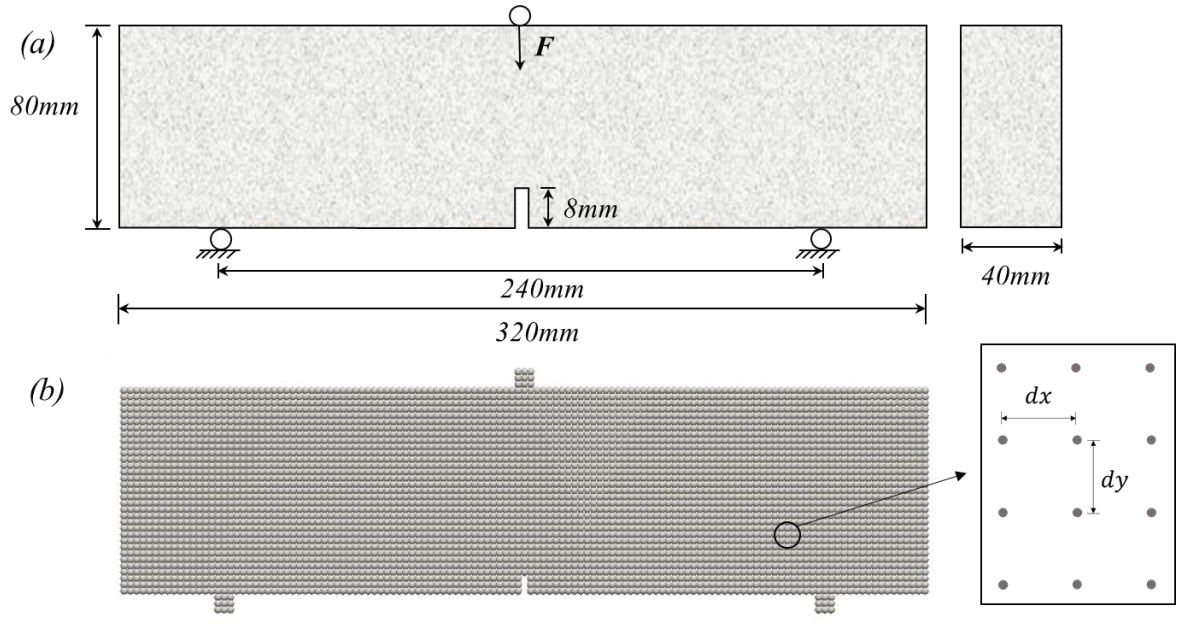

Figure 6.0–5. Geometry and boundary condition of three-point bending test: (a) Experimental setup; (b) SPH simulation setup

Table 6.0-2. Material properties of the three-point bending test

Material properties	
Young's Modulus (E)	45GPa
Poisson's ratio (v)	0.24
Density (ρ)	2.4g/cm^3
Tensile strength(f_t)	2.9MPa
Cohesion (c)	2.9MPa
Friction angle (φ)	37°
Dilation angle (ψ)	5°
Mode I fracture energy (G_I)	47.17Nm
Mode II fracture energy (G_{II})	47.17Nm
Peak displacement (δ_0)	16.4μm
Secant normal stiffness (K_{n0})	10^{14}Pa/m
Secant shear stiffness (K_{s0})	10^{11}Pa/m

for all the tests. In the numerical simulations, three-layer boundary particles are generated to impose boundary conditions as shown in Figure 6.0–5(b). The boundary particles have the same discretisation size and density as the real particles. To simulate the point loading at the top mid-span in the experiment, a vertical velocity is applied on the top boundary particles. A downward velocity of 1mm/s with ramp loading is adopted in this example, as in the three-point bending test in Chapter 5, in which the dynamic effect due to loading was investigated, which showed that the quasi-static condition could be achieved using that velocity. Therefore, the velocity of the top boundary particles is set as $v_x = 0, v_y = -1\ \text{mm/s}$. On the other hand, the vertical motion of the bottom boundary particles is fixed, but it allows free movement in the horizontal direction, so $v_y = 0$. The stresses of all boundary particles are updated in the same way as the real particles which form the computational domain of the beam, but the boundary particles always remain elastic. The compression stress and vertical displacement of real particles near the loading particles are recorded during the simulation process and are subsequently used for comparison with the experimental data and the simulation result in Chapter 5 using the pure mode I constitutive model.

Figure 6.0–6 provides a comparison between the experiment and the SPH simulation including the pure mode I and mixed-mode constitutive models for the compressive force-deflection curve. It can be seen that the SPH model with the embedded mixed-mode cohesive fracture law can capture the overall response of the force-deflection curve in the experiment. The force

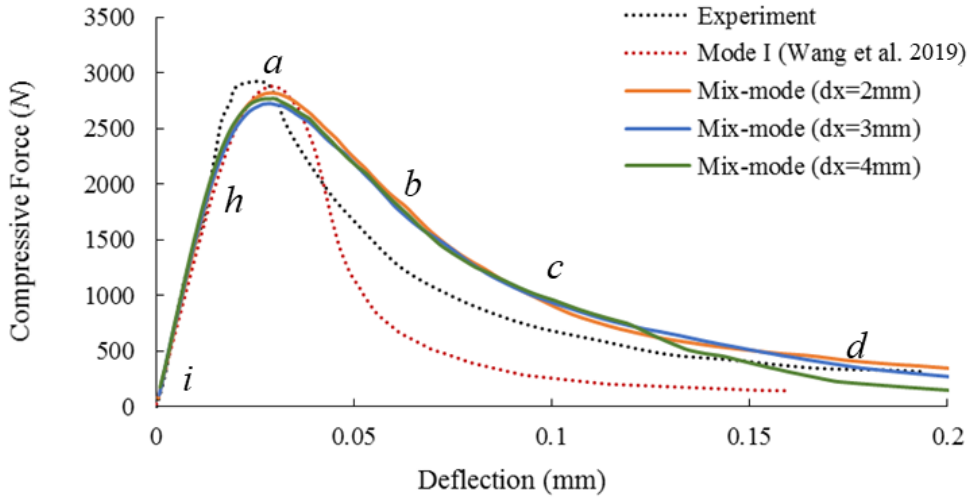

Figure 6.0–6. Compressive force and deflection relationship of the three-point bending test

initially displays linear behaviour until fracture is initiated (i.e. from *i* to *h* in Figure 6.0–6). This is then followed by the hardening response up to the peaking load (i.e. from *h* to *a* in Figure 6.0–6). Subsequently, the model experiences softening behaviour where the stress is reduced with the increasing deflection, as shown in Figure 6.0–6(*a*-*d*). The corresponding fracture patterns of (*a*) to (*d*) are illustrated in Figure 6.0–7. Figure 6.0–7(*a*) shows the fracture propagation when the compression force reaches its peak as marked in Figure 6.0–6(*a*). At this point, the damage has been propagating to around half of the beam height, which is consistent with the description in the mode I three-point bending test in Chapter 5. Then, the fracture keeps propagating towards to the loading point shown in Figure 6.0–7(*b*-*d*), resulting in a continuous penetrating fracture pattern in the middle of the beam. During the stages of both hardening and softening, the specimen experiences fracture initiation, propagation and finally damage, which is the consequence of the progressive damage of the material in the cohesive fracture zone of each damaged SPH particle. The model response using the mixed-mode cohesive fracture law is also compared with the behaviour using the double-scale model with the embedded mode I cohesive fracture law in Taylor SPH (Wang, 2019), as shown in Figure 6.0–6. More ductile behaviour can be observed in the result of the current model as the shear component of the cohesive fracture included in the mixed-mode model produces a more realistic response in capturing the correct fracture energy resistance. The results of the force-deflection curve using three different particle discretisation sizes are also plotted in Figure 6.0–6. It can be seen that the numerical results are quite similar among the three cases, although

some minor differences exist. This suggests that the numerical approach is less sensitive to spatial discretisation (or the initial space between two consecutive particles).

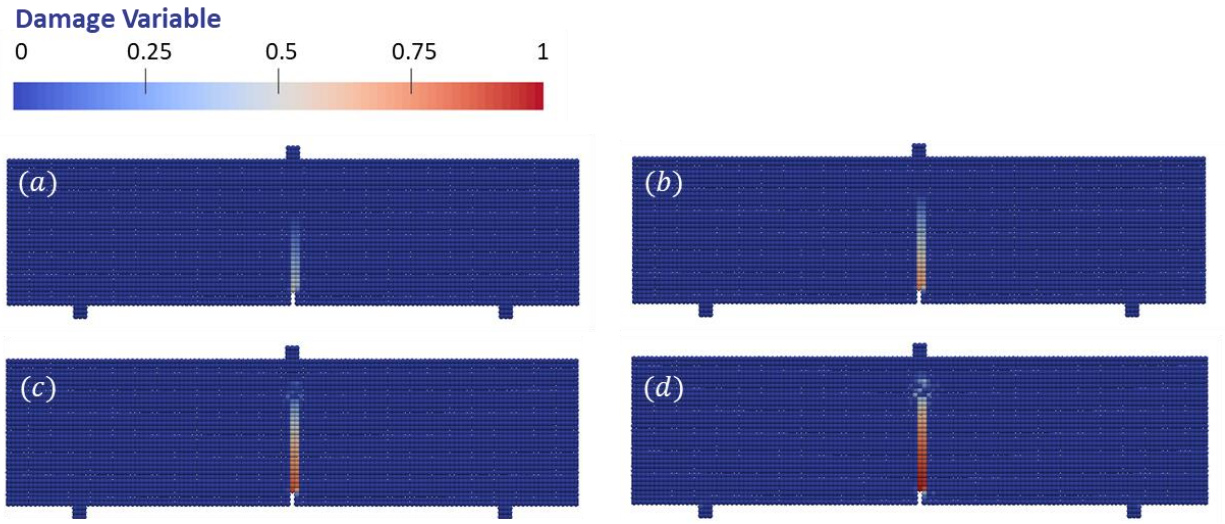

Figure 6.0–7. Fracture propagation and its final pattern in the three-point bending test

6.5.2. Semi-circular bending test

The second application considered is a series of semi-circular bending tests on Johnstone, which were carried out by Lim et al. (1994). The aim of this example is to examine the predictive capability of the SPH model under a wide range of mixed-mode loading conditions. The geometry and boundary conditions of the test in the experiment are shown in Figure 6.0–8(a). As in the three-point bending test, the semi-circular specimens with the radius of 47.5mm and thickness of 20mm are supported by two rollers 47.5mm apart and loaded by another roller on top of the mid-span. Notches with the length of 16.6mm are created with different notch angles varying from 0° to 60° with respect to the vertical axis, to investigate the influences of the notch angle on the peak load (P) and the fracture toughness (K_I, K_{II}), which are calculated as follows:

$$K_I = \frac{P}{2rt}\sqrt{\pi a}Y_I \tag{6.38}$$

$$K_{II} = \frac{P}{2rt}\sqrt{\pi a}Y_{II} \tag{6.39}$$

where K_I and K_{II} are respectively mode I and mode II fracture toughness; r is the specimen radius; t is the specimen thickness; a is the notch length; Y_I and Y_{II} are mode I and mode II normalised stress intensity factors. As the values of Y_I and Y_{II} can be obtained from the data of

Lin et al. (1993), K_I and K_{II} can be calculated based on the above equation once the peak load (P) is known. The material properties of Johnstone are listed in Table 6.0-1. The friction angle and dilation angle are respectively taken as 33° and 4° for average quality rock masses in Hoek and Brown (1997) for the following examples.

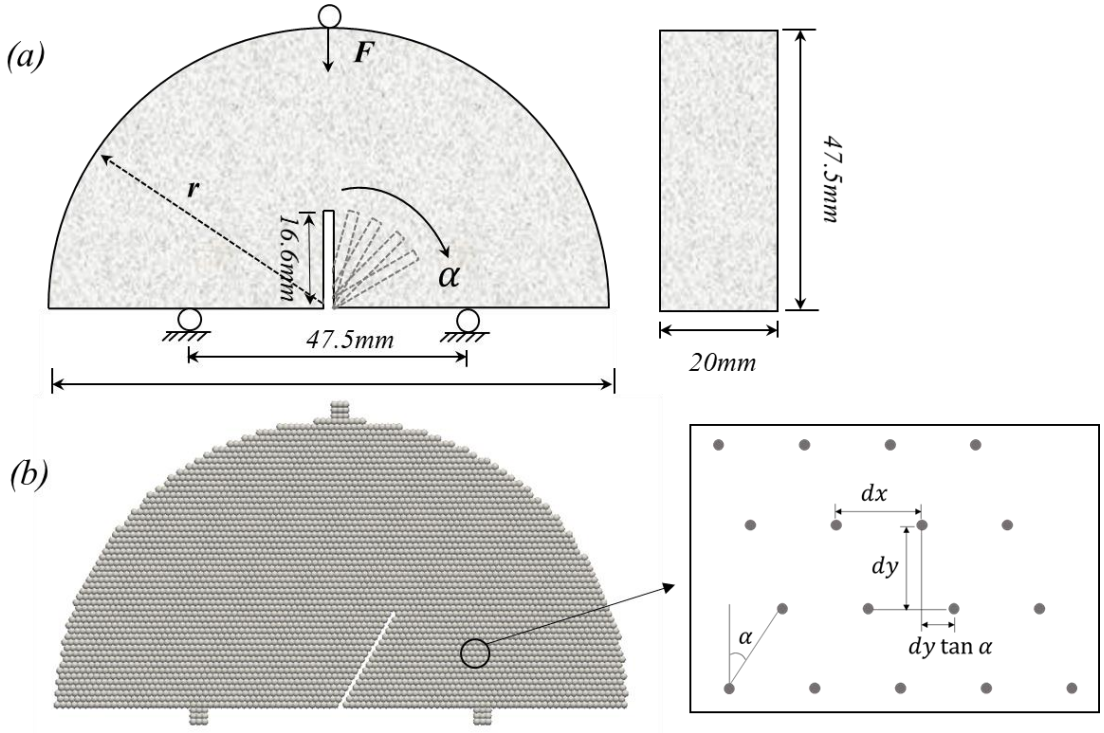

Figure 6.0–8. Geometry and boundary conditions for the semicircular bending test: (a) Experimental setup; (b) SPH simulation setup when rotational angle = 30°.

Figure 6.0–8 shows the corresponding SPH configuration of the semicircular bending test with a notch angle of 30 degrees. In the tests, a particle discretisation of 0.95mm is used, resulting in a total number of 3,995 SPH particles for specimen generation. To create accurate notch angles using reasonable particle numbers, the initial SPH arrangement in this test is unlike the traditional one such as the three-point bending test in Section 6.5.1. The initial location of each SPH particle in the semicircular bending tests is related to the notch angle as shown in Figure 6.0–8*b*. As in the three-point bending tests, three layers of boundary particles are generated for simulating the point loading in the experiments. The velocities of the top boundary particles are $v_x = 0, v_y = -2$ mm/s, and the velocities of the bottom boundary particles are as $v_y = 0$. Since Johnstone rocks are classified as soft rocks with a relatively small elastic Young's modulus, both artificial viscosity and artificial stress are used in this test to stabilise the

numerical solutions. Ramp loading is also applied to alleviate the dynamic effect of the sudden loading. The stresses of boundary particles are updated in the same way as in the three-point bending test. The stresses of real particles near the loading particles are recorded during the simulation process, from which the peak load and fracture toughness are obtained for comparison with the experimental data.

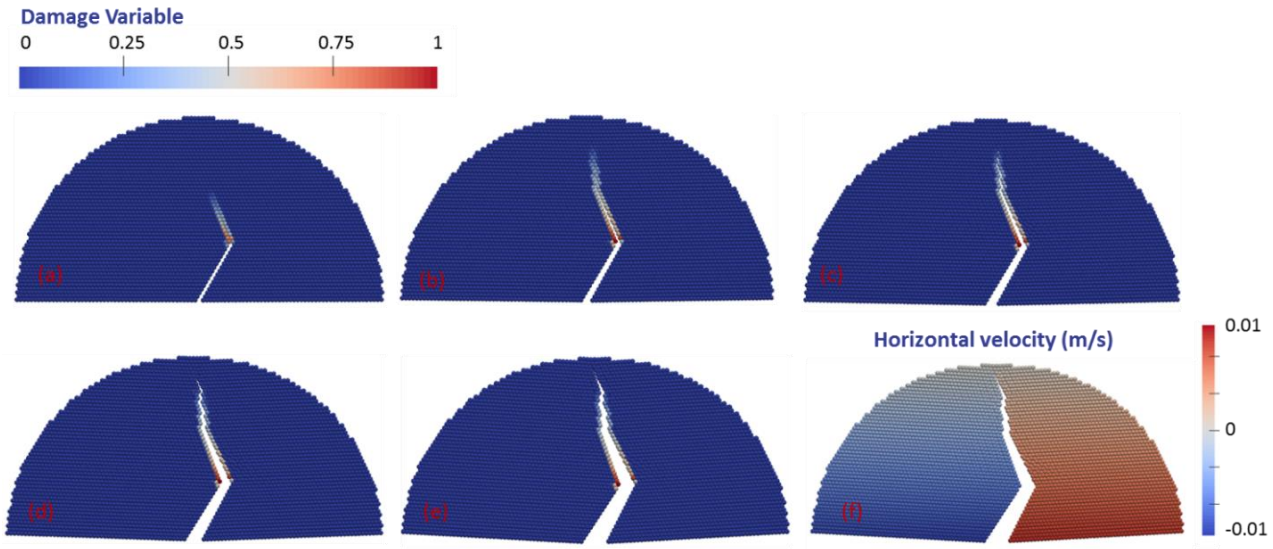

Figure 6.0–9. Fracture pattern for rotational angle = 30° in the semicircular bending test with tensile instability treatment. (a-e) fracture development; (f) horizontal velocity for final fracture pattern.

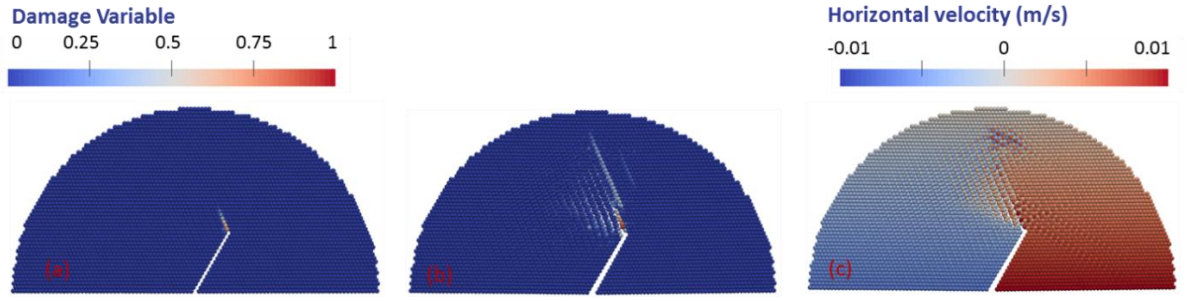

Figure 6.0–10. Numerical results for rotational angle = 30° in the semicircular bending test without tensile instability treatment. (a-b) fracture development; (c) horizontal velocity profile

Figure 6.0–9 illustrates the progressive development of fracture and the horizontal velocity profile at the failure stage for the semicircular specimen with the rotational angle of 30°. As seen in Figure 6.0–9(*a*), some particles near the tip of the notch are the first damaged, showing

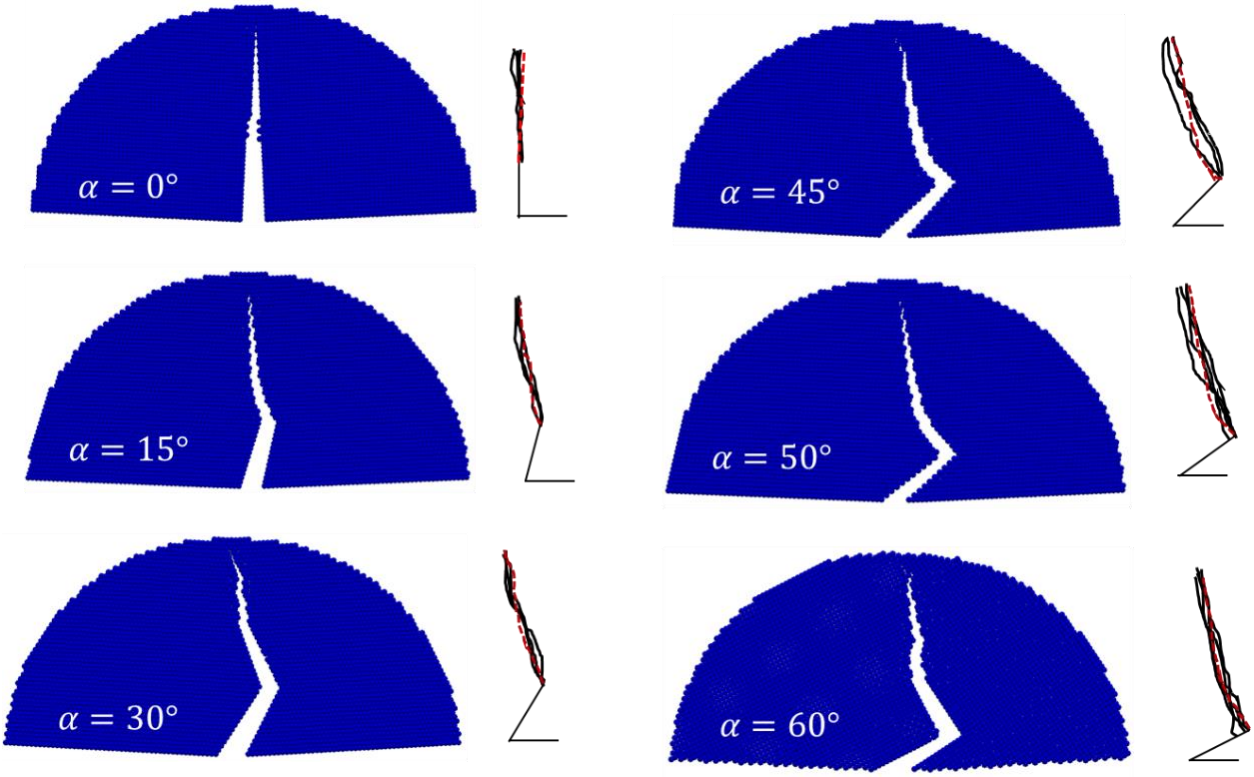

Figure 6.0–11. Comparison of final fracture patterns between experimental and numerical results in the semicircular bending test.

that the fracture initiates at the location of the notch tip. Then the fracture propagates toward the loading point (Figure 6.0–9*b-d*), and eventually a vertical curvilinear fracture pattern is formed in the middle of the sample (Figure 6.0–9*e*). The horizontal velocity profile corresponding to Figure 6.0–9(*e*) is also plotted in Figure 6.0–9(*f*). It can be seen that the particles on the left side of the fracture move to the left while the particles on the other side move to the right; thus the sample is finally split into two halves. In this approach, SPH particle itself could not be cracked visually, however each damaged SPH particle possesses a fracture process zone and the material behaviour within the fracture process zone will contribute to the decrease in the overall stress state of the SPH particle, thereby resulting in the separation between two damaged SPH particles. The same test without using the artificial stress is also plotted in Figure 6.0–10. The result remains stable when the fracture is initiated (Figure 6.0–10a), but becomes unstable during the post-failure process (Figure 6.0–10b-c). Unrealistic fracture and particle clustering are observed in Figure 6.0–10b-c, which indicates that a tensile instability problem occurs in SPH. By comparing those two results, it can be concluded that the tensile instability problem can be completely removed and good numerical stability can be achieved by adopting just this artificial stress term.

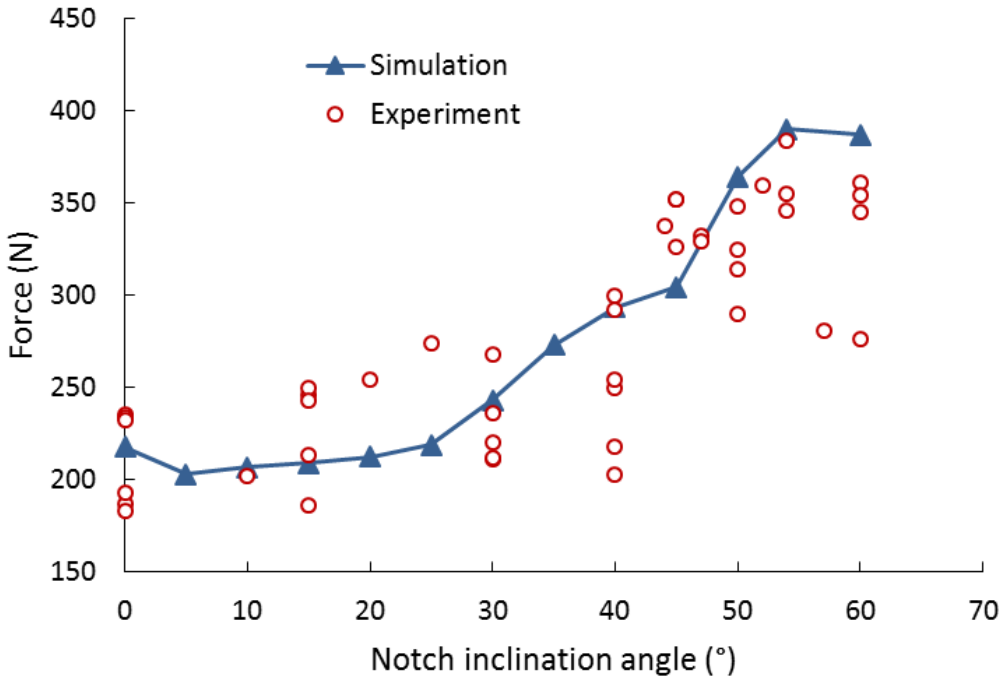

Figure 6.0–12. Comparison between experimental and numerical results in peak force against the notch inclination angle of the semicircular bending test

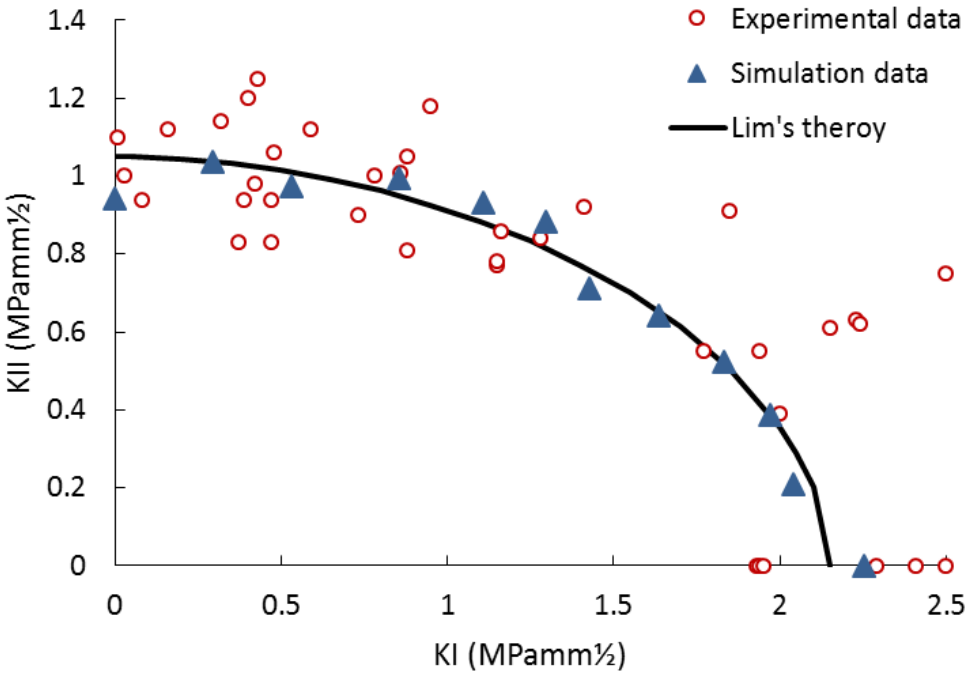

Figure 6.0–13. Comparison between experimental and numerical results in mode II fracture toughness against mode I fracture toughness in terms of different notch inclination angles.

Figure 6.0–11 depicts comparisons of the mixed-mode fracture envelope between experiments and SPH simulations for the different notch inclination angles $\alpha = 0°, 15°, 30°, 45°, 50°$ and $60°$. It shows that the simulation fracture patterns marked as red lines match the experimental results well (shown as black lines). The final fracture pattern is a vertical straight line when $\alpha = 0°$ (pure mode I). When $\alpha > 0°$, the sample is subjected to mixed-mode or pure mode II loading, resulting in curvilinear fracture paths. For all simulation cases, the fractures initiate from the notch tip and then propagate toward upper loading point, while the experiments show that a few fractures tend to initiate behind the notch tip when the notch angle is beyond $\alpha = 50°$. Nevertheless, the simulation results still can successfully predict the overall fracture envelope in experiments, demonstrating the capability of the traditional SPH model for capturing fracture development under various complex loading conditions.

Meanwhile, the comparison of peak load between experiments and simulations for the notch inclination angles varying from $0°$ to $60°$ with the internal increment of $5°$ is plotted in Figure 6.0–12. It is noted here that a notch angle of $54°$ (instead of $55°$) is used in the current test as the sample is subjected to pure mode II loading condition when $\alpha = 54°$ (Lim et al. 1994). The SPH simulation can capture well the increasing trend of the peak load with the increasing notch angles in the experiment. Additionally, Figure 6.0–13 compares the predictions of fracture toughness in SPH simulation against the experimental results and Lim's theory (Lim et al. 1994). The simulation results fall perfectly within the experimental data ranges even though the fracture toughness data in the experiments are quite scattered. Nevertheless, the numerical results agree closely with the empirical fracture toughness envelope which was proposed by Lim et al. (1994) and is represented as a black line in Figure 6.0–13. This result further confirms that the model can accurately predict the mixed-mode fracture behaviour of rocks in the semicircular bending test.

6.5.3. Brazilian test

To further demonstrate the predictive capability of the traditional SPH model in capturing mixed-mode rock fracture behaviour, a series of mixed-mode Brazilian tests with different internal diameters performed by Li et al. (2016) is simulated as the last application. The geometry and loading conditions of the specimen in the experiments are shown in Figure 6.0–14(*a*). Specimens drilled from a marble block are first prepared, with the diameter (*D*) of 50mm and thickness (*t*) of 25mm. Then a circular disc with the diameter (*d*) varying from 5mm to 25mm is cut off at the centre of the specimens, resulting in the ring-shaped specimens with

different diameter ratios (*d/D*) from 0.1 to 0.5. Specimens are sandwiched directly between two platens, over which a static force is applied. The material properties of the marble are listed in Table 6.0-3. The tensile strength is obtained from the experiment by (Li et al. 2016), while other material properties of marble come from the work of Li et al. (2018).

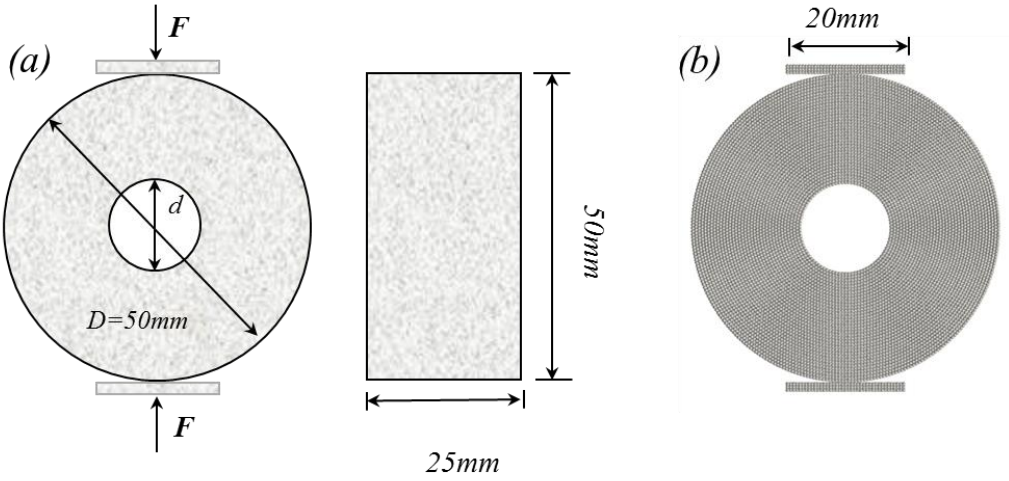

Figure 6.0–14. Geometry and boundary condition of the Brazilian test: (a) Experimental setup; (b) SPH simulation setup for $\alpha = 0.3$.

Table 6.0-3. Material properties of marble in the Brazilian test

Material properties of marble	
Young's modulus (E)	49GPa
Poisson's ratio (v)	0.19
Density (ρ)	2.7g/cm^3
Tensile strength(f_t)	3.6MPa
Cohesion (c)	10MPa
Friction angle (φ)	33°
Dilation angle (ψ)	4°
Mode I fracture energy (G_I)	30Nm
Mode II fracture energy (G_{II})	30Nm
Peak displacement (δ_0)	8.5μm
Secant normal stiffness (K_{n0})	10^{14}Pa/m
Secant shear stiffness (K_{s0})	10^{11}Pa/m

The corresponding numerical setup in SPH is shown in Figure 6.0–14 (*b*). To perfectly create the shape of a circular cut-off using a reasonable number of particles, particles that form the

ring sample are radially distributed in this test. The particle discretisation size of 0.5mm is used for all the simulations, resulting in a total number of 7651 particles for a specimen without the central hole. The particle number decreases with a larger diameter ratio (d/D). To simulate those two platens in the experiment, three layers of boundary particles with the spatial discretisation size of 0.5mm are generated in the traditional way as in the three-point bending test. The velocities of top boundary particles are set as $v_x = 0, v_y = -1\text{mm/s}$, while the velocities of the bottom boundary particles are $v_x = 0, v_y = 1\ \text{mm/s}$.

The fracture development of ring specimens with different diameter ratios (*d/D*) in the Brazilian test is shown in Figure 6.0–15 (*a*-*c*). It can be seen from Figure 6.0–15 that the fracture initiates from the surface of the internal hole along the diametral loading line in all ring specimens. However, specimens with different diameter ratios have different fracture envelopes. To be more specific, the fracture initiates and propagates towards the upper and lower platens, eventually forming a vertical diametrial crack along the loading line when the diameter ratio $d/D < 0.3$. Although some particles near the outer ring are slightly damaged when $d/D = 0.2$, the secondary crack has not been formed before the first crack is fully formed. With an increasing *d/D* ($d/D \geq 0.3$), secondary cracks form in the direction perpendicular to the loading line, always lagging behind the vertical cracks. The secondary cracks are initiated from the surface of the outer bound of the ring and propagate to the centre, eventually resulting in four-pan-shaped failure. The final fracture patterns in SPH simulation and experiment are shown in Figure 6.0–15(*d*) and Figure 6.0–15(*e*) respectively. It can be seen that fracture pattern in the simulations match well the fracture patterns observed in the experiments, although there exists a lightly difference in the secondary cracks when $d/D \geq 0.3$. In the experiment, the secondary cracks perpendicular to the loading line cut through the specimen, splitting the rock specimen into four pieces, however the secondary cracks fail to propagate through the specimen. This indicates that the rock specimen used for the laboratory experiment is more brittle compared with the simulated specimen. The difference may be due to the inaccurate measurement of input parameters (such as fracture energy and tensile strength) in the experiment, which was directly applied in the SPH simulation. Overall, the proposed model could capture well the fracture patterns observed in the experiments, indicating that our SPH is capable of simulating multiple cracks under mixed-mode loading and predicting the progressive failure of specimens in Brazilian tests.

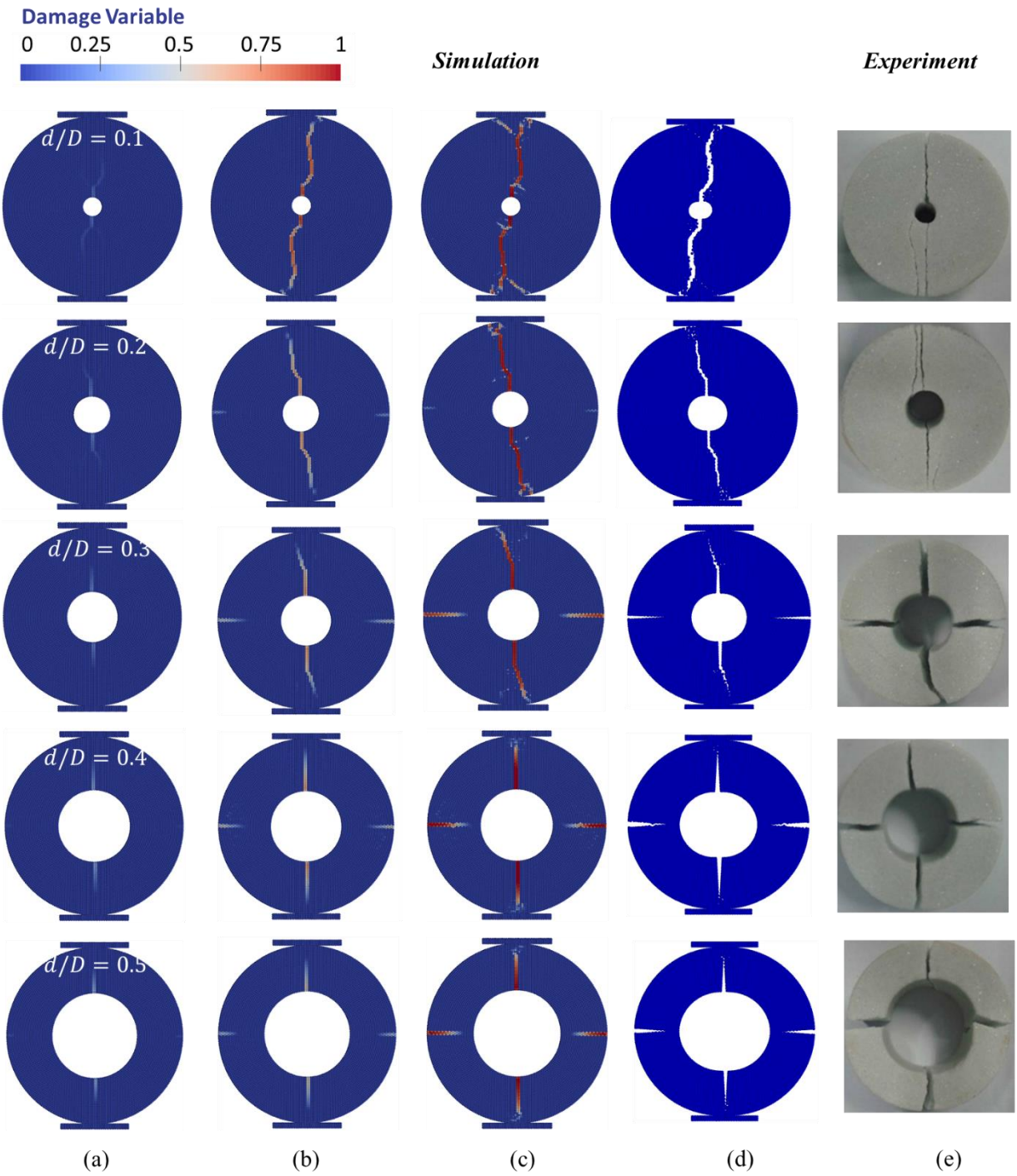

Figure 6.0–15. Fracture development in SPH simulation and final fracture patterns of numerical and experimental results with respect to different diameter ratios (d/D) in the Brazilian test.

Figure 6.0–16 shows the comparison of peak load between SPH simulations and experiments with respect to different diameter ratios. It can be seen that the numerical model can capture well the trend of change in peak load exhibited in the experiment. When *d/D* = 0, which means there is no hole in the specimen, the peak load is the highest among all cases. Although it is

slightly greater than the average value of the experimental results, the peak load predicted by SPH simulation falls perfectly within the range of experimental data when $d/D = 0$. With an increasing diameter ratio d/D, a linearly decreasing trend in peak load becomes evident. This is because the specimen with greater d/D has shorter fracture routes, thus requiring less fracture energy and a smaller peak load compared with specimens with smaller d/D.

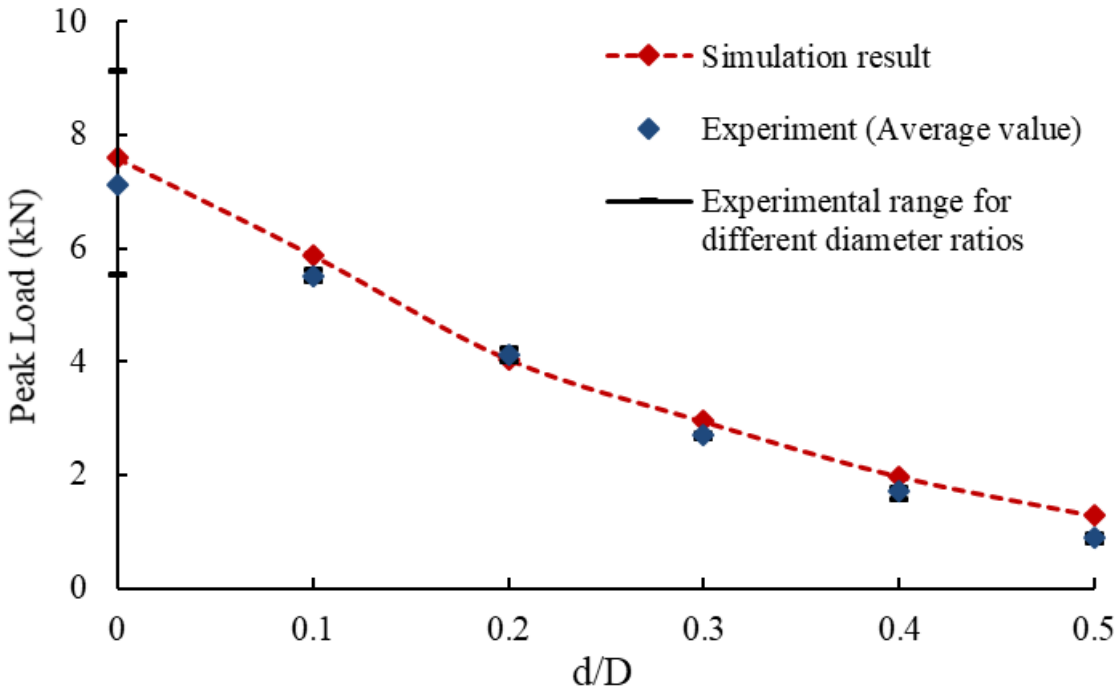

Figure 6.0–16. Comparison of peak load between simulation and experimental results with respect to different ratio (d/D) in the Brazilian test.

6.6. Conclusions

A numerical approach that combines the conventional SPH method and a size-dependent constitutive model with an embedded mixed-mode cohesive fracture was presented for modelling rock fractures under both pure mode I and mixed-mode loading conditions. Through three numerical comparisons with experimental results, the proposed numerical framework was demonstrated to be able to predict the underlying failure mechanism of different rock types under a wide range of loading conditions. Successful applications of the conventional SPH method to model progressive rock fractures confirmed its simplicity, versatility and efficiency in solving complex problems, thanks to the simple tensile instability treatment technique.

Compared to the Taylor-SPH method in the previous work reported in Chapter 5, the conventional SPH is much simpler and more robust as it does not require special treatment of free-surface boundary conditions. Thus, with its mesh-free nature, the conventional SPH method has great flexibility in simulating fracture and complete detachment of rocks under various loading conditions. Another key feature of the model is its ability to take into account intrinsic regularisation effects and size-dependent behaviour, thanks to the introduction of a length parameter into the constitutive structure. Furthermore, since the fracture topology is represented by a set of damaged SPH particles, each of which possesses its own fracture plane and has arbitrary direction depending on the loading condition, the proposed numerical model is capable of capturing multiple and complex fractures.

Chapter 7

Cracking SPH Particle Framework for Modelling of Dynamic Mode Rock Fracture

7.1. Introduction

In the previous two chapters, the behaviour of rock fractures under quasi-static loading was successfully simulated using the proposed SPH framework. While Chapter 5 focused on pure mode I rock factures and the size dependency on the mechanical properties and fracturing processes, Chapter 6 took into account mixed-mode fractures of rocks by employing a mixed-mode cohesive fracture law to describe the behaviour fracture process zone of SPH damaged particles. Now, the proposed SPH framework is extended to simulate pure mode I and mixed-mode rock fractures under dynamic loadings.

In this study, the effect of loading rate on the fracture behaviour and mechanical properties of rocks is investigated using the SPH fracturing approach that combines mesh-free smoothed particle hydrodynamics with a continuum constitutive model. The loading rate effect is incorporated either by developing a rate-dependent constitutive model or by making use of the dynamic nature of SPH. In the first approach, the strain rate effect is incorporated into the mixed-mode cohesive fracture law which describes the behaviour of the fracture process zone under different dynamic loadings. In the second approach, the inherent rate effects predicted by the model are a consequence of the dynamic nature of SPH and the flexibility in the facture orientation of each SPH fracturing particle based on the current loading conditions.

This chapter is organised as follows. In Section 7.2, the formulations of the SPH fracturing approach are briefly described. Section 7.3 presents the first approach for simulating dynamic rock fractures, and 7.4 presents the second approach for simulating dynamic rock fractures. Importantly, to examine the capability of these two numerical approaches for capturing mode

I and mixed-mode failure of rock and rock-like materials under dynamic loadings, mixed-mode ring tests are conducted using the first approach and three numerical examples, notched semicircular bending tests, Brazilian disc tests and mixed-mode three-point bending tests, are simulated using the second approach, and the results of these tests are presented and discussed in Sections 7.3 and 7.4 respectively. The conclusions of this study are presented in Section 7.5.

7.2. SPH framework with an embedded fracture zone

7.2.1. Traditional SPH approximation of governing equations

As the traditional SPH method can deal naturally with free boundaries without any special treatment, it is very flexible in dealing with complex fracture patterns under dynamic loadings. Therefore, the traditional SPH method with tensile instability treatment is used in this work as the numerical platform for simulating dynamic rock fractures. The traditional SPH framework begins with the governing equations of rocks which consist of mass and momentum conservation equations and a constitutive relationship that links stresses to strains through a set of equations as follows:

$$\frac{\mathrm{D}\rho}{\mathrm{D}t} = -\rho\nabla\cdot\mathbf{v} \tag{7.1a}$$

$$\frac{\mathrm{D}\mathbf{v}}{\mathrm{D}t} = \frac{1}{\rho}\nabla\cdot\boldsymbol{\sigma} + \mathbf{b} \tag{7.1b}$$

$$\frac{\mathrm{D}\boldsymbol{\sigma}}{\mathrm{D}t} = \mathbf{D}_{ef}:\dot{\boldsymbol{\varepsilon}} \tag{7.1c}$$

where ρ is the material density; $\mathbf{v}$ is the velocity vector; $\boldsymbol{\sigma}$ is the stress tensor; $\mathbf{b}$ is the vector component of acceleration due to external forces; $\mathbf{D}_{ef}$ is the material stiffness matrix; $\mathrm{D}(\cdot)/\mathrm{D}t$ is the material derivative and $\dot{\boldsymbol{\varepsilon}}$ is the strain rate tensor, which can be calculated by velocity through the kinematic relation:

$$\dot{\boldsymbol{\varepsilon}} = [\nabla\cdot\mathbf{v} + (\nabla\cdot\mathbf{v})^{\mathrm{T}}]/2 \tag{7.2}$$

The above governing equations are approximated by using the traditional SPH method with a corrective technique on the gradient approximation of SPH, leading to:

$$\frac{\mathrm{D}\rho_i}{\mathrm{D}t} = \sum_{j=1}^{N} m_j(\mathbf{v}_i - \mathbf{v}_j)\cdot\nabla W_{ij}^{C} \tag{7.3a}$$

$$\frac{\mathrm{D}\mathbf{v}_i}{\mathrm{D}t} = \sum_{j=1}^{N} m_j\left(\frac{\boldsymbol{\sigma}_i+\boldsymbol{\sigma}_j}{\rho_i\rho_j} + \boldsymbol{C}_{ij}\right)\cdot\nabla W_{ij}^{C} + \mathbf{b}_i \tag{7.3b}$$

$$\frac{\mathrm{D}\boldsymbol{\sigma}_i}{\mathrm{D}t} = \mathbf{D}_{ef}:\left[\frac{1}{2}\sum_{j=1}^{N}\frac{m_j}{\rho_j}(\mathbf{v}_j - \mathbf{v}_i)\cdot\nabla W_{ij}^{C} + \frac{1}{2}\left(\sum_{j=1}^{N}\frac{m_j}{\rho_j}(\mathbf{v}_j - \mathbf{v}_i)\cdot\nabla W_{ij}^{C}\right)^{T}\right] \tag{7.3c}$$

where ∇W_{ij}^{C} is the corrected kernel gradient as

$$\nabla W_{ij}^{C} = \mathbf{L}(\mathbf{x}_i)\nabla W_{ij} \tag{7.4}$$

where the normalisation matrix $\mathbf{L}(\mathbf{x}_i)$ can be defined as:

$$\mathbf{L}(\mathbf{x}_i) = \begin{pmatrix} \sum_{j=1}^{N} \frac{m_j}{\rho_j}(x_j - x_i)\nabla_{x_i} W_{ij} & \sum_{j=1}^{N} \frac{m_j}{\rho_j}(x_j - x_i)\nabla_{y_i} W_{ij} \\ \sum_{j=1}^{N} \frac{m_j}{\rho_j}(y_j - y_i)\nabla_{x_i} W_{ij} & \sum_{j=1}^{N} \frac{m_j}{\rho_j}(y_j - y_i)\nabla_{y_i} W_{ij} \end{pmatrix}^{-1} \tag{7.5}$$

As well as the corrective technique, a stabilisation term $\mathbf{C}_{ij}$ is added to equation (7.3b), consisting of artificial viscosity and artificial stress (Bui et al. 2008). Detailed explanation and formulations were presented Chapter 3. In this study, artificial viscosity is the only stabilisation term used to regularise strong shockwave propagation, as all numerical examples in this work concern hard rocks. Young's modulus of hard rocks is large enough to generate a strong influence of artificial viscosity in the momentum equation, thus mitigating the tensile instability problem without use of an artificial stress term. The constant parameters for the artificial viscosity in this study are chosen as 0.5 and 0 for terms associated with the linear and quadratic in the velocity divergence, respectively. However, it is suggested to use both artificial viscosity and artificial stress to eliminate tensile instability issues in soft rocks.

7.2.2. Continuum constitutive model for dynamic fracturing

In this work, the continuum-based size-dependent constitutive model developed in Chapter 6 for simulating mixed-mode rock fractures under quasi-static loading is employed. This continuum constitutive model is based on the double scale model which was originally developed by Nguyen et al. (2012), Nguyen et al. (2014) for strain localisation applications. Then it was extended to simulate the size dependency and rock fracture behaviour under pure mode I in Chapter 5 by incorporating a tensile-failure cohesive fracture law. In Chapter 6, a mixed-mode cohesive fracture law for capturing the plastic and damage evolution of rocks was developed and incorporated into the continuum constitutive model to capture mixed-mode failure of rocks under quasi-static loading. Details of the continuum-based constitutive model with the embedded mixed-mode cohesive fracture law were comprehensively introduced in Chapter 6, and thus only the general formulations are briefly presented in this section.

7.2.2.1. Double scale model

In the double scale model, the representative volume element (RVE) is considered as homogenous and elastic before the fracture is initiated. Once the fracture is detected, RVE is

regarded as a composite material comprising a fracture process zone and its surrounding bulk, which responses under loading are distinct. The material inside the fracture process zone is under inelastic loading, while outside bulk is assumed as elastic. The interaction between two distinct zones is connected by a set of kinematic enhancements and continuity conditions across the fracture plane. The overall (or macro) stress-strain increment of the whole considered element in double scale model can be expressed as:

$$d\boldsymbol{\sigma} = \mathbf{a}_0 \left(d\boldsymbol{\varepsilon} - \frac{1}{H}\mathbf{n} d[\![\mathbf{u}]\!] \right) \tag{7.6}$$

in which the increment of the displacement jump $d[\![\mathbf{u}]\!]$ can be calculated as:

$$d[\![\mathbf{u}]\!] = \left(\frac{1}{H}\mathbf{n}^T\mathbf{a}_0\mathbf{n} + \mathbf{K}^t \right)^{-1} \mathbf{n}^T\mathbf{a}_0 d\boldsymbol{\varepsilon} = \mathbf{C}^{-1}\mathbf{n}^T\mathbf{a}_0 d\boldsymbol{\varepsilon} \tag{7.7}$$

It can be seen from equations (7.6 and 7.7) that the stress increment can be calculated once the tangent stiffness of the cohesive fracture law $\mathbf{K}^t$ is known. Next, the mixed-mode cohesive fracture law is introduced for calculating the tangent stiffness.

7.2.2.2. Mixed-mode cohesive fracture law for fracture process zone

The mixed-mode cohesive fracture law coupling damage mechanics and plasticity theory developed in Chapter 6 is employed in this study to describe the behaviour of rock material within the FPZ. The cohesive law relates the tractions ($\mathbf{t}_c$) and the corresponding displacement jumps ($\mathbf{u}_c$) across two faces of the FPZ. The incremental displacement jump ($d\mathbf{u}_c$) can be partitioned into elastic ($d\mathbf{u}_c^e$) and inelastic $\left(d\mathbf{u}_c^p\right)$ parts, representing reversible and irreversible displacements, respectively:

$$d\mathbf{u}_c = d\mathbf{u}_c^e + d\mathbf{u}_c^p \tag{7.8}$$

The traction state of the material in the FPZ can be calculated by the elastic displacement jump as:

$$d\mathbf{t}_c = \mathbf{P}\mathbf{K}_{c0}^s d\mathbf{u}_c^e \tag{7.9}$$

$$\text{with} \quad \mathbf{K}_{c0}^s = \begin{bmatrix} K_n & 0 \\ 0 & K_s \end{bmatrix} \quad \text{and} \quad \boldsymbol{P} = \begin{cases} \begin{bmatrix} 1-D & 0 \\ 0 & 1-D \end{bmatrix} & when\ t_{c(n)} \geq 0 \\ \begin{bmatrix} 1 & 0 \\ 0 & 1-D \end{bmatrix} & when\ t_{c(n)} < 0 \end{cases} \tag{7.10}$$

where $\mathbf{K}_c^s = \mathbf{P}\mathbf{K}_{c0}^s$ is the secant stiffness matrix of the cohesive fracture zone; $\mathbf{K}_{c0}^s$ denotes the elastic secant stiffness matrix of the cohesive fracture zone; $\mathbf{P}$ is a parameter matrix with

respect to the normal traction $t_{c(n)}$; D is the damage variable characterising the degradation of material strength due to fracture, which evolves with inelastic displacement jumps shown as:

$$D = \max\left(D_{pre}, 1 - e^{-\left(\frac{u_n^p}{\delta_0} + \frac{u_s^p}{\delta_0}\right)}\right) \tag{7.11}$$

where D_{pre} is the damage variable in the previous step, δ_0 is the displacement jump corresponding to the peak normal traction, u_n^p and u_s^p are respectively normal and shear inelastic displacement jumps, which are introduced later.

Now, a modified form of the Mohr-Coulomb failure criterion is adopted as the failure function to represent failure states under the combined influence of normal and shear tractions. The failure criterion is expressed as:

$$f(t_n, t_s, D) = {t_s}^2 - 2c_0(1-D)\tan\phi\,(\sigma_{t0}(1-D) - t_n) - \tan^2\phi\,({t_n}^2 - (\sigma_{t0}(1-D))^2) \tag{7.12}$$

where ϕ is the friction angle of the material; c_0 and σ_{t0} represent the initial cohesion and tensile strength.

In addition, a non-associated plastic potential is also used in this study, taking into account the effect of the dilatancy angle, the formulation of which is written as:

$$g(t_n, t_s, D) = {t_s}^2 - 2c_0(1-D)\tan\psi\,(\sigma_{t0}(1-D) - t_n) - \tan^2\psi\,({t_n}^2 - (\sigma_{t0}(1-D))^2) \tag{7.13}$$

where ψ is the dilatancy angle of the material. The incremental plastic displacement jump can be computed by the non-associate flow rule as:

$$d\boldsymbol{u}_{\mathrm{c}}^{\mathrm{p}} = d\lambda \frac{\partial g}{\partial \boldsymbol{t}_{\mathrm{c}}} \tag{7.14}$$

where $d\lambda$ is the plastic multiplier, which is non-negative and can be determined based on the current traction state and loading history.

The above description shows the key formulations of the mixed-mode cohesive fracture law which describes the behaviour of the fracture zone during the fracturing process, while the surrounding bulk behaves elastically. Those two distinct responses are coupled by the traction continuity across the boundaries of the fracture process zone. Therefore, an implicit stress return mapping algorithm must be applied to achieve the traction continuity condition and at the same time to update the stresses of two distinct zones. The detailed implementation algorithm was presented in Chapter 6, and thus is not repeated here.

7.3. Rate effect incorporation by the constitutive model

7.3.1. Dynamic increase factors of rocks

As the experimental results show, tensile strength is much more rate sensitive than other mechanical properties such as Young's modulus, Poisson's ratio and energy absorption capacity, and thus only the strength enhancement behaviour is considered in this approach. The strain/loading rate effect on tensile strength for rock or similar quasi-brittle materials is incorporated into the mixed-mode cohesive fracture model through a dynamic increase factor (DIF) with respect to the strain/loading rate. The relationship between DIF representing the ratio of dynamic to static tensile strength with strain/loading rate has been intensively investigated. For example, Liu et al. (2018) summarised experimental data of tensile tests on different types of rock and plotted the dynamic increase factors with different strain rates as shown in Figure 7.0–1. The DIF increases gradually when the strain rate is less than 10^0/s, but grows rapidly when the strain rate is greater than 10^0/s. Therefore, two empirical equations are developed to show such a large distinction, and they are expressed as:

$$DIF = \begin{cases} 1 + 0.70\dot{\varepsilon}_t^{0.18} & for\ \dot{\varepsilon}_t < 10^0 s^{-1} \\ 1 + 0.70\dot{\varepsilon}_t^{0.18} & for\ \dot{\varepsilon}_t \geq 10^0 s^{-1} \end{cases} \tag{7.15}$$

where $\dot{\varepsilon}_t$ is the strain rate in tensile tests, the value of which can be measured from the strain gauges attached to the specimen.

Apart from the strain rate, the loading rate is another parameter to represent the input loading in the experiment, which is the elastic stiffness of the tensile strength-time curve. In many dynamic tests involving cored-shape specimens such as Brazilian tests and semicircular bending tests, the strain rate is difficult to measure due to the shape of the specimen, and thus the loading rate rather than strain rate is often used in those tests. Therefore, an empirical relationship between the DIF and the loading rate is also proposed based on tensile tests on different rocks such as sandstones (Huang et al. 2010, Huang et al. 2010), granites (Zhao and Li 2000, Dai et al. 2010, Dai et al. 2010, Dai and Xia 2010, Xia et al. 2013), tuffs (Yan et al. 2012), basalts (Yan et al. 2012) and marbles (Yao et al. 2017), shown in Figure 7.0–2.

It can be seen from Figure 7.0–2 that the DIF increases gradually when the loading rate is less than 100/s, but grows rapidly when the strain rate is greater than 100/s, thus dividing Figure 7.0–2 into two zones with distinct responses. Therefore, like the empirical relationship between the DIF and the strain rate, two equations are generated for two zones as:

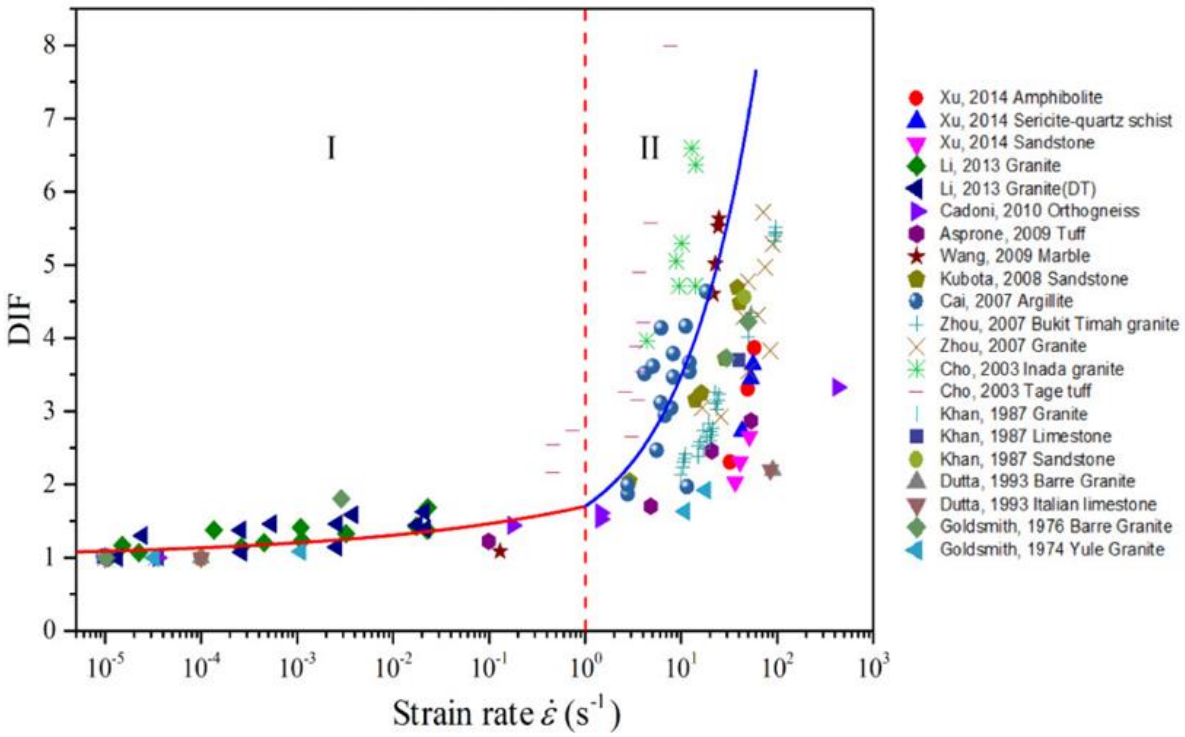

Figure 7.0–1. DIF for tensile strength of rocks as a function of strain rate (Liu et al. 2018)

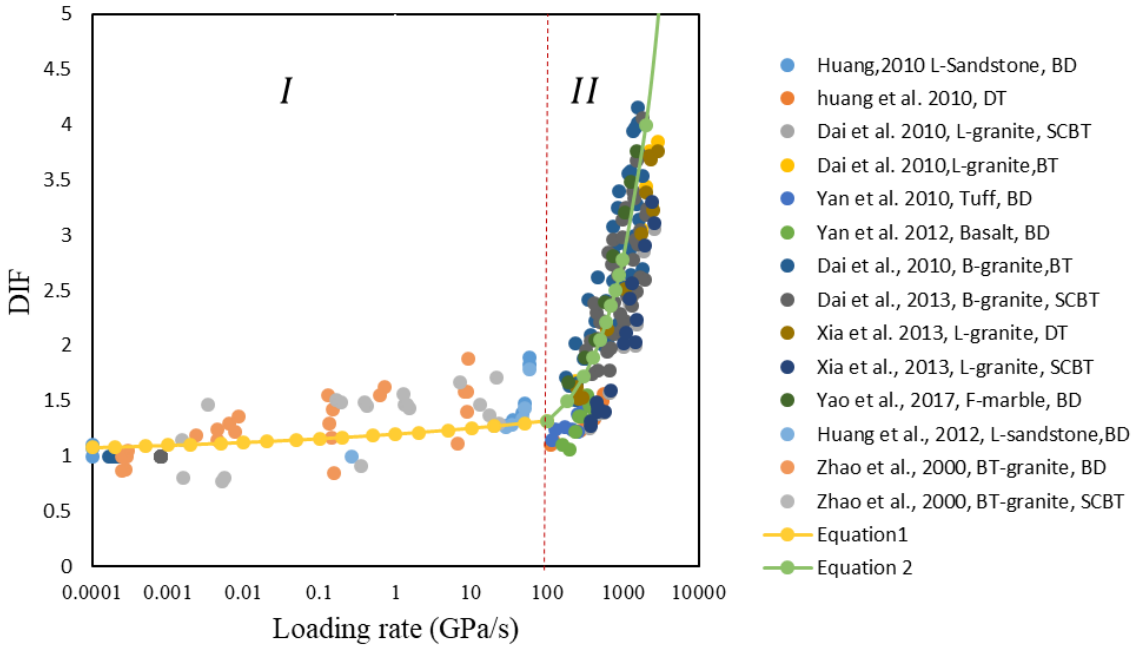

Figure 7.0–2. DIF for tensile strength of rocks with a function of loading rate (Zhao and Li 2000, Dai et al. 2010, Dai and Xia 2010, Dai et al. 2010, Huang et al. 2010, Huang et al. 2010, Yan et al. 2011, Huang et al. 2012, Yan et al. 2012, Dai et al. 2013, Xia et al. 2013, Yao et al. 2017)

$$DIF = \begin{cases} 1 + 0.20\dot{\sigma}_t^{0.10} & for\ \dot{\sigma}_t < 10^2 Gpa/s \\ 1 + 0.01\dot{\sigma}_t^{0.75} & for\ \dot{\sigma}_t \geq 10^2 GPa/s \end{cases} \quad (7.16)$$

The rate-dependent cohesive fracture law now can be developed by incorporating the DIF with respect to loading rate or strain rate respectively presented in equation (7.15) and (7.16) into the mixed-mode cohesive fracture law introduced in Section 7.2.2. The failure criterion and non-associated plastic potential in the rate-dependent cohesive fracture law are:

$$f = {t_s}^2 - 2c_0(1-D)\tan\phi\,(DIF \times \sigma_{t0}(1-D) - t_n) - \tan^2\phi\,({t_n}^2 - (DIF \times \sigma_{t0}(1-D))^2) \quad (7.17a)$$

$$g = {t_s}^2 - 2c_0(1-D)\tan\psi\,(DIF \times \sigma_{t0}(1-D) - t_n) - \tan^2\psi\,({t_n}^2 - (DIF \times \sigma_{t0}(1-D))^2) \quad (7.17b)$$

The geometries of the initial yield function with different DIFs are illustrated in Figure 7.0–3. It can be seen that the introduction of DIF leads to a change in the geometry of the yield function, thereby influencing the normal and shear plastic deformations of materials in the fracture process zone. The rate-dependent mixed-mode cohesive fracture law is incorporated into the continuum constitutive model for simulating rock fractures under dynamic loading in the next section.

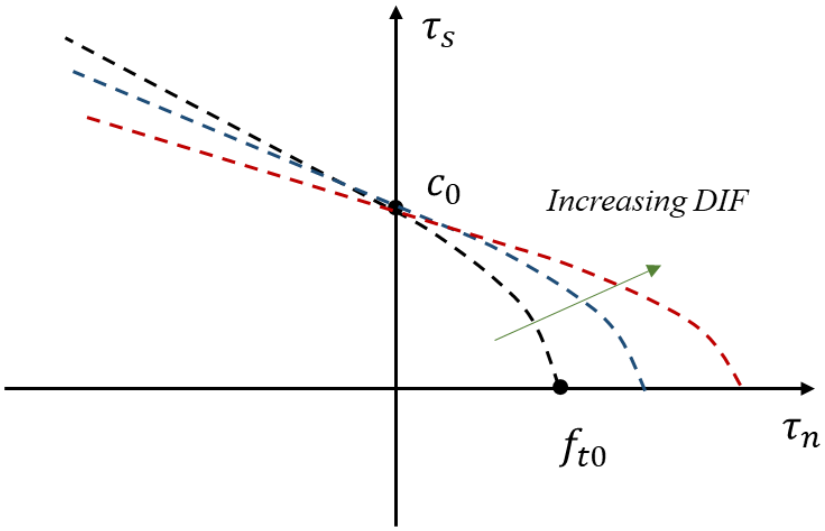

Figure 7.0–3. Geometries of the initial yield function with different DIFs.

7.3.2. Mixed-mode ring tests

In this section, a series of ring tests with different internal diameters performed by Li et al. (2016) are simulated to examine the capability of the SPH framework with the rate-dependent continuum constitutive model to predict the strain rate effects on the behaviour of rock fractures.

Tests under quasi-static loadings were conducted under quasi-static loading and compared with the experimental data reported in Chapter 6 for demonstrating the predictive capability of the traditional SPH model to capture the mixed-mode rock fracture behaviour. The geometry and loading conditions of the specimen in the experiments are shown in Figure 7.0–4*a*. Specimens drilled from a marble block are first prepared, with the diameter (*D*) of 50mm and thickness (*t*) of 25mm. A circular disc with the diameter (*d*) varying from 5mm to 25mm was then cut off at the centre of the specimens, resulting in ring specimens with different diameter ratios (*d/D*) from 0.1 to 0.5. The specimens are sandwiched directly between two platens with the length of 20mm, over which a static force is applied. The static material properties of marble are listed in Table 7.0-1.

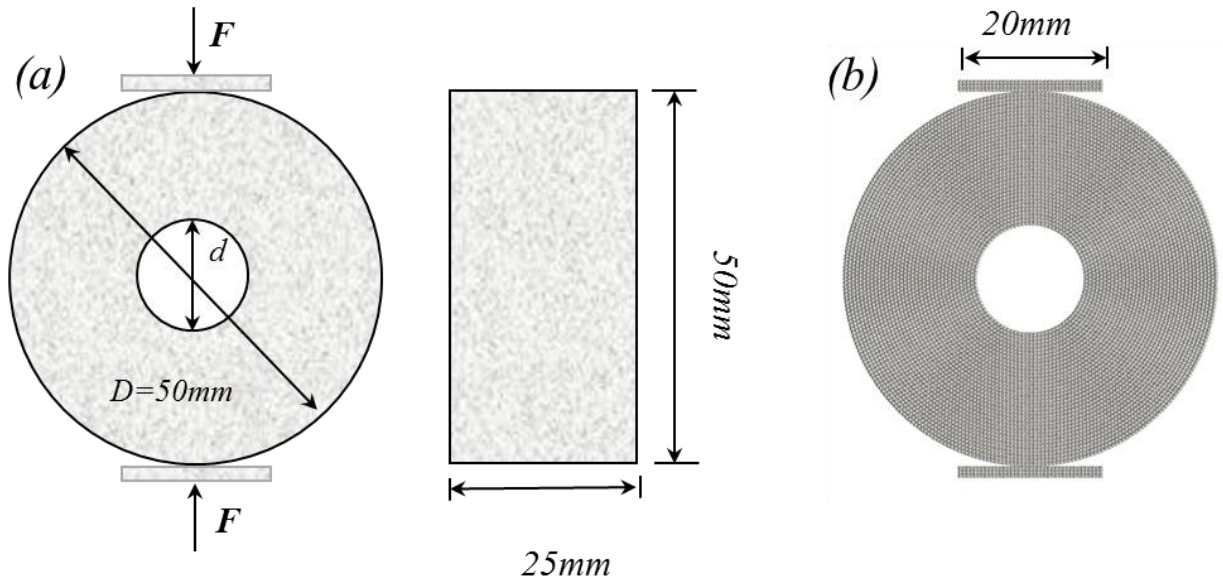

Figure 7.0–4. Geometry and boundary condition for the Brazilian test: (a) Experimental setup; (b) SPH simulation setup for $\alpha = 0.3$.

The corresponding numerical configuration in SPH is shown in Figure 7.0–4*b*. To perfectly create the shape of a circular cut-off using a reasonable number of particles, particles that form the ring sample are radially distributed in this test. The particle discretisation size of 0.5mm is used for all the simulations, resulting in a total number of 7651 particles for a specimen without a central hole. The particle number decreases with a larger value of the diameter ratio (d/D). To simulate those two platens in the experiment, three layers of boundary particles with the spatial discretisation size of 0.5mm, resulting in 303 SPH particles in total, are generated for

each boundary. A high vertical velocity as $0.17m/s$ is imposed on the top boundary and boundary particles to achieve the dynamic loading condition. A ramp loading is also applied to stabilise the numerical solution. In summary, the boundary conditions for this test are as follows: velocities of the top boundary particles are set as $v_x = 0, v_y = -0.17m/\mathrm{s}$, while the velocities of bottom boundary particles are $v_x = 0, v_y = 0.17m/\mathrm{s}$. During tests, peak loads are recorded to calculate the dynamic tensile strength of specimens with different internal diameters under the dynamic indirect tensile loading using the equation:

$$\sigma_{td} = \frac{P}{\pi R t}(6 + 38\frac{r^2}{R^2}) \tag{7.15}$$

where σ_{td} is the dynamic tensile strength, P is the peak load applied to the specimen, r and R are respectively the internal and external radius.

Table 7.0-1. Material properties of marble in the ring tests

Material properties of marble	
Young's modulus ($\boldsymbol{E}$)	$\mathbf{49GPa}$
Poisson's ratio ($\boldsymbol{\nu}$)	$\mathbf{0.19}$
Density ($\boldsymbol{\rho}$)	$\mathbf{2.7g/cm^3}$
Tensile strength($\boldsymbol{f_t}$)	$\mathbf{3.6MPa}$
Cohesion ($\boldsymbol{c}$)	$\mathbf{10MPa}$
Friction angle ($\boldsymbol{\varphi}$)	$\mathbf{33°}$
Dilation angle ($\boldsymbol{\psi}$)	4°
Mode I fracture energy ($\boldsymbol{G_I}$)	$\mathbf{30Nm}$
Mode II fracture energy ($\boldsymbol{G_{II}}$)	$\mathbf{30Nm}$
Peak displacement ($\boldsymbol{\delta_0}$)	$\mathbf{8.5\mu m}$
Secant normal stiffness ($\boldsymbol{K_{n0}}$)	$\mathbf{10^{14}Pa/m}$
Secant shear stiffness ($\boldsymbol{K_{s0}}$)	$\mathbf{10^{11}Pa/m}$

The fracture developments of ring specimens with different diameter ratios (*d/D*) in indirect tensile tests are shown in Figure 7.0–5. It can be seen from Figure 7.0–5 that specimens with different diameter ratios have different fracture development, although all fractures initiate

from the surface of the internal hole along the diametral loading line in all ring specimens. To be specific, only one final fracture is developed at the end within the ring specimen when *d/D* < *0.3*, while a secondary fracture forms together with the fracture along the loading diameter when $d/D \geq 0.3$, which is similar to the quasi-static cases presented in Chapter 6. However, there are more damaged zones observed under dynamic loading. When *d/D = 0.1*, two lines of slightly damaged SPH particles are formed, indicating fracture branching after the initiation of the fracture. Then one fracture continues to propagate towards the loading plates while the other one stops developing. The fracture development of the specimen with *d/D = 0.2* is similar to that with *d/D = 0.1*, except that some SPH particles near the outer rings are slightly damaged. With an increase in *d/D* ($d/D \geq 0.3$), fracture branching disappears in the loading direction and secondary cracks are formed in the direction perpendicular to the loading line, always lagging behinds the vertical cracks. Two secondary cracks are initiated from the surface of the outer bound of the ring and propagated to the centre, eventually resulting in a four-pan-shaped failure. The final fracture patterns in the SPH simulation and experiment are shown in Figure 7.0–6. It can be seen that although the numerical simulation does not capture perfectly the secondary cracks in the specimen with $d/D \leq 0.2$, the overall fracture patterns obtained by the traditional SPH method with a rate-dependent constitutive model match the experimental observations, indicating that the proposed approach is capable of capturing the progressive failure of ring specimens under dynamic loadings.

The comparison between the experimental and simulation results for the dynamic tensile strength of specimens with different internal diameters is plotted in Figure 7.0–7. It can be seen that the numerical model captures well the trend of change in dynamic tensile strength exhibited in the experiment, although the numerical results are slightly lower than the experimental results for some cases. With an increase in internal diameter, there is a linearly decreasing trend in the calculated dynamic tensile strength, indicating that failure of the ring specimen with the large internal diameter requires much less energy than the failure of the ring specimen with small internal holes. A linear relationship between the dynamic tensile strength and the diameter ratio is obtained based on the simulation results, which is expressed as:

$$\sigma_{td} = -122.43\left(\frac{d}{D}\right) + 104.78 \tag{7.16}$$

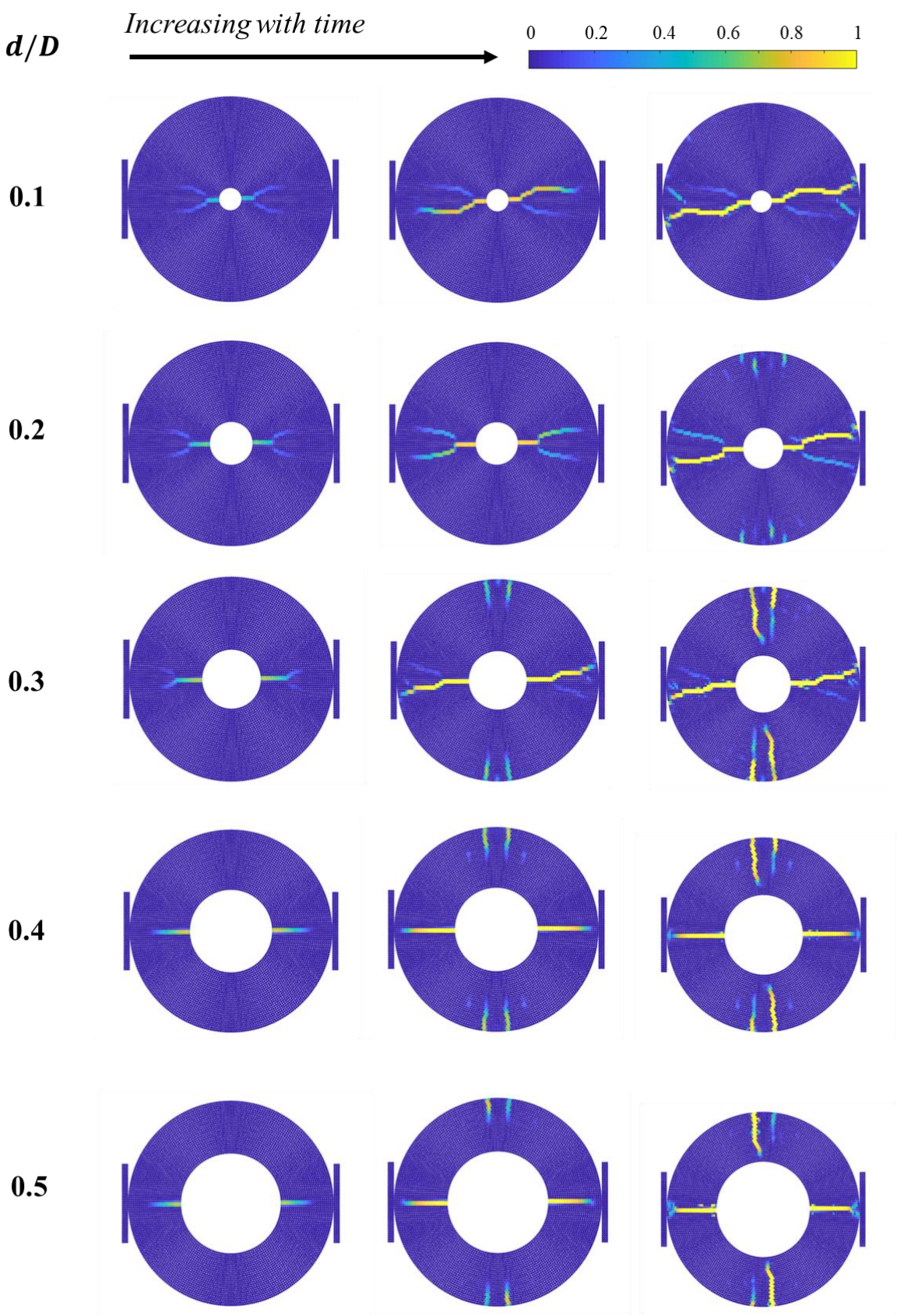

Figure 7.0–5. Fracture propagation in specimens with different d/D ratios

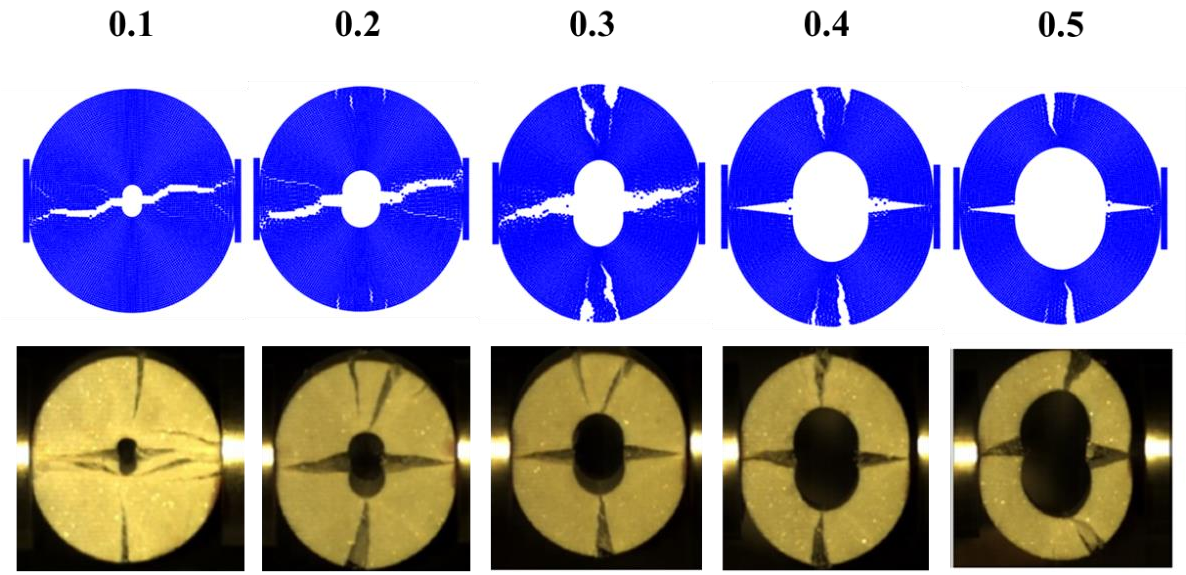

Figure 7.0–6. Comparison between simulation and experiment in the final fracture patterns of specimens with different d/D ratios under dynamic loading.

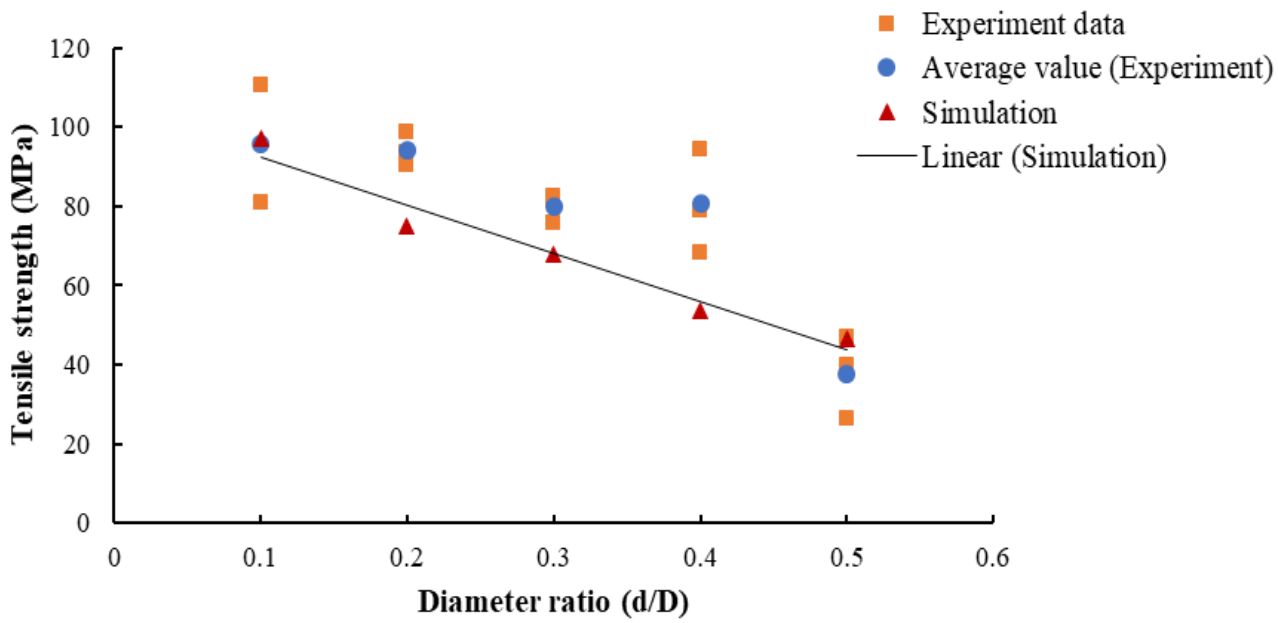

Figure 7.0–7. Comparison of experimental and simulation results for dynamic tensile strength of specimens with different internal diameter.

7.4. Rate effect enhancement by dynamic SPH method

7.4.1. Elliptical force-displacement loading

In the second approach, the traditional SPH framework combined with the mixed-mode continuum constitutive model presented in Section 7.2 is applied. The loading rate effect is enhanced by imposing a nonlinear force or acceleration to the SPH loading particles, similar to the input loading in the split Hopkinson bar system that is the most widely used equipment for dynamic tests. Figure 7.0–8 shows the typical stress input history of a dynamic test on rocks in the split Hopkinson bar by Fakhimi et al. (2018). In the split Hopkinson bar system, the stress wave, normally with the duration of 100 to 200 μs, is generated by the gas gun's launching the striker. Then it is propagated through the bar towards the specimen and split into a reflected wave and a transmitted wave. While the reflected wave is reflected away from the specimen and travels back to the incident bar, the transmitted wave travels through the specimen and into the transmitted bar, causing plastic deformation in the specimen (Gilat et al. 2009).

To simulate the transmitted pulse in the split Hopkinson bar, the elliptical force or acceleration history depicted in Figure 7.0–9 is applied to the SPH loading particles, resulting in a nonlinear increase in velocity of SPH loading particles, which is very different from the constantly applied velocity in the first approach. In Figure 7.0–9, a_{max} is the maximum value of acceleration applied to the loading particles, the value of which depends on the input strain/loading rates or the input stress history in the experiments. t_f is the duration of applied loading, which is normally chosen between 100 and 200 μs for consistency with the experimental setup. The acceleration a of the loading particles at time t can be calculated by the following equation:

$$\left(\frac{a}{a_{max}}\right)^2 + \left(\frac{t-t_f/2}{t_f/2}\right)^2 = 1 \tag{7.17}$$

The imposed loading condition accelerates the wave propagation within the computational domain in SPH simulation, thanks to the dynamic nature of the SPH method. Furthermore, owing to the fact that the fracture geometry is represented by a set of damaged particles, over which the fracture plane is defined and can be in any orientation depending on the stress condition, the proposed approach could naturally simulate complex fracture patterns due to the dynamic loadings.

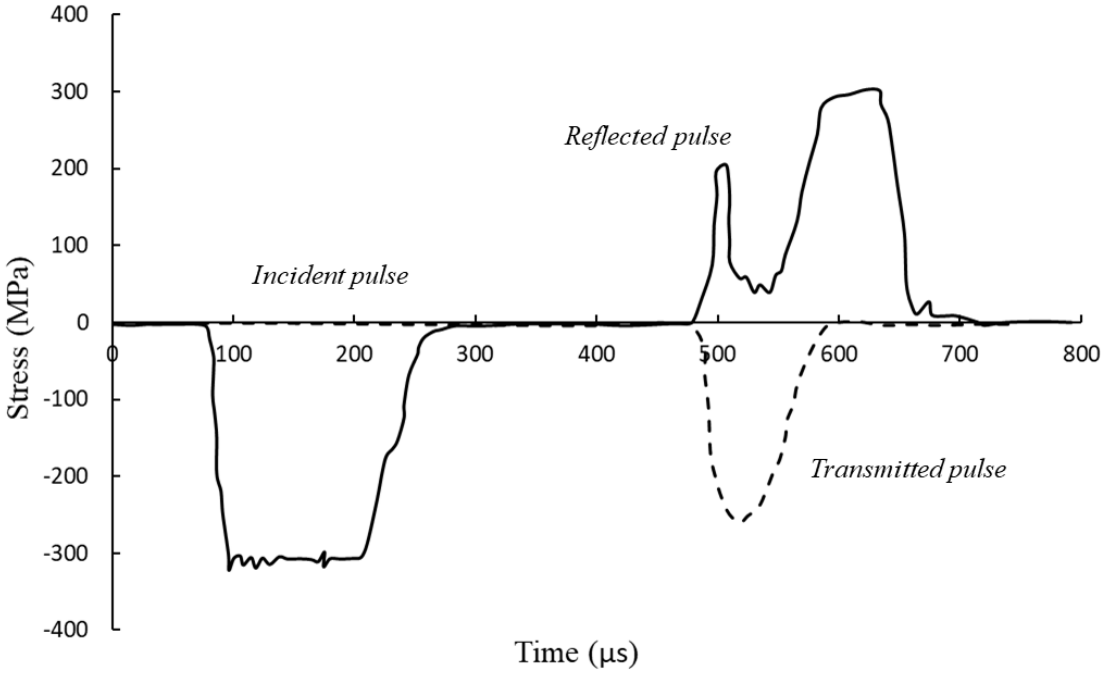

Figure 7.0–8. A typical stress input history of dynamic loading on rocks in split Hopkinson bar system (Fakhimi et al. 2018).

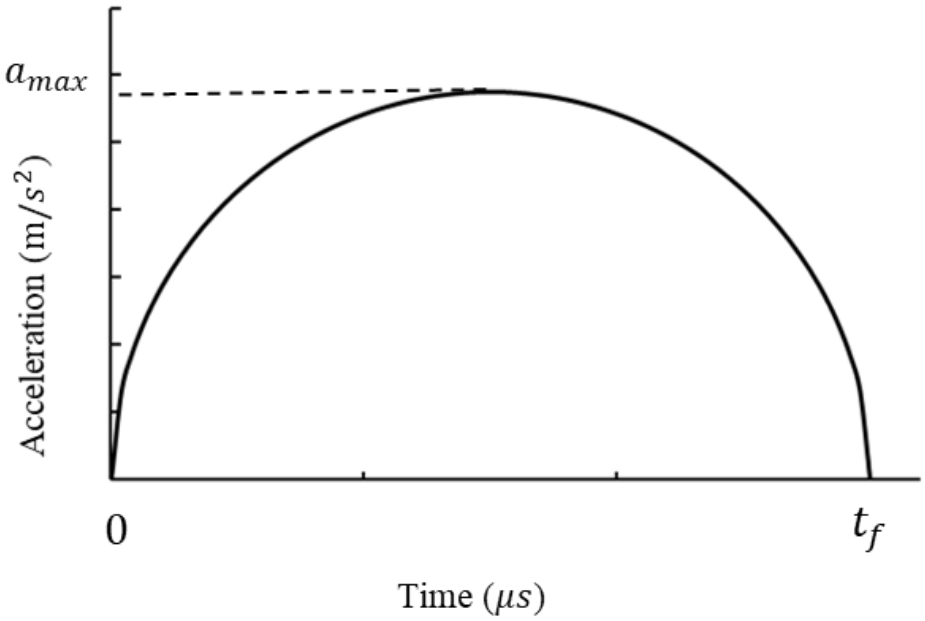

Figure 7.0–9. Force or acceleration input history in SPH framework

7.4.2. Dynamic rock fracture applications

In this section, three laboratory tests of rock and rock-like materials under a wide range of loading rates are simulated using the second approach. Numerical results are then compared with the experimental results to examine the capability of the proposed model for predicting the process of rock fracture propagation and its final fracture pattern, as well as for capturing the mechanical behaviour of rock fractures under static and dynamic loadings.

7.4.2.1. Notched semi-circular bending test

In the first application, the notched semicircular bending (NSCB) test of Fangshan marble is performed. Fangshan marble is a fine-grained rock material consisting of dolomite (98%) and quartz (2%), thus is considered as homogeneous and isotropic. The material properties obtained from experiment (Zhang and Zhao 2013) and DEM simulations (Gui et al. 2016) are presented in Table 7.0-2. In the experiment, the NSCB specimen with the radius of 25mm and thickness of 20mm was sandwiched between the incident bar and the transmission bar in the Split Hopkinson Bar system, shown in Figure 7.0–10a. Before testing, a notch of 5mm was machined in the middle of the specimen perpendicular to the diameter direction. During the test, a striking speed of 2.25m/s was generated by gas gun impacting the incident bar, resulting in a portion of the dynamic stress pulses travelling through the specimen and inducing its fracture.

Table 7.0-2. Material properties of Fangshan marble in NSCB test.

Material properties of Fangshan marble	
Young's Modulus (E)	85GPa
Poisson's ratio (v)	0.3
Density (ρ)	2.8g/cm^3
Tensile strength(f_t)	9.5MPa
Cohesion (c)	10MPa
Friction angle (φ)	40°
Dilation angle (ψ)	10°
Mode I fracture toughness (K_{Ic})	$1.6\text{Mpa}\sqrt{m}$
Mode II fracture toughness (K_{IIc})	$1.6\text{Mpa}\sqrt{m}$
Peak displacement (δ_0)	3μm
Secant normal stiffness (K_{n0})	10^{14}Pa/m
Secant shear stiffness (K_{s0})	10^{11}Pa/m

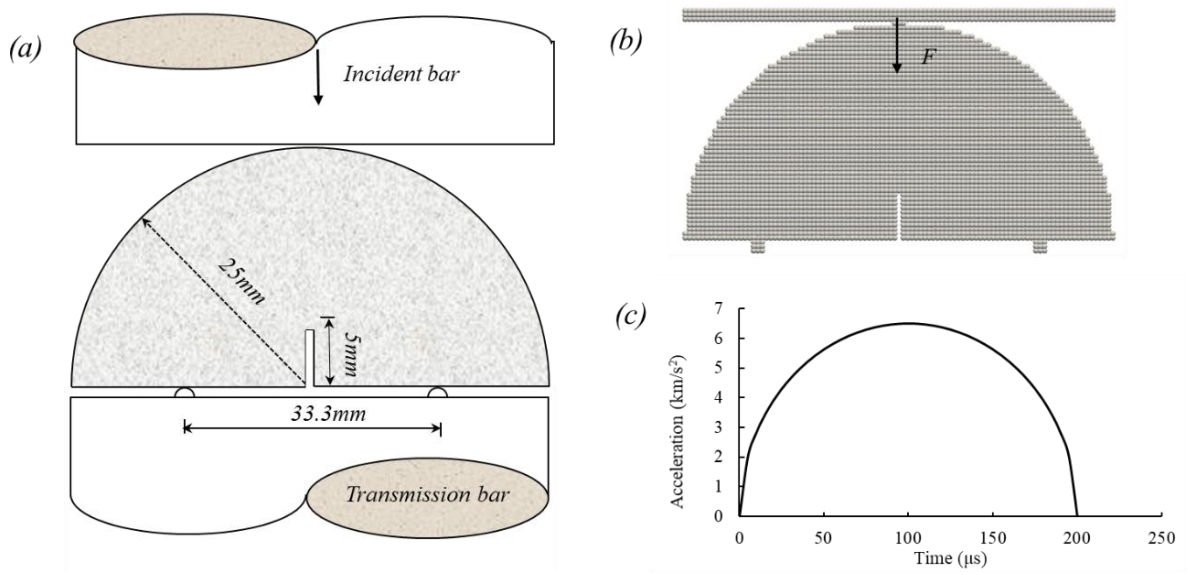

Figure 7.0–10. Setup of notched semicircular bending test: (a) Schematic of NSCB specimen in split Hopkinson pressure bar system; (b) Initial SPH configuration in simulation; (c) Input loading with time in the simulation.

In the SPH simulation, the particle discretisation size of 0.5mm is used. Thus, the NSCB specimen is generated by 4,123 SPH particles, while the boundary is simulated by 167 SPH particles, as shown in Figure 7.0–10b. Input loading as a function of time, shown as Figure 7.0–10c, is imposed vertically on the top of the boundary to simulate the loading applied by the split Hopkinson bar, while the horizontal velocity of those particles is zero. The ellipse shape of the acceleration-time curve with the duration of $200\mu s$ is selected as it can better capture the trend of loading in the experiment, which increases rapidly at the beginning and gradually tapers off until reaching the peak loading. In the test, the peak acceleration of 6.5 kN/s^2 is applied. The particles at the bottom boundary are allowed to move freely in the horizontal direction while remaining fixed vertically. During the test, the fracture initiation and propagation are monitored, while the force applied to the top layer of the specimen is also recorded with time for calculating Mode I dynamic fracture initiation toughness for comparison with the experiment. The dynamic initial fracture toughness can be calculated as:

$$K_{Id} = Y_I\left(\frac{S}{R}\right)\frac{P(t_f)\sqrt{\pi a}}{2RB} \tag{7.18}$$

where 2S is the span of the specimen; R is the radius of the specimen; t_f is time-to-fracture, $P(t_f)$ is load force when $t = t_f$; a and B are the notch length and the thickness of specimen; $Y_I\left(\frac{S}{R}\right)$ is the mode I normalised intensity factor, which can be expressed as:

$$Y_I\left(\frac{S}{R}\right) = 3.638 - 0.139\left(\frac{a}{R}\right) + 0.039\exp\left[7.387\left(\frac{a}{R}\right)\right] \quad \text{for } \frac{\text{S}}{\text{R}} = 0.667 \qquad (7.19)$$

In this test, the notch length to radius ratio (a/R) is 0.2, resulting in the value of $Y_I\left(\frac{S}{R}\right)$ of 3.78.

Figure 7.0–11 shows a comparison of fracture propagation in the NSCB specimen between experiment and simulation. The white arrow indicates the tip of the crack at different times. It can be seen from the experimental results in Figure 7.0–11 that at $40\mu s$, the fracture has been initiated at the notch tip and propagates along the loading direction, leading to the tip of the crack located around 2mm from the notch tip. In the SPH simulation, on the other hand, the time when the tip of crack moves to 2mm in the same location as that described for the experiment is $65\,\mu s$ (shown in Figure 7.0–11a). After its initiation, the fracture keeps propagating up to stage b, where the crack tip in the experiment moves to 6.68mm at $t = 45\mu s$, while the simulation result shows a similar location of the crack tip (7mm) at $t = 73\mu s$. At stages c and d, the crack tip locations in the experiment are respectively 12mm and 16.5mm from the notch tip, whereas the tip of crack in the SPH simulation (12.5mm at stage c and 17mm at stage d) has moved a little further compared with experiment. Finally, a horizontal fracture pattern is formed in the middle of the specimen. Figure 7.0–12 compares the position of the crack tip at different times between experiment and simulation. Overall, the fracture propagation with time in the NSCB test represented by SPH fracturing particles matches the experimental observation well, although the crack initiation in simulation is postponed compared to that in the experiment.

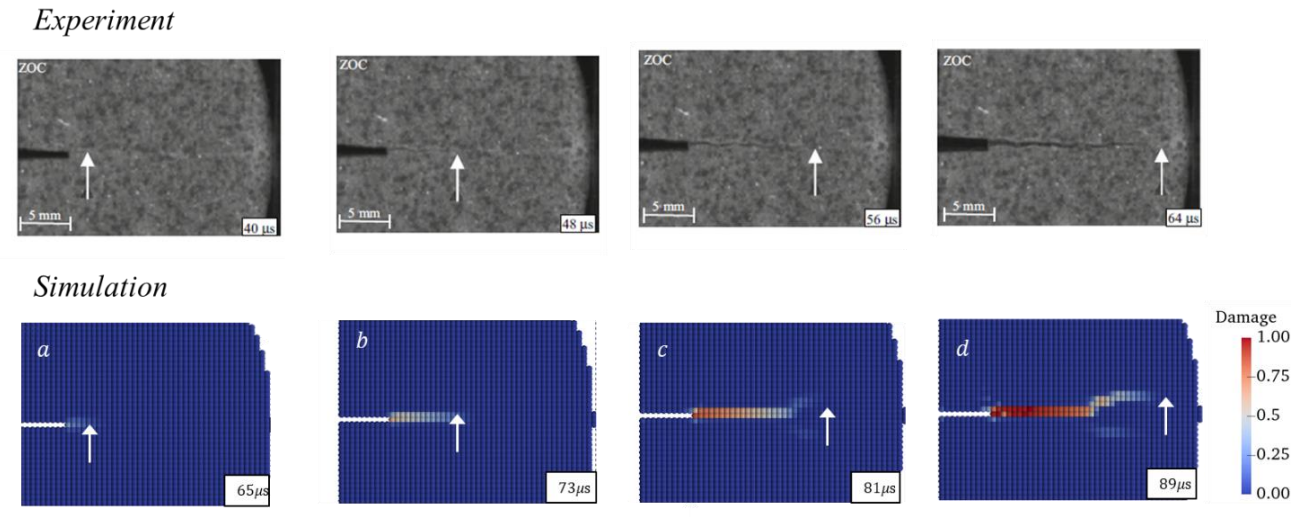

Figure 7.0–11. Comparison of crack propagation process in notched semicircular bending test between experiment (top) and simulation (bottom).

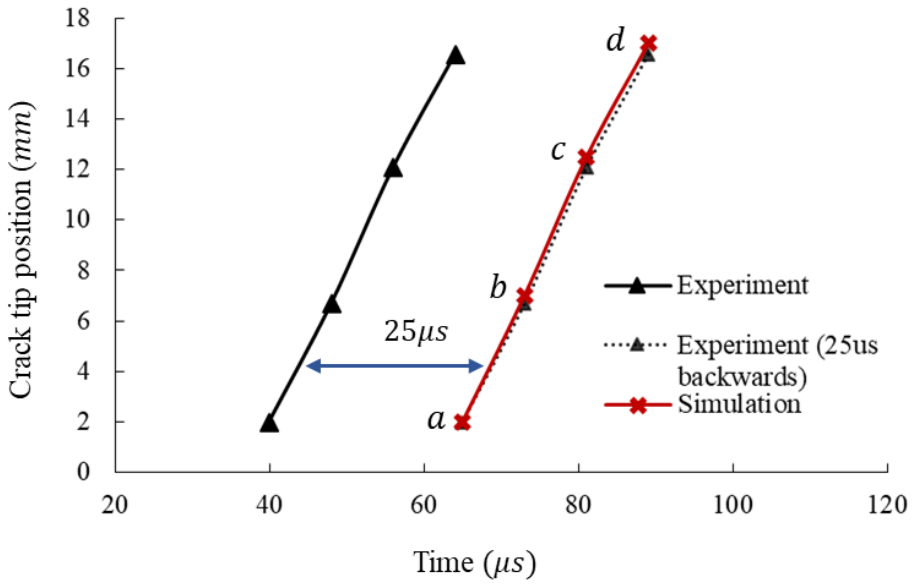

Figure 7.0–12. Comparison of crack tip positions with time between experiment and simulation of notched semicircular bending test

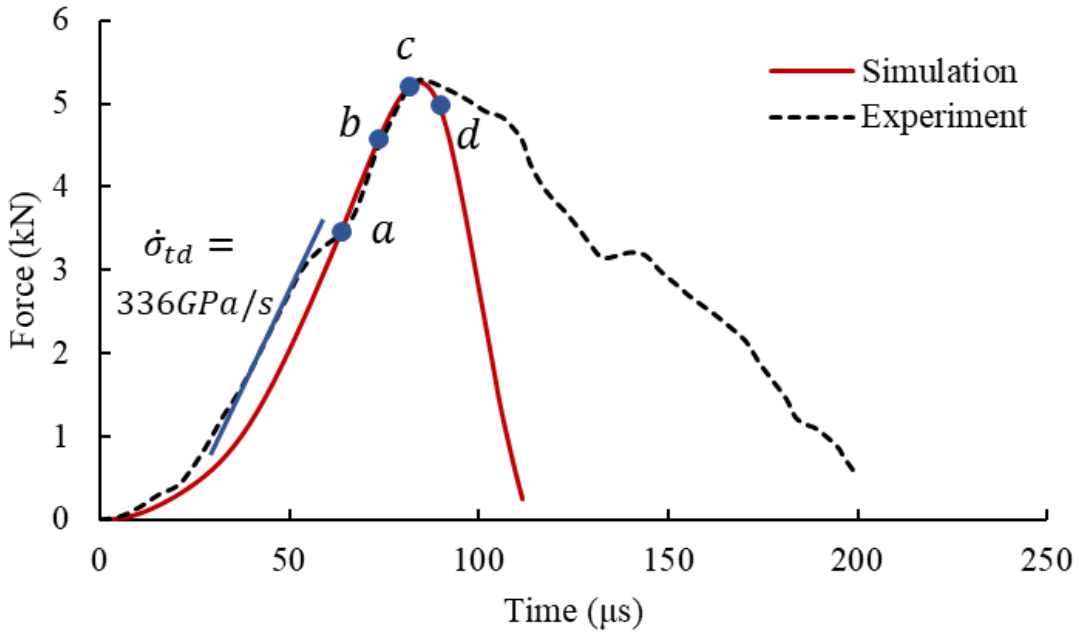

Figure 7.0–13. Comparison of the force-time curves between experiment and simulation of notched semicircular bending test

Figure 7.0–13 compares the evolution of applied force between the experimental and simulation results. The corresponding forces at stages (a) to (d) in Figure 7.0–11 are also marked in Figure 7.0–13. It can be seen that the simulation result using the SPH method

matches the experimental data well, especially for the prediction of peak load. Fracture has been initiated before the force reaches 3.45kN (stage a). Then the force increases linearly to the peak up to 3.26kN when the fracture keeps propagating (from stage a to stage c). After that, the sample goes into the post-peak failure stage in which the stress decreases with time. Compared with the experiment, the NSCB specimen in SPH shows more brittle behaviour, and further investigation is required to confirm this difference.

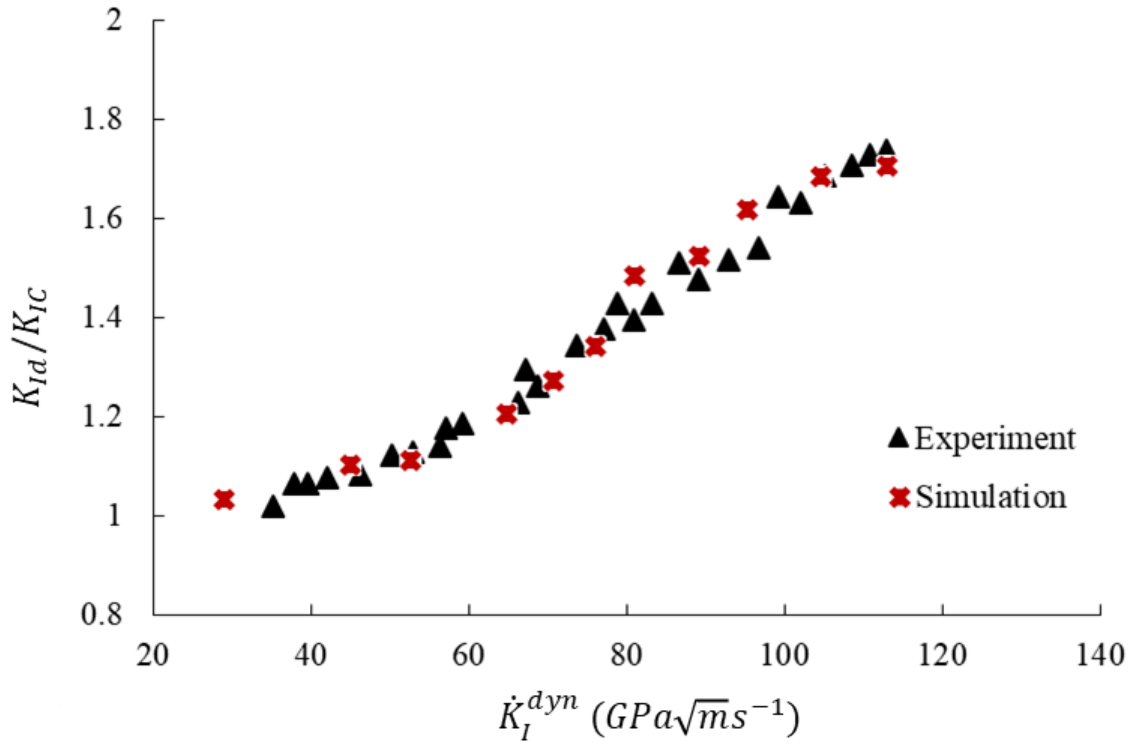

Figure 7.0–14. Comparison of normalised dynamic crack initiation toughness with loading rate between experiment and simulation of notched semicircular bending test

Figure 7.0–14 compares the normalised dynamic crack initiation toughness (K_{Id}/K_{Ic}) with the loading rate between the experiment and the simulation of the NSCB test. Normalised dynamic crack initiation toughness is the ratio of the dynamic crack initiation toughness (K_{Id}) to the static fracture toughness (K_{Ic}) of material. The dynamic crack initiation toughness, which is defined as the dynamic crack toughness at time to fracture, can be calculated based on equation (7.18), while the loading rate ($\dot{K}_I^{dyn}$) is the slope of the dynamic fracture toughness at that point. It can be seen from Figure 7.0–14 that the normalised dynamic crack initiation toughness increases almost linearly with the increase in loading rate. This indicates that with a high input

loading, the specimen requires more energy to resist fracturing. Overall, the simulation and experimental results match very well in terms of the trend of the normalised dynamic crack initiation toughness with different loading rates, further showing the capability of the SPH fracturing method to capture rock fractures under dynamic loading.

7.4.2.2. Brazilian Disc Test

A series of Brazilian disc (BD) tests for Fangshan marble conducted by Zhang and Zhao (2013) are replicated under a wide range of dynamic loadings in this example. Figure 7.0–15a shows specimen dimensions of the BD tests and their boundary conditions in the experiment. A disc with the diameter of 50mm and thickness of 20mm was sandwiched between the incident bar and the transmission bar, similar to the laboratory test of NSCB. A striking velocity was applied to the incident bar and transmitted to the BD specimen. Based on the experimental configuration, a BD specimen with the same dimensions is generated by 3,505 SPH particles, while the top and bottom boundaries are each simulated by 201 SPH particles, as shown in Figure 7.0–15b. The discretisation particle size in this test is 0.75mm. To simulate the dynamic force impacting on the specimen, a vertical force as a function of time as illustrated in Figure 7.0–16 is applied to the top boundary. The material properties in the BD test are the same as those in the NSCB test, as provided in Table 7.0-2. During the simulation, the applied force on the top of the specimen is recorded with time, for calculating the dynamic strength (σ_{td}) under different loading conditions using the equation:

$$\sigma_{td}(\dot{\sigma}_{td}) = \frac{2P}{\pi DB} \tag{7.20}$$

where $\dot{\sigma}_{td}$ is the loading rate in the tensile strength-time curve, as determined by the slope of the stress history from the time of stress equilibrium and ending to the time-to-fracture; P is the peak load applied on the specimen; D and B are respectively the diameter and thickness of the specimen.

Figure 7.0–17 shows the comparison of strength history under the loading case of $\dot{\sigma}_{td} = 830Gpa/s$ between experiment and simulation. It can be seen that the overall prediction in SPH agrees well with the experimental result, although a more brittle fracturing response under dynamic loading is observed in the simulation, similar to that in the described NSCB test. This is attributed to the inaccurate material properties in the experiment, which were adopted as the

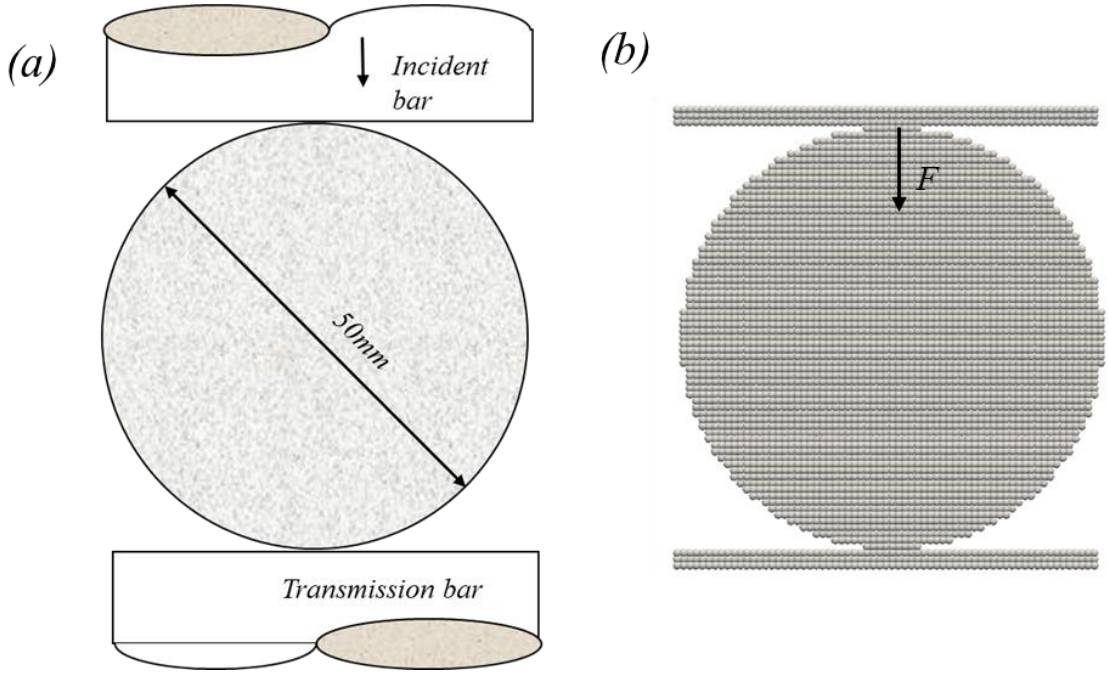

Figure 7.0–15. Setup of Brazilian disc (BD) test: (a). Schematic of BD specimen in the split Hopkinson pressure bar system; (b). Initial SPH configuration in simulation.

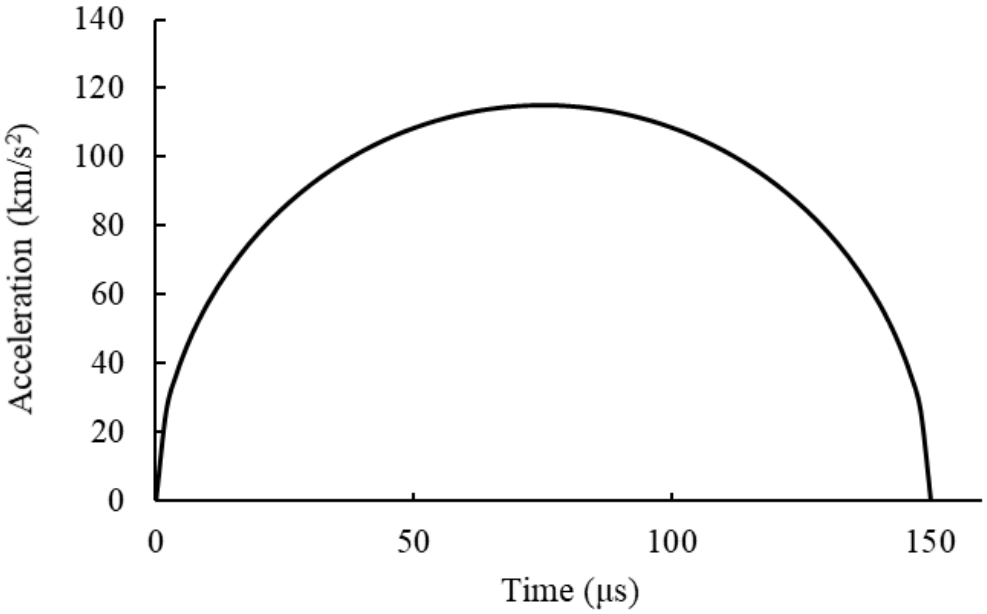

Figure 7.0–16. Input loading with time in the simulation of the Brazilian disc test

input parameters for the simulation. Nevertheless, the predicted tensile strength using the fracturing SPH framework is 32.7MPa, which is very close to the experimental result (32.5MPa). The corresponding fracture patterns of the specimen at stages (a-e) marked in the

strength history are shown in Figure 7.0–18. Fracture initiation occurs at the stage (a), where damage to some SPH particles in the middle of the specimen has begun, as shown in Figure 7.0–18a. The calculated stress in Figure 7.0–17 reaches around 15MPa at stage (a) and continues to increase until the peak. Meanwhile, fracture propagates vertically towards the loading plates, leading to a vertical fracture pattern in the middle of the specimen (see Figure 7.0–18 b-c). Once the fracture propagates near to the loading plates, a transition from tensile failure to shear failure occurs, resulting in a curving fracture formed near the boundaries. This tensile-shear failure transition under dynamic loadings was also observed in the experiment, suggesting that the SPH fracturing approach automatically captures the fracture patterns under dynamic loadings. Figure 7.0–18e shows the final fracture pattern of the BD specimen under dynamic loading. A vertical fracture band is formed in the middle of the specimen, splitting the disc into two halves. The corresponding stress at stage (e) is marked in Figure 7.0–17, which shows that the specimen experiences softening behaviour at that stage.

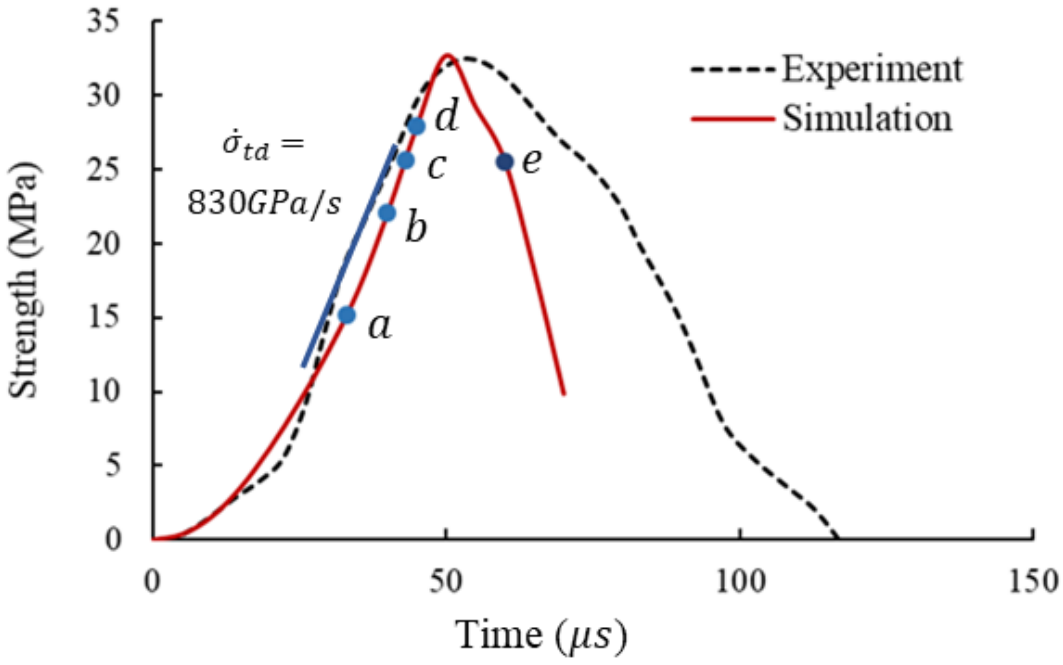

Figure 7.0–17. Comparison of dynamic tensile strength with time between experiment and simulation of Brazilian disc test

Figure 7.0–19 shows a comparison of the normalised dynamic tensile strength of Fangshan marble between experiment and simulation. The normalised dynamic tensile strength (σ_{td}/σ_t) is the ratio of dynamic tensile strength to static tensile strength. Given that the dynamic tensile

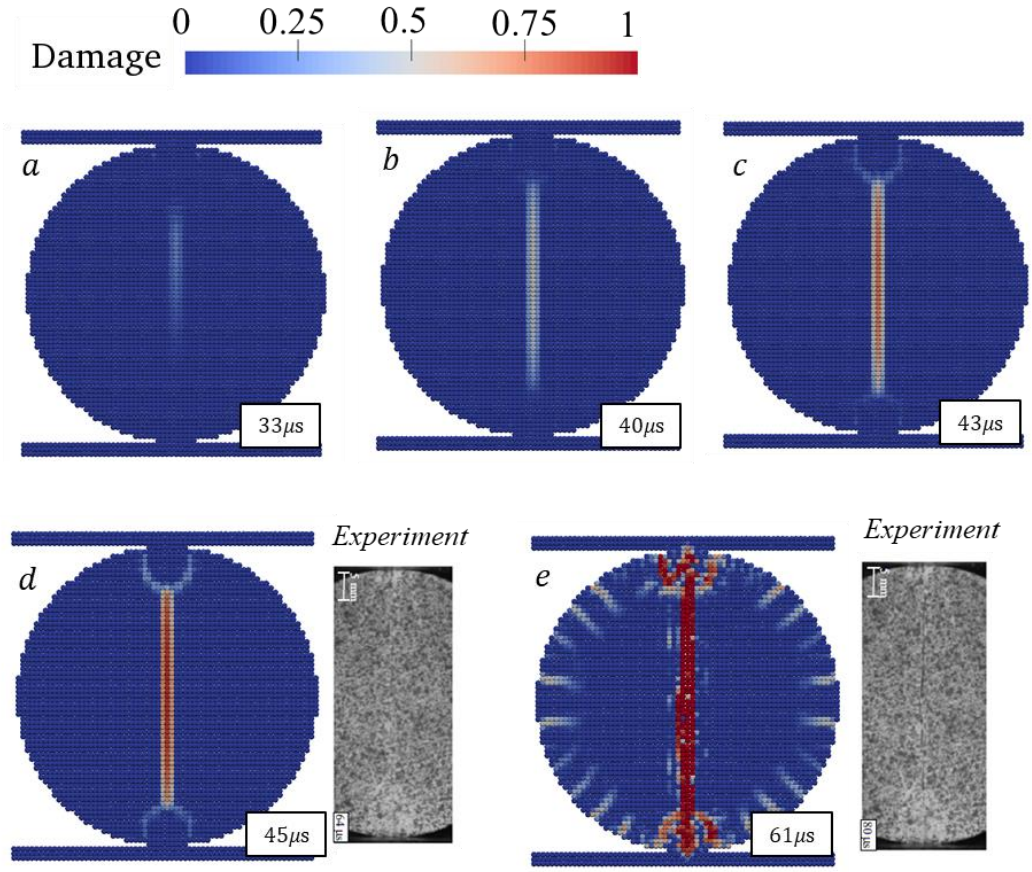

Figure 7.0–18. Fracture propagation in SPH simulation of Brazilian disc test

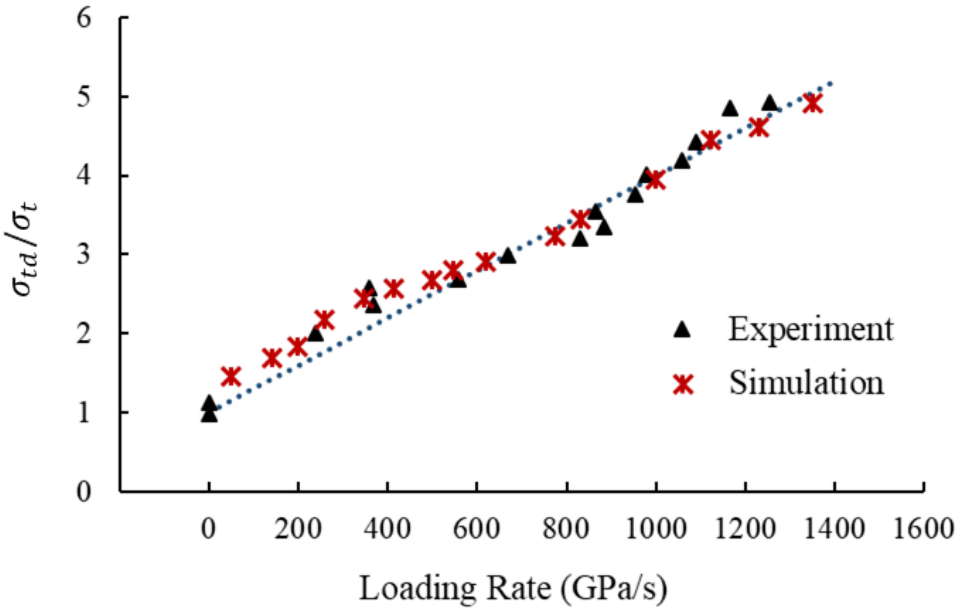

Figure 7.0–19. Comparison of normalised dynamic tensile strength with loading rate between experiment and simulation of Brazilian disc test

strength can be calculated by equation (7.20) and the value of the static tensile strength of Fangshan marble is 9.5MPa as provided by experiment, the normalised dynamic tensile strength in the simulation can be easily calculated. It can be seen from Figure 7.0–19 that the simulation using the fracturing SPH method can capture well the increasing trend of normalised dynamic tensile strength with the increasing loading rates in the experiment. A linear relationship between the normalised dynamic tensile strength and loading rate can be derived based on the simulation results, as:

$$\sigma_{td}/\sigma_t = 0.003 \times \dot{\sigma}_{td} + 1.0 \tag{7.21}$$

7.4.2.3. Mixed-mode three-point bending test

In the last example, mixed-mode fractures of the three-point bending specimen subjected to both static and dynamic loading are simulated. Figure 7.0–20a shows the specimen dimensions and boundary conditions of the three-point bending test (John and Shah 1990). The specimen is 203.2mm in length, 76.2mm in depth and 25.4mm in thickness. A vertical notch with the length of 19mm was machined at the bottom of the specimen. The distance between the notch and the centreline of the specimen was $\gamma L/2$ where γ is a coefficient determining the location of the notch. Specimens with five different notch locations ($\gamma = 0.5, 0.7, 0.718, 0.766, 0.875$) were prepared for the test, in order to investigate different fracture modes of concrete under different loadings. The notched specimen was supported by two rollers and loaded by another rolled placed at the top mid-span of the beam. Static loading with a strain rate of $10^{-6}/\mathrm{s}$ and dynamic loading with a strain rate of 0.5/s were applied on the specimen through the top roller. The material properties of concrete provided in the experiment are listed in Table 7.0-3.

In the 2D SPH simulation, the specimen is generated by 7,790 SPH particles as shown in Figure 7.0–20b. The particle discretisation size (dx) in this example is 1.5mm. For the boundary conditions, nine SPH particles forming three layers are generated to simulate the point loading in the experiment. In the simulation, it is very difficult to apply a slow strain rate of $10^{-6}/\mathrm{s}$ to the specimen as it will result in very high computational cost. Under this circumstance, a very small constant velocity with the value of 1mm/s is chosen here to achieve a quasi-static loading condition, similar to the static rock fracture applications reported in previous chapters. The small velocity is vertically applied on the top boundary particles for the static loading condition, while the horizontal movement of those particles is fixed. As in the dynamic cases, a dynamic loading following an ellipsoidal acceleration-time relationship (illustrated in Figure 7.0–21) is

applied to the top SPH boundary particles. The bottom boundary particles are allowed to move freely horizontally while the vertical movement is fixed.

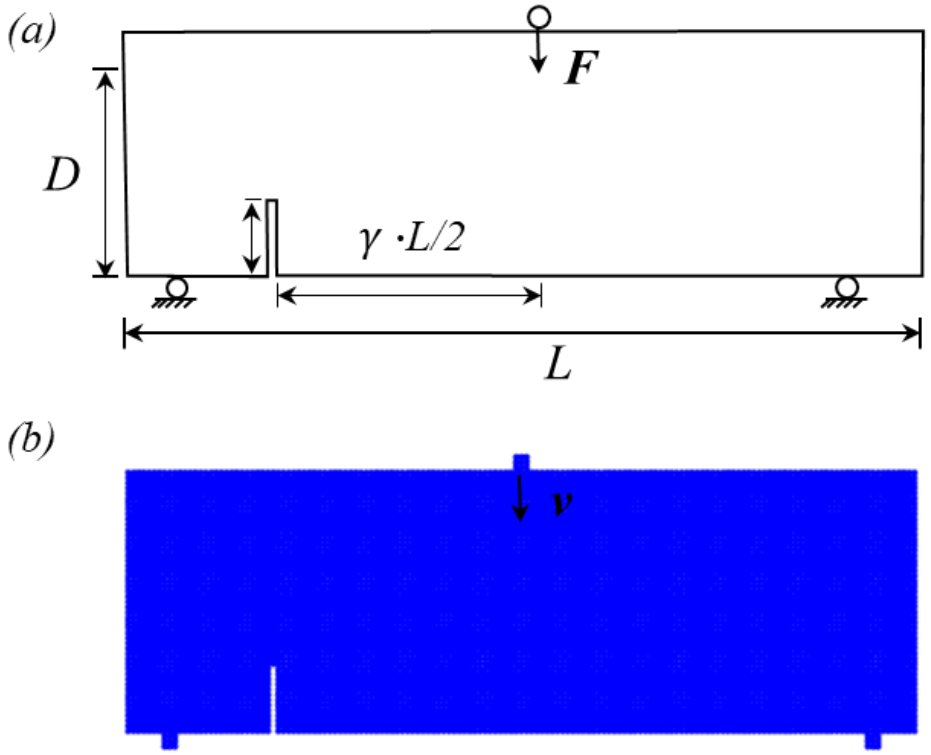

Figure 7.0–20. Schematic of the three-point bending test: (a). Experiment; (b). Simulation

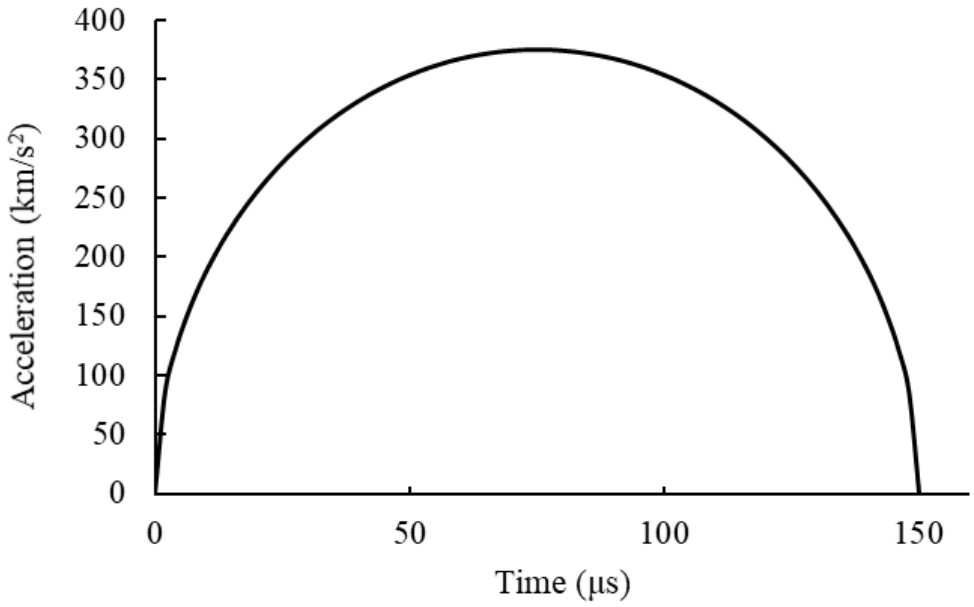

Figure 7.0–21. Input loading with time in the simulation of the Brazilian disc test

Table 7.0-3. Material properties of the material for three-point bending test

Material properties for three-point bending test	
Young's Modulus ($\boldsymbol{E}$)	$\boldsymbol{29GPa}$
Poisson ratio ($\boldsymbol{v}$)	$\boldsymbol{0.2}$
Density ($\boldsymbol{\rho}$)	$\boldsymbol{2.4g/cm^3}$
Tensile strength($\boldsymbol{f_t}$)	$\boldsymbol{3MPa}$
Cohesion ($\boldsymbol{c}$)	$\boldsymbol{3MPa}$
Friction angle ($\boldsymbol{\varphi}$)	$\boldsymbol{32°}$
Dilation angle ($\boldsymbol{\psi}$)	$\boldsymbol{5°}$
Mode I fracture energy ($\boldsymbol{G_{IC}}$)	$\boldsymbol{30.1Nm}$
Mode II fracture energy ($\boldsymbol{G_{IIc}}$)	$\boldsymbol{30.1Nm}$
Peak displacement ($\boldsymbol{\delta_0}$) *under static loading*	$\boldsymbol{10\mu m}$
Peak displacement ($\boldsymbol{\delta_0}$) *under dynamic loading*	$\boldsymbol{3\mu m}$
Secant normal stiffness ($\boldsymbol{K_{n0}}$)	$\boldsymbol{10^{14}Pa/m}$
Secant shear stiffness ($\boldsymbol{K_{s0}}$)	$\boldsymbol{10^{11}Pa/m}$

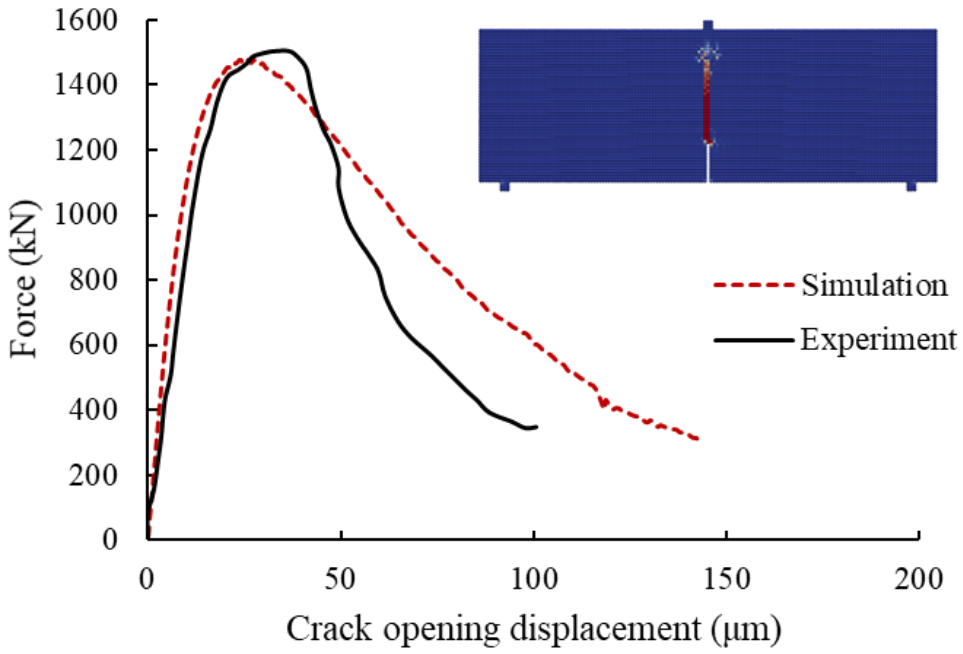

Figure 7.0–22. Comparison of force-crack opening displacement curve between experiment and simulation of three-point bending test with a centrally located notch.

Figure 7.0–22 shows the comparison of the force-crack opening displacement curve between the experiment and the SPH simulation for the three-point bending specimen with a centrally

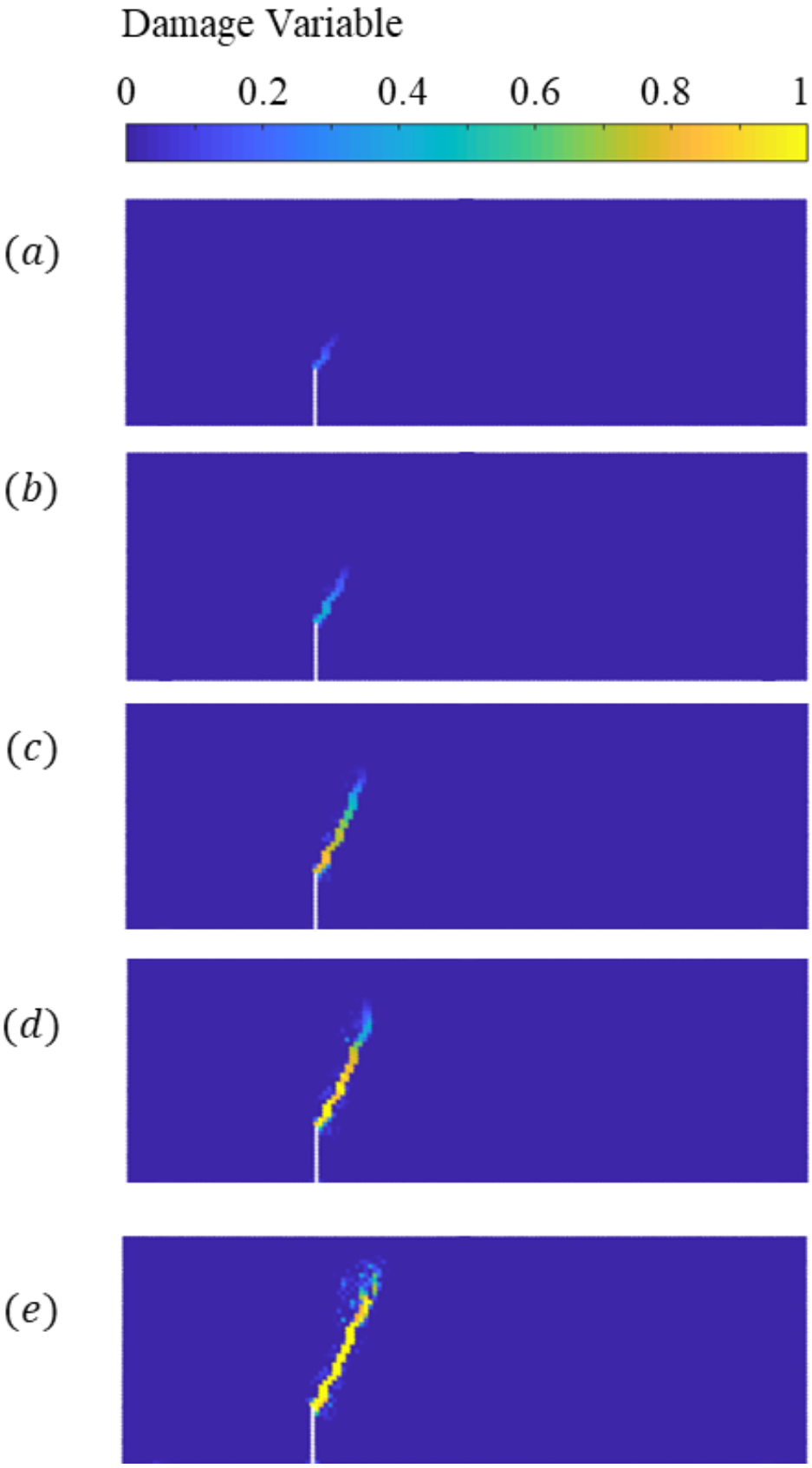

Figure 7.0–23. Fracture initiation, propagation and final fracture pattern in specimen with γ=0.5 under static loading.

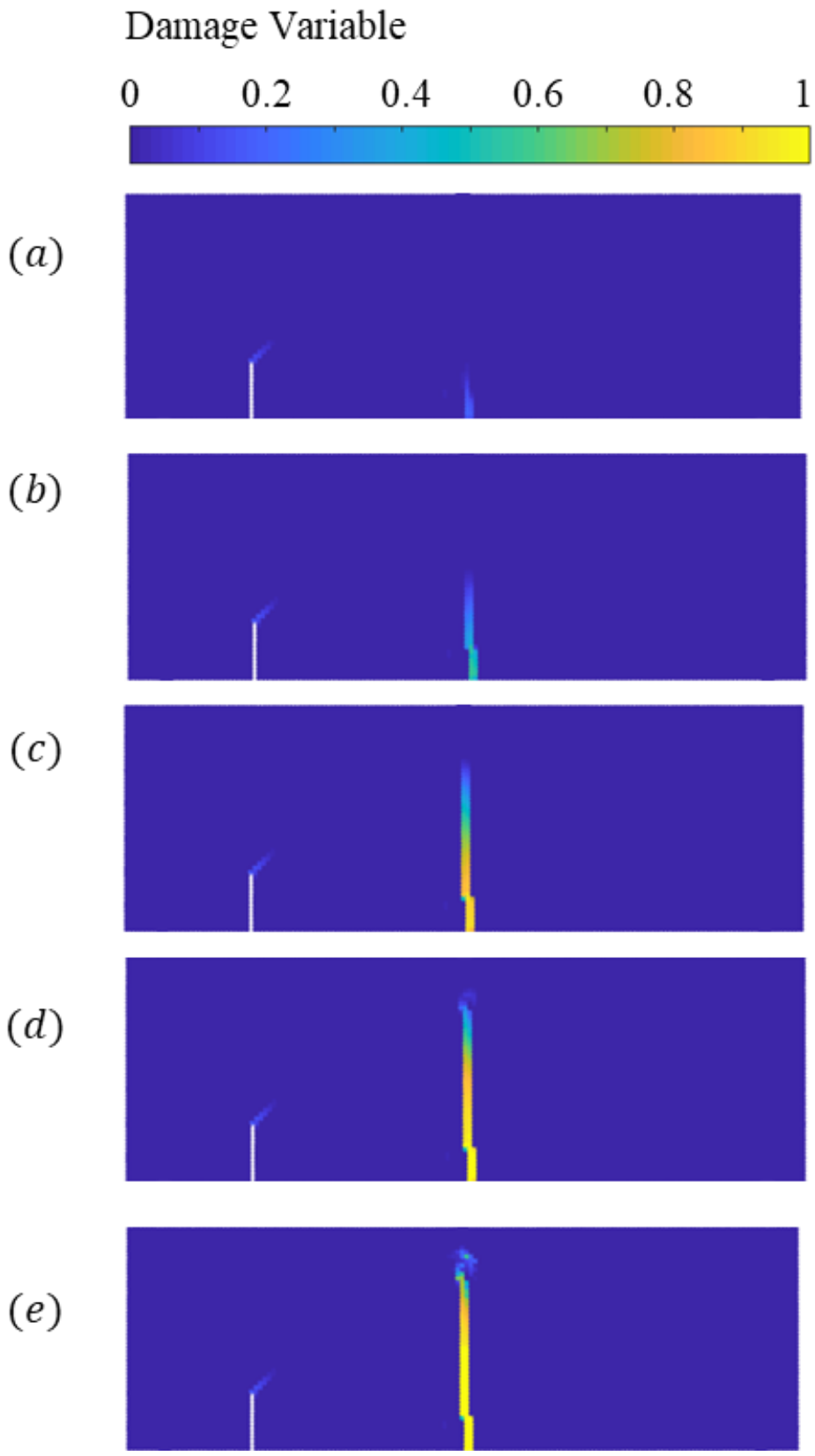

Figure 7.0–24. Fracture initiation, propagation and final fracture pattern in specimen with γ=0.7 under static loading.

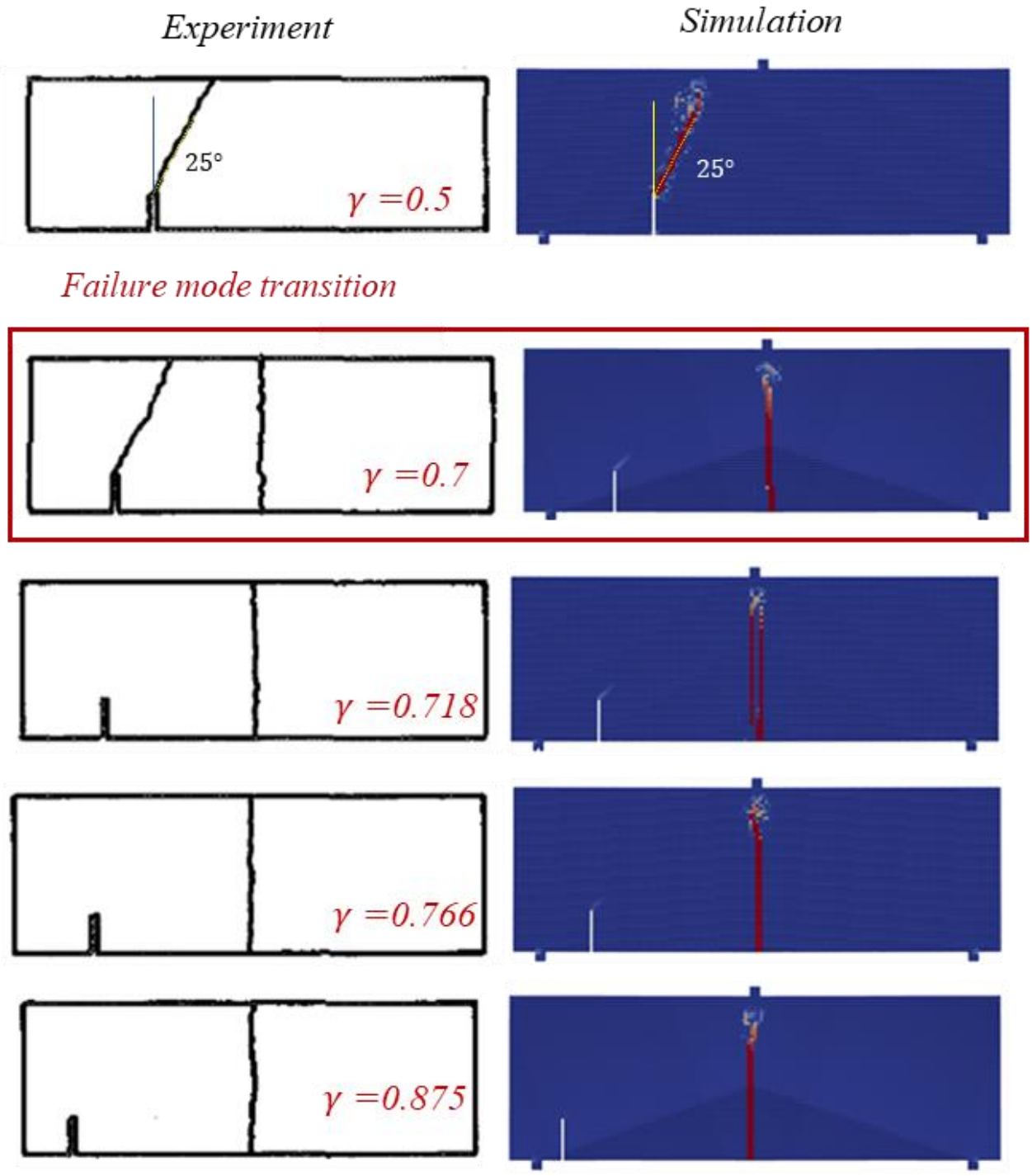

Figure 7.0–25. Comparison of final fracture pattern between experiment and simulation of three-point bending test with different notch locations under static loading.

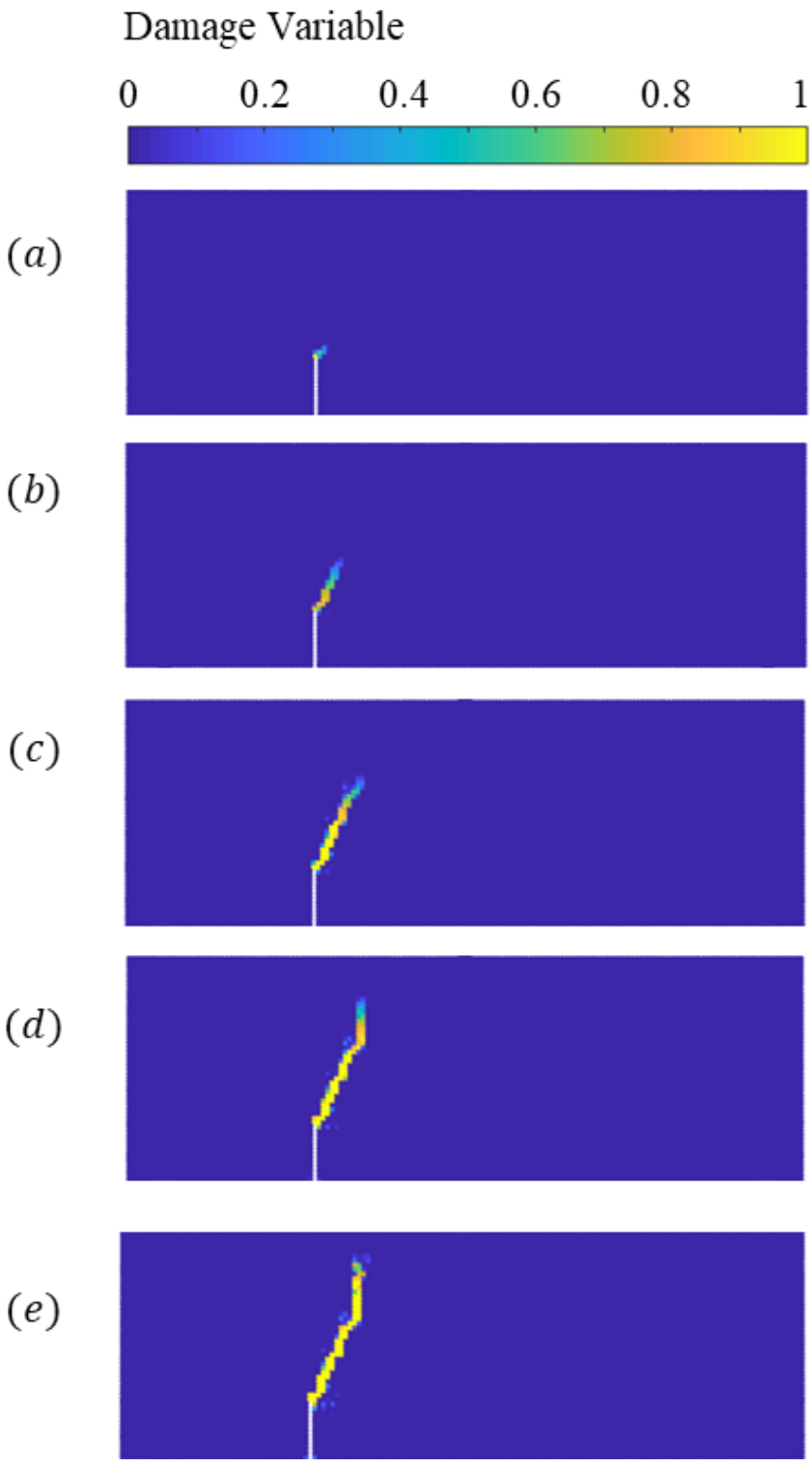

Figure 7.0–26. Fracture initiation, propagation and final fracture pattern in specimen with γ=0.5 under dynamic loading.

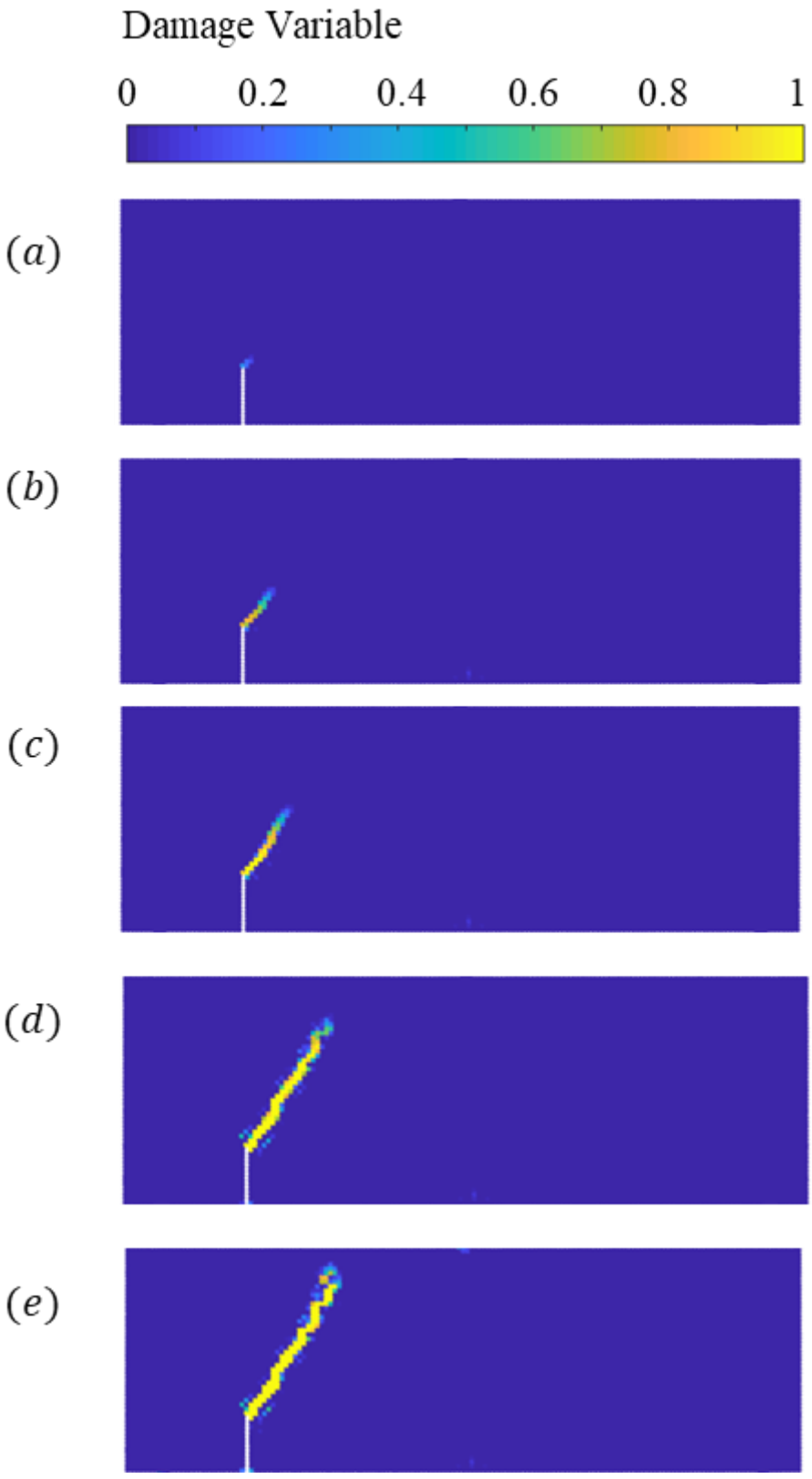

Figure 7.0–27. Fracture initiation, propagation and final fracture pattern in specimen with γ=0.718 under dynamic loading.

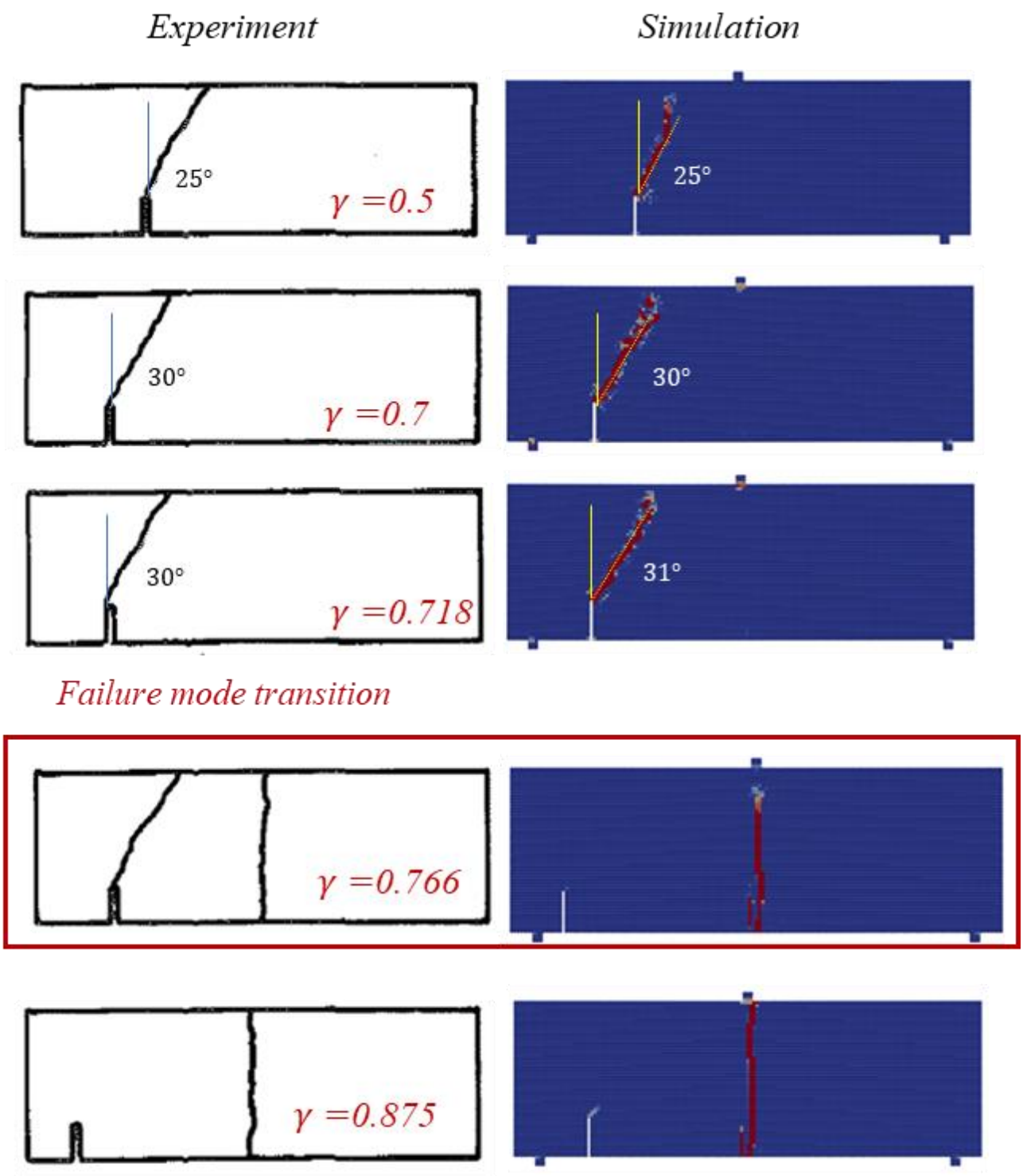

Figure 7.0–28.Comparison of final fracture pattern between experiment and simulation of three-point bending test with different notch locations under dynamic loading.

point bending test under static loading using the provided input parameters. The final fracture pattern for the specimen with the centrally located notch is also shown in Figure 7.0–22. SPH located notch under static loading conditions. During the loading process, the specimen

undergoes three stages: elastic loading, hardening up to a peak, and softening until failure of the beam. Overall, the force-crack opening displacement curve obtained by SPH simulation matches the experimental curve well, although the experimental data shows that the specimen experiences a slightly longer hardening stage and more brittle fracture behaviour. The result confirms that the SPH model captured the mechanical behaviour of the concrete in the three-particles in the middle of the beam are fully damaged, resulting in a vertical fracture pattern at the end.

After validation of the model in capturing the mode I fracture and corresponding force development with crack opening displacement under static loading, the SPH fracturing model is next used to investigate the effect of loading on the mixed-mode (mode I and II) fractures of concrete. Figure 7.0–23 shows the fracture initiation, propagation and final fracture pattern of the specimen with $\gamma = 0.5$ under static loading. It can be seen that fracture initiates from the notch tip and gradually propagates towards the top-mid-span of the specimen. Figure 7.0–24 shows the fracture development of the specimen with $\gamma = 0.7$ under static loading. Unlike the cases of $\gamma = 0.5$, two fractures initiating from the notch tip and the bottom-mid-span of the specimen are observed in Figure 7.0–24(a). Then the fracture initiating from the bottom-mid-span begins to propagate towards the loading point, while the fracture initiated from the tip of the notch stops developing, as shown in Figure 7.0–24(b-e). Finally, a vertical fracture is formed in the middle of the specimen.

Figure 7.0–25 shows the comparison between simulation and experimental results in terms of the final fracture patterns of the three-point bending test with different locations of the notch under static loading. It can be seen that when $\gamma = 0.5$, a fracture pattern with the inclination angle of 25 degrees is obtained using the proposed SPH framework, which is consistent with the experimental results of John and Shah (1990). As the notch is moved further from the midspan ($\gamma \geq 0.7$), flexural failure occurs in which fracture initiates from the bottom mid-span of the specimen and propagates vertically towards loading points. Therefore, a mode transition from mixed-mode failure to flexural failure occurs at $\gamma = 0.7$ under static loading in the simulation, which perfectly matches the experimental results. Figure 7.0–26 and Figure 7.0–27 present the fracture initiation, propagation and final fracture pattern of the specimen with $\gamma = 0.5$ and $\gamma = 0.718$ respectively under dynamic loading. It can be seen that the overall fracture developments of these two cases are very similar. The fracture initiates from the tip of the notch and propagates upwards at a certain inclination angle.

However, it can be seen from Figure 7.0–27 that some particles near the bottom-mid-specimen are damaged when $\gamma = 0.718$, indicating that another small fracture initiates from the bottom-mid-specimen. Figure 7.0–28 shows the simulation results of the final fracture patterns for the three-point bending specimen under dynamic loading in comparison with the experimental results. It can be seen that when $\gamma = 0.5$, the final fracture pattern under dynamic loading is very similar to fracture development under static loading. However, the fracture still occurs at the notch tip, as the notch is further offset from the midspan ($\gamma \leq 0.718$) when impact loading is applied on the specimen, in contrast to the flexural failure under static loading. Larger inclination angles of 30 degrees and 31degrees are observed in the figures of final fracture pattern with γ = 0.7 and $\gamma = 0.718$ respectively compared with the angle of the final fracture pattern with γ = 0.5. This observation in simulation matches perfectly the experimental results and the analytical solution using a maximum energy release rate criterion developed by Hussain et al. (1974), in which a 30-degree inclination angle was calculated for the case of γ = 0.718. When the value of γ is greater than or equal to 0.766, a vertical fracture pattern in the middle of the specimen is observed. Therefore, the transition point from mixed-mode failure to flexural failure in the three-point bending test under dynamic loading is at γ = 0.766, indicating that the specimen is designed to fail in a brittle tension-shear manner under dynamic loading, as opposed to the ductile flexural manner under static loading. Overall, the simulation result captured the final fracture patterns in the experiment well, showing the capability of the SPH fracturing model to predict the rate-sensitive mixed-mode failures under a wide range of loading rates without any ad-hoc treatments for rate dependency.

7.5. Conclusions

In this work, the fracture behaviour of rocks and rock-like materials under dynamic loadings was simulated using SPH fracturing particles. Two approaches were proposed to incorporate the loading rate effect into the SPH framework with a mixed-mode constitutive model. The first approach introduced the loading rate effect into the mixed-mode cohesive fracture law; the second approach considered the loading rate effect by applying an elliptical force history to the SPH particles. From the findings, the following conclusions can be drawn:

- Indirect tensile testing of marble ring specimens with different d/D ratios were simulated using the first approach. The results showed that ring specimens under dynamic loading had more fractures than those under static loading presented in Chapter 6, which agreed well with experimental observation. This result suggests that a numerical approach which

combines the traditional SPH with a rate-dependent continuum constitutive model could capture the loading rate effect on the behaviour of rock fractures.

- A series of notched semicircular bending tests under different dynamic loading conditions were performed using the second approach. Since it is well known that the dynamic initiation fracture toughness of rocks is strongly affected by the loading rate, that phenomenon was also investigated in this example. The good agreement between simulation and experimental results indicated that the SPH fracturing approach was capable of predicting normalised dynamic initiation fracture toughness and capturing pure mode I fracture initiation and propagation under dynamic loading.
- The loading effect on the tensile strength of rock was also investigated with the Brazilian disc specimen, using the second approach. Tensile failure at the centre of the specimen and shear failure near the loading plates were observed in SPH simulation, consistent with experimental results. A linear relationship between normalised tensile strength and loading rate was obtained.
- In the last application, mixed-mode (including mode I) fracture of concrete was simulated using a three-point bending specimen with notches offset from the midspan. As the notch moved farther from the midspan, a transition from mixed-mode failure to mode I flexural failure was observed. The transition points under static loading and dynamic loading were respectively $\gamma = 0.7$ and $\gamma = 0.766$, indicating that dynamic loading could result in a more brittle diagonal tension-shear failure compared with static loading. The simulation prediction matched the experimental results perfectly, demonstrating the suitability of the SPH method for predicting the rate-sensitive fracture of rock and rock-like materials.

Chapter 8

Conclusions and Recommendations for Future Research

8.1. Conclusions

In this research, an advanced computational framework that possesses intrinsic length and time scales was developed for simulating rock fractures under quasi-static and dynamic loadings. Emphasis was placed on the development of a continuum constitutive model which could realistically capture the underlying failure mechanism and correctly describe the behaviour of the fracture process zone and surrounding material of rocks. From the analysis of numerous published experimental results, it was found that the fracturing process and mechanical properties such as strength and fracture toughness of rocks were strongly affected by specimen size and loading rate. Therefore, size and loading rate effects were also considered in this work by respectively incorporating the length parameter and rate effect into the constitutive equations. To accommodate these new constitutive models, two numerical platforms, the Taylor SPH and traditional SPH, were developed based on the mesh-free smoothed particle hydrodynamics (SPH) method. The combination of the proposed constitutive models with the SPH method resulted in a robust computational tool for rock fracture modelling.

The development of the proposed computational framework can be divided into three main parts:

1) development of a robust SPH framework for simulations of rock fractures;
2) development of a continuum constitutive model with embedded time and length effects for simulation of rock fractures;
3) implementation of the new computational framework which combines the SPH method and the continuum constitutive model in rock fracture applications.

In the following sections, the major conclusions from the three parts of the research are discussed for the three stages of rock fracture simulations.

8.1.1. Simulation of size-dependent behaviour and pure mode I failures of rock fractures under quasi-static loading

1) To accurately capture the fracturing processes of rocks, the two-step Taylor SPH framework was adopted and in-house codes of Taylor SPH were developed to provide a stable numerical platform for incorporating any suitable constitutive model. As demonstrated in the numerical tests in Chapter 3, the Taylor SPH method which combines the corrected SPH technique, the stress point approach, with the Taylor time integration scheme can provide a very accurate and stable solution for solving the governing equations of rocks under tensile loading.
2) To capture the high gradient of strain deformation in the fracture process zone of rock masses, a new continuum constitutive model was proposed, which was derived from the generic double-scale continuum constitutive framework for strain localisation with a finite shear band thickness. In this work, the shear band thickness is assumed to approach zero, thus leading to a scale-dependent constitutive model with an embedded fracture process zone. The fracture process zone is modelled by a mode I linear or exponential cohesive fracture law for describing the irreversible deformation and stiffness reduction within the fracture process zone under tensile-only loading, while the behaviour of the material outside zone is assumed to be elastic, following Hooke's law. A length parameter for describing the relative size of the fracture process zone with the surrounding bulk is embedded in the constitutive equation, which helps to minimise mesh sensitivity issues and capture the size-dependent behaviour in rocks. Verification testing of the proposed model at the constitutive level was conducted and thus it was shown that this constitutive model can correctly represent the distinct responses of material in the fracture process zone and the surrounding material under tensile loading.
3) A rigorous SPH framework that combined the Taylor SPH method and the size-dependent constitutive model was developed to model pure mode I rock fractures. This is the first rigorous SPH framework featuring an intrinsic length scale. The new SPH framework provides a fundamental basis that bridges the constitutive and structural aspects via a length parameter obtained directly from the particle size, which enables the framework to correctly capture size-dependent behaviour of rocks. Furthermore, through a series of numerical tests of rock fractures, it was proved that the proposed SPH framework could capture the

experimentally-observed fracture development of rocks and handle extremely large deformation and fracture detachment. Furthermore, the model's responses to spatial discretisation were examined to highlight the advantages of the proposed approach. As demonstrated, the proposed approach is insensitive to spatial discretisation (i.e. it is mesh independent) thanks to the inclusion of the characteristic length in the constitutive model. Although a simple cohesive fracture law was adopted in developing the framework, the proposed scale-dependent numerical framework is able to model pure mode I rock fractures and size-dependency behaviour without suffering from any numerical instability (such as are due to short-length-scale noise or use of the traditional approach) or spatial-discretisation-dependent issues which are inherent in the SPH method.

8.1.2. Simulation of mixed-mode failures under quasi-static loading

1) Traditional SPH with the tensile instability treatment approach instead of the Taylor SPH framework was adopted for simulating mixed-mode rock fractures, and thus in-house codes for traditional SPH were also developed in this study. Although the Taylor SPH can provide a very accurate solution of rock fractures, the traditional SPH with the tensile instability treatment approach is more flexible and easier to implement, as it does not require an extra set of particles for removing tensile instability as well as special treatment for free surface boundary conditions. Instead, the stabilisation term and corrective technique were adopted in the traditional SPH method to eliminate tensile instability and boundary deficiency. The traditional SPH with the tensile instability treatment approach was shown to be a stable and powerful numerical platform for simulating rock behaviour under complex loadings.
2) To capture the behaviour of rock fractures under mixed-mode loading, a mixed-mode cohesive fracture law instead of the simple cohesive fracture law for pure mode I rock fracture simulations was proposed and incorporated into the double-scale framework. The incorporation of this mixed-mode cohesive fracture law gives the framework the ability to model more complex fracture problems accounting for both tensile and shear cracks and multiple fractures. The proposed cohesive fracture model uses a single yield failure surface together with damage-plasticity coupling in a traction-displacement jump relationship. This enables modelling of the material in the fracture process zone at different stages of deformation under combined tensile and shear loading conditions. In particular, key inelastic responses of the material in the fracture process zone, including residual deformations, strength and stiffness reduction, and evolution of damage, are accounted for.

3) A new SPH framework that combines the traditional SPH with the tensile instability treatment method with the mixed-mode continuum constitutive model was developed for simulating complex rock fracturing processes under mixed-mode loading. The proposed SPH framework captures well the post-peak behaviour of rock. Thanks to the strong coupling of damage and plasticity, the interaction between irreversible deformation and progressive fracture occurring within the fracture process zone during the course of loading can be captured properly. Consequently, the proposed SPH approach can predict well the fracture toughness envelope obtained from experimental and analytical analyses under a range of mixed-mode loadings. Furthermore, as demonstrated through a series of numerical tests, the proposed SPH framework is able to handle all the numerical difficulties associated with existing numerical methods such as crack propagation, fracture separation and mesh-dependency.

8.1.3. Simulate behaviour of rock fractures under dynamic loading

1) Traditional SPH with a tensile instability treatment method used for mixed-mode rock fracture analyses under static loading was adopted to simulate dynamic rock fractures. To incorporate the rate effect into the SPH method, an elliptical stress history was applied on the SPH boundary particles to simulate the stress wave generated in the split Hopkinson bar. This loading method resulted in a nonlinear input velocity instead of a constant one that was adopted in the quasi-static cases. Thanks to the dynamic nature of SPH, the new loading method combined with any suitable constitutive model provided a robust numerical framework for simulating dynamic rock fractures without any ad hoc treatments.
2) To capture the responses of rocks under a wide range of high loading/strain rates, another approach is to develop a rate-dependent constitutive model. In this study, a rate-dependent mixed-mode cohesive fracture law was proposed in which only the rate effect on tensile strength was considered. The rate effect was introduced by incorporating a dynamic increase factor (DIF) with respect to the loading/strain rate into the model. To do so, the shapes of the yield surface and the non-associated plastic potential change with different DIF, enabling the model to capture the plastic and damage behaviour of the material in the fracture process zone under combined tensile and shear dynamic loadings.
3) In this study, two approaches to modelling dynamic rock fractures were proposed. The first incorporated the rate effect by introducing DIF into the cohesive fracture model, resulting in rate-dependent continuum model combined with the traditional SPH framework. The second approach incorporated the rate effect by employing an elliptical force-time

relationship as the input loading into the traditional SPH framework with the mixed-mode continuum constitutive model. Good agreement between the simulation results using those two approaches and experimental results demonstrated the capacity of both proposed models to capture the responses and failures of rocks under high loading rates. Although the rate dependency only on the tensile strength of rocks was considered in the first approach, the introduction of DIF enabled the model automatically build up the different criteria for fracture initiation under different high loading rates. As a consequence, macro-responses and complex multiple failure patterns of the rocks were successfully predicted. On the other hand, the unique input loading in the second approach gave the model notable capability to capture the mechanical and fracture properties of rock under dynamic loading without any ad hoc treatment, thanks to the dynamic nature of the SPH method. Moreover, owing to the flexibility of each SPH particle in determining the fracture orientation based on the stress state, together with the mesh-free nature of the SPH, both proposed approaches were able to capture the fracturing processes of rocks under complex dynamic loadings.

At the end of this research, a continuum-based constitutive model with embedded discontinuity was developed, taking into account the spatial and temporal scale effects. In particular, a rate-dependent mixed mode cohesive fracture law was formulated and coupled with the continuum constitutive framework with embedded discontinuity which possesses the length scale effect. The new constitutive model was incorporated with the mesh-free SPH method to produce a robust computational tool for rock fracture modelling under both quasi-static and dynamic loadings. It was shown through those three stages that the proposed SPH approach is robust as it does not represent the crack as a continuous surface, and thus is particularly flexible in simulating complex crack patterns and large deformations. In addition, because the behaviour within the fracture process zone under mixed-mode loading can be reflected, the mechanical properties, the dissipated energy and consequently the fracture patterns can be reflected naturally in the model. Furthermore, the proposed framework can successfully capture the effects of the loading rate and specimen size on the mechanical and fracture properties as well as the fracturing processes of rocks observed in experiments.

8.2. Recommendations for future research

In this work, an accurate numerical framework for the prediction of mixed-mode rock fractures under quasi-static and dynamic loadings has been established. However, the proposed approach has not been extended to large-scale applications of rocks and discrete fracture network problems. To do that, the continuum constitutive model needs to be further developed to

enhance the model's behaviour in simulating complex rock fractures. Further research directions leading towards a more effective and powerful modelling approach are suggested. They can be summaries as follows:

- Although the simulation results showed that the proposed framework could simulate the complex fracture patterns under both quasi-static and dynamic loading, the framework has not been used for simulating problems involving discrete fracture networks. The current SPH framework has only one fracture process zone in each SPH particle, which is a simplified consideration, as rock masses in reality can possess more than one fracture. Therefore, a micromechanics-based model can be developed and incorporated into the double-scale model to yield a more realistic model for simulating the behaviour of rock fractures. To be specific, the constitutive law based on micromechanics-based models with weak planes can replace the elastic stiffness matrix in the current model for describing the surrounding material of fracture process zone. The combination of micromechanical effects in the surrounding material with the localised behaviour in the process fracture zone would help the model to remove stress-locking issues and account for multiple fractures within rock masses naturally.
- Another recommendation for future research is to extend the SPH framework to large-scale applications and 3D applications. This task is very straightforward to undertake as the proposed framework does not require the remeshing technique of FE methods and the contact updating of DE methods, thus resulting in quite low computational cost. Another feature of the proposed SPH framework is the insensitivity of the numerical solutions to the spatial discretisation. Therefore, the use of a coarse size of spatial discretisation in large-scale applications which require less computational cost can still achieve desirable and reliable numerical results.

References

Addessi, D., S. Marfia and E. Sacco (2002). "A plastic nonlocal damage model." Computer methods in applied mechanics and engineering **191**(13-14): 1291-1310.

Akazawa, T. (1943). "New test method for evaluating internal stress due to compression of concrete (the splitting tension test)(part 1)." J Jpn Soc Civ Eng **29**: 777-787.

Al-Shayea, N. A. (2005). "Crack propagation trajectories for rocks under mixed mode I–II fracture." Engineering Geology **81**(1): 84-97.

Albuquerque, E., P. Sollero and M. Aliabadi (2004). "Dual boundary element method for anisotropic dynamic fracture mechanics." International journal for numerical methods in engineering **59**(9): 1187-1205.

Alehossein, H. and J. Boland (2004). "Strength, toughness, damage and fatigue of rock."

Aliabadian, Z., M. Sharafisafa, M. Nazemi and T. Kazerani (2012). "Discrete element modeling of wave and fracture propagation in delay time breakage." Dynamic Web Programming and HTML5: 401.

Aliha, M. and M. Ayatollahi (2012). "Analysis of fracture initiation angle in some cracked ceramics using the generalized maximum tangential stress criterion." International Journal of Solids and Structures **49**(13): 1877-1883.

Aliha, M. R. M. and M. R. Ayatollahi (2011). "Mixed mode I/II brittle fracture evaluation of marble using SCB specimen." Procedia Engineering **10**: 311-318.

Andreev, G. (1991). "A review of the Brazilian test for rock tensile strength determination. Part I: calculation formula." Mining science and Technology **13**(3): 445-456.

Andreev, G. (1991). "A review of the Brazilian test for rock tensile strength determination. Part II: contact conditions." Mining science and Technology **13**(3): 457-465.

Antonellini, M. A., A. Aydin and D. D. Pollard (1994). "Microstructure of deformation bands in porous sandstones at Arches National Park, Utah." Journal of structural Geology **16**(7): 941-959.

Ardebili, M. A. H., S. M. S. Kolbadi, M. Heshmati and H. Mirzabozorg (2012). "Nonlinear analysis of concrete structural components using co-axial rotating smeared crack model." Journal of Applied Sciences(Faisalabad) **12**(3): 221-232.

Ariffin, A. K., S. Huzni, M. J. M. Nor and N. A. N. Mohamed (2006). Hybrid finite-discrete element simulation of crack propagation under mixed mode loading condition. Key Engineering Materials, Trans Tech Publ.

Askes, H., A. Suiker and L. Sluys (2002). "A classification of higher-order strain-gradient models–linear analysis." Archive of Applied Mechanics **72**(2-3): 171-188.

Asprone, D., E. Cadoni, A. Prota and G. Manfredi (2009). "Dynamic behavior of a Mediterranean natural stone under tensile loading." International Journal of Rock Mechanics and Mining Sciences **46**(3): 514-520.

Atkinson, C., R. Smelser and J. Sanchez (1982). "Combined mode fracture via the cracked Brazilian disk test." International journal of fracture **18**(4): 279-291.

Ayatollahi, M. and M. Aliha (2008). "On the use of Brazilian disc specimen for calculating mixed mode I–II fracture toughness of rock materials." Engineering Fracture Mechanics **75**(16): 4631-4641.

Ayatollahi, M., M. R. Moghaddam and F. Berto (2015). "A generalized strain energy density criterion for mixed mode fracture analysis in brittle and quasi-brittle materials." Theoretical and Applied Fracture Mechanics **79**: 70-76.

Ayatollahi, M. and K. Sedighiani (2012). "Mode I fracture initiation in limestone by strain energy density criterion." Theoretical and Applied Fracture Mechanics **57**(1): 14-18.

Ayatollahi, M. and M. Sistaninia (2011). "Mode II fracture study of rocks using Brazilian disk specimens." International Journal of Rock Mechanics and Mining Sciences **48**(5): 819-826.

Ayatollahi, M. R. and M. R. M. Aliha (2007). "Fracture toughness study for a brittle rock subjected to mixed mode I/II loading." International Journal of Rock Mechanics and Mining Sciences **44**(4): 617-624.

Ayatollahi, M. R., M. R. M. Aliha and M. M. Hassani (2006). "Mixed mode brittle fracture in PMMA—An experimental study using SCB specimens." Materials Science and Engineering: A **417**(1-2): 348-356.

Aydin, A. and A. Basu (2005). "The Schmidt hammer in rock material characterization." Engineering Geology **81**(1): 1-14.

Bailey, C. and M. Cross (1995). "A finite volume procedure to solve elastic solid mechanics problems in three dimensions on an unstructured mesh." International journal for numerical methods in engineering **38**(10): 1757-1776.

Bakun-Mazor, D., Y. H. Hatzor and W. S. Dershowitz (2009). "Modeling mechanical layering effects on stability of underground openings in jointed sedimentary rocks." International Journal of Rock Mechanics and Mining Sciences **46**(2): 262-271.

Banks-Sills, L. and Y. Bortman (1986). "A mixed-mode fracture specimen: analysis and testing." International journal of fracture **30**(3): 181-201.

Barbero, M., G. Barla and A. Zaninetti (1996). Dynamic shear strength of rock joints subjected to impulse loading. International journal of rock mechanics and mining sciences & geomechanics abstracts, Elsevier.

Barron, K. (1971). Brittle fracture initiation in and ultimate failure of rocks: Part I—Isotropic Rock. International Journal of Rock Mechanics and Mining Sciences & Geomechanics Abstracts, Elsevier.

Bažant, Z. P. and M. T. Kazemi (1991). Size dependence of concrete fracture energy determined by RILEM work-of-fracture method. Current Trends in Concrete Fracture Research, Springer**:** 121-138.

Bažant, Z. P. and Y.-N. Li (1997). "Cohesive crack with rate-dependent opening and viscoelasticity: I. mathematical model and scaling." International journal of fracture **86**(3): 247-265.

Bažant, Z. P. and F. B. Lin (1988). "Non‐local yield limit degradation." International journal for numerical methods in engineering **26**(8): 1805-1823.

Bažant, Z. P. and B. H. Oh (1983). "Crack band theory for fracture of concrete." Matériaux et construction **16**(3): 155-177.

Bellec, J. and J. Dolbow (2003). "A note on enrichment functions for modelling crack nucleation." Communications in Numerical Methods in Engineering **19**(12): 921-932.

Bellego, C. L., B. Gérard and G. Pijaudier-Cabot (2000). "Chemo-mechanical effects in mortar beams subjected to water hydrolysis." Journal of engineering mechanics **126**(3): 266-272.

Belytschko, T. and T. Black (1999). "Elastic crack growth in finite elements with minimal remeshing." International Journal for Numerical Methods in Engineering **45**(5): 601-620.

Belytschko, T., H. Chen, J. Xu and G. Zi (2003). "Dynamic crack propagation based on loss of hyperbolicity and a new discontinuous enrichment." International Journal for Numerical Methods in Engineering **58**(12): 1873-1905.

Belytschko, T., Y. Y. Lu and L. Gu (1994). "Element ‐ free Galerkin methods." International journal for numerical methods in engineering **37**(2): 229-256.

Benz, W. and E. Asphaug (1995). "Simulations of brittle solids using smooth particle hydrodynamics." Computer physics communications **87**(1-2): 253-265.

Betti, E. (1874). Teoria della elasticità, Pieraccini.

Bieniawski, Z. (1975). "The point-load test in geotechnical practice." Engineering Geology **9**(1): 1-11.

Bieniawski, Z. T. (1974). "Estimating the strength of rock materials." Journal of the Southern African Institute of Mining and Metallurgy **74**(8): 312-320.

Blanc, T. and M. Pastor (2013). "A stabilized smoothed particle hydrodynamics, Taylor–Galerkin algorithm for soil dynamics problems." International Journal for Numerical and Analytical Methods in Geomechanics **37**(1): 1-30.

Blandford, G. E., A. R. Ingraffea and J. A. Liggett (1981). "Two ‐ dimensional stress intensity factor computations using the boundary element method." International journal for numerical methods in engineering **17**(3): 387-404.

Blanton, T. (1981). Effect of strain rates from 10-2 to 10 sec-1 in triaxial compression tests on three rocks. International Journal of Rock Mechanics and Mining Sciences & Geomechanics Abstracts, Elsevier.

Bonora, N. (1997). "A nonlinear CDM model for ductile failure." Engineering Fracture Mechanics **58**(1-2): 11-28.

Borja, R. I. (2000). "A finite element model for strain localization analysis of strongly discontinuous fields based on standard galerkin approximation." Computer Methods in Applied Mechanics and Engineering **190**(11): 1529-1549.

Borja, R. I. (2004). "Computational modeling of deformation bands in granular media. II. Numerical simulations." Computer methods in applied mechanics and engineering **193**(27-29): 2699-2718.

Borja, R. I. and A. Aydin (2004). "Computational modeling of deformation bands in granular media. I. Geological and mathematical framework." Computer methods in applied mechanics and engineering **193**(27-29): 2667-2698.

Borja, R. I., R. A. Regueiro and T. Y. Lai (2000). "FE modeling of strain localization in soft rock." Journal of Geotechnical and Geoenvironmental Engineering **126**(4): 335-343.

Borst, R. d., J. J. C. Remmers and A. Needleman (2006). "Mesh-independent discrete numerical representations of cohesive-zone models." Engineering Fracture Mechanics **73**(2): 160-177.

Bosco, E., V. Kouznetsova and M. Geers (2015). "Multi‐scale computational homogenization–localization for propagating discontinuities using X‐FEM." International journal for numerical methods in engineering **102**(3-4): 496-527.

Brenne, S., M. Molena, F. Stöckert and M. Alber (2013). Hydraulic and sleeve fracturing laboratory experiments on 6 rock types. ISRM International Conference for Effective and Sustainable Hydraulic Fracturing, International Society for Rock Mechanics and Rock Engineering.

Brighi, B., M. Chipot and E. Gut (1998). "Finite differences on triangular grids." Numerical Methods for Partial Differential Equations: An International Journal **14**(5): 567-579.

Broms, B. B. (1966). A note on strength properties of rock. 1st ISRM Congress, International Society for Rock Mechanics and Rock Engineering.

Brook, N. (1979). "Estimating the traxial strength of rocks." Int. J. Rock Mech. Min. Sci. Geomech. Abstr **16**: 261-264.

Broujerdian, V. and M. T. Kazemi (2010). "Smeared rotating crack model for reinforced concrete membrane elements." ACI Structural Journal **107**(4): 411.

Buchholz, F., P. Pirro, H. Richard and K. Dreyer (1987). Numerical and experimental mixed-mode analysis of a compact tension-shear specimen. Proceedings of the fourth International Conference on Numerical methods in fracture mechanics, Pineridge Press, Swansea.

Bui, H. H. (2007). Lagrangian mesh-free particle method (SPH) for large deformation and post-failure of geomaterial using elasto-plastic constitutive models, 立命館大学.

Bui, H. H. and R. Fukagawa (2013). "An improved SPH method for saturated soils and its application to investigate the mechanisms of embankment failure: Case of hydrostatic pore-water pressure." International Journal for Numerical and Analytical Methods in Geomechanics **37**(1): 31-50.

Bui, H. H. and R. Fukagawa (2013). "An improved SPH method for saturated soils and its application to investigate the mechanisms of embankment failure: Case of hydrostatic pore‐water pressure." International Journal for Numerical and Analytical Methods in Geomechanics **37**(1): 31-50.

Bui, H. H., R. Fukagawa, K. Sako and S. Ohno (2008). "Lagrangian meshfree particles method (SPH) for large deformation and failure flows of geomaterial using elastic-plastic soil constitutive model." International Journal for Numerical and Analytical Methods in Geomechanics **32**(12): 1537-1570.

Bui, H. H., R. Fukagawa, K. Sako and S. Ohno (2008). "Lagrangian meshfree particles method (SPH) for large deformation and failure flows of geomaterial using elastic–plastic soil constitutive model." International Journal for Numerical and Analytical Methods in Geomechanics **32**(12): 1537-1570.

Bui, H. H., R. Fukagawa, K. Sako and J. C. Wells (2011). "Slope stability analysis and discontinuous slope failure simulation by elasto-plastic smoothed particle hydrodynamics (SPH)." Géotechnique **61**(7): 565-574.

Bui, H. H., J. K. Kodikara, A. Bouazza, A. Haque and P. G. Ranjith (2014). "A novel computational approach for large deformation and post‐failure analyses of segmental retaining wall systems." International Journal for Numerical and Analytical Methods in Geomechanics **38**(13): 1321-1340.

Bui, H. H. and G. D. Nguyen (2017). "A coupled fluid-solid SPH approach to modelling flow through deformable porous media." International Journal of Solids and Structures **125**: 244-264.

Bui, H. H., K. Sako and R. Fukagawa (2007). "Numerical simulation of soil–water interaction using smoothed particle hydrodynamics (SPH) method." Journal of Terramechanics **44**(5): 339-346.

Bui, H. H., K. Sako, R. Fukagawa and J. Wells (2008). SPH-based numerical simulations for large deformation of geomaterial considering soil-structure interaction. The 12th International Conference of International Association for Computer Methods and Advances in Geomechanics (IACMAG).

Burnett, D. and H. Schreyer (2019). "A mesh objective method for modeling crack propagation using the smeared crack approach." International journal for numerical methods in engineering **117**(5): 574-603.

Butler, K. M., E. Oñate, S. R. Idelsohn and R. Rossi (2007). Modeling polymer melt flow using the particle finite element method. Eleventh International Interflam Conference, London, England.

Cadoni, E. and C. Albertini (2011). "Modified Hopkinson bar technologies applied to the high strain rate rock tests." Advances in rock dynamics and applications. CRC Press, USA: 79-104.

Cargill, J. S. and A. Shakoor (1990). Evaluation of empirical methods for measuring the uniaxial compressive strength of rock. International Journal of Rock Mechanics and Mining Sciences & Geomechanics Abstracts, Elsevier.

Carneiro, F. (1943). A new method to determine the tensile strength of concrete. Proceedings of the 5th meeting of the Brazilian Association for Technical Rules.

Cauvin, A. and R. B. Testa (1999). "Damage mechanics: basic variables in continuum theories." International Journal of Solids and Structures **36**(5): 747-761.

Červenka, J. and V. K. Papanikolaou (2008). "Three dimensional combined fracture–plastic material model for concrete." International Journal of Plasticity **24**(12): 2192-2220.

Chambon, G., R. Bouvarel, D. Laigle and M. Naaim (2011). "Numerical simulations of granular free-surface flows using smoothed particle hydrodynamics." Journal of Non-Newtonian Fluid Mechanics **166**(12-13): 698-712.

Chang, S.-H., C.-I. Lee and S. Jeon (2002). "Measurement of rock fracture toughness under modes I and II and mixed-mode conditions by using disc-type specimens." Engineering Geology **66**(1-2): 79-97.

Charsley, A., C. Martin and D. McCreath (2003). "Sleeve-fracturing limitations for measuring in situ stress in an anisotropic stress environment." International Journal of Rock Mechanics and Mining Sciences **40**(1): 127-136.

Charsley, A. D. (2000). "Interpretation of Sleeve Fracturing for Stress Memurement."

Chemenda, A. I. and D. Mas (2016). "Dependence of rock properties on the Lode angle: Experimental data, constitutive model, and bifurcation analysis." Journal of the Mechanics and Physics of Solids **96**: 477-496.

Chen, C.-S., E. Pan and B. Amadei (1998). "Determination of deformability and tensile strength of anisotropic rock using Brazilian tests." International Journal of Rock Mechanics and Mining Sciences **35**(1): 43-61.

Chen, C.-S., E. Pan and B. Amadei (1998). "Fracture mechanics analysis of cracked discs of anisotropic rock using the boundary element method." International Journal of Rock Mechanics and Mining Sciences **35**(2): 195-218.

Chen, J., J. Beraun and T. Carney (1999). "A corrective smoothed particle method for boundary value problems in heat conduction." International journal for numerical methods in engineering **46**(2): 231-252.

Chen, L., J.-F. Shao and H. Huang (2010). "Coupled elastoplastic damage modeling of anisotropic rocks." Computers and Geotechnics **37**(1-2): 187-194.

Chen, L., C. Wang, J. Liu, J. Liu, J. Wang, Y. Jia and J. Shao (2015). "Damage and plastic deformation modeling of beishan granite under compressive stress conditions." Rock Mechanics and Rock Engineering **48**(4): 1623-1633.

Chen, P. W., T. Huang, J. Yang and G. X. Zhang (2006). Numerical simulation of rock fracture under dynamic loading using Manifold method. Key Engineering Materials, Trans Tech Publ.

Chen, P. W., T. Huang, J. Yang and G. X. Zhang (2006). "Numerical Simulation of Rock Fracture under Dynamic Loading Using Manifold Method." Key Engineering Materials **324-325**: 235-238.

Chen, R., K. Xia, F. Dai, F. Lu and S. Luo (2009). "Determination of dynamic fracture parameters using a semi-circular bend technique in split Hopkinson pressure bar testing." Engineering Fracture Mechanics **76**(9): 1268-1276.

Chen, W.-F. and D.-J. Han (2007). Plasticity for structural engineers, J. Ross Publishing.

Chen, W. and T. Qiu (2011). "Numerical simulations for large deformation of granular materials using smoothed particle hydrodynamics method." International Journal of Geomechanics **12**(2): 127-135.

Chen, W. and T. Qiu (2011). Simulation of fluid flow through porous media using smoothed particle hydrodynamics method. Geo-Frontiers 2011: Advances in Geotechnical Engineering**:** 4195-4203.

Chen, W. and G. Ravichandran (1997). "Dynamic compressive failure of a glass ceramic under lateral confinement." Journal of the Mechanics and Physics of Solids **45**(8): 1303-1328.

Chiarelli, A.-S., J.-F. Shao and N. Hoteit (2003). "Modeling of elastoplastic damage behavior of a claystone." International Journal of Plasticity **19**(1): 23-45.

Chiou, Y.-J., Y.-M. Lee and R.-J. Tsay (2002). "Mixed mode fracture propagation by manifold method." International journal of fracture **114**(4): 327-347.

Christensen, R., S. Swanson and W. Brown (1972). "Split-Hopkinson-bar tests on rock under confining pressure." Experimental Mechanics **12**(11): 508-513.

Christianson, M., M. Board and D. Rigby (2006). UDEC simulation of triaxial testing of lithophysal tuff. Golden Rocks 2006, The 41st US Symposium on Rock Mechanics (USRMS), American Rock Mechanics Association.

Cieślik, J. (2013). "Scalar damage variable determined in the uniaxial and triaxial compression conditions of sandstone samples." Studia Geotechnica et Mechanica **35**(1): 73-84.

Claydon, P. (1992). "Maximum energy release rate distribution from a generalized 3D virtual crack extension method." Engineering Fracture Mechanics **42**(6): 961-969.

Cleary, P. W. and J. J. Monaghan (1999). "Conduction modelling using smoothed particle hydrodynamics." Journal of Computational Physics **148**(1): 227-264.

Cleary, P. W. and M. Prakash (2004). "Discrete–element modelling and smoothed particle hydrodynamics: potential in the environmental sciences." Philosophical Transactions of the Royal Society of London. Series A: Mathematical, Physical and Engineering Sciences **362**(1822): 2003-2030.

Coggan, J., R. Pine, D. Stead and J. Rance (2003). Numerical modelling of brittle rock failure using a combined finite-discrete element approach: implications for rock engineering design. 10th ISRM Congress, International Society for Rock Mechanics.

Cristescu, N. (1986). "Damage and failure of viscoplastic rock-like materials." International Journal of Plasticity **2**(2): 189-204.

Cristescu, N. (1994). "A procedure to determine nonassociated constitutive equations for geomaterials." International Journal of Plasticity **10**(2): 103-131.

Cummins, S. J. and M. Rudman (1999). "An SPH projection method." Journal of Computational Physics **152**(2): 584-607.

Cundall, P. A. and O. D. Strack (1979). "A discrete numerical model for granular assemblies." Geotechnique **29**(1): 47-65.

Cuss, R., E. Rutter and R. Holloway (2003). "The application of critical state soil mechanics to the mechanical behaviour of porous sandstones." International Journal of Rock Mechanics and Mining Sciences **40**(6): 847-862.

Dahou, A., J. Shao and M. Bederiat (1995). "Experimental and numerical investigations on transient creep of porous chalk." Mechanics of Materials **21**(2): 147-158.

Dai, F., R. Chen, M. J. Iqbal and K. Xia (2010). "Dynamic cracked chevron notched Brazilian disc method for measuring rock fracture parameters." International Journal of Rock Mechanics and Mining Sciences **47**(4): 606-613.

Dai, F., R. Chen and K. Xia (2010). "A semi-circular bend technique for determining dynamic fracture toughness." Experimental Mechanics **50**(6): 783-791.

Dai, F., S. Huang, K. Xia and Z. Tan (2010). "Some Fundamental Issues in Dynamic Compression and Tension Tests of Rocks Using Split Hopkinson Pressure Bar." Rock Mechanics and Rock Engineering **43**(6): 657-666.

Dai, F. and K. Xia (2010). "Loading Rate Dependence of Tensile Strength Anisotropy of Barre Granite." Pure and Applied Geophysics **167**(11): 1419-1432.

Dai, F., K. Xia and S. N. Luo (2008). "Semicircular bend testing with split Hopkinson pressure bar for measuring dynamic tensile strength of brittle solids." Rev Sci Instrum **79**(12): 123903.

the dynamic increase factor is the ratio

Dai, F., K. Xia and L. Tang (2010). "Rate dependence of the flexural tensile strength of Laurentian granite." International Journal of Rock Mechanics and Mining Sciences **47**(3): 469-475.

Dai, F., K. Xia, H. Zheng and Y. X. Wang (2011). "Determination of dynamic rock Mode-I fracture parameters using cracked chevron notched semi-circular bend specimen." Engineering Fracture Mechanics **78**(15): 2633-2644.

Dai, F., K. Xia, J. P. Zuo, R. Zhang and N. W. Xu (2013). "Static and Dynamic Flexural Strength Anisotropy of Barre Granite." Rock Mechanics and Rock Engineering **46**(6): 1589-1602.

Das, R. and P. Cleary (2010). "Effect of rock shapes on brittle fracture using Smoothed Particle Hydrodynamics." Theoretical and Applied Fracture Mechanics **53**(1): 47-60.

De Borst, R. (1987). "Smeared cracking, plasticity, creep, and thermal loading—A unified approach." Computer methods in applied mechanics and engineering **62**(1): 89-110.

De Borst, R. and P. Nauta (1985). "Non-orthogonal cracks in a smeared finite element model." Engineering Computations **2**(1): 35-46.

Demirdžić, I. and D. Martinović (1993). "Finite volume method for thermo-elasto-plastic stress analysis." Computer methods in applied mechanics and engineering **109**(3-4): 331-349.

Dhakal, G., T. Yoneda, M. Kato and K. Kaneko (2002). "Slake durability and mineralogical properties of some pyroclastic and sedimentary rocks." Engineering Geology **65**(1): 31-45.

Dias-da-Costa, D., J. Alfaiate, L. Sluys and E. Júlio (2009). "A discrete strong discontinuity approach." Engineering Fracture Mechanics **76**(9): 1176-1201.

Dias-da-Costa, D., J. Alfaiate, L. Sluys and E. Júlio (2010). "A comparative study on the modelling of discontinuous fracture by means of enriched nodal and element techniques and interface elements." International journal of fracture **161**(1): 97.

Dias ‐ da ‐ Costa, D., J. Alfaiate, L. Sluys, P. Areias and E. Júlio (2013). "An embedded formulation with conforming finite elements to capture strong discontinuities." International journal for numerical methods in engineering **93**(2): 224-244.

DiMaggio, F. L. and I. S. Sandler (1971). "Material model for granular soils." Journal of engineering mechanics.

Dimitri, R., N. Fantuzzi, Y. Li and F. Tornabene (2017). "Numerical computation of the crack development and SIF in composite materials with XFEM and SFEM." Composite Structures **160**: 468-490.

Douillet-Grellier, T., B. D. Jones, R. Pramanik, K. Pan, A. Albaiz and J. R. Williams (2016). "Mixed-mode fracture modeling with smoothed particle hydrodynamics." Computers and Geotechnics **79**: 73-85.

Dufour, N., H. Wong, C. Arson, F. Deleruyelle and J.-M. Pereira (2012). "A thermodynamically consistent framework for saturated viscoplastic rock-materials subject to damage." Mechanics Research Communications **45**: 15-21.

Dutta, P. K. and K. Kim (1993). High-strain-rate tensile behavior of sedimentary and igneous rocks at low temperatures, COLD REGIONS RESEARCH AND ENGINEERING LAB HANOVER NH.

Duyi, Y. and W. Zhenlin (2001). "A new approach to low-cycle fatigue damage based on exhaustion of static toughness and dissipation of cyclic plastic strain energy during fatigue." International Journal of Fatigue **23**(8): 679-687.

Dwivedi, R., A. Soni, R. Goel and A. Dube (2000). "Fracture toughness of rocks under sub-zero temperature conditions." International Journal of Rock Mechanics and Mining Sciences **37**(8): 1267-1275.

Dyka, C. and R. Ingel (1995). "An approach for tension instability in smoothed particle hydrodynamics (SPH)." Computers & structures **57**(4): 573-580.

Eibl, J. (1988). "Concrete structures under impact and impulsive loading." CEB-Bulletin d'Information(187): 1-183.

Elkadi, A. and J. Van Mier (2006). "Experimental investigation of size effect in concrete fracture under multiaxial compression." International journal of fracture **140**(1-4): 55-71.

Erdogan, F. and G. Sih (1963). "On the crack extension in plates under plane loading and transverse shear."

Erzar, B. and P. Forquin (2010). "An experimental method to determine the tensile strength of concrete at high rates of strain." Experimental Mechanics **50**(7): 941-955.

Fakhimi, A., P. Azhdari and J. Kimberley (2018). "Physical and numerical evaluation of rock strength in Split Hopkinson Pressure Bar testing." Computers and Geotechnics **102**: 1-11.

Fang, Z. (2001). A local degradation approach to the numerical analysis of brittle fractures in heterogeneous rocks, Imperial College London (University of London).

Feenstra, P. H. and R. de Borst (1995). "Constitutive model for reinforced concrete." Journal of engineering mechanics **121**(5): 587-595.

Feist, C. and G. Hofstetter (2006). "An embedded strong discontinuity model for cracking of plain concrete." Computer methods in applied mechanics and engineering **195**(52): 7115-7138.

Fengnian, J. and Y. Haijie (1998). "Loading-rate effect of rock." Chinese Journal of Rock Mechanics and Engineering **17**(6): 711-717.

Fengnian, J., J. Meirong and G. Xiaoling (2004). "Defining damage variable based on energy dissipation." Chinese Journal of Rock Mechanics and Engineering **23**(12): 1976-1980.

Ferté, G., P. Massin and N. Moës (2016). "3D crack propagation with cohesive elements in the extended finite element method." Computer methods in applied mechanics and engineering **300**: 347-374.

Forquin, P., G. Gary and F. Gatuingt (2008). "A testing technique for concrete under confinement at high rates of strain." International Journal of Impact Engineering **35**(6): 425-446.

Fossum, A. F. and J. T. Fredrich (2000). Cap plasticity models and compactive and dilatant pre-failure deformation, Sandia National Labs., Albuquerque, NM (US); Sandia National Labs ….

Fowell, R., J. Hudson, C. Xu and X. Zhao (1995). Suggested method for determining mode I fracture toughness using cracked chevron notched Brazilian disc (CCNBD) specimens. International Journal of Rock Mechanics and Mining Sciences and Geomechanics Abstracts.

Franklin, J. and R. Chandra (1972). The slake-durability test. International Journal of Rock Mechanics and Mining Sciences & Geomechanics Abstracts, Elsevier.

Franklin, J., S. ZONGQI, B. Atkinson, P. Meredith, F. Rummel, W. Mueller, Y. Nishimatsu, H. Takahahsi, L. Costin and A. Ingraffea (1988). "Suggested methods for determining the fracture toughness of rock." INTERNATIONAL JOURNAL OF ROCK MECHANICS AND MINING & GEOMECHANICS ABSTRACTS **25**(2).

Franklin, J. A. (1971). "Triaxial strength of rock materials." Rock mechanics **3**(2): 86-98.

Franklin, J. A. and M. B. Dusseault (1989). Rock engineering.

Frew, D., M. J. Forrestal and W. Chen (2001). "A split Hopkinson pressure bar technique to determine compressive stress-strain data for rock materials." Experimental Mechanics **41**(1): 40-46.

Frew, D. J., S. A. Akers, W. Chen and M. L. Green (2010). "Development of a dynamic triaxial Kolsky bar." Measurement Science and Technology **21**(10): 105704.

Frew, D. J., S. A. Akers, W. Chen and M. L. Green (2010). "Development of a dynamic triaxial Kolsky bar." Measurement Science and Technology **21**(10).

Fryer, Y., C. Bailey, M. Cross and C.-H. Lai (1991). "A control volume procedure for solving the elastic stress-strain equations on an unstructured mesh." Applied Mathematical Modelling **15**(11-12): 639-645.

Fuenkajorn, K. and S. Klanphumeesri (2010). "Laboratory determination of direct tensile strength and deformability of intact rocks." Geotechnical Testing Journal **34**(1): 97-102.

Garcia-Sanchez, F., R. Rojas-Diaz, A. Sáez and C. Zhang (2007). "Fracture of magnetoelectroelastic composite materials using boundary element method (BEM)." Theoretical and Applied Fracture Mechanics **47**(3): 192-204.

Garipov, T., J. White, A. Lapene and H. Tchelepi (2016). Thermo-hydro-mechanical model for source rock thermal maturation. 50th US Rock Mechanics/Geomechanics Symposium, American Rock Mechanics Association.

Gary, G. and P. Bailly (1998). "Behaviour of quasi-brittle material at high strain rate. Experiment and modelling." European Journal of Mechanics-A/Solids **17**(3): 403-420.

Gilat, A., T. Schmidt and A. Walker (2009). "Full field strain measurement in compression and tensile split Hopkinson bar experiments." Experimental Mechanics **49**(2): 291-302.

Gingold, R. A. and J. J. Monaghan (1977). "Smoothed particle hydrodynamics: theory and application to non-spherical stars." Monthly notices of the royal astronomical society **181**(3): 375-389.

Goldsmith, W., J. Sackman and C. Ewerts (1976). Static and dynamic fracture strength of Barre granite. International Journal of Rock Mechanics and Mining Sciences & Geomechanics Abstracts, Elsevier.

Gong, J. and L. Malvern (1990). "Passively confined tests of axial dynamic compressive strength of concrete." Experimental Mechanics **30**(1): 55-59.

Gouveia, A. V., J. A. Barros, Á. F. Azevedo and J. Sena-Cruz (2008). Multi-fixed smeared 3D crack model to simulate the behavior of fiber reinforced concrete structures. Challenges for civil construction (CCC2008): proceedings...: bridge science and applications with engineering towards innovative solutions for construction: safety, sustainability and rehabilitation with innovative solutions, Universidade do Porto. Faculdade de Engenharia (FEUP).

Gran, J., A. Florence and J. Colton (1989). "Dynamic triaxial tests of high-strength concrete." Journal of engineering mechanics **115**(5): 891-904.

Grassl, P. and M. Jirásek (2006). "Damage-plastic model for concrete failure." International Journal of Solids and Structures **43**(22-23): 7166-7196.

Grassl, P., D. Xenos, U. Nyström, R. Rempling and K. Gylltoft (2013). "CDPM2: A damage-plasticity approach to modelling the failure of concrete." International Journal of Solids and Structures **50**(24): 3805-3816.

Gray III, G. and W. R. Blumenthal (2000). "Split-Hopkinson pressure bar testing of soft materials." ASM handbook **8**: 488-496.

Gray, J. P., J. J. Monaghan and R. Swift (2001). "SPH elastic dynamics." Computer methods in applied mechanics and engineering **190**(49-50): 6641-6662.

Gray, J. P., J. J. Monaghan and R. P. Swift (2001). "SPH elastic dynamics." Computer Methods in Applied Mechanics and Engineering **190**(49–50): 6641-6662.

Griffith, A. A. (1921). "VI. The phenomena of rupture and flow in solids." Philosophical transactions of the royal society of london. Series A, containing papers of a mathematical or physical character **221**(582-593): 163-198.

Gui, Y.-L., H. H. Bui, J. Kodikara, Q.-B. Zhang, J. Zhao and T. Rabczuk (2015). "Modelling the dynamic failure of brittle rocks using a hybrid continuum-discrete element method with a mixed-mode cohesive fracture model." International Journal of Impact Engineering.

Gui, Y.-L., H. H. Bui, J. Kodikara, Q.-B. Zhang, J. Zhao and T. Rabczuk (2016). "Modelling the dynamic failure of brittle rocks using a hybrid continuum-discrete element method with a mixed-mode cohesive fracture model." International Journal of Impact Engineering **87**: 146-155.

Gui, Y., H. Bui and J. Kodikara (2015). "An application of a cohesive fracture model combining compression, tension and shear in soft rocks." Computers and Geotechnics **66**: 142-157.

Gui, Y. and G.-F. Zhao (2015). "Modelling of laboratory soil desiccation cracking using DLSM with a two-phase bond model." Computers and Geotechnics **69**: 578-587.

Gui, Y., Z. Zhao, J. Kodikara, H. H. Bui and S. Yang (2016). "Numerical modelling of laboratory soil desiccation cracking using UDEC with a mix-mode cohesive fracture model." Engineering Geology **202**: 14-23.

Gutfraind, R. and S. B. Savage (1998). "Flow of fractured ice through wedge-shaped channels: smoothed particle hydrodynamics and discrete-element simulations." Mechanics of Materials **29**(1): 1-17.

Hagan, P. (1992). The cuttability of rock using a high pressure water jet. Western Australia Conference on Mining Geomechanics. Proceedings of the Western Australian Conference on Mining Geomechanics.

Haghighat, E. and S. Pietruszczak (2015). "On modeling of discrete propagation of localized damage in cohesive‐frictional materials." International Journal for Numerical and Analytical Methods in Geomechanics **39**(16): 1774-1790.

Hajibeygi, H., D. Karvounis and P. Jenny (2011). "A hierarchical fracture model for the iterative multiscale finite volume method." Journal of Computational Physics **230**(24): 8729-8743.

Handin, J., H. a. Heard and J. Magouirk (1967). "Effects of the intermediate principal stress on the failure of limestone, dolomite, and glass at different temperatures and strain rates." Journal of Geophysical Research **72**(2): 611-640.

Haramy, K. and M. DeMarco (1985). Use of the Schmidt hammer for rock and coal testing. The 26th US Symposium on Rock Mechanics (USRMS), American Rock Mechanics Association.

Hariri Ard, M. A., S. M. S. Kolbadi, M. Heshmati and H. Mirzabozor (2012). "Nonlinear analysis of concrete structural components using co-axial rotating smeared crack model." Journal of Applied Sciences **12**: 221-232.

Hattel, J. and P. Hansen (1995). "A control volume-based finite difference method for solving the equilibrium equations in terms of displacements." Applied Mathematical Modelling **19**(4): 210-243.

Hatzor, Y. H. and R. Benary (1998). "The stability of a laminated voussoir beam: back analysis of a historic roof collapse using DDA." International Journal of Rock Mechanics and Mining Sciences **35**(2): 165-181.

Hatzor, Y. H., I. Wainshtein and D. B. Mazor (2010). "Stability of shallow karstic caverns in blocky rock masses." International Journal of Rock Mechanics and Mining Sciences **47**(8): 1289-1303.

Hauser, F. E. (1966). "Techniques for measuring stress-strain relations at high strain rates." Experimental Mechanics **6**(8): 395-402.

Hayakawa, K. and S. Murakami (1997). "Thermodynamical modeling of elastic-plastic damage and experimental validation of damage potential." International Journal of Damage Mechanics **6**(4): 333-363.

He, M., H. Cao and A. Evans (1990). "Mixed-mode fracture: the four-point shear specimen." Acta Metallurgica et Materialia **38**(5): 839-846.

Hentz, S., F. V. Donzé and L. Daudeville (2004). "Discrete element modelling of concrete submitted to dynamic loading at high strain rates." Computers & structures **82**(29): 2509-2524.

Herreros, M. and M. Mabssout (2011). "A two-steps time discretization scheme using the SPH method for shock wave propagation." Computer methods in applied mechanics and engineering **200**(21): 1833-1845.

Hight, D., A. Gens and M. Symes (1983). "The development of a new hollow cylinder apparatus for investigating the effects of principal stress rotation in soils." Géotechnique **33**(4): 355-383.

Hoek, E. (1964). "Fracture of anisotropic rock." Journal of the South African Institute of Mining and Metallurgy **64**(10): 501-523.

Hoskins, E. (1969). The failure of thick-walled hollow cylinders of isotropic rock. International Journal of Rock Mechanics and Mining Sciences & Geomechanics Abstracts, Elsevier.

Hrennikoff, A. (1941). "Solution of problems of elasticity by the framework method." J. Appl. Mech.

Hu, D., Q. Zhu, H. Zhou and J. Shao (2010). "A discrete approach for anisotropic plasticity and damage in semi-brittle rocks." Computers and Geotechnics **37**(5): 658-666.

Huang, S., R. Chen and K. Xia (2010). "Quantification of dynamic tensile parameters of rocks using a modified Kolsky tension bar apparatus." Journal of Rock Mechanics and Geotechnical Engineering **2**(2): 162-168.

Huang, S., R. Chen and K. W. Xia (2010). "Quantification of dynamic tensile parameters of rocks using a modified Kolsky tension bar apparatus." Journal of Rock Mechanics and Geotechnical Engineering **2**(2): 162-168.

Huang, S., K. Xia and F. Dai (2012). "Establishment of a dynamic Mohr–Coulomb failure criterion for rocks." International Journal of Nonlinear Sciences and Numerical Simulation **13**(1): 55-60.

Huang, S., K. Xia, F. Yan and X. Feng (2010). "An Experimental Study of the Rate Dependence of Tensile Strength Softening of Longyou Sandstone." Rock Mechanics and Rock Engineering **43**(6): 677-683.

Huang, W. and X. Gao (2004). "Tresca and von Mises yield criteria: a view from strain space." Philosophical magazine letters **84**(10): 625-629.

Hucka, V. (1965). A rapid method of determining the strength of rocks in situ. International Journal of Rock Mechanics and Mining Sciences & Geomechanics Abstracts, Elsevier.

Hussain, M., S. Pu and J. Underwood (1974). Strain energy release rate for a crack under combined mode I and mode II. Fracture analysis: Proceedings of the 1973 national symposium on fracture mechanics, part II, ASTM International.

Ingraffea, A. R. (1981). Mixed-mode fracture initiation in Indiana limestone and Westerly granite. The 22nd US Symposium on Rock Mechanics (USRMS), American Rock Mechanics Association.

Irwin, G. R. (1958). "Fracture." In: Handbuch der Physik. Springer Verlag, Berlin **6**.

Irwin, G. R. (1959). "Analysis of stresses and strains near the end of a crack traversing a plate." J. Appl. Mech. **24**(361-364).

Janson, J. and J. Hult (1977). "Damage mechanics and fracture mechanics: a combined approach." J. Mec. Appl **1**: 69-84.

Jia, Y., X. Song, G. Duveau, K. Su and J.-F. Shao (2007). "Elastoplastic damage modelling of argillite in partially saturated condition and application." Physics and Chemistry of the Earth, Parts A/B/C **32**(8-14): 656-666.

Jian-An, H. and W. Sijing (1985). An experimental investigation concerning the comprehensive fracture toughness of some brittle rocks. International Journal of Rock Mechanics and Mining Sciences & Geomechanics Abstracts, Elsevier.

Jianhong, Y., F. Wu and J. Sun (2009). "Estimation of the tensile elastic modulus using Brazilian disc by applying diametrically opposed concentrated loads." International Journal of Rock Mechanics and Mining Sciences **46**(3): 568-576.

Jin, J. and N. Cristescu (1998). "An elastic/viscoplastic model for transient creep of rock salt." International Journal of Plasticity **14**(1-3): 85-107.

Jin, J., X. Li, G. Wang and Z. Yin (2012). "Failure modes and mechanisms of sandstone under cyclic impact loadings." Journal of Central South University (Science and Technology) **43**(4): 1453-1461.

Jing, L. (2003). "A review of techniques, advances and outstanding issues in numerical modelling for rock mechanics and rock engineering." International Journal of Rock Mechanics and Mining Sciences **40**(3): 283-353.

Jirásek, M. (2011). Damage and smeared crack models. Numerical modeling of concrete cracking, Springer**:** 1-49.

Jirásek, M. and Z. P. Bažant (1995). "Particle model for quasibrittle fracture and application to sea ice." Journal of engineering mechanics **121**(9): 1016-1025.

Jirasek, M., S. Rolshoven and P. Grassl (2004). "Size effect on fracture energy induced by non‐locality." International Journal for Numerical and Analytical Methods in Geomechanics **28**(7‐8): 653-670.

Jirásek, M. and T. Zimmermann (1998). "Analysis of rotating crack model." Journal of engineering mechanics **124**(8): 842-851.

Jirásek, M. and T. Zimmermann (1998). "Rotating crack model with transition to scalar damage." Journal of engineering mechanics **124**(3): 277-284.

John, R. and S. P. Shah (1990). "Mixed-mode fracture of concrete subjected to impact loading." Journal of Structural Engineering **116**(3): 585-602.

Kachanov, L. (1958). "On the time to failure under creep conditions, Izv." AN SSSR, Otd. Tekhn. Nauk **8**(26-31): 8.

Kahraman, S. and M. Fener (2007). "Predicting the Los Angeles abrasion loss of rock aggregates from the uniaxial compressive strength." Materials Letters **61**(26): 4861-4865.

Kahraman, S. and O. Toraman (2008). "Predicting Los Angeles abrasion loss of rock aggregates from crushability index." Bulletin of Materials Science **31**(2): 173-177.

Karami, A. and D. Stead (2008). "Asperity degradation and damage in the direct shear test: a hybrid FEM/DEM approach." Rock mechanics and rock engineering **41**(2): 229-266.

Katz, O., Z. Reches and J.-C. Roegiers (2000). "Evaluation of mechanical rock properties using a Schmidt Hammer." International Journal of Rock Mechanics and Mining Sciences **37**(4): 723-728.

Kawakita, M. and S. Kinoshita (1981). "The dynamic fracture properties of rocks under confining pressure." Memoirs of the Faculty of Engineering, Hokkaido University= 北海道大学工学部紀要 **15**(4): 467-478.

Kazerani, T., Z.-Y. Yang and J. Zhao (2012). "A discrete element model for predicting shear strength and degradation of rock joint by using compressive and tensile test data." Rock mechanics and rock engineering **45**(5): 695-709.

Kazerani, T., G. Zhao and J. Zhao (2010). "Dynamic fracturing simulation of brittle material using the distinct lattice spring method with a full rate-dependent cohesive law." Rock Mechanics and Rock Engineering **43**(6): 717-726.

Kazerani, T. and J. Zhao (2010). "Micromechanical parameters in bonded particle method for modelling of brittle material failure." International Journal for Numerical and Analytical Methods in Geomechanics **34**(18): 1877-1895.

Ke, T. (1997). Application of DDA to simulate fracture propagation in solid. Proceedings of the Second International Conference on Analysis of Discontinuous Deformation, Kyoto, Japan.

Kenner, V. H., S. H. Advani and T. G. Richard (1982). A study of fracture toughness for an anisotropic shale. The 23rd US Symposium on Rock Mechanics (USRMS), American Rock Mechanics Association.

Kermani, E. and T. Qiu (2017). Simulation of seepage through fixed porous media using the smoothed particle hydrodynamics method. Geotechnical Frontiers 2017**:** 699-708.

Kermani, E. and T. Qiu (2018). "Simulation of quasi-static axisymmetric collapse of granular columns using smoothed particle hydrodynamics and discrete element methods." Acta Geotechnica: 1-15.

Khan, K. and N. Al-Shayea (2000). "Effect of specimen geometry and testing method on mixed mode I–II fracture toughness of a limestone rock from Saudi Arabia." Rock Mechanics and Rock Engineering **33**(3): 179-206.

Kim, J. and G. J. Moridis (2013). "Development of the T+ M coupled flow–geomechanical simulator to describe fracture propagation and coupled flow–thermal–geomechanical processes in tight/shale gas systems." Computers & geosciences **60**: 184-198.

Klepaczko, J. and A. Brara (2001). "An experimental method for dynamic tensile testing of concrete by spalling." International Journal of Impact Engineering **25**(4): 387-409.

Kolo, I., R. K. Abu Al-Rub and R. L. Sousa (2016). "Computational Modelling of Fracture Propagation in Rocks Using a Coupled Elastic-Plasticity-Damage Model." Mathematical Problems in Engineering **2016**.

Kolsky, H. (1949). "An investigation of the mechanical properties of materials at very high rates of loading." Proceedings of the Physical Society. Section B **62**(11): 676.

Koo, C. and J. Chern (1997). Modeling of progressive fracture in jointed rock by DDA method. In Proceedings of the Second International Conference on Analysis of Discontinuous Deformation, Kyoto, Japan.

Kourdey, A., M. AIheib, J. Piguet and T. Korini (2001). "Evaluation of slope stability by numerical methods." S. arkk. a, Eloranta, editors. Rock mechanics—a challenge for society. Swetz and Zeitlinger Lisse, ISBN **90**(2651): 821.

Kovari, K., A. Tisa, H. Einstein and J. Franklin (1983). "Suggested methods for determining the strength of rock materials in triaxial compression: revised version." Intl J of Rock Mech & Mining Sci & Geomechanic Abs **20**(6).

Krajcinovic, D. (1985). "Continuous damage mechanics revisited: basic concepts and definitions."

Kranz, R. L. (1983). "Microcracks in rocks: a review." Tectonophysics **100**(1-3): 449-480.

Krätzig, W. B. and R. Pölling (1998). "Elasto-plastic damage-theories and elasto-plastic fracturing-theories–A comparison." Computational Materials Science **13**(1-3): 117-131.

Krishnan, G., X. Zhao, M. Zaman and J.-C. Roegiers (1998). "Fracture toughness of a soft sandstone." International Journal of Rock Mechanics and Mining Sciences **35**(6): 695-710.

Kubota, S., Y. Ogata, Y. Wada, G. Simangunsong, H. Shimada and K. Matsui (2008). "Estimation of dynamic tensile strength of sandstone." International Journal of Rock Mechanics and Mining Sciences **45**(3): 397-406.

Lankford, J. (1981). "The role of tensile microfracture in the strain rate dependence of compressive strength of fine-grained limestone-analogy with strong ceramics." International Journal of Rock Mechanics and Mining Science **18**(2).

Larsson, R., K. Runesson and S. Sture (1996). "Embedded localization band in undrained soil based on regularized strong discontinuity—theory and FE-analysis." International Journal of Solids and Structures **33**(20-22): 3081-3101.

Le Bellégo, C., J. F. Dubé, G. Pijaudier-Cabot and B. Gérard (2003). "Calibration of nonlocal damage model from size effect tests." European Journal of Mechanics-A/Solids **22**(1): 33-46.

Le, L., G. Nguyen, H. Bui, A. Sheikh and A. Kotousov (2020). Localisation and Lode-Angle Dependence of Geomaterial Behaviour. ACMSM25, Springer**:** 581-590.

Le, L. A., G. D. Nguyen and H. H. Bui (2020). Predicting onset and orientation of localisation bands using a cohesive-frictional model. CIGOS 2019, Innovation for Sustainable Infrastructure, Springer**:** 311-316.

Le, L. A., G. D. Nguyen, H. H. Bui, A. H. Sheikh and A. Kotousov (2018). "Localised failure mechanism as the basis for constitutive modelling of geomaterials." International Journal of Engineering Science **133**: 284-310.

Le, L. A., G. D. Nguyen, H. H. Bui, A. H. Sheikh and A. Kotousov (2019). "Incorporation of micro-cracking and fibre bridging mechanisms in constitutive modelling of fibre reinforced concrete." Journal of the Mechanics and Physics of Solids **133**: 103732.

Lemaitre, J. and J.-L. Chaboche (1994). Mechanics of solid materials, Cambridge university press.

Li, D.-y., W. Tao, T.-j. Cheng and X.-l. Sun (2016). "Static and dynamic tensile failure characteristics of rock based on splitting test of circular ring." Transactions of Nonferrous Metals Society of China **26**(7): 1912-1918.

Li, D. and L. N. Y. Wong (2013). "The Brazilian disc test for rock mechanics applications: review and new insights." Rock Mechanics and Rock Engineering **46**(2): 269-287.

Li, H., J. Zhao and T. Li (1999). "Triaxial compression tests on a granite at different strain rates and confining pressures." International Journal of Rock Mechanics and Mining Sciences **36**(8): 1057-1063.

Li, Q. and F. Ansari (1999). "Mechanics of damage and constitutive relationships for high-strength concrete in triaxial compression." Journal of engineering mechanics **125**(1): 1-10.

Li, X., F. Feng and D. Li (2018). "Numerical simulation of rock failure under static and dynamic loading by splitting test of circular ring." Engineering Fracture Mechanics **188**: 184-201.

Li, X., H. Lai and D. Gu (1993). "Energy absorption of rock fragmentation under impulsive loads with different wave forms." Trans Nonferr Metal Soc **3**(1): 1-5.

Li, Y.-N. and Z. P. Bažant (1997). "Cohesive crack model with rate-dependent opening and viscoelasticity: II. Numerical algorithm, behavior and size effect." International journal of fracture **86**(3): 267-288.

Li, Y., N. Fantuzzi and F. Tornabene (2013). "On mixed mode crack initiation and direction in shafts: strain energy density factor and maximum tangential stress criteria." Engineering Fracture Mechanics **109**: 273-289.

Libersky, L. D. and A. G. Petschek (1991). Smooth particle hydrodynamics with strength of materials. Advances in the free-Lagrange method including contributions on adaptive gridding and the smooth particle hydrodynamics method, Springer**:** 248-257.

Libersky, L. D., A. G. Petschek, T. C. Carney, J. R. Hipp and F. A. Allahdadi (1993). "High-Strain Lagrangian Hydrodynamics - a 3-Dimensional Sph Code for Dynamic Material Response." Journal of Computational Physics **109**(1): 67-75.

Lim, I., I. Johnston and S. Choi (1993). "Stress intensity factors for semi-circular specimens under three-point bending." Engineering Fracture Mechanics **44**(3): 363-382.

Lim, I., I. Johnston and S. Choi (1994). Assessment of mixed-mode fracture toughness testing methods for rock. International journal of rock mechanics and mining sciences & geomechanics abstracts, Elsevier.

Lim, I., I. Johnston, S. Choi and J. Boland (1994). Fracture testing of a soft rock with semi-circular specimens under three-point bending. Part 2—mixed-mode. International journal of rock mechanics and mining sciences & geomechanics abstracts, Elsevier.

Lin, H. and S. Atluri (2001). "The meshless local Petrov-Galerkin (MLPG) method for solving incompressible Navier-Stokes equations." CMES- Computer Modeling in Engineering and Sciences **2**(2): 117-142.

Lindholm, U. (1974). Review of dynamic testing techniques and material behavior. Mechanical properties at high rates of strain.

Lipkin, J., K. Schuler and T. Parry (1979). Dynamic torsional failure of limestone tubes, Sandia Labs., Albuquerque, NM (USA); Oxford Univ.(UK). Dept. of Engineering Science.

Liu, D. (1980). "Ore-bearing rock blasting physical process." Beijing, Metallurgical industry press: 428-433.

Liu, G.-R. and M. B. Liu (2003). Smoothed particle hydrodynamics: a meshfree particle method, World scientific.

Liu, K., Q. Zhang and J. Zhao (2018). Dynamic increase factors of rock strength. International Conference on Rock Dynamics and Applications (RocDyn) 2018, CRC Press.

Liu, X., J. Ning, Y. Tan and Q. Gu (2016). "Damage constitutive model based on energy dissipation for intact rock subjected to cyclic loading." International Journal of Rock Mechanics and Mining Sciences **85**: 27-32.

Ljunggren, C. and O. Stephansson (1986). Sleeve fracturing-a borehole technique for in-situ determination of rock deformability and rock stresses. ISRM International Symposium, International Society for Rock Mechanics and Rock Engineering.

Logan, J. M. and J. Handin (1970). Triaxial compression testing at intermediate strain rates. The 12th US Symposium on Rock Mechanics (USRMS), American Rock Mechanics Association.

Lucy, L. B. (1977). "A numerical approach to the testing of the fission hypothesis." The astronomical journal **82**: 1013-1024.

Luong, M. P. (1990). "Tensile and shear strengths of concrete and rock." Engineering Fracture Mechanics **35**(1-3): 127-135.

Lv, X., Y. Zhao, X. Huang, G. Xia and X. Su (2007). "A matrix-free implicit unstructured multigrid finite volume method for simulating structural dynamics and fluid–structure interaction." Journal of Computational Physics **225**(1): 120-144.

Ma, G., X. An and L. He (2010). "The numerical manifold method: a review." International Journal of Computational Methods **7**(01): 1-32.

Ma, G., X. Wang and F. Ren (2011). "Numerical simulation of compressive failure of heterogeneous rock-like materials using SPH method." International Journal of Rock Mechanics and Mining Sciences **48**(3): 353-363.

Ma, G. W., X. J. Wang and F. Ren (2011). "Numerical simulation of compressive failure of heterogeneous rock-like materials using SPH method." International Journal of Rock Mechanics and Mining Sciences **48**(3): 353-363.

Mabssout, M. and M. Herreros (2013). "Runge–Kutta vs Taylor-SPH: Two time integration schemes for SPH with application to Soil Dynamics." Applied Mathematical Modelling **37**(5): 3541-3563.

Mahajan, R. and K. Ravi-Chandar (1989). "An experimental investigation of mixed-mode fracture." International journal of fracture **41**(4): 235-252.

Maleki, K. and A. Pouya (2010). "Numerical simulation of damage–Permeability relationship in brittle geomaterials." Computers and Geotechnics **37**(5): 619-628.

Maranini, E. and T. Yamaguchi (2001). "A non-associated viscoplastic model for the behaviour of granite in triaxial compression." Mechanics of Materials **33**(5): 283-293.

Margevicius, R., J. Riedle and P. Gumbsch (1999). "Fracture toughness of polycrystalline tungsten under mode I and mixed mode I/II loading." Materials Science and Engineering: A **270**(2): 197-209.

Mariano, P. M. and F. L. Stazi (2004). "Strain localization due to crack–microcrack interactions: X-FEM for a multifield approach." Computer methods in applied mechanics and engineering **193**(45): 5035-5062.

Masuda, K., H. Mizutani and I. Yamada (1987). "Experimental study of strain-rate dependence and pressure dependence of failure properties of granite." Journal of Physics of the Earth **35**(1): 37-66.

Matsuoka, H. and T. Nakai (1985). "Relationship among tresca, mises, mohr-coulomb and matsuoka-nakai failure criteria." Soils and Foundations **25**(4): 123-128.

Mazars, J. and G. Pijaudier-Cabot (1989). "Continuum damage theory—application to concrete." Journal of engineering mechanics **115**(2): 345-365.

Mi, Y. and M. Aliabadi (1992). "Dual boundary element method for three-dimensional fracture mechanics analysis." Engineering Analysis with Boundary Elements **10**(2): 161-171.

Michelis, P. and E. Brown (1986). "A yield equation for rock." Canadian Geotechnical Journal **23**(1): 9-17.

Miller, T. and J. Cheatham Jr (1972). A new yield condition and hardening rule for rocks. International Journal of Rock Mechanics and Mining Sciences & Geomechanics Abstracts, Elsevier.

Mirsayar, M. and P. Park (2016). "Modified maximum tangential stress criterion for fracture behavior of zirconia/veneer interfaces." Journal of the mechanical behavior of biomedical materials **59**: 236-240.

Mises, R. v. (1913). "Mechanik der festen Körper im plastisch-deformablen Zustand." Nachrichten von der Gesellschaft der Wissenschaften zu Göttingen, Mathematisch-Physikalische Klasse **1913**: 582-592.

Mishra, D. and A. Basu (2012). "Use of the block punch test to predict the compressive and tensile strengths of rocks." International Journal of Rock Mechanics and Mining Sciences **51**: 119-127.

Mohamad-Hussein, A. and J.-F. Shao (2007). "Modelling of elastoplastic behaviour with non-local damage in concrete under compression." Computers & structures **85**(23-24): 1757-1768.

Mohr, D., G. Gary and B. Lundberg (2010). "Evaluation of stress–strain curve estimates in dynamic experiments." International Journal of Impact Engineering **37**(2): 161-169.

Monaghan, J. (1997). "SPH and Riemann solvers." Journal of Computational Physics **136**(2): 298-307.

Monaghan, J. and A. Kocharyan (1995). "SPH simulation of multi-phase flow." Computer physics communications **87**(1-2): 225-235.

Monaghan, J. J. (1994). "Simulating free surface flows with SPH." Journal of Computational Physics **110**(2): 399-406.

Monaghan, J. J. (1995). "Simulating gravity currents with SPH lock gates." Applied Mathematics Reports and Preprints, Monash University, Melbourne, Australia.

Monaghan, J. J. (1997). "Implicit SPH drag and dusty gas dynamics." Journal of Computational Physics **138**(2): 801-820.

Monaghan, J. J. (2000). "SPH without a tensile instability." Journal of Computational Physics **159**(2): 290-311.

Monaghan, J. J. (2002). "SPH compressible turbulence." Monthly notices of the royal astronomical society **335**(3): 843-852.

Monaghan, J. J. and R. A. Gingold (1983). "Shock simulation by the particle method SPH." Journal of Computational Physics **52**(2): 374-389.

Monaghan, J. J. and J. C. Lattanzio (1985). "A refined particle method for astrophysical problems." Astronomy and astrophysics **149**: 135-143.

Morris, J. P. (1996). Analysis of smoothed particle hydrodynamics with applications, Monash University Australia.

Morris, J. P. (2000). "Simulating surface tension with smoothed particle hydrodynamics." International journal for numerical methods in fluids **33**(3): 333-353.

Morris, J. P., P. J. Fox and Y. Zhu (1997). "Modeling low Reynolds number incompressible flows using SPH." Journal of Computational Physics **136**(1): 214-226.

Mortazavi, A. and P. Katsabanis (2001). "Modelling burden size and strata dip effects on the surface blasting process." International Journal of Rock Mechanics and Mining Sciences **38**(4): 481-498.

Motamedi, M., D. Weed and C. Foster (2016). "Numerical simulation of mixed mode (I and II) fracture behavior of pre-cracked rock using the strong discontinuity approach." International Journal of Solids and Structures **85**: 44-56.

Munjiza, A., D. Owen and N. Bicanic (1995). "A combined finite-discrete element method in transient dynamics of fracturing solids." Engineering computations **12**(2): 145-174.

Navarro, V., J. Alonso, B. Calvo and J. Sánchez (2010). "A constitutive model for porous rock including effects of bond strength degradation and partial saturation." International Journal of Rock Mechanics and Mining Sciences **47**(8): 1330-1338.

Neto, A. H. F. and R. I. Borja (2018). "Continuum hydrodynamics of dry granular flows employing multiplicative elastoplasticity." Acta Geotechnica **13**(5): 1027-1040.

Nguyen, C. T., C. T. Nguyen, H. H. Bui, G. D. Nguyen and R. Fukagawa (2017). "A new SPH-based approach to simulation of granular flows using viscous damping and stress regularisation." Landslides **14**(1): 69-81.

Nguyen, G. D., I. Einav and A. M. Korsunsky (2012). "How to connect two scales of behaviour in constitutive modelling of geomaterials." Géotechnique Letters **2**(3): 129-134.

Nguyen, G. D., A. M. Korsunsky and J. P.-H. Belnoue (2015). "A nonlocal coupled damage-plasticity model for the analysis of ductile failure." International Journal of Plasticity **64**: 56-75.

Nguyen, G. D., A. M. Korsunsky and I. Einav (2014). "A constitutive modelling framework featuring two scales of behaviour: fundamentals and applications to quasi-brittle failure." Engineering Fracture Mechanics **115**: 221-240.

Nguyen, G. D., C. T. Nguyen, H. H. Bui and V. P. Nguyen (2016). "Constitutive modelling of compaction localisation in porous sandstones." International Journal of Rock Mechanics and Mining Sciences **83**: 57-72.

Nguyen, G. D., C. T. Nguyen, V. P. Nguyen, H. H. Bui and L. Shen (2016). "A size-dependent constitutive modelling framework for localised failure analysis." Computational Mechanics **58**(2): 257-280.

Nguyen, N. H., H. H. Bui, G. D. Nguyen and J. Kodikara (2017). "A cohesive damage-plasticity model for DEM and its application for numerical investigation of soft rock fracture properties." International Journal of Plasticity.

Nguyen, N. H., H. H. Bui, G. D. Nguyen, J. Kodikara, S. Arooran and P. Jitsangiam (2017). "A thermodynamics-based cohesive model for discrete element modelling of fracture in cemented materials." International Journal of Solids and Structures **117**: 159-176.

Nguyen, T. T., H. H. Bui, T. D. Ngo and G. D. Nguyen (2017). "Experimental and numerical investigation of influence of air-voids on the compressive behaviour of foamed concrete." Materials & Design.

Niandou, H. (1994). Etude du comportement rhéologique et modélisation de l'argilité de tournemire: Applications à la stabilité d'ouvrages souterrains, Lille 1.

Ning, Y., J. Yang, X. An and G. Ma (2011). "Modelling rock fracturing and blast-induced rock mass failure via advanced discretisation within the discontinuous deformation analysis framework." Computers and Geotechnics **38**(1): 40-49.

Norbury, D. (1986). "The point load test." Geological Society, London, Engineering Geology Special Publications **2**(1): 325-329.

Obert, L. A. (1964). Triaxial method for determining the elastic constants of stress relief cores, US Dept. of the Interior, Bureau of Mines.

Oliver, J. (1989). "A consistent characteristic length for smeared cracking models." International journal for numerical methods in engineering **28**(2): 461-474.

Oliver, J. (1996). "Modelling strong discontinuities in solid mechanics via strain softening constitutive equations. Part 1: fundamentals." International journal for numerical methods in engineering **39**(21): 3575-3600.

Oliver, J., M. Cervera and O. Manzoli (1999). "Strong discontinuities and continuum plasticity models: the strong discontinuity approach." International Journal of Plasticity **15**(3): 319-351.

Oliyer, J. (1995). "Continuum modelling of strong discontinuities in solid mechanics using damage models." Computational Mechanics **17**(1-2): 49-61.

Olsson, W. A. (1999). "Theoretical and experimental investigation of compaction bands in porous rock." Journal of Geophysical Research: Solid Earth **104**(B4): 7219-7228.

Oñate, E., M. Cervera and O. Zienkiewicz (1994). "A finite volume format for structural mechanics." International journal for numerical methods in engineering **37**(2): 181-201.

Ozcelik, Y. (2011). "Predicting Los Angeles abrasion of rocks from some physical and mechanical properties." Scientific Research and Essays **6**(7): 1612-1619.

Paliwal, B., Y. Hammi, R. Moser and M. Horstemeyer (2017). "A three-invariant cap-plasticity damage model for cementitious materials." International Journal of Solids and Structures **108**: 186-202.

Pan, P.-Z., X.-T. Feng and J. Hudson (2012). "The influence of the intermediate principal stress on rock failure behaviour: a numerical study." Engineering Geology **124**: 109-118.

Pan, W., D. Li, A. M. Tartakovsky, S. Ahzi, M. Khraisheh and M. Khaleel (2013). "A new smoothed particle hydrodynamics non-Newtonian model for friction stir welding: Process modeling and simulation of microstructure evolution in a magnesium alloy." International Journal of Plasticity **48**: 189-204.

Pastor, M., T. Blanc, B. Haddad, S. Petrone, M. S. Morles, V. Drempetic, D. Issler, G. Crosta, L. Cascini and G. Sorbino (2014). "Application of a SPH depth-integrated model to landslide run-out analysis." Landslides **11**(5): 793-812.

Pastor, M., B. Haddad, G. Sorbino, S. Cuomo and V. Drempetic (2009). "A depth ‐ integrated, coupled SPH model for flow ‐ like landslides and related phenomena." International Journal for Numerical and Analytical Methods in Geomechanics **33**(2): 143-172.

Paterson, M. and D. Olgaard (2000). "Rock deformation tests to large shear strains in torsion." Journal of structural Geology **22**(9): 1341-1358.

Peerlings, R. H., R. de Borst, W. M. Brekelmans and J. De Vree (1996). "Gradient enhanced damage for quasi ‐ brittle materials." International journal for numerical methods in engineering **39**(19): 3391-3403.

Peerlings, R. H. J. (1999). "Enhanced damage modelling for fracture and fatigue."

Peng, C., X. Guo, W. Wu and Y. Wang (2016). "Unified modelling of granular media with Smoothed Particle Hydrodynamics." Acta Geotechnica **11**(6): 1231-1247.

Peng, R., H. Xie and Y. Ju (2007). "Analysis of energy dissipation and damage evolution of sandstone during tensile process." Chin J Rock Mech Eng **26**(12): 2526-2531.

Perkins, R., S. Green and M. Friedman (1970). Uniaxial stress behavior of porphyritic tonalite at strain rates to 103/second. International Journal of Rock Mechanics and Mining Sciences & Geomechanics Abstracts, Elsevier.

Perras, M. A. and M. S. Diederichs (2014). "A Review of the Tensile Strength of Rock: Concepts and Testing." Geotechnical and Geological Engineering **32**(2): 525-546.

Perrone, N. and R. Kao (1975). "A general finite difference method for arbitrary meshes." Computers & structures **5**(1): 45-57.

Petersson, P.-E. (1981). Crack growth and development of fracture zones in plain concrete and similar materials, Division, Inst.

Phan, D. G., G. D. Nguyen and H. H. Bui (2017). "A constitutive model for size dependent behaviour of soils."

Pietruszczak, S. and E. Haghighat (2015). "Modeling of deformation and localized failure in anisotropic rocks." International Journal of Solids and Structures **67**: 93-101.

Pietruszczak, S. and Z. Mroz (1981). "Finite element analysis of deformation of strain - softening materials." International journal for numerical methods in engineering **17**(3): 327-334.

Pietruszczak, S. and X. Niu (1993). "On the description of localized deformation." International Journal for Numerical and Analytical Methods in Geomechanics **17**(11): 791-805.

Pietruszczak, S. and G. Xu (1995). "Brittle response of concrete as a localization problem." International Journal of Solids and Structures **32**(11): 1517-1533.

Pijaudier-Cabot, G. and Z. P. Bažant (1987). "Nonlocal damage theory." Journal of engineering mechanics **113**(10): 1512-1533.

Pimanmas, A. and K. Maekawa (2001). "Multi-directional fixed crack approach for highly anisotropic shear behavior in precracked RC members." Doboku Gakkai Ronbunshu **2001**(669): 293-307.

Portela, A., M. Aliabadi and D. Rooke (1992). "The dual boundary element method: effective implementation for crack problems." International journal for numerical methods in engineering **33**(6): 1269-1287.

Pourhosseini, O. and M. Shabanimashcool (2014). "Development of an elasto-plastic constitutive model for intact rocks." International Journal of Rock Mechanics and Mining Sciences **66**: 1-12.

Price, A. and I. Farmer (1979). Application of yield models to rock. International Journal of Rock Mechanics and Mining Sciences & Geomechanics Abstracts, Elsevier.

Qu, Q. L., J. L. Wu, B. D. Guo and Y. P. Qin (2013). Numerical simulation of sphere impacting water by SPH with hydrodynamics. Advanced Materials Research, Trans Tech Publ.

Rabczuk, T. (2013). "Computational methods for fracture in brittle and quasi-brittle solids: state-of-the-art review and future perspectives." ISRN Applied Mathematics **2013**.

Rabczuk, T. and T. Belytschko (2004). "Cracking particles: a simplified meshfree method for arbitrary evolving cracks." International journal for numerical methods in engineering **61**(13): 2316-2343.

Rahimi, R. and R. Nygaard (2015). "Comparison of rock failure criteria in predicting borehole shear failure." International Journal of Rock Mechanics and Mining Sciences **79**: 29-40.

Rashid, Y. (1968). "Ultimate strength analysis of prestressed concrete pressure vessels." Nuclear engineering and design **7**(4): 334-344.

Reichmuth, D. R. (1962). Correlation of force-displacement date with physical properties of rock for percursive drilling systems, Univ. of Minnesota.

Reichmuth, D. R. (1967). Point load testing of brittle materials to determine tensile strength and relative brittleness. The 9th US Symposium on Rock Mechanics (USRMS), American Rock Mechanics Association.

Reinoso, J., M. Paggi and C. Linder (2017). "Phase field modeling of brittle fracture for enhanced assumed strain shells at large deformations: formulation and finite element implementation." Computational Mechanics **59**(6): 981-1001.

Reyes, O. and H. Einstein (1991). Failure mechanisms of fractured rock-a fracture coalescence model. 7th ISRM Congress, International Society for Rock Mechanics and Rock Engineering.

Richard, H. and K. Benitz (1983). "A loading device for the creation of mixed mode in fracture mechanics." International journal of fracture **22**(2): R55-R58.

Rittel, D., S. Lee and G. Ravichandran (2002). "A shear-compression specimen for large strain testing." Experimental Mechanics **42**(1): 58-64.

Rodriguez, J., J. Carbonell, J. Cante and J. Oliver (2016). "The particle finite element method (PFEM) in thermo‐mechanical problems." International journal for numerical methods in engineering **107**(9): 733-785.

Rodríguez, J. M., J. Carbonell, J. Cante and J. Oliver (2017). "Continuous chip formation in metal cutting processes using the Particle Finite Element Method (PFEM)." International Journal of Solids and Structures.

Rome, J., J. Isaacs and S. Nemat-Nasser (2002). Hopkinson techniques for dynamic triaxial compression tests. Recent advances in experimental mechanics, Springer**:** 3-12.

Rots, J. G. (1988). "Computational modeling of concrete fracture."

Rots, J. G., P. Nauta, G. Kuster and J. Blaauwendraad (1985). "Smeared crack approach and fracture localization in concrete." HERON, 30 (1), 1985.

Rusnak, J. and C. Mark (2000). "Using the point load test to determine the uniaxial compressive strength of coal measure rock."

Saksala, T. (2010). "Damage–viscoplastic consistency model with a parabolic cap for rocks with brittle and ductile behavior under low‐velocity impact loading." International Journal for Numerical and Analytical Methods in Geomechanics **34**(13): 1362-1386.

Salari, M. R., S. Saeb, K. J. Willam, S. J. Patchet and R. C. Carrasco (2004). "A coupled elastoplastic damage model for geomaterials." Computer methods in applied mechanics and engineering **193**(27-29): 2625-2643.

Salimzadeh, S. and N. Khalili (2015). "A three-phase XFEM model for hydraulic fracturing with cohesive crack propagation." Computers and Geotechnics **69**: 82-92.

Samaniego, E. and T. Belytschko (2005). "Continuum–discontinuum modelling of shear bands." International journal for numerical methods in engineering **62**(13): 1857-1872.

Sanborn, S. E. and J. H. Prévost (2011). "Frictional slip plane growth by localization detection and the extended finite element method (XFEM)." International Journal for Numerical and Analytical Methods in Geomechanics **35**(11): 1278-1298.

Shakoor, A. and C. Brown (1996). "Development of a quantitative relationship between unconfined compressive strength and Los Angeles abrasion loss for carbonate rocks." Bulletin of the International Association of Engineering Geology-Bulletin de l'Association Internationale de Géologie de l'Ingénieur **53**(1): 97-103.

Shan, R., Y. Jiang and B. Li (2000). "Obtaining dynamic complete stress–strain curves for rock using the split Hopkinson pressure bar technique." International Journal of Rock Mechanics and Mining Sciences **37**(6): 983-992.

Shao, J.-F., Y. Jia, D. Kondo and A.-S. Chiarelli (2006). "A coupled elastoplastic damage model for semi-brittle materials and extension to unsaturated conditions." Mechanics of Materials **38**(3): 218-232.

Shao, J.-F., Q.-Z. Zhu and K. Su (2003). "Modeling of creep in rock materials in terms of material degradation." Computers and Geotechnics **30**(7): 549-555.

Shao, J., K. Chau and X. Feng (2006). "Modeling of anisotropic damage and creep deformation in brittle rocks." International Journal of Rock Mechanics and Mining Sciences **43**(4): 582-592.

Shao, J. F. and J. W. Rudnicki (2000). "A microcrack-based continuous damage model for brittle geomaterials." Mechanics of Materials **32**(10): 607-619.

Shao, S. and E. Y. Lo (2003). "Incompressible SPH method for simulating Newtonian and non-Newtonian flows with a free surface." Advances in water resources **26**(7): 787-800.

Sharpe, W. N. (2008). Springer handbook of experimental solid mechanics, Springer Science & Business Media.

Sheikh, B. and T. Qiu (2019). Modeling the Impact Force from a Dry Granular Flow Using Smoothed Particle Hydrodynamics Method. Geo-Congress 2019: Geotechnical Materials, Modeling, and Testing, American Society of Civil Engineers Reston, VA.

Sheorey, P. (1984). "Schmidt hammer rebound data for estimation of large scale in situ coal strength." Int. J. Rock Mech. Min. Sci. Geomech. Abstr.;(United States) **21**(1).

Sheorey, P. R. (1997). Empirical rock failure criteria, AA Balkema.

Shetty, D. K., A. R. Rosenfield and W. H. Duckworth (1987). "Mixed-mode fracture in biaxial stress state: application of the diametral-compression (Brazilian disk) test." Engineering Fracture Mechanics **26**(6): 825-840.

Shi, G.-H. (1992). "Discontinuous deformation analysis: a new numerical model for the statics and dynamics of deformable block structures." Engineering computations **9**(2): 157-168.

Shi, G.-h. (1992). Manifold method of material analysis, DTIC Document.

Sih, G. (1973). "Some basic problems in fracture mechanics and new concepts." Engineering Fracture Mechanics **5**(2): 365-377.

Sih, G. and E. Madenci (1983). "Fracture initiation under gross yielding: strain energy density criterion." Engineering Fracture Mechanics **18**(3): 667-677.

Simo, J. and J. Ju (1987). "Strain-and stress-based continuum damage models—II. Computational aspects." International Journal of Solids and Structures **23**(7): 841-869.

Simo, J. C. and J. Ju (1987). "Strain-and stress-based continuum damage models—I. Formulation." International Journal of Solids and Structures **23**(7): 821-840.

Singh, D., V. Sastry and P. Srinivas (1989). Effect of strain rate on mechanical behaviour of rocks. ISRM International Symposium, International Society for Rock Mechanics and Rock Engineering.

Singh, T., A. Verma, V. Singh and A. Sahu (2005). "Slake durability study of shaly rock and its predictions." Environmental Geology **47**(2): 246-253.

Sluys, L. and A. Berends (1998). "Discontinuous failure analysis for mode-I and mode-II localization problems." International Journal of Solids and Structures **35**(31-32): 4257-4274.

Somigliana, C. (1885). "Sopra l'equilibrio di un corpo elastico isotropo." Il Nuovo Cimento (1877-1894) **17**(1): 140-148.

Song, J. H., P. Areias and T. Belytschko (2006). "A method for dynamic crack and shear band propagation with phantom nodes." International Journal for Numerical Methods in Engineering **67**(6): 868-893.

Souley, M., G. Armand, K. Su and M. Ghoreychi (2011). "Modeling the viscoplastic and damage behavior in deep argillaceous rocks." Physics and Chemistry of the Earth, Parts A/B/C **36**(17-18): 1949-1959.

Stephansson, O. (1983). Rock stress measurement by sleeve fracturing. 5th ISRM Congress, International Society for Rock Mechanics and Rock Engineering.

Strömberg, L. and M. Ristinmaa (1996). "FE-formulation of a nonlocal plasticity theory." Computer methods in applied mechanics and engineering **136**(1-2): 127-144.

Sukumar, N. and T. Belytschko (2000). "Arbitrary branched and intersecting cracks with the extended finite element method." Int. J. Numer. Meth. Eng **48**: 1741-1760.

Sulsky, D., S.-J. Zhou and H. L. Schreyer (1995). "Application of a particle-in-cell method to solid mechanics." Computer physics communications **87**(1-2): 236-252.

Sun, C.-T., Z. Jin and C. Sun (2012). "CHAPTER 3 The Elastic Stress Field around a Crack Tip." Fracture Mechanics: 25-75.

Suresh, S., C. Shih, A. Morrone and N. O'Dowd (1990). "Mixed‐mode fracture toughness of ceramic materials." Journal of the American Ceramic Society **73**(5): 1257-1267.

Swegle, J. (1992). Report at Sandia National Laboratories, August.

Swegle, J. and S. Attaway (1995). "On the feasibility of using smoothed particle hydrodynamics for underwater explosion calculations." Computational Mechanics **17**(3): 151-168.

Swegle, J., D. Hicks and S. Attaway (1995). "Smoothed particle hydrodynamics stability analysis." Journal of Computational Physics **116**(1): 123-134.

Swoboda, G. and Q. Yang (1999). "An energy-based damage model of geomaterials—I. Formulation and numerical results." International Journal of Solids and Structures **36**(12): 1719-1734.

Swoboda, G. and Q. Yang (1999). "An energy-based damage model of geomaterials—II. Deductionof damage evolution laws." International Journal of Solids and Structures **36**(12): 1735-1755.

Takeda, H., S. M. Miyama and M. Sekiya (1994). "Numerical simulation of viscous flow by smoothed particle hydrodynamics." Progress of theoretical physics **92**(5): 939-960.

Talesnick, M. and E. Bloch-Friedman (1999). "Compatibility of different methodologies for the determination of elastic parameters of intact anisotropic rocks." International Journal of Rock Mechanics and Mining Sciences **36**(7): 919-940.

Talesnick, M. and M. Brafman (1998). "Small strain deformation characteristics of two chalks subjected to varying stress conditions." Quarterly Journal of Engineering Geology and Hydrogeology **31**(3): 161-174.

Talesnick, M. and S. Frydman (1990). "The preparation of hollow cylinder specimens from undisturbed tube samples of soft clay." Geotechnical Testing Journal **13**(3): 243-249.

Talesnick, M. and M. Ringel (1999). "Completing the hollow cylinder methodology for testing of transversely isotropic rocks: torsion testing." International Journal of Rock Mechanics and Mining Sciences **36**(5): 627-639.

Talesnick, M. L., M. Lee and B. Haimson (1995). "On the determination of elastic material parameters of transverse isotropic rocks from a single test specimen." Rock Mechanics and Rock Engineering **28**(1): 17-35.

Tao, X. and D. V. Phillips (2005). "A simplified isotropic damage model for concrete under bi-axial stress states." Cement and Concrete Composites **27**(6): 716-726.

Taylor, G. A. (1996). A vertex based discretisation scheme applied to material non-linearity within a multi-physics finite volume framework, University of Greenwich.

Theocaris, P. and N. Andrianopoulos (1982). "A modified strain-energy density criterion applied to crack propagation."

Tresca, H. (1864). "On the yield of solids at high pressures." Comptes Rendus Academie des Sciences **59**: 754.

Ugur, I., S. Demirdag and H. Yavuz (2010). "Effect of rock properties on the Los Angeles abrasion and impact test characteristics of the aggregates." Materials characterization **61**(1): 90-96.

Van Mier, J. G. (1986). Fracture of concrete under complex stress, Faculty of Civil Engineering, Delft University of Technology.

Van Vliet, M. R. and J. G. Van Mier (2000). "Experimental investigation of size effect in concrete and sandstone under uniaxial tension." Engineering Fracture Mechanics **65**(2): 165-188.

Veiskarami, M. and M. M. Tamizdoust (2017). "Bifurcation analysis in sands under true triaxial conditions with coaxial and noncoaxial plastic flow rules." Journal of engineering mechanics **143**(10): 04017120.

VonNeumann, J. and R. D. Richtmyer (1950). "A method for the numerical calculation of hydrodynamic shocks." Journal of applied physics **21**(3): 232-237.

Vořechovský, M. and V. Sadílek (2008). "Computational modeling of size effects in concrete specimens under uniaxial tension." International journal of fracture **154**(1-2): 27-49.

Voyiadjis, G. Z. and R. K. A. Al-Rub (2005). "Gradient plasticity theory with a variable length scale parameter." International Journal of Solids and Structures **42**(14): 3998-4029.

Vu, V. D., A. H. Sheikh, G. D. Nguyen and L. Shen (2017). "A kinematically enhanced constitutive model for elastic and inelastic analysis of unidirectional fibre reinforced composite materials." International Journal of Mechanical Sciences **126**: 171-185.

Vyazmensky, A., D. Stead, D. Elmo and A. Moss (2010). "Numerical analysis of block caving-induced instability in large open pit slopes: a finite element/discrete element approach." Rock mechanics and rock engineering **43**(1): 21-39.

Wang, C., Z. Zhu and H. Liu (2016). "On the I‐II mixed mode fracture of granite using four‐point bend specimen." Fatigue & Fracture of Engineering Materials & Structures **39**(10): 1193-1203.

Wang, Q., X. Jia, S. Kou, Z. Zhang and P.-A. Lindqvist (2004). "The flattened Brazilian disc specimen used for testing elastic modulus, tensile strength and fracture toughness of brittle rocks: analytical and numerical results." International Journal of Rock Mechanics and Mining Sciences **41**(2): 245-253.

Wang, Y.-X., P. Cao, Y.-H. Huang, R. Chen and J.-T. Li (2012). "Nonlinear damage and failure behavior of brittle rock subjected to impact loading." Int. J. Nonlinear Sci. Numer. Simul. **13**(1): 61-68.

Weibull, W. (1951). "A statistical distribution function of wide applicability." Journal of applied mechanics **18**(3): 293-297.

Weibull, W., W. Weibull, S. Physicist, W. Weibull, S. Physicien and W. Weibull (1949). A statistical representation of fatigue failures in solids, Elander.

Weihe, S., B. Kröplin and R. De Borst (1998). "Classification of smeared crack models based on material and structural properties." International Journal of Solids and Structures **35**(12): 1289-1308.

Wells, G. and L. Sluys (2001). "A new method for modelling cohesive cracks using finite elements." International Journal for Numerical Methods in Engineering **50**(12): 2667-2682.

Westergaard, H. M. (1939). "Bearing pressures and cracks." Trans AIME, J. Appl. Mech. **6**: 49-53.

Wheel, M. (1996). "A geometrically versatile finite volume formulation for plane elastostatic stress analysis." The Journal of Strain Analysis for Engineering Design **31**(2): 111-116.

Wheel, M. (1999). "A mixed finite volume formulation for determining the small strain deformation of incompressible materials." International journal for numerical methods in engineering **44**(12): 1843-1861.

Williams, J. and P. Ewing (1972). "Fracture under complex stress—the angled crack problem." International Journal of Fracture Mechanics **8**(4): 441-446.

Wong, E.-H. and Y.-W. Mai (2015). Robust Design of Microelectronics Assemblies Against Mechanical Shock, Temperature and Moisture, Woodhead Publishing.

Wong, T.-f., H. Szeto and J. Zhang (1992). "Effect of loading path and porosity on the failure mode of porous rocks."

Wu, C. H. (1978). "Maximum-energy-release-rate criterion applied to a tension-compression specimen with crack." Journal of Elasticity **8**(3): 235-257.

Wu, J.-Y. (2017). "A unified phase-field theory for the mechanics of damage and quasi-brittle failure." Journal of the Mechanics and Physics of Solids **103**: 72-99.

Xia, K., S. Huang and F. Dai (2013). "Evaluation of the frictional effect in dynamic notched semi-circular bend tests." International Journal of Rock Mechanics and Mining Sciences(62): 148-151.

Xie, H., Y. Ju and L. Li (2005). "Criteria for strength and structural failure of rocks based on energy dissipation and energy release principles." Chinese Journal of Rock Mechanics and Engineering **24**(17): 3003-3010.

Yagiz, S. (2009). "Assessment of brittleness using rock strength and density with punch penetration test." Tunnelling and Underground Space Technology **24**(1): 66-74.

Yan, F., X.-T. Feng, R. Chen, K. Xia and C. Jin (2011). "Dynamic Tensile Failure of the Rock Interface Between Tuff and Basalt." Rock Mechanics and Rock Engineering **45**(3): 341-348.

Yan, F., X.-T. Feng, R. Chen, K. Xia and C. Jin (2012). "Dynamic tensile failure of the rock interface between tuff and basalt." Rock Mechanics and Rock Engineering **45**(3): 341-348.

Yao, W., T. He and K. Xia (2017). "Dynamic mechanical behaviors of Fangshan marble." Journal of Rock Mechanics and Geotechnical Engineering **9**(5): 807-817.

Yarema, S. Y. and G. Krestin (1967). "Determination of the modulus of cohesion of brittle materials by compressive tests on disc specimens containing cracks." Appl. Mech. Rev.;(United States) **2**(1).

Yazdani, S. and H. Schreyer (1990). "Combined plasticity and damage mechanics model for plain concrete." Journal of engineering mechanics **116**(7): 1435-1450.

Yin, T., X. Li, W. Cao and K. Xia (2015). "Effects of Thermal Treatment on Tensile Strength of Laurentian Granite Using Brazilian Test." Rock Mechanics and Rock Engineering **48**(6): 2213-2223.

You, M. (2009). "True-triaxial strength criteria for rock." International Journal of Rock Mechanics and Mining Sciences **46**(1): 115-127.

Yu, M.-h. (2002). "Advances in strength theories for materials under complex stress state in the 20th century." Appl. Mech. Rev. **55**(3): 169-218.

Yu, M.-H., Y.-W. Zan, J. Zhao and M. Yoshimine (2002). "A unified strength criterion for rock material." International Journal of Rock Mechanics and Mining Sciences **39**(8): 975-989.

Yu, Y.-l. (1992). "Study on dynamic characteristic of rocks using triaxial SHPB." Chin J Geotech Eng **14**(3): 76-79.

Yudhbir, Y., W. Lemanza and F. Prinzl (1983). An empirical failure criterion for rock masses. 5th ISRM congress, International Society for Rock Mechanics and Rock Engineering.

Yukio, U., I. Kazuo, Y. Tetsuya and A. Mitsuru (1983). "Characteristics of brittle fracture under general combined modes including those under bi-axial tensile loads." Engineering Fracture Mechanics **18**(6): 1131-1158.

Yumlu, M. and M. Ozbay (1995). A study of the behaviour of brittle rocks under plane strain and triaxial loading conditions. International journal of rock mechanics and mining sciences & geomechanics abstracts, Elsevier.

Zhang, D. Z., X. Ma and P. T. Giguere (2011). "Material point method enhanced by modified gradient of shape function." Journal of Computational Physics **230**(16): 6379-6398.

Zhang, G.-x., Y. Zhao, G.-H. Shi and X.-C. Peng (2007). "Toppling failure simulation of rock slopes by numerical manifold method." Yantu Gongcheng Xuebao(Chinese Journal of Geotechnical Engineering) **29**(6): 800-805.

Zhang, G., Y. Sugiura, H. Hasegawa and F. Chen (2000). Crack propagation by manifold and singular boundary element method. International conference on engineering computational technology.

Zhang, H., L. Li, X. An and G. Ma (2010). "Numerical analysis of 2-D crack propagation problems using the numerical manifold method." Engineering analysis with boundary elements **34**(1): 41-50.

Zhang, H. and L. Zhou (2006). "Numerical manifold method for dynamic nonlinear analysis of saturated porous media." International Journal for Numerical and Analytical Methods in Geomechanics **30**(9): 927-951.

Zhang, J., W. Xu, H. Wang, R. Wang, Q. Meng and S. Du (2016). "A coupled elastoplastic damage model for brittle rocks and its application in modelling underground excavation." International Journal of Rock Mechanics and Mining Sciences **84**: 130-141.

Zhang, Q. and J. Zhao (2014). "A review of dynamic experimental techniques and mechanical behaviour of rock materials." Rock mechanics and rock engineering **47**(4): 1411-1478.

Zhang, Q. B. and J. Zhao (2013). "Determination of mechanical properties and full-field strain measurements of rock material under dynamic loads." International Journal of Rock Mechanics and Mining Sciences **60**: 423-439.

Zhang, Q. B. and J. Zhao (2013). "A Review of Dynamic Experimental Techniques and Mechanical Behaviour of Rock Materials." Rock Mechanics and Rock Engineering **47**(4): 1411-1478.

Zhang, Q. B. and J. Zhao (2014). "A review of dynamic experimental techniques and mechanical behaviour of rock materials." Rock mechanics and rock engineering **47**(4): 1411-1478.

Zhang, W., B. Dai, Z. Liu and C. Zhou (2016). "Modeling discontinuous rock mass based on smoothed finite element method." Computers and Geotechnics **79**: 22-30.

Zhang, X., K. Krabbenhoft, D. Pedroso, A. Lyamin, D. Sheng, M. V. Da Silva and D. Wang (2013). "Particle finite element analysis of large deformation and granular flow problems." Computers and Geotechnics **54**: 133-142.

Zhang, Y. and X. Zhuang (2018). "Cracking elements: A self-propagating strong discontinuity embedded approach for quasi-brittle fracture." Finite Elements in Analysis and Design **144**: 84-100.

Zhang, Z., S. Kou, L. Jiang and P.-A. Lindqvist (2000). "Effects of loading rate on rock fracture: fracture characteristics and energy partitioning." International Journal of Rock Mechanics and Mining Sciences **37**(5): 745-762.

Zhang, Z., Y. Yu and Q. Zhao (1993). "Influences of loading rates on fracture toughness of gabbro and marble." ROSSMANITH H P. Fracture and Damage of Concrete and Rock FDCR-2. London: E & FN Spon: 418-425.

Zhao, G.-F., N. Khalili, J. Fang and J. Zhao (2012). "A coupled distinct lattice spring model for rock failure under dynamic loads." Computers and Geotechnics **42**: 1-20.

Zhao, G.-F., J.-J. Lian, A. R. Russell and J. Zhao (2016). "Three-dimensional DDA and DLSM coupled approach for rock cutting and rock penetration." International Journal of Geomechanics **17**(5): E4016015.

Zhao, G.-F., A. R. Russell, X. Zhao and N. Khalili (2014). "Strain rate dependency of uniaxial tensile strength in Gosford sandstone by the Distinct Lattice Spring Model with X-ray micro CT." International Journal of Solids and Structures **51**(7): 1587-1600.

Zhao, G. and N. Khalili (2012). "Graphics processing unit based parallelization of the distinct lattice spring model." Computers and Geotechnics **42**: 109-117.

Zhao, G. and N. Khalili (2012). "A lattice spring model for coupled fluid flow and deformation problems in geomechanics." Rock Mechanics and Rock Engineering **45**(5): 781-799.

Zhao, G. and J. Zhao (2010). Microscopic numerical modelling of the dynamic strength of brittle rock, Research Publishing Services, No 83 Genting Lane,# 08-01, Genting Building ….

Zhao, G. F., J. Fang, L. Sun and J. Zhao (2013). "Parallelization of the distinct lattice spring model." International Journal for Numerical and Analytical Methods in Geomechanics **37**(1): 51-74.

Zhao, G. F., J. Fang and J. Zhao (2011). "A 3D distinct lattice spring model for elasticity and dynamic failure." International Journal for Numerical and Analytical Methods in Geomechanics **35**(8): 859-885.

Zhao, H. and G. Gary (1996). "On the use of SHPB techniques to determine the dynamic behavior of materials in the range of small strains." International Journal of Solids and Structures **33**(23): 3363-3375.

Zhao, J. (2000). "Applicability of Mohr–Coulomb and Hoek–Brown strength criteria to the dynamic strength of brittle rock." International Journal of Rock Mechanics and Mining Sciences **37**(7): 1115-1121.

Zhao, J. and H. Li (2000). "Experimental determination of dynamic tensile properties of a granite." International Journal of Rock Mechanics and Mining Sciences **37**(5): 861-866.

Zhao, J., H. Li, M. Wu and T. Li (1999). "Dynamic uniaxial compression tests on a granite." International Journal of Rock Mechanics and Mining Sciences **36**(2): 273-277.

Zhao, P., F. Lu, R. Chen, Y. Lin, J. Li, L. Lu and G. Sun (2011). "A technique for combined dynamic compression-shear test." Review of Scientific Instruments **82**(3): 035110.

Zhao, S., H. H. Bui, V. Lemiale and G. D. Nguyen (2017). SPH Simulation of Strain Localisation in Geomaterials Using a Visco-Plastic Constitutive Model. Poromechanics VI**:** 1876-1883.

Zhao, S., H. H. Bui, V. Lemiale, G. D. Nguyen and F. Darve (2019). "A generic approach to modelling flexible confined boundary conditions in SPH and its application." International Journal for Numerical and Analytical Methods in Geomechanics **43**(5): 1005-1031.

Zhou, F., J.-F. Molinari and T. Shioya (2005). "A rate-dependent cohesive model for simulating dynamic crack propagation in brittle materials." Engineering Fracture Mechanics **72**(9): 1383-1410.

Zhou, H., Y. Jia and J.-F. Shao (2008). "A unified elastic–plastic and viscoplastic damage model for quasi-brittle rocks." International Journal of Rock Mechanics and Mining Sciences **45**(8): 1237-1251.

Zhou, H., K. Zhang and X. Feng (2011). "A coupled elasto-plastic-damage mechanical model for marble." Science China Technological Sciences **54**(1): 228-234.

Zhou, X.-p., Q.-h. Qian and H.-q. Yang (2010). "Effect of loading rate on fracture characteristics of rock." Journal of Central South University of Technology **17**: 150-155.

Zhou, Y. X., K. Xia, X. B. Li, H. B. Li, G. W. Ma, J. Zhao, Z. L. Zhou and F. Dai (2012). "Suggested methods for determining the dynamic strength parameters and mode-I fracture toughness of rock materials." International Journal of Rock Mechanics and Mining Sciences **49**: 105-112.

Zhu, J. (2013). "DEM modeling of wave propagation through jointed rock mass." Rock Dynamics and Applications-State of the Art: 443.

Zhu, J., G. Zhao, X. Zhao and J. Zhao (2011). "Validation study of the distinct lattice spring model (DLSM) on P-wave propagation across multiple parallel joints." Computers and Geotechnics **38**(2): 298-304.

Zipf Jr, R. K. and Z. Bieniawski (1986). Mixed mode testing for fracture toughness of coal based on critical-energy-density. The 27th US Symposium on Rock Mechanics (USRMS), American Rock Mechanics Association.

Zipf, R. K. and Z. Bieniawski (1988). Microscopic studies of fractures generated under mixed mode loading. The 29th US Symposium on Rock Mechanics (USRMS), American Rock Mechanics Association.